



HAL
open science

Computer-aided generation, 3D-printing and experimental study of porous and composite materials

Zahra Hooshmand Ahoor

► **To cite this version:**

Zahra Hooshmand Ahoor. Computer-aided generation, 3D-printing and experimental study of porous and composite materials. Mechanical engineering [physics.class-ph]. Institut Polytechnique de Paris, 2023. English. NNT: 2023IPPAX031 . tel-04432693

HAL Id: tel-04432693

<https://theses.hal.science/tel-04432693v1>

Submitted on 1 Feb 2024

HAL is a multi-disciplinary open access archive for the deposit and dissemination of scientific research documents, whether they are published or not. The documents may come from teaching and research institutions in France or abroad, or from public or private research centers.

L'archive ouverte pluridisciplinaire **HAL**, est destinée au dépôt et à la diffusion de documents scientifiques de niveau recherche, publiés ou non, émanant des établissements d'enseignement et de recherche français ou étrangers, des laboratoires publics ou privés.



INSTITUT
POLYTECHNIQUE
DE PARIS

NNT : 2023IPPAX031

Thèse de doctorat



Computer-aided generation, 3D-printing and experimental study of porous and composite materials

Thèse de doctorat de l'Institut Polytechnique de Paris
préparée à l'École polytechnique

École doctorale n°626 École doctorale de l'Institut Polytechnique de Paris (EDIPP)
Spécialité de doctorat : Mécanique des fluides et des solides, acoustique

Thèse présentée et soutenue à Palaiseau, le 21 avril, par

ZAHRA HOOSHMAND AHOOR

Composition du Jury :

M. Eric CHARKALUK Directeur de Recherche, LMS, C.N.R.S, École polytechnique	Président
M. Justin DIRRENBARGER Maître de conférences et HDR, PIMM, Conservatoire National des Arts et Métiers (CNAM)	Rapporteur
M. Benoît ROMAN Directeur de Recherche, PMMH, ESPCI, C.N.R.S, Sorbonne Université	Rapporteur
Mme. Christelle COMBESCURE Maître de conférences, Ecoles de Saint-Cyr Coëtquidan, Université Bretagne Sud	Examinatrice
M. Vikram DESHPANDE Professeur, Department of Engineering, University of Cambridge	Examineur
M. Dennis KOCHMANN Professeur, Department of Mechanical and Process Engineering, ETH Zürich	Examineur
M. Konstantinos DANAS Directeur de Recherche, LMS, C.N.R.S, École polytechnique	Directeur de thèse
Mme. Gabriella TARANTINO Maître de conférences, ICMO, C.N.R.S, Université Paris-Saclay	Co-Encadrante

**Computer-aided generation,
3D-printing and experimental study
of porous and composite materials**

Ph.D. Thesis
Submitted by

Zahra HOOSHMAND AHOOR

Thesis advisors:

**Konstantinos DANAS
Gabriella TARANTINO**

Laboratoire de Mécanique des Solids (LMS)
École Polytechnique
Institute Polytechnique de Paris

To my family...

Acknowledgments

This thesis was conducted at the Laboratoire de Mécanique des Solides (LMS) as part of the doctoral program of Ecole Polytechnique, mainly funded by the school, as well as partially by the prestigious Gaspard Monge fellowship.

I would like to express my deepest gratitude and appreciation to all those who have supported me during this thesis preparation process.

First and foremost, I am immensely grateful to my thesis advisor Professor Kostas Danas. It has been an honor and a privilege to work alongside him, and I am grateful for the knowledge and skills I have gained under his mentorship. His deep knowledge, expertise, and unwavering support have shaped the direction of this research. His valuable insights, constructive feedback, and dedication to my academic growth have been truly invaluable.

I would also like to extend my sincere thanks to my thesis co-advisor Professor Gabriella Tarantino. Her exceptional guidance, constructive feedback, and insightful suggestions have significantly helped the development and quality of this work. Her support and mentorship have not only contributed to the academic rigor of this thesis but have also played a vital role in my personal and professional growth.

I would also like to thank Professor Benoit Roman and Professor Justin Dirrenberger for spending their valuable time to read and comment on my thesis manuscript. My gratitude is also extended to the members of my thesis committee, Professor Eric Charkaluk for accepting to be the president of my thesis committee as well as Professor Vikram Deshpande, Professor Dennis Kochmann and Professor Christelle Combescure for participating in my thesis committee and their valuable input and suggestions.

A special word of thanks goes to the staff and all of the people at LMS who have supported me and provided such a warm and helpful environment. In particular, I would like to thank Alexandra, Anna and Valerie for their support in the complicated administrative process. Furthermore, I am grateful for all the equipment and technical support that was provided by Abdelfattah. I would also like to thank Vincent, Hakim, Simon, as well as the entire team of engineers and technicians for their great technical contribution during the preparation of the experimental setup. Several results would not have been possible without their help. Moreover, I would like to acknowledge my friends and colleagues Kubra, Nikhil, Martin and Nina for their support and for the wonderful and memorable times we shared together.

I would like to extend my deepest gratitude to my parents Abolfazl and Masumeh and

my brother Mahdi for their unconditional love, encouragement, and support throughout this endeavor. Their constant belief in my abilities has been a driving force behind my accomplishments. I am forever grateful for their sacrifices and support to perform my studies abroad.

As a final note, my heartfelt appreciation goes to my husband, Iman. This work could not have been accomplished without his constant support, motivation, understanding, patience and sacrifice of his own time to create a conducive environment for my research and writing.

Abstract

The present study deals with computer-aided design, 3D-printing, large strain numerical simulation, and experimental testing of random geometries with focus on porous materials. In particular, we attempt to assess the effect of random porous features on the mechanical response at large strain by comparing the response of well-chosen random and periodic porous geometries. We first investigate the computer-aided design process of a variety of porous geometries including random polydisperse porous materials with spherical and ellipsoidal voids, standard eroded Voronoi geometries, hexagonal honeycombs, and TPMS structures. In addition, we propose a novel computer-design strategy to obtain a new type of random Voronoi-type porous materials called M-Voronoi (from mechanically grown) with smooth void shapes and variable intervoid ligament sizes that can reach very low relative densities. This is achieved via a numerical, large strain, nonlinear elastic, void growth mechanical process. The proposed M-Voronoi method is general and can be applied to create both two and three-dimensional random geometries and allows the formation of isotropic or anisotropic materials. The void growth process is a direct consequence of mass conservation and the incompressibility of the surrounding nonlinear elastic matrix phase and the final achieved relative density may be analytically estimated in terms of the determinant of the applied deformation gradient. The extremely low densities in the M-Voronoi geometries are achieved through an intermediate remesh step in the virtual fabrication process. For this purpose, we developed a versatile and general remeshing algorithm based on the geometry reconstruction of an orphan mesh that can handle arbitrarily complex meshes, including those that contain voids or multiple phases. Moreover, the studied random geometries are general to model seamlessly a wide range of composites involving particles, multi-phase, and even polycrystals with finite interfaces under mechanical or coupled loads (e.g. magneto-electro mechanical, etc.).

In the next part of the study, we fabricate the designed porous materials by means of a polymer 3D-printer via PolyJet technology and a UV-curable resin called TangoBlack which is a highly viscous soft polymer with brittle fracture. Meanwhile, the viscous behavior of TangoBlack is studied under uni-axial tensile, loading-unloading, and relaxation tests on a new proposed specimen geometry and is subsequently characterized by a nonlinear rubber viscoelastic model for incompressible isotropic elastomers. We then use this material to 3D-print the designed two-dimensional porous materials with square representative geometries and isotropic/anisotropic features in terms of void size and realization. The mechanical response of the fabricated porous materials is experimentally investigated

by testing them under uni-axial large strain compression and very low strain rates. We show that the randomness of the proposed M-Voronoi geometries and their non-uniform intervoid ligament size leads to enhanced mechanical properties at large compressive strains with no apparent peak-stress and strong hardening well before densification, while they become very close to random eroded Voronoi geometries at low densities.

In the last part of this study, we investigate numerically the mechanical properties of the three-dimensional random porous geometries consisting of M-Voronoi, polydisperse porous materials with spherical voids, and the classical TPMS-like geometries. The simulations are performed at large strains under compression loading while considering the matrix an elastic-perfectly plastic material without hardening. We observe an enhanced plastic flow stress in the geometries with random topologies as opposed to the TPMS periodic structures. This behavior is explained by noting that deformation localizes in geometries with a periodic pattern, contrary to the random geometries which exhibit a rather diffused localization.

Key words: Architected materials, Porous materials, Void growth, additive manufacturing, finite strain experiments, homogenization

Résumé

Cette étude porte sur la conception assistée par ordinateur, l'impression 3D, la simulation numérique à grandes transformations et la caractérisation expérimentale de géométries aléatoires, en mettant l'accent sur les matériaux poreux. En particulier, nous cherchons à quantifier l'effet des architectures aléatoires sur la réponse mécanique en grandes transformations de géométries poreuses aléatoires et périodiques bien choisies. Dans un premier temps, nous nous intéressons à la conception assistée par ordinateur d'une variété de géométries poreuses, y compris les matériaux contenant des distributions aléatoires de pores sphériques et ellipsoïdaux, des structures Voronoï, à d'abeilles et TPMS. Par ailleurs, nous proposons une nouvelle famille de matériaux poreux de type Voronoï appelés M-Voronoï (de mécaniquement cultivé) contenant de pores de taille hétérogène et de ligaments d'épaisseur variable. Ces matériaux peuvent atteindre des densités relatives très faibles, et sont obtenus à l'aide de simulations numériques par un processus de croissance de pores dans une matrice élastique non linéaire et à grandes transformations. La méthode M-Voronoï proposée est versatile et peut être appliquée pour créer des géométries aléatoires bidimensionnelles et tridimensionnelles avec (an-)isotropie contrôlée. Cette méthode de génération découle de la conservation de la masse et de l'incompressibilité de la matrice. Les densités extrêmement faibles des géométries M-Voronoï sont obtenues par une étape intermédiaire de remaillage dans le processus de fabrication virtuelle. Pour ce faire, un nouveau algorithme de remaillage a été proposé. Ceci repose sur la reconstruction de la géométrie d'un maillage orphelin qui peut traiter des maillages arbitrairement complexes, contenant des phases multiples. De ce fait, les géométries M-Voronoï peuvent être utilisés pour modéliser de nombreux matériaux composites (y compris ceux à renfort de particules), ainsi que les polycristaux sous des charges mécaniques ou couplées (par exemple magnéto-électro-mécanique, etc.).

Dans un deuxième temps, nous nous sommes intéressés à la caractérisation expérimentale des matériaux poreux ainsi obtenus. Ceux-ci ont été fabriqués par impression 3D polymère via la technologie PolyJet en utilisant une résine, appelée TangoBlack moue hautement visqueuse, dont la loi de comportement a été quantifiée à l'aide des essais mécaniques et caractérisé par un modèle viscoélastique non linéaire formulé pour les élastomères isotropes incompressibles. Par la suite, des essais de compression uni-axiales ont été menés pour étudier la réponse mécanique de structures poreuses 3D-imprimées en Tangoblack. Ceux-ci ont montrés que, dans le régime de grandes transformations les géométries M-Voronoï ont des propriétés mécaniques améliorées du fait de leur architecture poreuse.

Notamment, leur réponse sous compression durcie bien avant la densification et devient similaire à celle de géométries Voronoï aléatoires érodées à de faibles densités.

Dans la dernière partie de cette étude, nous avons étudié à l'aide de simulations numériques les propriétés mécaniques des géométries poreuses aléatoires tridimensionnelles constituées de M-Voronoï, de matériaux poreux polydispersés avec des vides sphériques, et des géométries classiques de type TPMS. Les simulations ont été menées à grandes transformations sous une charge de compression tout en considérant la matrice comme un matériau élastique-parfaitement plastique sans durcissement. Ces résultats ont montré que l'écoulement plastique accrue dans les géométries à topologies aléatoires par rapport aux structures périodiques TPMS. Ce comportement est expliqué en observant que la déformation se localise dans les géométries avec motif périodique, contrairement aux géométries aléatoires qui présentent une localisation plutôt diffusée.

Mots clés: Matériaux architecturés, Matériaux poreux, Croissance de cavités, Fabrication additive, Expériences de déformation finie, Homogénéisation

Contents

1	Introduction	1
1.1	Randomness versus periodicity	1
1.2	Morphogenesis methods	6
1.3	Scope of the study	8
1.4	Organization of the thesis	9
2	Random and periodic geometries: a selective review	13
2.1	What is RSA algorithm?	14
2.1.1	General concepts of the RSA algorithm	15
2.2	RSA algorithm in three-dimensional space	17
2.2.1	Microstructure parameters of the 3D RSA algorithm	17
2.2.2	Description of the general structure of the RSA algorithm	18
2.2.3	The minimum distance between two ellipsoids	20
2.2.4	The minimum distance between an ellipsoid and a plane	23
2.2.5	The periodicity of the unit-cell	24
2.2.6	An extension of the RSA algorithm to achieve large volume fractions	25
2.3	RSA algorithm in two-dimensions	26
2.3.1	Microstructure parameters of the 2D RSA algorithm	27
2.3.2	The minimum distance between two ellipses	28
2.3.3	The minimum distance between an ellipse and the unit-cell boundaries	29
2.3.4	The periodicity of a 2D unit-cell	29
2.4	The eroded Voronoi (E-Voronoi) method	30
2.5	Hexagonal lattices	31
2.5.1	Prescribed L_W and N_W	33
2.5.2	Prescribed L_H and N_H	34
2.6	Triply periodic minimal surfaces (TPMS) structures	35
2.7	Concluding remarks	38
3	The M-Voronoi	41
3.1	M-Voronoi morphogenesis method	42
3.2	Relative density and porosity evolution	46
3.3	Geometry reconstruction and Remeshing	48

3.3.1	Description of 2D remeshing algorithm	51
3.3.2	Application of 2D remeshing algorithm in M-Voronoi	57
3.4	M-Voronoi in convex cell domains	58
3.5	Effect of initial volume fraction and attainable relative density	61
3.6	E-Voronoi and RSA versus M-Voronoi	63
3.7	Anisotropic M-Voronoi	64
3.8	The assembly of the porous cells into macroscopic structures	68
3.9	Concluding remarks	69
3.A	Appendix A. Equality between the applied and average deformation gradients	70
3.B	Appendix B. Algorithms for remeshing a 2D orphan mesh by constructing the geometry	71
4	3D-printing, experiments and numerical assessment for 2D M-Voronoi	73
4.1	3D-printing method	74
4.2	Characterization and modeling of TangoBlack material	75
4.2.1	TangoBlack reported characteristics	75
4.2.2	The design of the specimen and experimental setup	75
4.2.3	Testing protocol	82
4.2.4	Optical strain measurement	84
4.2.5	Tensile test and high strain rates deformations	84
4.2.6	Loading-Unloading and cyclic tensile tests	88
4.2.7	Single-step Relaxation tests	90
4.2.8	Constitutive modeling of viscoelastic behavior of TangoBlack	94
4.2.9	Fracture and ultimate tensile properties of TangoBlack	99
4.2.10	Fracture in Relaxation tests	100
4.2.11	Neo-Hookean modeling at low strain rates	102
4.3	3D-printing method and limits for porous geometries	104
4.4	3D-printing interruption strategy	104
4.5	Experimental results and discussion	107
4.5.1	Testing protocol	107
4.5.2	Representativity and isotropy of M-Voronoi	108
4.5.3	Comparison among the three geometries	113
4.5.4	Comparison with Honeycombs	116
4.5.5	Anisotropic M-Voronoi	118
4.6	Numerical results and discussions	118
4.7	Concluding remarks	122
5	M-Voronoi in 3D	125
5.1	The M-Voronoi morphogenesis method in 3D	126
5.2	Geometry reconstruction and Remeshing in 3D	129
5.2.1	Description of 3D remeshing algorithm	129
5.2.2	The span of the 3D remeshing technique	133

5.3	Attainable relative density in 3D M-Voronoi	135
5.4	Large strain simulation of 3D M-Voronoi	137
5.4.1	Plasticity in random and periodic structures	138
5.5	Concluding remarks	145
5.A	Appendix A. Algorithms for remeshing a 3D orphan mesh by constructing the geometry	146
6	Conclusion	149
6.1	Concluding remarks	149
6.2	Perspectives	152

List of Figures

1.1	Periodic lattices and their geometrical imperfections created by the manufacturing process: (a) 20 mm cube lattice structures based on the BCC unit cell (Smith et al., 2013), (b) Octet-truss lattice material made from a casting aluminum alloy, LM25 (Deshpande et al., 2001), (c) SEM images of lattice struts showing the variation of strut diameter along its length (Smith et al., 2013), (d) Geometrical irregularities in an L-PBF lattice: strut waviness and strut cross-section variation on a horizontal strut (Liu et al., 2017), (e) Example of filleted cubic lattice showing excess material accumulated on the down-facing surface of the horizontal struts (Benedetti et al., 2021), (f) Boundary irregularity and spherical pores of varying sizes in a beam of a Pantographic structure that is additively manufactured by aluminum (De Angelo et al., 2019), (g) Imperfections of a pantographic sheet with a beam diameter of 1mm manufactured of AlSi10Mg (De Angelo et al., 2019).	3
1.2	Composite materials with random inclusions: (a) optical micrograph of the Al-matrix composites containing a dense random packing of polygonal Al ₂ O ₃ particles (Tarantino and Mortensen, 2022), (b) cedar (Gibson et al., 2010), (c) Alporas metallic foam (Gibson, 2000), (d) Scanning electron microscopy (SEM) images of carbonyl iron (CI) particles in silicone matrix (Perales-Martínez et al., 2017), (e) skull (Gibson et al., 2010), (f) trabecular bone (Gibson et al., 2010), (g) Histological cross-sections of the healthy (left) and pathologic(right) muscle tissues (Spyrou et al., 2019), (h) SEM image of the NdFeB particles in the PDMS matrix (Linke et al., 2016), (i) Microstructure of rigid polyurethane foam (Kairyte et al., 2020).	4
2.1	Realizations of microstructures with different types of distributions: (a) Monodisperse, (b) Polydispersity only in size, (c) Polydispersity only in shape, and (d) Polydispersity in size and shape.	16
2.2	A cuboidal RSA microstructure that contains random inclusions and the characteristics of an ellipsoidal geometry: the aspect ratios $\omega_1^r = c^r/a^r$ and $\omega_2^r = c^r/b^r$ the orthonormal vectors \mathbf{n}_1^r , \mathbf{n}_2^r and \mathbf{n}_3^r .	17

2.3	A schematic representation of the iterative algorithm for finding the minimum distance between two arbitrarily oriented ellipsoids. The picture has been taken from Anoukou et al. (2018) and has been modified according to our parameters.	22
2.4	A rectangular RSA microstructure containing random 2D inclusions and the characteristics of an ellipse: the aspect ratio ω^r and the orthonormal vectors \mathbf{n}_1^r and \mathbf{n}_2^r	27
2.5	Generation of E-Voronoi geometries. (a) Random distribution of seeds. (b) To obtain the desired density, the cell walls are eroded and offset with a specific thickness. (c) The final E-Voronoi geometry with a surrounding solid box.	30
2.6	(a) A single unit-cell of the considered hexagonal lattice. (b) The geometrical parts of a half single hexagon unit-cell.	32
2.7	A honeycomb structure with horizontal length L_W and vertical length L_H , where $L_H \approx L_W$. The N_W and N_H denote the number of cells in the horizontal and vertical directions, respectively.	33
2.8	A 3D model of Gyroid minimal surface	35
2.9	The TPMS Designer graphical user interface.	36
2.10	A Gyroid lattice with 50% solid volume fraction and $5 \times 5 \times 5$ cells.	36
2.11	Flowchart of the steps for surface mesh quality improvement and conversion of the surface mesh to the volume mesh for numerical simulations.	37
2.12	The improvement of the surface mesh quality by Meshlab in a MATLAB generated mesh. (a) A surface mesh generated by MATLAB with a low quality and large mesh size. (b) The same mesh with improved quality and smaller mesh size.	38
3.1	Computational process for the generation of the M-Voronoi material. For illustration purposes, the diagram shows the four steps required to obtain a virtual M-Voronoi geometry starting from a square unit cell containing a discrete number of mono-sized circular pores. Step 1: Random distribution of circular holes in a square domain. Step 2: Application of uniform displacement boundary conditions. Step 3: Numerical FE simulation at large strains using nonlinear elastic energy minimization and incompressible matrix behavior. The zoom image shows locally the deformed mesh. The color bar indicates the maximum principal logarithmic strain. Step 4: Uniform re-scaling of the deformed geometry to the desired size. Remeshing (as shown in the zoomed image), 3D extrusion and STL generation of the final geometry used for 3D-printing.	43
3.2	Evolution of porosity $c = 1 - \rho$ as a function of the applied determinant of the deformation gradient, as obtained by numerical simulations and the analytical expression (3.14).	47

3.3	The geometry containing non-smooth void boundaries generated by Abaqus from orphan mesh.	50
3.4	2D remeshing algorithm for an orphan mesh based on geometry reconstruction. For illustration purposes, a simple orphan mesh containing a void is demonstrated. The diagram shows the four steps required to remesh an orphan mesh. Step 1: Reading the nodes and elements of the orphan mesh. Step 2: Finding the free sides of the elements. Step 3: Constructing the geometry of the orphan mesh. Step 4: Remeshing the new mesh with an arbitrary mesh algorithm.	51
3.5	Different 2D element types and their number of nodes.	52
3.6	Reorganizing the order of the stored nodes for each quadratic element.	52
3.7	An illustrative example of a 2D orphan mesh containing free and shared lines corresponding to the blue and red colors, respectively.	53
3.8	2D geometry entities built in a bottom-up manner with the OpenCASCADE kernel in Gmsh: points, lines, curve loops, surfaces, and physical surfaces.	54
3.9	Flowchart of 2D geometry reconstruction from the identified free lines of an orphan mesh	55
3.10	Gmsh Boolean operator. The surface P_1 is the rectangular matrix surface and P_2 is the inclusion surface. The first row displays the geometry and the second row corresponds to the meshed surfaces. (a) Without the Boolean operator, two surfaces are overlapping and are not distinguishable. (b) The BooleanDifference operator removes the inclusion surface. (c) The BooleanFragments operator preserves the inclusion surface and creates a conformal mesh at the interface between the inclusion and matrix	56
3.11	Remeshing steps applied to an orphan mesh of M-Voronoi containing extremely deformed elements and the corresponding new mesh with significantly higher quality.(as shown in the zoomed image)	57
3.12	M-Voronoi containing particles instead of voids. The void regions can be meshed by applying the BooleanFragments operator.	58
3.13	Representative M-Voronoi porous geometries for porous domains with different shapes: (a-d) isotropic geometries obtained using a rectangular cell subjected to equi-biaxial tension ($\lambda_1^{\text{app}} = \lambda_2^{\text{app}} = \lambda^{\text{app}} > 1$); (e-h) anisotropic geometries obtained using a rectangular cell subjected to biaxial tension ($2\lambda_2^{\text{app}} = \lambda_1^{\text{app}} = \lambda^{\text{app}} > 1$) and isotropic geometries obtained using respectively a (i-j) circular and a (k-l) triangular cell subjected to equi-biaxial load. The initial geometries in (a), (e), (i) and (k) are obtained using the RSA algorithm and monodisperse circular voids at relative density $\rho_0 = 0.9$. All deformed cells are scaled for visualization reasons.	60

3.14	M-Voronoi obtained by using a RSA geometry with initial relative density (a) $\rho_0 = 0.9$, (b) $\rho_0 = 0.7$ and (c) $\rho_0 = 0.5$ as shown in the insets of the first row. The $\rho = 0.01$ geometries in, are obtained by using the corresponding $\rho = 0.1$ as an initial geometry after remeshing it. The top color bar indicates the final relative density ρ	61
3.15	The effect of the intermediate re-launching step on M-Voronoi final geometries. The simulations have been stopped when the intermediate density ρ_i is achieved and the deformed geometry is extracted and remeshed. Then, the simulation is re-launched to obtain the final density ρ . (a),(b) M-Voronoi geometries of identical initial and final density ($\rho_0 = 0.5$ and $\rho = 0.05$), but with and without the intermediate M-Voronoi geometry, respectively. (c),(d) M-Voronoi geometries of identical initial and final density ($\rho_0 = 0.9$ and $\rho = 0.1$), but with and without the intermediate M-Voronoi geometry, respectively.	62
3.16	Random porous geometries: (a) E-Voronoi. (b) RSA polydisperse circles. (c) M-Voronoi obtained by using a RSA geometry with initial relative density $\rho_0 = 0.9$. The relative densities less than $\rho = 0.1$ are obtained by an intermediate remeshing step. The top color bar indicates the final relative density ρ	64
3.17	The variation of λ_2^{app} as a function of the anisotropy parameter η at different applied deformations $\det \mathbf{F}^{\text{app}}$. The red region shows the range of η and $\det \mathbf{F}^{\text{app}}$ leading to compressive deformations $\lambda_2^{\text{app}} < 1$ in the anisotropic generation process.	65
3.18	The generation process of an anisotropic M-Voronoi material with $\eta = 2$ obtained using a rectangular cell ($L_1 = 1$ and $L_2 = 2$) subjected to non equi-biaxial tension loading. The initial geometry in (a) is obtained using the RSA algorithm and monodisperse circular voids at the relative density $\rho_0 = 0.9$. (c) and (d) indicate the deformations at intermediate values of stretch. The final anisotropic geometry in (d) has a square shape with $l_1 = l_2 = 2.44$ and the relative density $\rho = 0.3$. The color bar indicates the maximum principal logarithmic strain.	66
3.19	Isotropic and anisotropic M-Voronoi geometries with identical relative density $\rho = 0.3$ and different anisotropy parameters: (a) $\eta = 1$, isotropic M-Voronoi (b) $\eta = 0.5$, (c) $\eta = 2$, (d) $\eta = 4$	67
3.20	Assembly of individual M-Voronoi cells into a macroscopic geometry. (a) Ecole Polytechnique Logo. (b) Finite Volume Element (FVE) discretization with arbitrary porosity and anisotropy. (c) Numerical creation and assembly of the individual porous cells. (d) 3D-printed specimen.	68
4.1	The density measurement of a polymerized TangoBlack FLX973 sample. The measured density corresponds to 1.14576 g/cm^3	76

4.2	The TangoBlack dog-bone specimen. (a) The designed dog-bone geometry with a $12 \times 12 \text{ mm}^2$ cross-section. (b) The experimental setup for a tensile test on the specimen. (c) The lateral view of the sample held in the hydraulic grips. (d) The TangoBlack sample that was early broken at the edges of the top grip.	77
4.3	(a) I-shape design of TangoBlack specimen with VeroWhite Plus grips. (b) The stress field and deformation of the specimen under uni-axial tension. (c) The stress field in the deformed TangoBlack specimen is concentrated near the VeroWhite Plus contact region. The color bar indicates the von Mises stress field in MPa.	78
4.4	(a) The curved I-shape design of the TangoBlack specimen with geometrically reinforced VeroWhite Plus grips. (b) The stress field and deformation of the specimen under uni-axial tension. (c) The stress field in the deformed TangoBlack specimen is concentrated near the contact region with VeroWhite Plus. The color bar indicates the von Mises stress field in MPa.	79
4.5	The tensile test on the second proposed geometry to assess the fracture point of the TangoBlack sample. The sample broke in the pointed section, where it gets in contact with the VeroWhite Plus grips.	80
4.6	(a) The final I-shape design of the TangoBlack specimen with geometrically reinforced VeroWhite Plus grips. (b) The 3D-printed parts in the experimental setup. (c) The numerical simulation of the specimen under uni-axial tension and the corresponding stress field in the assembly of the parts and TangoBlack individually. (d) The TangoBlack specimen after the tensile test, broke in the middle part of the sample. The color bar indicates the von Mises stress field in MPa.	81
4.7	The dimensions of the 3D-printed TangoBlack and VeroWhite parts. All numbers are in mm units.	82
4.8	The assembly of the final experimental setup consisting of different parts. Two side plates are screwed to VeroWhite Plus parts in order to prevent the curved parts from buckling when the cross-section of the specimen is small.	83
4.9	Tensile test setups with two different tensile testing machines MTS 100 kN (on the left side) and MTS 250 kN (on the right side).	83
4.10	The optical strain measurement method by point tracking employed to measure the local strain fields. (a) The longitudinal and transverse strain measurements by means of four white dots. (b) The longitudinal strain measured by only two white dots. (c) Using the callipers to measure the strain in the large deformations and high strain rates, where the tracking by points becomes difficult.	85
4.11	Dimensions of the specimens used in the tensile tests. The measured effective length of samples 1 and 2 corresponds to 78 mm and 45 mm, respectively. The out-of-plane thickness of both samples is 6mm.	86

4.12	Tensile experiments results for TangoBlack at different strain rates 0.0007-2.1 s ⁻¹ until failure. The × shows the breaking point of the sample. Inset shows the initial slope of the curves at different strain rates until 1% strain. Stress values correspond to engineering or first Piola-Kirchhoff stresses, and strain values correspond to engineering strains.	87
4.13	Loading-unloading tests at various strain rates: 0.0001 s ⁻¹ , 0.01 s ⁻¹ , 0.06 s ⁻¹ , 0.1 s ⁻¹ , 0.7 s ⁻¹ , 1.4 s ⁻¹ , 2.2 s ⁻¹ . The specimen is unloaded just before the ultimate stress at each strain rate is reached. Stress values correspond to engineering or first Piola-Kirchhoff stresses, and strain values correspond to engineering strains.	88
4.14	Cyclic loading-unloading tests with three cycles at various strain rates: (a) 0.06 s ⁻¹ , (b) 0.7 s ⁻¹ , (c) 1.4 s ⁻¹ , (d) 2.2 s ⁻¹ . The specimen is unloaded just before the ultimate stress of each strain rate is reached, whereas the re-loading started upon achieving zero displacement. Stress values correspond to engineering or first Piola-Kirchhoff stresses, and strain values correspond to engineering strains.	89
4.15	The dimensions of the specimens used in the relaxation tests. The measured effective length of samples 3 and 4 corresponds to 120 mm and 55 mm, respectively. In sample 3, the out of plane thickness is 6mm, whereas in sample 4, it is 3.3mm.	91
4.16	Nominal strain as a function of time during the relaxation test performed on a TangoBlack specimen with the geometry of sample 3. The dashed line indicates the expected strain curve from the dog-bone geometry with the dimension of sample 4.	92
4.17	Single-step relaxation tests at different strain rates and levels: (a) Strain rate= 0.02s ⁻¹ tested at 14%, 22% and 37% strain levels. (b) Strain rate= 0.1s ⁻¹ tested at 15% and 19.6% strain levels. (c) Strain rate= 0.83s ⁻¹ tested at 17%, 19% and 20% strain levels. (d) Strain rate= 2.2s ⁻¹ tested at 14% and 16% strain levels. The × shows the break point of the sample. Stress values correspond to engineering or first Piola-Kirchhoff stresses, and strain values correspond to engineering strains.	93
4.18	The modeling of the experimental data of TangoBlack with the viscoelastic incompressible model proposed by Kumar and Lopez-Pamies (2016) and the material parameters in the table 4.4. TangoBlack is subjected to uniaxial tension loading-unloading at different constant strain rates: (a) 0.06 s ⁻¹ , (b) 0.7 s ⁻¹ , (c) 1.4 s ⁻¹ . (d) Single-step relaxation test with the strain held at 0.15 and the primary strain rate 0.02 s ⁻¹ . Stress values correspond to engineering or first Piola-Kirchhoff stresses, and strain values correspond to engineering strains.	98

4.19	Failure envelope for TangoBlack FLX 973 from data obtained at various strain rates. (a) The Cauchy stress at break σ_{uni}^b as a function of the principal stretch at break λ^b at different strain rates. (b) The logarithmic values of the Cauchy stress at break $\log(\sigma_{uni}^b)$ as a function of the logarithmic values of the principal stretch at break $\log(\lambda^b)$ at different strain rates.	99
4.20	The failure envelope of the TangoBlack material and the result of the tensile test at 1.3 s^{-1} strain rate. Points A and B indicate the initiation of the relaxation. The red region represents the stress and strain values where the fracture occurs during the relaxation process. In contrast, the green region shows stress and strain values without fracture when relaxed.	101
4.21	The modeling of the experimental data of TangoBlack at two strain rates 0.66 s^{-1} and 0.0007 s^{-1} with Neo-Hookean viscous incompressible model for hyperelastic materials. The \times shows the breaking point of the sample. Stress values correspond to engineering or first Piola-Kirchhoff stresses, and strain values correspond to engineering strains.	103
4.22	3D-printing accuracy test of TangoBlack material with circular and rectangular voids. The minimum pore diameter and intervoid thickness ligament that may be 3D-printed once-off with acceptable accuracy are $\sim 300 \mu\text{m}$ and $\sim 600 \mu\text{m}$ respectively.	105
4.23	(a,b) M-Voronoi and (c,d) E-Voronoi 3D-printed specimens with relative density $\rho = 0.1$. The specimens are obtained in (a,c) without and (b,d) with the interruption strategy.	106
4.24	The effect of interruption method on hexagons with a constant intervoid ligament thickness that are 3D-printed a)without interruption method, and b)with interruption method. The relative density of the geometry corresponds to $\rho = 0.05$	106
4.25	(a) M-Voronoi, (b) E-Voronoi and (c) RSA 3D-printed specimens with no interruption strategy and $\rho = 0.2$	107
4.26	Experimental representativity study for M-Voronoi with $\rho = 0.3$ in terms of number of voids N_p . (a) Stress-strain response of the M-Voronoi with different number of voids and (b) engineering stress as a function of N_p for different levels of the overall strain. (c) Optical images of the corresponding realizations for different N_p . The values of stress and strain correspond to their nominal or engineering values.	109
4.27	Experimental representativity study for M-Voronoi with $\rho = 0.3$ in terms of number of realizations and number of voids. Stress-strain response for four different realizations for (a) $N_p = 30$ and (b) $N_p = 200$. Corresponding optical images of the realizations for (c) $N_p = 30$ and (d) $N_p = 200$. The values of stress and strain correspond to their nominal or engineering values.	110

-
- 4.28 The scatter in the stress-strain response induced by four different realizations of M-Voronoi geometries with $\rho = 0.3$ and number of voids $N_p = 30, 200$. The straight dotted lines indicate the average value over the strain range considered in the figure. 111
- 4.29 Experimental representativity study for RSA with $\rho = 0.1$ in terms of number of realizations. (a) Stress-strain response for four different realizations. (b) Stress-strain realization scatter. The straight dotted line indicates the average value over the strain range considered in the figure. (c) Corresponding optical images of the realizations considered. The values of stress and strain correspond to their nominal or engineering values. 112
- 4.30 Compression experiments and corresponding optical images for the M-Voronoi, E-Voronoi and RSA geometries for relative densities (a) $\rho = 0.4$ and (b) $\rho = 0.3$. For all cases, snapshots are shown of the three geometries selected at three intermediate strains levels, denoted with (1), (2) and (3). The green lines indicate zones of strong localization and fracturing of the intervoid ligaments. The in-plane dimensions of the undeformed specimens are $100 \times 100 \text{ mm}^2$. The values of stress and strain correspond to their nominal or engineering values. 114
- 4.31 Compression experiments and corresponding optical images for the M-Voronoi, E-Voronoi and RSA geometries for different relative densities (a) $\rho = 0.2$ and (b) $\rho = 0.1$. For all cases, snapshots are shown of the three geometries selected at three intermediate strains levels, denoted with (1), (2) and (3). The green lines indicate zones of strong localization and fracturing of the intervoid ligaments. The RSA for $\rho = 0.2, 0.1$ are non-representative due to fabrication limitations. The in-plane dimensions of the undeformed specimens are $100 \times 100 \text{ mm}^2$. The values of stress and strain correspond to their nominal or engineering values. 115
- 4.32 Compression experiments and corresponding optical images for the M-Voronoi, Honeycombs along the longitudinal and transverse direction for two relative densities (a) $\rho = 0.4$ and (b) $\rho = 0.1$. For all cases, snapshots are shown of the three relevant geometries selected at three intermediate strains levels, denoted with (1), (2) and (3). The green lines indicate zones of strong localization and fracturing of the intervoid ligaments. The in-plane dimensions of the undeformed specimens are $100 \times 100 \text{ mm}^2$. The values of stress and strain correspond to their nominal or engineering values. 117
-

-
- 4.33 Compression experiments and corresponding optical images for the isotropic and anisotropic M-Voronoi along the longitudinal and transverse direction for $\rho = 0.3$. For all cases, snapshots are shown of the three relevant geometries selected at three intermediate strains levels, denoted with (1), (2) and (3). The green lines indicate zones of strong localization and fracturing of the intervoid ligaments. The in-plane dimensions of the undeformed specimens are $100 \times 100 \text{ mm}^2$. The values of stress and strain correspond to their nominal or engineering values. 119
- 4.34 Comparison between the compression experimental and numerical results for the M-Voronoi, E-Voronoi and RSA geometries for relative density 0.4. For all cases, snapshots of the experimental samples and numerical geometries are shown of the three geometries selected at three intermediate strain levels, denoted with (1), (2) and (3). The legend indicates the maximum principal logarithmic strain values. The green lines indicate zones of strong localization and fracturing of the intervoid ligaments. The values of stress and strain correspond to their nominal or engineering values. 120
- 4.35 Comparison between the compression experimental and numerical results for the M-Voronoi, E-Voronoi and RSA geometries for relative density 0.3. For all cases, snapshots of the experimental samples and numerical geometries are shown of the three geometries selected at three intermediate strain levels, denoted with (1), (2) and (3). The legend indicates the maximum principal logarithmic strain values. The green lines indicate zones of strong localization and fracturing of the intervoid ligaments. The values of stress and strain correspond to their nominal or engineering values. 121
- 5.1 Computational process for the generation of the 3D M-Voronoi material. For illustration purposes, the diagram shows the four steps required to obtain a virtual M-Voronoi geometry starting from a cubic unit cell containing a discrete number of mono-sized spherical voids. **Step 1:** Random distribution of spherical voids in a cubic domain with initial relative density $\rho = 0.7$. **Step 2:** Application of displacement boundary conditions. **Step 3:** Numerical FE simulation at large strains using nonlinear elastic energy minimization and incompressible matrix behavior. The final relative density corresponds to $\rho = 0.3$. The cut image shows inside of the deformed geometry. The color bar indicates the maximum principal logarithmic strain. **Step 4:** Remeshing and uniform re-scaling of the deformed geometry to the desired size. The final 3D M-Voronoi and its containing inclusions are uniformly re-scaled to the size of the initial geometry. . . . 127
-

5.2	3D remeshing algorithm for an orphan mesh based on geometry reconstruction. For illustration purposes, a simple 3D orphan mesh containing a spherical void is demonstrated. The diagram shows the four steps required to remesh an orphan mesh. Step 1: Reading the nodes and elements of the orphan mesh. Step 2: Finding the free surfaces of the elements. The green color corresponds to accepted free surfaces, whereas the red regions are rejected shared surfaces. Step 3: Constructing the geometry of the orphan mesh. Step 4: Remeshing the new mesh with an arbitrary mesh algorithm.	130
5.3	Three possible scenarios in the geometry construction method of the Fortran algorithm. New and old identified free surfaces are shown in red and gray, respectively. Noderef 1 and Noderef 2 are two reference nodes, from which the new red surface is constructed. The new surface is characterized by three geometry entities, Noderef 3 , Line 23 and Line 13 . The table shows the conditions in each case. Case 1: All three entities are new. Case 2: only one line of the new surface is new. Case 3: All three entities were previously added.	132
5.4	Flowchart of 3D geometry reconstruction from the identified free surfaces of an orphan mesh with Fortran and Python versions of the algorithm . . .	133
5.5	The limitations of the 3D remeshing algorithm in the case of quadratic elements. (a) The possible node connection methods for a free surface of a quadratic tetrahedral element type. We note that the nodes are not in the same plane. (b) The degenerate cases of each connection method when excessive element distortion exists. In both cases, the red line overlaps the neighboring elements.	134
5.6	3D M-Voronoi obtained by using RSA geometry with initial relative density $\rho_0 = 0.7$ (The first geometry). The color bar indicates the final relative density ρ and the right images represent the void shapes inside of the geometry. The densities $\rho > 0.2$ are obtained by using the corresponding $\rho = 0.3$ as an initial geometry after remeshing it.	136
5.7	(a) Gyroid lattices created by the method described in Section 2.6 with $5 \times 5 \times 5$ unit-cells. (b) M-Voronoi with 110 voids obtained by using a RSA geometry with initial relative density $\rho_0 = 0.7$. (c) Polydisperse RSA geometries with various sphere sizes. All geometries are created at four different porosities $\rho = 0.4, 0.3, 0.2$ and 0.1 , except RSA that is not realizable at relative density $\rho = 0.1$	140
5.8	Large strains compression simulations for M-Voronoi, RSA and Gyroid geometries at three different directions for relative densities (a) $\rho = 0.42$ and (b) $\rho = 0.33$. The values of stress and strain correspond to their nominal or engineering values.	141

5.9	Deformations of M-Voronoi, RSA and Gyroid geometries with the relative density $\rho = 0.42$ at three different strain levels, denoted with (1), (2) and (3). The legend indicates the plastic strain equivalent (PEEQ) values. The values of stress and strain correspond to their nominal or engineering values.	142
5.10	Deformations of M-Voronoi, RSA and Gyroid geometries with the relative density $\rho = 0.33$ at three different strain levels, denoted with (1), (2) and (3). The legend indicates the plastic strain equivalent (PEEQ) values. The values of stress and strain correspond to their nominal or engineering values.	143
5.11	Large strains compression simulations for M-Voronoi geometries at four different relative densities $\rho = 0.42, 0.33, 0.20,$ and 0.1 . The values of stress and strain correspond to their nominal or engineering values.	144
6.1	A 3D-printed two-phase composite with random RSA geometry consisting of TangoBlack plus matrix and VeroWhite plus spherical inclusions.	153
6.2	An example of the application of random geometries in coupled magneto-mechanical problems. The geometry contains 500 particles with a 0.4 volume fraction and is proposed to model hard magnetorheological elastomers (h-MREs). (a) The pre-magnetized microstructure. m_2 denotes the magnetization in the vertical direction. (b) The deformation of the permanently magnetized microstructure under mechanical tensile loading. (c) The magnetic induction field b_2 in the deformed microstructure. The contours illustrate particle interactions.	154

Chapter 1

Introduction

Contents

1.1 Randomness versus periodicity	1
1.2 Morphogenesis methods	6
1.3 Scope of the study	8
1.4 Organization of the thesis	9

1.1 Randomness versus periodicity

The characteristics of composite materials can be classified in a variety of ways. Given that the subject is vast, we focus in the following mostly on porous or cellular materials. There is an important classification that pertains to the topologies of porous materials and divides them into periodic and random topologies. Studies of periodic cellular materials date back to the 1950s. Geometries of this type are often created by repeating elementary unit-cells in 2D or 3D. These materials have been extensively used to design lightweight cellular materials with high strength-to-weight ratios. Furthermore, the effect of unit-cell geometry on periodic cellular materials has also been investigated extensively. Nevertheless, the inherent instabilities of these geometries are not adequately addressed in these studies ([Singamaneni and Tsukruk, 2010](#)). Instabilities in periodic geometries often result in buckles and localized deformations ([Combescure et al., 2016, 2020](#); [Balit et al., 2021](#); [Dong et al., 2015](#); [Andrew et al., 2021](#)). Moreover, these geometries are often designed to be 3D-printed with different materials such as polymers and metals and various 3D-printing methods like powder bed fusion ([Heinl et al., 2007](#)), stereolithography ([Hengsbach and Lantada, 2014](#)) and 3D laser lithography ([Schaedler et al., 2011](#)). However, no 3D-printing technique is flawless, and all of them produce varying levels of imperfections in the printed parts depending on the 3D-printing accuracy. Figures [1.1a,b](#) represent the examples of the manufactured periodic geometries, while Figures [1.1c,d,e,f,g](#) illustrate the

geometrical imperfections created by the 3D-printing process. In most periodic cellular materials, imperfections include missing geometrical elements (such as beams, holes, and walls), varying cross-section, waviness, misplaced nodes, additional voids, joint separations, material augmentation, etc. (De Angelo et al., 2019; Grenestedt, 1998; Grenestedt and Tanaka, 1998; Ronan et al., 2016). Noteworthy is the study of Symons and Fleck (2008) on the imperfection sensitivity of the effective elastic properties for three planar isotropic lattices: fully triangulated, the Kagome grid, and the hexagonal honeycomb. It is shown that the moduli of the chosen lattices are degraded significantly by imperfections. The imperfection sensitivity of periodic cellular materials results in an experimental response that is not in accordance with the numerically predicted response. This is due to the fact that the numerical model does not account for imperfections. Periodic cellular materials are also characterized by their direction-dependent mechanical properties and inherent anisotropy (Dirrenberger et al., 2013). In this case, anisotropy can be viewed as an undesirable property, especially when the structure is exposed to an unknown load (i.e. a load of unknown magnitude and direction).

In contrast to periodic cellular materials, random topologies are more common in nature and biological tissues. Furthermore, natural periodic materials that are interpreted as periodic geometries often contain a certain irregularity. Honeycombs of bees, for example, are not as perfect as numerically designed hexagonal lattices (Ashby and Gibson, 1997). Figures 1.2a-i represent a few examples of random topologies containing irregular voids or particles that are observed in different natural porous materials. In these materials, not only do the voids have varying sizes and shapes, but also a gradient of porosity and consequently mechanical properties might be present (see Figure 1.2c). The complexity of the structural topology in random cellular materials makes their geometry realization very challenging. Several structural models have been developed by replacing the actual random topology with those that have simpler periodic or random geometries. Replacing random geometry with a periodic structure has two major drawbacks. First, they lack microstructural characteristics such as random cell size, shape, orientation, and position. Secondly, they often have instabilities and direction-dependent properties, which make their response far from random geometry (see Warren and Kraynik (1997) for liquid foams, and Simone and Gibson (1998) for metal foams). One of the most popular methods for the numerical construction of random foams is tomography scanning of the real microstructure, which creates exact random geometry. This method uses X-ray computed tomography scans to characterize the microstructures (Ghazi et al., 2020; Wang et al., 2021). As a drawback, this method requires the user to perform the scanning procedure each time in order to analyze the samples numerically. In this regard, it is necessary to construct realistic random geometries based on the general properties of real microstructures rather than on the exact properties of the microstructures themselves. Using additive manufacturing techniques, we can also design random geometries with controlled properties.

Many studies have been conducted on methods of creating random geometries. One of the oldest random geometries corresponds to microstructures containing randomly dis-

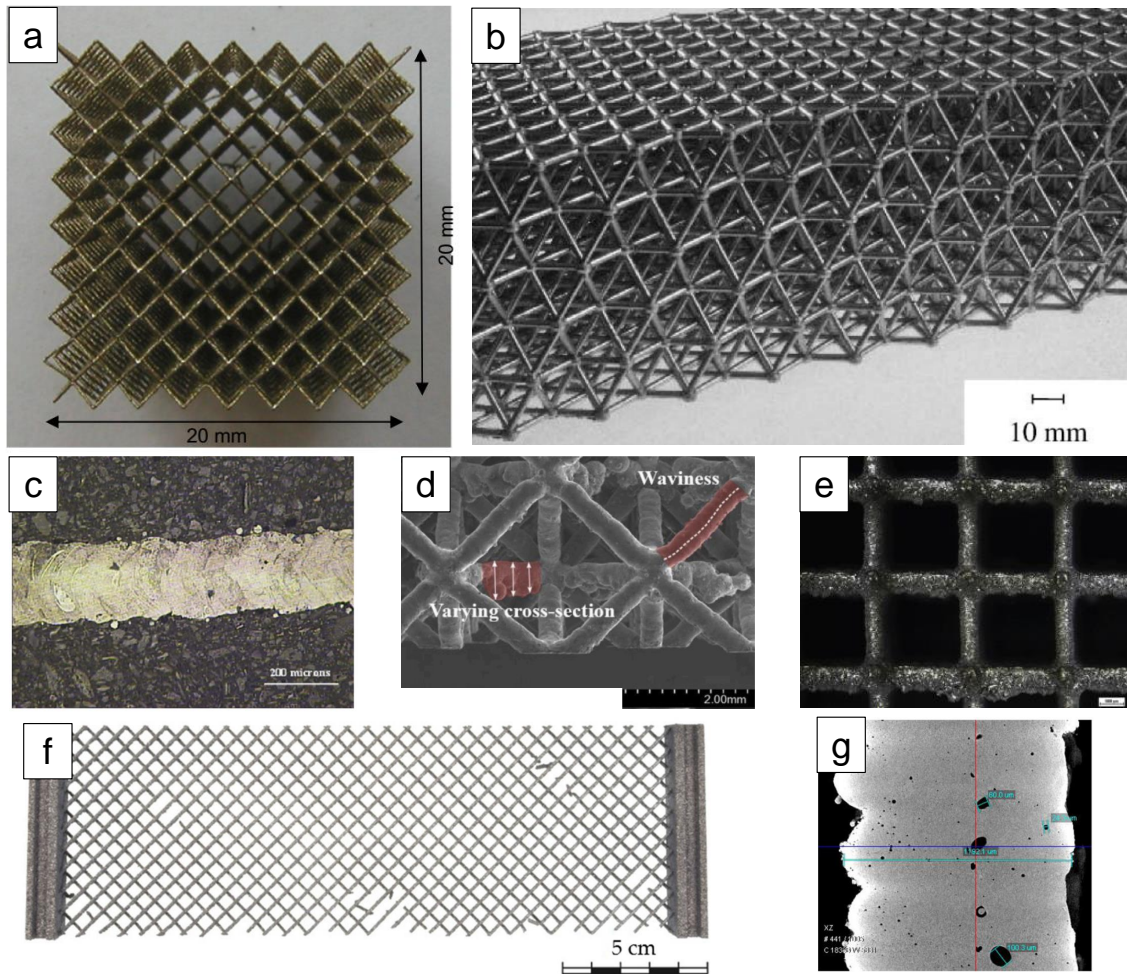


Figure 1.1: Periodic lattices and their geometrical imperfections created by the manufacturing process: (a) 20 mm cube lattice structures based on the BCC unit cell (Smith et al., 2013), (b) Octet-truss lattice material made from a casting aluminum alloy, LM25 (Deshpande et al., 2001), (c) SEM images of lattice struts showing the variation of strut diameter along its length (Smith et al., 2013), (d) Geometrical irregularities in an L-PBF lattice: strut waviness and strut cross-section variation on a horizontal strut (Liu et al., 2017), (e) Example of filleted cubic lattice showing excess material accumulated on the down-facing surface of the horizontal struts (Benedetti et al., 2021), (f) Boundary irregularity and spherical pores of varying sizes in a beam of a Pantographic structure that is additively manufactured by aluminum (De Angelo et al., 2019), (g) Imperfections of a pantographic sheet with a beam diameter of 1mm manufactured of AlSi10Mg (De Angelo et al., 2019).

tributed spherical voids generated by the random sequential adsorption (RSA) or random closed packing (RCP) methods (Lubachevsky et al., 1991; Torquato, 2002). In the con-

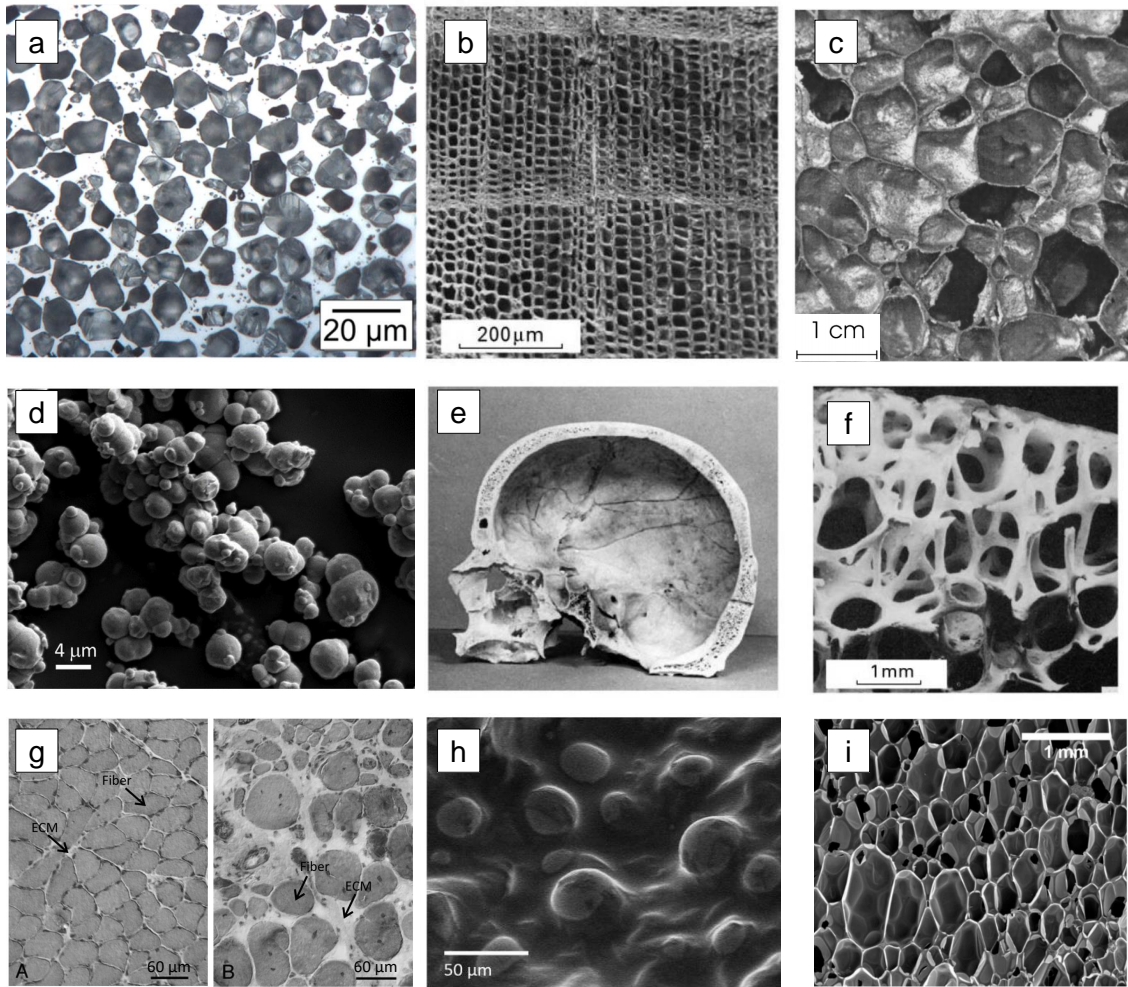


Figure 1.2: Composite materials with random inclusions: (a) optical micrograph of the Al-matrix composites containing a dense random packing of polygonal Al_2O_3 particles (Tarantino and Mortensen, 2022), (b) cedar (Gibson et al., 2010), (c) Alporas metallic foam (Gibson, 2000), (d) Scanning electron microscopy (SEM) images of carbonyl iron (CI) particles in silicone matrix (Perales-Martínez et al., 2017), (e) skull (Gibson et al., 2010), (f) trabecular bone (Gibson et al., 2010), (g) Histological cross-sections of the healthy (left) and pathologic(right) muscle tissues (Spyrou et al., 2019), (h) SEM image of the NdFeB particles in the PDMS matrix (Linke et al., 2016), (i) Microstructure of rigid polyurethane foam (Kairytė et al., 2020).

text of the RSA algorithm, several modifications have been applied to employ it in more general cases. Segurado and Llorca (2002) modified the algorithm to create RSA geometries with periodic unit-cell boundaries while keeping the minimum distance between the voids. Later on, Pierard et al. (2007) extended the RSA algorithm to create random

ellipsoidal inclusions. In the work of [Lopez-Pamies et al. \(2013\)](#), another modification to the RSA algorithm has been proposed to construct polydisperse microstructures with different families of particle sizes. The most general case of the RSA algorithm is proposed by [Anoukou et al. \(2018\)](#) which contains all the aforementioned features. It employs a robust and iterative numerical method to find the minimum distance between the inclusions. It is imperative to note that one of the major limitations of RSA geometries is their limited range of inclusion volume fractions (porosity in the case of voids). With the RSA algorithm, due to the irreversible nature of the sequential process, it is difficult to achieve large volume fractions while maintaining the non-overlapping condition. It becomes even more challenging if the inclusions must be distributed in a monodisperse manner. In this case, the maximum volume fraction approximately corresponds to 0.38 and 0.55 for 3D and 2D RSA, respectively ([Feder \(1980\)](#), [Cooper \(1988\)](#)). In order to overcome the volume fraction limit, one must create polydisperse distributions to fill the unit-cell with smaller inclusion sizes. Nevertheless, even with polydisperse distribution, reaching large volume fractions with representative microstructure (greater than 0.8 in 3D and 0.9 in 2D) becomes extremely difficult and requires a large number of inclusions. In terms of manufacturing, depending on the method employed, a minimum distance between inclusions must be maintained. This value is determined by the accuracy of the 3D printing process. This constraint will lead to an increasingly large small-to-large void size ratio, which will result in large polydispersity when reaching a large volume fraction of the inclusions. We will show in this study that current additive manufacturing technologies have difficulties producing material geometries with a representative response, especially in the nonlinear regime. As a final point, we would like to point out that the anisotropy of RSA geometries can be imposed and controlled by the use of ellipsoidal inclusions oriented in a particular direction ([Anoukou et al., 2018](#)).

Another type of random porous geometries corresponds to Voronoi tessellation geometries that are generated by the Laguerre-Voronoi diagram algorithm. This algorithm divides the space into polygonal cells with constant thickness and variable length ([Spyrou et al., 2019](#)). The use of Voronoi geometries is very common in the simulation of polycrystalline microstructures which are modeled as composite materials. In this study, we are specifically interested in porous Voronoi geometries. In this case, the Voronoi tessellation geometries lack two significant characteristics of real random geometries which are the variable cell wall thickness and the smooth corners. These two limitations make Voronoi tessellation geometries prone to localized deformation when subjected to compressive loading.

Spinodal topologies are another type of random geometries ([Hsieh et al., 2019](#); [Kumar et al., 2020](#)). These geometries cover a limited density range between 0.7 and 0.2 ([Maskery et al., 2017](#); [Hsieh et al., 2019](#)), whereas corresponding shell models can achieve ultra-low densities but usually lead to an anisotropic response beyond the linear elastic response. However, in the latter, due to their perfect periodicity, they are susceptible to long wavelength instabilities and localization bands that span the entire specimen. In turn, Gaussian type topologies have only a limited range of mechanical responses and

are known to be non-optimal (Roberts and Garboczi, 2001; Zerhouni et al., 2021) when compared with rigorous mathematical bounds in linear elasticity but can be versatile in obtaining isotropic and anisotropic responses by design (Kumar et al., 2020). By contrast, RSA porous geometries (Zerhouni et al., 2019; Tarantino et al., 2019) are mechanically nearly optimal in the linear regime as their moduli have been shown (both numerically and experimentally) to lie very close to the Hashin-Shtrikman bounds (Hashin and Shtrikman, 1963).

We close this section with a summary of the main points discussed in random and periodic cellular materials. In contrast to periodic geometries, random topologies inherently contain imperfections because they are naturally imperfect. Therefore, the existing imperfections in 3D-printing methods are expected to not significantly affect the response of random topologies. This advantage has made them resilient when subjected to unknown mechanical loading. Furthermore, since they distribute the deformation, they do not show instabilities or banding localization at the global microstructure level. In turn, they contain local buckling instabilities in the individual cell walls. It is important to note that as compared to random geometries, achieving large porosities in periodic topologies is much easier. Both RSA and spinodal random topologies are unable to reach large porosities with representative geometries. In contrast, the Voronoi tessellation method enables us to reach a full range of porosity. However, these geometries comprise a constant wall thickness and sharp corners, leading to a more localized response. Finally, in contrast to the periodic topologies, providing a sufficient number of inclusions in random geometries results in an isotropic response in both small and large strains.

1.2 Morphogenesis methods

Numerous living organisms, from plants to animals, possess a distinctive internal architecture that evolves during ontogeny. Morphological evolution in natural systems underpins a variety of life functions, including growth, locomotion and predation. For example, plants transport water and other minerals through an intricate network of hollow channels, the *aerenchyma*, whose size and shape change during plant growth (Corson et al., 2009; Zhao et al., 2018). Likewise, skeletal muscles enable us to run and walk via the contraction of multiply innervated (randomly distributed) fibers whose surrounding connective tissue, the *extracellular matrix*, thickens during motoneuron lesions (Tidball and Wehling-Henricks, 2004; Spyrou et al., 2019). These are only a few enticing examples that show the functional diversity enabled in living organisms by morphogenesis.

Unlike nature where morphogenesis occurs naturally via multiple actuation mechanisms (chemical, mechanical, electrical, thermal, etc.), synthetic systems require robust computational algorithms or man-made processing methods to evolve. Over the past two decades, significant efforts have been made to harness computational morphogenesis in synthetic structures. Examples are numerous and can be found in many areas of research including materials science (Portela et al., 2020; Tarantino et al., 2019; Zerhouni et al., 2019; Kumar et al., 2020), mechanobiology (Spyrou et al., 2019; Zhao et al., 2018; Ma

et al., 2021), design (Martínez et al., 2016, 2018; Aage et al., 2017; Baandrup et al., 2020; Panetta et al., 2021) and architecture (Menges, 2012; Roudavski, 2009). In particular, in the context of materials science and mechanics, today one is able to mimic complex heterogeneous structures that are reminiscent of bone (Portela et al., 2020; Kumar et al., 2020; Martínez et al., 2016, 2018; Aage et al., 2017; Wu et al., 2017), skeletal muscles (Spyrou et al., 2019), plants (Faisal et al., 2012; Zhao et al., 2018) and even particle-reinforced polymers (Segurado and Llorca, 2002; Lopez-Pamies et al., 2013) and geomaterials (Roberts and Teubner, 1995; Roberts and Garboczi, 2001). Traditionally, computational morphogenesis has relied on voxel-based algorithms that enable generating complex distributions of Voronoi polyhedra. The latter typically consist of beam elements with uniform thickness and variable length, which are arranged in a disordered manner to form either a 2D (Spyrou et al., 2019; Tekoglu et al., 2011) or a 3D structure (Martínez et al., 2016, 2018; Aage et al., 2017; Baandrup et al., 2020). In the context of additive manufacturing, Voronoi polyhedra generated by tessellation enables the design of multi-phase composite structures and can feature very low solid densities, if the inclusion phase is taken as void. On the other hand, tessellated Voronoi cellular materials contain points of high stress concentration thereby proving highly sensitive to geometrical and fabrication defects like many truss- and shell-based lattices (Ashby and Gibson, 1997; Onck et al., 2001; Papka and Kyriakides, 1994, 1998; Deshpande et al., 2001; Symons and Fleck, 2008; O’Masta et al., 2017; Liu et al., 2017; Bonatti and Mohr, 2019). They may thus be further optimized especially for use in applications where large nonlinear deformations, buckling loads and fractures are involved (e.g. energy, bending stiffness). To overcome this issue, in very recent years novel periodic plate-based cellular materials (see for instance Tancogne-Dejean et al. (2018); Wang and Sigmund (2021)) as well as non-periodic porous architectures have been designed, optimized and studied experimentally. Notable examples include double gyroid nanolattices (Crossland et al., 2008; Prusty et al., 2020) and microlattices (Maskery et al., 2017) very recently extended to stochastic geometries (Al-Ketan et al., 2021), as well as spinoidal Gaussian architectures using both threshold and phase-field methods (Teubner, 1991; Roberts and Teubner, 1995; Roberts and Garboczi, 2001; Hsieh et al., 2019; Khristenko et al., 2020) and machine-learning techniques (Kumar et al., 2020). Another random geometry is that of polydisperse (i.e. multiple size) particulate microstructures designed via a random adsorption algorithm (RSA) combined with computational homogenization (Torquato, 2002; Segurado and Llorca, 2002; Lopez-Pamies et al., 2013; Anoukou et al., 2018; Tarantino et al., 2019; Zerhouni et al., 2019). Of course a large class of low-density random porous solids involves foams (see for instance Deshpande and Fleck (2000) and Gong and Kyriakides (2005)). In the present study, we will include a two-dimensional equivalent of the foam geometry, that of standard Voronoi to be discussed later.

More generally, most lightweight porous materials are great candidates for energy absorption and structural applications because of their particular compressive response which may be divided into three regimes: (i) an initial almost linear regime up to a peak-stress, (ii) a stress-oscillating plateau or very low hardening regime and finally (iii)

a strongly hardening regime, called as densification. Without giving the most general discussion here for the sake of brevity, one may attribute the peak-stress and subsequent plateau to a combination of an elastic buckling instability and/or plastic localization or even secondary bifurcations (see for instance discussions in [Ashby and Gibson \(1997\)](#), [Triantafyllidis and Schraad \(1998\)](#) and [Schaedler and Carter \(2016\)](#)). In brittle polymers, fracture of ligaments occurs before or immediately after elastic instabilities following the peak-stress ([Thornton and Magee, 1975](#); [Ashby and Gibson, 1997](#); [Triantafillou and Gibson, 1990](#); [Bi et al., 2020](#)). In turn, the recent study of [Luan et al. \(2022\)](#) has focused on the compressive response of flexible elastomers, where the effect of smoothness of the intervoid ligaments and polydispersity of void size has been addressed numerically. Therein, those two geometrical characteristics have been shown to affect both the initial stiffness of foams (which is in qualitative agreement with the experimental work of [Zerhouni et al. \(2019\)](#)) as well as the level of the peak-stress.

1.3 Scope of the study

The present thesis is concerned with materials with random topologies, with a particular focus on porous materials. In this regard, we assess the mechanical response of random porous materials at large strains by numerical simulations or experimental testing. After studying a variety of existing random porous geometries, we propose a novel computational morphogenesis process allowing to design of random (i.e. non-periodic) composite materials that contain *smooth, polydisperse* Voronoi-type inclusions with *non-uniform* intervoid ligament thicknesses randomly embedded into a base matrix phase. This process is developed drawing inspiration from prior studies on epithelial cell remodeling ([Liu et al., 2010](#); [Kasza et al., 2014](#)) and is implemented using a finite-element (FE) framework. The response of the resulting geometries is studied numerically and experimentally. Specifically, it consists of deforming numerically – under uniform displacement (Dirichlet) boundary conditions – an arbitrarily-shaped convex cell that contains a discrete number of circular void inclusions. The latter are randomly dispersed into a non-linear elastic matrix phase and are generated via the general-purpose RSA algorithm developed in [Segurado and Llorca \(2002\)](#) and [Lopez-Pamies et al. \(2013\)](#). Countless composite architectures can be generated with this process depending on the type of the inclusion phase, which may be void, solid, or fluid-like and can potentially span relative densities from zero to unity. The full density range and especially the large porosities are achieved through a numerical intermediate remeshing step in the M-Voronoi generation process. To facilitate numerical deformation reaching large porosities, we develop an algorithm to remesh an extremely deformed orphan mesh. This has been done through geometry reconstruction of the orphan mesh and subsequent mesh generation with higher quality.

For illustrative purposes, we first focus on two-dimensional porous inclusions embedded in a semi-brittle polymer solid. To begin with, the mechanical properties of the base polymer matrix which is a highly viscous material are investigated. We will perform a mechanical characterization of this material by carrying out different tests such as tensile,

loading-unloading, cyclic, and relaxation tests. Then we will 3D-print two-dimensional porous materials with this polymer as a matrix. Subsequently, we will thoroughly investigate experimentally the mechanical response of porous architectures at various relative densities. The newly developed void geometries closely resemble the polyhedra obtained by standard Voronoi tessellations but differ in two ways; they comprise non-uniform intervoid ligament thickness and have smooth void boundaries. Due to the mechanically-grown origin of the void geometry, we call these materials M-Voronoi throughout the study. We note that the heart of the process, which is based on numerical nonlinear elastic energy minimization and uniform displacement boundary conditions, is independent of the dimension and shape of the primary cell (provided it is convex). The latter allows the seamless assembly of the individual cells (of any porosity) in macro-geometries of any shape and variable spatial stiffness. We will show in particular that the M-Voronoi exhibit continuous strong hardening (and thus no apparent peak-stress) well before densification. The second part of this study is concerned with the extension of this method to three-dimensional space. It is observed that this method is able to produce 3D polygonal smooth shape voids with variant wall thicknesses. These geometries are called 3D M-Voronoi. Using a matrix that is elastic-perfectly plastic without hardening, we numerically evaluate the mechanical properties of the 3D geometries at large compressive strains. Specifically, the random 3D M-Voronoi geometries are compared with the random RSA and Gyroid lattices of the same porosity.

1.4 Organization of the thesis

Following this introduction, the thesis is organized as follows:

In Chapter 2, we selectively review the computer-aided design of several well-chosen random and periodic geometries. In Section 2.1, we review the origin of the RSA algorithm and its general concepts. The modified algorithms to create 3D and 2D RSA geometries are briefly discussed in Sections 2.2 and 2.3, respectively. Subsequently, in Section 2.4, we describe the Voronoi tessellation algorithm implemented in this study. The design process of two periodic geometries corresponding to hexagonal lattices and TPMS structures is discussed in Sections 2.5 and 2.6, respectively.

In Chapter 3, the general numerical construction process of the M-Voronoi geometry is presented. In Section 3.1, we discuss in detail all the numerical steps and assumptions of the developed method. The governing equations for porosity evolution are described in Section 3.2. Further, a novel algorithm has been proposed for the remeshing of 2D orphan meshes that contain multiple phases or voids without corresponding CAD models. The proposed remeshing method enables us to achieve large porosities in M-Voronoi geometries by an intermediate remeshing step. The mesh reconstruction algorithm is described in Section 3.3. Subsequently, various representative numerical realizations of porous M-Voronoi topologies are obtained in different unit-cell geometries (Section 3.4). Furthermore, in Section 3.7, the M-Voronoi method has been extended to create anisotropic M-Voronoi geometries with tunable mechanical properties. In Section 3.8, triangular, trapezoidal,

and rectangular M-Voronoi cells are seamlessly assembled to design a complex structure with variable porosity in different regions.

Chapter 4 discusses the 3D-printing, experimental, and numerical study of randomly designed two-dimensional geometries. First, the mechanical properties of the base polymer material (TangoBlack) used in the 3D-printing of porous geometries are characterized in Section 4.2. This has been performed by testing the TangoBlack sample under tensile, loading-unloading, and relaxation tests. At ultimate stress values, the studied material exhibits brittle fractures while also showing highly viscous behavior. In Section 4.2.8, the nonlinear viscous behavior of TangoBlack is modeled using nonlinear hyperelastic viscous material modeling. The characterized material parameters at small strain rates are employed to model porous geometries manufactured with TangoBlack material as the matrix. The experimental methods including the 3D-printing strategy and the protocol for mechanical compression tests on random porous geometries are described in Section 4.3. Then, in Section 4.5.2 we analyze the representativity of the M-Voronoi response in terms of different realizations and the size of voids. Subsequently, in Section 4.5.3, we compare the M-Voronoi with two additional random porous geometries. The first comprises 2D RSA geometries, and the second is obtained by a uniformly eroded Voronoi tessellation algorithm, named E-Voronoi. Then, in order to make contact with the literature and further clarify the origin of the hardening response, we also compare the M-Voronoi with honeycomb materials (Section 4.5.4). The chapter ends with a selection of numerical simulations of the tested geometries under large strain compression loading.

In Chapter 5, we extend the M-Voronoi morphogenesis method to three-dimensional space to create random 3D porous geometries. In Section 5.2, the proposed two-dimensional remeshing algorithm is extended to the general three-dimensional case. We show in Section 5.3, that a full range density is attainable by the proposed M-Voronoi method. Subsequently, in Section 5.4, the obtained 3D M-Voronoi geometries are numerically studied by considering the matrix as an elastic perfectly plastic material. Additionally, RSA random geometries and Gyroid lattices were compared with 3D M-Voronoi, and we observed an enhanced plastic response in random topologies.

Key features of the developed method to create M-Voronoi and other random geometries are summarized in Chapter 6. Finally, in Section 6.2, we propose possible future directions of research in the context of this work.

List of publications

- Hooshmand-Ahoor, Z., Tarantino, M. G., and Danas, K., "Mechanically-grown morphogenesis of Voronoi-type materials: Computer design, 3D-printing and experiments." *Mechanics of Materials* 173 (2022): 104432.
- Luo, H., Hooshmand-Ahoor, Z., Danas, K., and Diani, J., "Mechanical responses of a nonlinear matrix with randomly distributed high volume fractions of spherical inclusions or pores." *Submitted*
- "Nonlinear elastic-viscoelastic and tensile strength of TangoBlack material: experiments and modeling" *In preparation*
- "Random Voronoi-type and RSA materials with on-demand porosity: compressive elastoplastic response and comparison with TPMS" *In preparation*

Chapter 2

Random and periodic geometries: a selective review

Chapter summary: This chapter provides a brief review of the computer-aided design process of selected random and periodic geometries that are used in the next chapters. The random geometries correspond to random polydisperse porous materials with non-overlapping spherical and ellipsoidal voids obtained by the random sequential adsorption (RSA) method, and standard eroded Voronoi geometries. In addition, the design process of two periodic geometries including hexagonal honeycombs and TPMS geometries (Gyroid) is studied. We first investigate the RSA algorithm in three-dimensional space while proposing a slightly different algorithm to find the minimum distance between the inclusions. Then, an extension of the RSA algorithm is developed to achieve a large volume fraction of the inclusions. The two-dimensional version of the RSA algorithm is then developed to generate random elliptical inclusions in a 2D unit-cell. In the next part, we review the standard eroded Voronoi method used to create Voronoi-type 2D geometries and we discuss the modifications applied to it, in order to use the final geometry under compression loading. The computer-design process of two periodic geometries corresponding to hexagonal honeycombs in 2D and Gyroid lattices in 3D is studied while discussing the governing equations.

Contents

2.1	What is RSA algorithm?	14
2.1.1	General concepts of the RSA algorithm	15
2.2	RSA algorithm in three-dimensional space	17
2.2.1	Microstructure parameters of the 3D RSA algorithm	17
2.2.2	Description of the general structure of the RSA algorithm	18
2.2.3	The minimum distance between two ellipsoids	20
2.2.4	The minimum distance between an ellipsoid and a plane	23
2.2.5	The periodicity of the unit-cell	24

2.2.6	An extension of the RSA algorithm to achieve large volume fractions	25
2.3	RSA algorithm in two-dimensions	26
2.3.1	Microstructure parameters of the 2D RSA algorithm	27
2.3.2	The minimum distance between two ellipses	28
2.3.3	The minimum distance between an ellipse and the unit-cell boundaries	29
2.3.4	The periodicity of a 2D unit-cell	29
2.4	The eroded Voronoi (E-Voronoi) method	30
2.5	Hexagonal lattices	31
2.5.1	Prescribed L_W and N_W	33
2.5.2	Prescribed L_H and N_H	34
2.6	Triply periodic minimal surfaces (TPMS) structures	35
2.7	Concluding remarks	38

2.1 What is RSA algorithm?

The construction of random spheres in a volume has always been a popular topic in many scientific communities including physics, material science, and chemical physics. In a broad sense, two types of random constructions of spheres in a volume exist, the *random close packing (RCP)* and the *random sequential adsorption (RSA)*. The RCP algorithm typically begins with fixed or rearranged seeds, which then grow until the target volume fraction is achieved. This algorithm was proposed by (Lubachevsky and Stillinger, 1990) for random packing of disks and (Lubachevsky et al., 1991) for random packing of spheres and it follows the primary works of (Mason et al., 1967) and (Adams and Matheson, 1972). The basic idea of the RSA algorithm was proposed by (Widom, 1966) which consists of randomly, irreversibly, and sequentially placing non-overlapping spheres into a volume. This algorithm has been used to generate equi-sized disks by (Rintoul and Torquato, 1997) and discussed in detail in Chapter 3 of (Torquato, 2002).

Several modifications have been applied to the RSA algorithm to employ it in more general cases. Segurado and Llorca (2002) modified the RSA algorithm to create *periodic* RSA microstructures while satisfying two essential geometric conditions: 1- the distance between any pair of particles has to exceed a minimum value (here noted as s_1), and 2- the distance between every particle and the unit cell faces has to be more than a minimum value (here noted as s_2). Using both conditions ensures adequate spatial discretization for numerical simulations or printing accuracy for the manufacturing process. Furthermore, in order to impose periodicity in the microstructure, all spheres that intersect the unit cell surfaces have been duplicated in three directions at the distance of the cell length.

In several studies, this form of RSA algorithm has been explained and implemented to create random spherical voids or particles. For instance, [Fritzen et al. \(2012\)](#) has used the periodic RSA microstructures for computational homogenization of elastoplastic porous metals. In the work of [Lopez-Pamies et al. \(2013\)](#), another modification to the RSA algorithm has been proposed to construct polydisperse microstructures with different families of particle sizes.

The extension of spheres to ellipsoids inclusions in the RSA algorithm has been proposed by [Pierard et al. \(2007\)](#). In that work, they construct a rectangular prism that contains random and homogeneous dispersion of identical unidirectional ellipsoids. Unlike spheres, the computation of the minimum distance between two ellipsoids is not straightforward, especially if the ellipsoids are oriented randomly. Therefore, [Pierard et al. \(2007\)](#) has used an iterative algorithm proposed by [Lin and Han \(2002\)](#) to compute the minimum distance between two randomly oriented ellipsoids.

In a more recent work by [Anoukou et al. \(2018\)](#), a general case of RSA algorithm has been proposed to construct periodic RSA microstructures containing non-overlapping randomly oriented inclusions of ellipsoidal shape that are uniformly distributed in the unit cell. Moreover, different families of inclusions could be specified to create polydispersity in size, shape, or polydispersity in size and shape. As a result, the algorithm will be able to achieve a larger volume fraction of inclusions. [Zerhouni \(2019\)](#) have proposed another extension to the RSA algorithm. This extension assists in achieving large volume fractions by automatically constructing unlimited numbers of inclusion families until the target volume fraction is achieved.

In this thesis, the latter form of the RSA algorithm with a slight modification has been used to create RSA structures. The modification concerns the intersection check method proposed by [Anoukou et al. \(2018\)](#) and will be discussed in Section 2.2.3. Eventually, the code contains all of the extended features of the RSA algorithm including automatic regression to facilitate obtaining large volume fractions. Furthermore, the 2D version of the RSA algorithm has been developed and described in detail in Section 2.3. In the following sections, we have followed the same notation as in [Anoukou et al. \(2018\)](#).

2.1.1 General concepts of the RSA algorithm

The consecutive generation of inclusions in the RSA method consists of placing randomly and sequentially non-overlapping objects into a volume. In this process, subsequent inclusions are accepted based on geometrical constraints relating to the previously accepted inclusions and the cell faces. In contrast to the RCP method, the acceptance of inclusions in the RSA method is irreversible, hence the position, size, and shape of the inclusions cannot be further modified. Generally, there are three types of geometrical conditions upon the acceptance of an inclusion:

- 1- Inclusions must not overlap and maintain a minimum distance s_1 between each other to ensure sufficient spatial discretization.
- 2- Inclusions must keep a minimum distance s_2 from the boundary surfaces to ensure

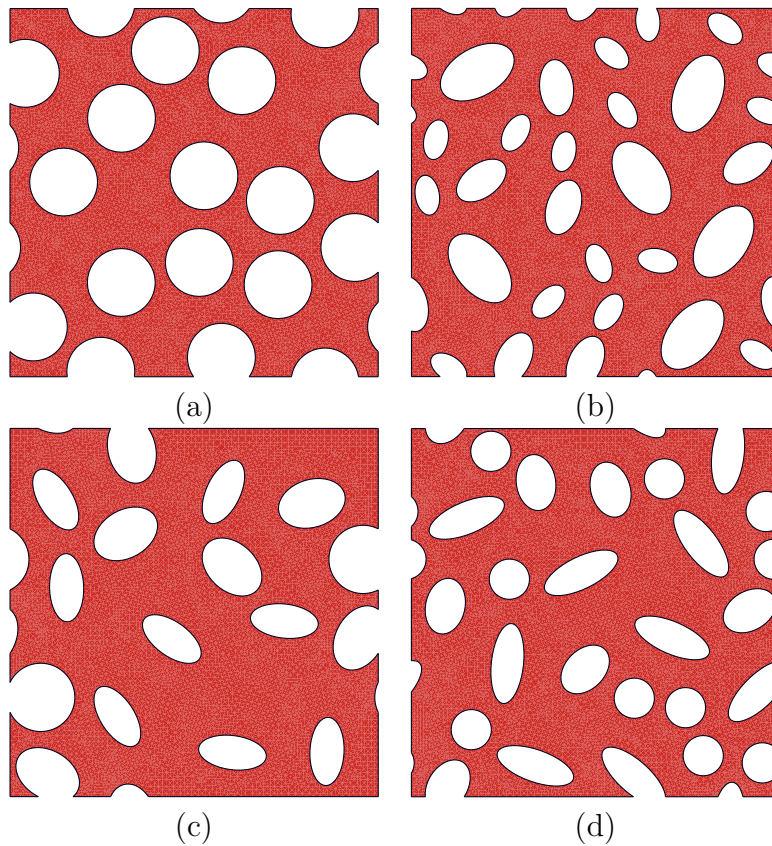


Figure 2.1: Realizations of microstructures with different types of distributions: (a) Monodisperse, (b) Polydispersity only in size, (c) Polydispersity only in shape, and (d) Polydispersity in size and shape.

sufficient spatial discretization.

3- Any inclusion which intersects with any of the boundary surfaces must be duplicated on the opposite surface to impose the periodicity of the microstructure.

Once a random inclusion in the matrix has been generated, the examination process will begin to evaluate the geometrical constraints. If all constraints are met, the inclusion would be accepted; otherwise, the process would have to be repeated with a new random inclusion.

Following the study of [Lopez-Pamies et al. \(2013\)](#), in a *monodisperse* microstructure, the inclusions are randomly located and oriented and have the same shape and size. However, in a *polydisperse* microstructure, the inclusions have a variety of sizes and shapes. For illustrative purposes, Figure 2.1 shows the examples of monodisperse and polydisperse distributions (polydispersity in size, shape, size and shape) in 2D.

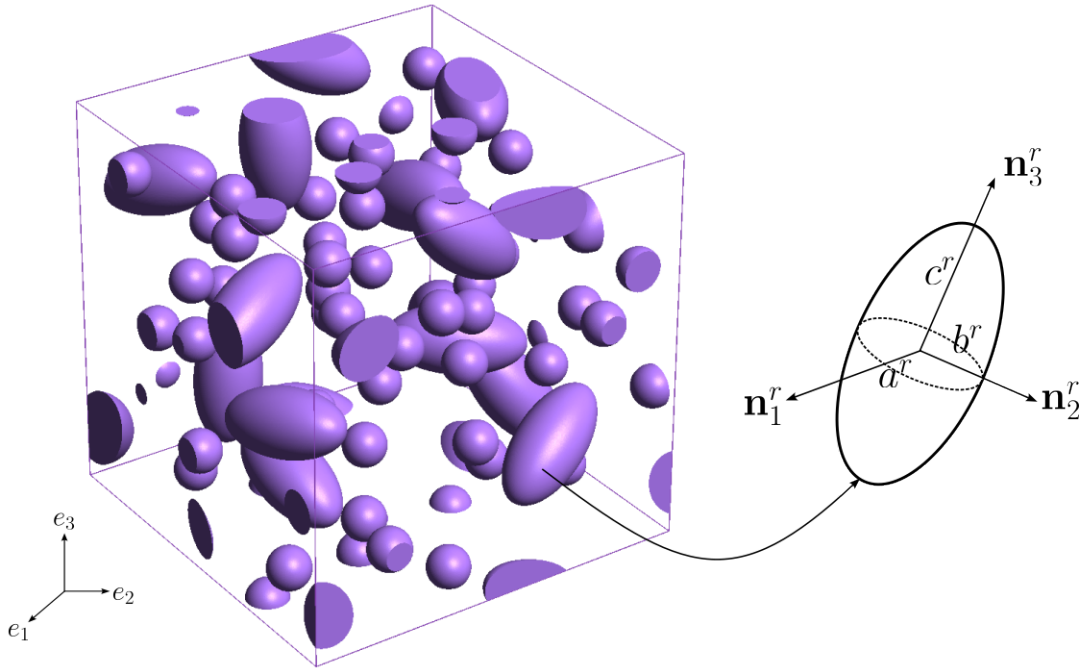


Figure 2.2: A cuboidal RSA microstructure that contains random inclusions and the characteristics of an ellipsoidal geometry: the aspect ratios $\omega_1^r = c^r/a^r$ and $\omega_2^r = c^r/b^r$ the orthonormal vectors \mathbf{n}_1^r , \mathbf{n}_2^r and \mathbf{n}_3^r .

2.2 RSA algorithm in three-dimensional space

In the present work, we have slightly modified the original algorithm of [Anoukou et al. \(2018\)](#) to make it more robust. For this reason, we find it useful to provide the details below.

2.2.1 Microstructure parameters of the 3D RSA algorithm

We consider a cuboidal unit-cell with dimensions L_1 , L_2 , and L_3 , and the total volume V . We note that the unit-cell shape options are limitless and not restricted to the cuboidal shape. The unit-cell volume consists of N_p phases, where the first phase corresponds to the matrix phase and $N_p - 1$ families of inclusions are embedded in the matrix. The volume of every family r is V^r , such that $\sum_{r=1}^{N_p} V^r = V$ and the corresponding volume fractions are $c^r = V^r/V$ such that $\sum_{r=2}^{N_p} c^r = c$, where c is the total volume fraction of the inclusions. Considering the inclusions to be ellipsoidal, every family r has two aspect ratios $\omega_1^r = c^r/a^r$ and $\omega_2^r = c^r/b^r$ ($r = 2, \dots, N_p$) and the orientation of every ellipsoidal inclusion is characterized by orthonormal basis vectors \mathbf{n}_i^r ($i = 1, 2, 3$). The characteristics of a random ellipsoidal inclusion embedded in a matrix are displayed in [Figure 2.2](#).

In order to calibrate the inclusion size and/or shape of every family/phase, we define a reference size of inclusions N^{ref} . In a monodisperse distribution, the reference number of inclusions is $N^{ref} = N$, where N is the total number of inclusions. In contrast, in a polydisperse distribution $N^{ref} < N$, and the reference number is obtained by using the reference number in monodisperse distribution for consistency. The total number of inclusions could be written as $\sum_{r=2}^{N^p} N^r = N$, where N^r corresponds to the number of inclusions in the family/phase r . In the most general case of polydispersity which is the size and shape polydispersity, the reference inclusion is a sphere of radius R^{ref} , from which all families are calibrated. Considering χ^r the size ratio of families, R^{ref} could be identified via the following relation ¹

$$c = \frac{V^{inc}}{V} = \frac{N^{ref} 4\pi R^{ref^3}}{3 L_1 L_2 L_3}. \quad (2.1)$$

Therefore

$$R^{ref} = \left(\frac{3 c L_1 L_2 L_3}{4\pi N^{ref}} \right)^{1/3}. \quad (2.2)$$

Subsequently, the characteristic lengths of each family of inclusions are described as follows:

$$c^r = \chi^r (\omega_1^r \omega_2^r)^{1/3} R_{ref}, \quad a^r = \frac{c^r}{\omega_1^r}, \quad b^r = \frac{c^r}{\omega_2^r}. \quad (2.3)$$

2.2.2 Description of the general structure of the RSA algorithm

Assuming the microstructural characterization described in Section 2.2.1, we give a precise description of the RSA algorithm structure below.

Initiation: we start with the first family of inclusions $r = 1$ and the current total volume fraction c^t being 0. As we iteratively add accepted inclusions, the total volume fraction will increase until the c^r has been achieved. Then, the construction of the next family will begin. At each iteration, we create a random inclusion with a random center position vector \mathbf{v}_i^r , a random orientation, and the semi-axes lengths a_i^r , b_i^r , c_i^r . The subscript i corresponds to the ellipsoidal inclusion number $i = 1, \dots, N$, and the superscript r determines the family/phase number.

General steps: For each phase $r = 2, \dots, N^p$, the RSA algorithm can be decomposed into the following steps:

Step 1: For the current volume fraction being $c^{r-1} \leq c^t < c^r$, we evaluate the semi-axis lengths of the inclusion i belonging to phase r with the general equations (2.2) and (2.3) developed in the Section 2.2.1. In sequential addition, we generate an inclusion with a random center position vector \mathbf{v}_i^r and a random orientation characterized with Euler

¹We note that if the unit-cell is not cuboidal, the total volume V does not have this form.

angles ϕ_i^r , θ_i^r , ψ_i^r .²

Step 2: We compute the minimum possible distance Δ_1 between a new inclusion i and any previously accepted inclusion $j = 1, \dots, i - 1$ including its 26 (9 in 2D) periodic images defined by the center to center translation vector $\mathbf{h} = (h_1, h_2, h_3)$ with $h_1, h_2, h_3 \in \{0, -L_i, L_i\}$. The computed distance will be compared to the minimum value s_1 , which corresponds to

$$s_1 = (\max(a_i^r, b_i^r, c_i^r) + \max(a_j^r, b_j^r, c_j^r)) \text{tol}_1, \quad (2.4)$$

where tol_1 is an input parameter. If for inclusion i and all of its periodic images $\Delta_1 < s_1$, the process is stopped and will be returned to the *Step 1* to generate a new random inclusion center and orientation. Otherwise, the algorithm proceeds to *Step 3*. This algorithm is described in Section 2.2.3 for 3D RSA and in Section 2.3.2 for 2D RSA.

Step 3: We compute the minimum possible distance Δ_2 between a new inclusion i and all the unit-cell boundary faces, including its 26 (9 in 2D) periodic images, and compare this distance to the minimum value s_2 , which corresponds to

$$s_2 = (\max(a_i^r, b_i^r, c_i^r)) \text{tol}_2, \quad (2.5)$$

where tol_2 is an input file. Similarly, if $\Delta_2 < s_2$ the algorithm is reset to *step1*, otherwise the inclusion is irreversibly accepted and the algorithm proceeds to *step 4*. The current volume fraction is then incremented by the volume fraction of the newly added inclusion i which corresponds to

$$c_{new}^t = c_{old}^t + \frac{4 \pi a_i^r b_i^r c_i^r}{3 L_1 L_2 L_3}. \quad (2.6)$$

The algorithm for this step is described in Section 2.2.4 for 3D RSA and in Section 2.3.3 for 2D RSA.

Step 4: If the accepted inclusion i intersects the unit-cell boundary faces, we ensure the periodicity of the unit-cell by adding periodic images of the inclusion. The periodicity algorithm is described in Section 2.2.5.³

²The ϕ_i^r and ψ_i^r are generated randomly in $[-\pi, \pi]$ interval, However the angle θ_i^r is obtained by randomly generating $\cos \theta_i^r \in [-1, 1]$ and then by setting $\theta_i^r = \cos^{-1}(\cos \theta_i^r)$. This allows to maintain a uniform distribution of points in a unit-cell.

³We note that the periodicity condition does not apply to all unit-cell geometries. For example, if the unit-cell is circular (spherical in 3D) or triangular, or an irregular quadrilateral, the periodicity is pointless.

2.2.3 The minimum distance between two ellipsoids

In this section, we discuss in detail the procedure used to compute the minimum distance between two randomly oriented ellipsoids. For non-spherical inclusions, the evaluation of the minimum distance is not as straightforward as for spheres in which the center-to-center distance is taken into account. Studies on the analytical methods evaluating the minimum distance between two algebraic surfaces, lead to solving complex nonlinear equations (Chen et al., 2006), which are unsuitable for numerical computations. Instead, we use the iterative method proposed by Lin and Han (2002) and used in the work of Pierard et al. (2007). Unlike existing analytical approaches, this algorithm is fast and has excellent convergence.

To compute the minimum distance, it is necessary to check whether two ellipsoids intersect. In the algorithm of Lin and Han (2002), the intersection is checked by solving two one-dimensional quadratic inequalities at each iteration. In the work of Anoukou et al. (2018), they modified the intersection identification of the algorithm of Lin and Han (2002) by using a lemma on the intersection of ellipsoids outlined in the book of Kurzhanski and Vályi (1997). According to these authors, the latter method is faster than the method proposed by Lin and Han (2002). In this work, we modify the method of Anoukou et al. (2018) by using the algorithm proposed by Lin and Han (2002), to check the intersection of the ellipsoids. We realized that this algorithm is way more general, simpler, and could be faster if we impose an important condition of the algorithm of Lin and Han (2002) while solving the set of two quadratic equations. Moreover, unlike the algorithm of Anoukou et al. (2018), this method can also be applied easily to the 2D version of the RSA algorithm.

We consider a general form of an arbitrarily oriented ellipsoid E_i in the following

$$E_i = E(\mathbf{v}_i; \mathbb{Z}_i) := \{\mathbf{x} : Q_i(\mathbf{x}) \leq 0\}, \quad (2.7)$$

where \mathbf{v}_i denotes the center position of the ellipsoid i and $Q_i(\mathbf{x})$ is a quadratic function and corresponds to

$$Q_i(\mathbf{x}) = (\mathbf{x} - \mathbf{v}_i)^T \mathbb{Z}_i (\mathbf{x} - \mathbf{v}_i) - 1. \quad (2.8)$$

\mathbb{Z}_i is a positive definite square 3×3 matrix that describes the shape and the orientation of the ellipsoid E_i . Its eigenvalues correspond to the semi-axis lengths of the ellipsoid i (i.e., a_i, b_i, c_i) and its eigenvectors are the orthonormal basis of the ellipsoid $\mathbf{n}_1, \mathbf{n}_2, \mathbf{n}_3$. Therefore, the matrix \mathbb{Z} for an arbitrarily oriented ellipsoid $E(\mathbf{v}; \mathbb{Z})$ is defined as

$$\mathbb{Z}_i = \frac{1}{c_i^2} (\omega_{i,1}^2 \mathbf{n}_{i,1} \otimes \mathbf{n}_{i,1} + \omega_{i,2}^2 \mathbf{n}_{i,2} \otimes \mathbf{n}_{i,2} + \mathbf{n}_{i,3} \otimes \mathbf{n}_{i,3}). \quad (2.9)$$

Indeed, the orientation of the ellipsoid is determined by the rotation matrix $\mathbb{R}_i(\phi_i, \theta_i, \psi_i)$ such that $\mathbf{n}_{i,j} = \mathbb{R}_i \mathbf{e}_j$ ($j = 1, 2, 3$) and \mathbf{e}_j determines the orthonormal basis of the reference

coordinate $(\mathbf{e}_1, \mathbf{e}_2, \mathbf{e}_3)$ (see Figure 2.2). Finally, the principal axes of the ellipsoid E_i could be expressed as⁴

$$\begin{aligned}\mathbf{n}_1 &= (\cos \phi \cos \psi - \cos \theta \sin^2 \phi, \cos \theta \cos \psi \sin \phi + \cos \phi \sin \psi, \sin \phi \sin \theta) \\ \mathbf{n}_2 &= (-\cos \psi \sin \phi - \cos \phi \cos \theta \sin \psi, \cos \phi \cos \theta \cos \psi - \sin \phi \sin \psi, \cos \phi \sin \theta) \\ \mathbf{n}_3 &= (\sin \theta \sin \psi, -\cos \psi \sin \theta, \cos \theta).\end{aligned}\quad (2.10)$$

The matrix \mathbb{Z}_i could be obtained by substitution of the $\mathbf{n}_1, \mathbf{n}_2, \mathbf{n}_3$ into the equation (2.9). All the mentioned equations could be modified to the 2D RSA code. For more discussion, see Section 2.3.

Considering two arbitrarily oriented ellipsoids defined respectively by $E_1 = E(\mathbf{v}_1; \mathbb{Z}_1)$ and $E_2 = E(\mathbf{v}_2; \mathbb{Z}_2)$ as described in equation (2.7), the minimum distance between two ellipsoids could be expressed as an optimization problem such that

$$d(E_1, E_2) = \min_{\mathbf{x}_1 \in E_1, \mathbf{x}_2 \in E_2} \|\mathbf{x}_1 - \mathbf{x}_2\|, \quad (2.11)$$

where $\|\cdot\|$ denotes the Euclidean norm. As we are looking for the minimum distance between two non-overlapping ellipsoids, we can restrict the selected points \mathbf{x}_i to those on the ellipsoids surfaces, which means $(\mathbf{x}_1 - \mathbf{v}_1)^T \mathbb{Z}_1 (\mathbf{x}_1 - \mathbf{v}_1) - 1 = 0$ and $(\mathbf{x}_2 - \mathbf{v}_2)^T \mathbb{Z}_2 (\mathbf{x}_2 - \mathbf{v}_2) - 1 = 0$.

In order to solve the optimization problem, we use the algorithm proposed by Lin and Han (2002) for intersection checking and minimization simultaneously. This method uses an iterative process where at each iteration number k , the ellipsoid E_i is locally approximated by a spherical ball which is tangent to the ellipsoidal surface at a single point \mathbf{x}_i^k and marches along the internal surface of the ellipsoid (Figure 2.3). Two constructed tangent spheres $B_1 = B(\mathbf{o}_1^k; \beta_1^k)$ and $B_2 = B(\mathbf{o}_2^k; \beta_2^k)$ are defined as

$$B_i = B(\mathbf{o}_i^k; \beta_i^k) := \{\mathbf{y} : \|\mathbf{y} - \mathbf{o}_i^k\| \leq \beta_i^k\}, \quad i = 1, 2 \quad (2.12)$$

where \mathbf{o}_i^k and β_i^k are the center and radius of the sphere B_i at the k^{th} iteration, respectively, and correspond to

$$\begin{aligned}\mathbf{o}_i^k &= \mathbf{x}_i^k - \frac{\gamma_i}{2} \mathbf{N}_i^k, \\ \beta_i^k &= \frac{\gamma_i}{2} \|\mathbf{N}_i^k\|,\end{aligned}\quad (2.13)$$

where $\mathbf{N}_i = \nabla Q_i$ denotes the normal to the ellipsoid surface E_i at the point \mathbf{x}_i . The parameter γ_i is the matrix norm of \mathbb{Z}_i and is related to its spectral radius $\rho(\mathbb{Z}_i)$, such that

$$\gamma_i = \frac{1}{\|\mathbb{Z}_i\|_F} \quad \text{and} \quad 0 < \gamma_i \leq \frac{1}{\rho(\mathbb{Z}_i)}, \quad (2.14)$$

⁴here we dropped the subscript i for simplifications.

where $\|\bullet\|_F$ is the Frobenius (Euclidean) norm.

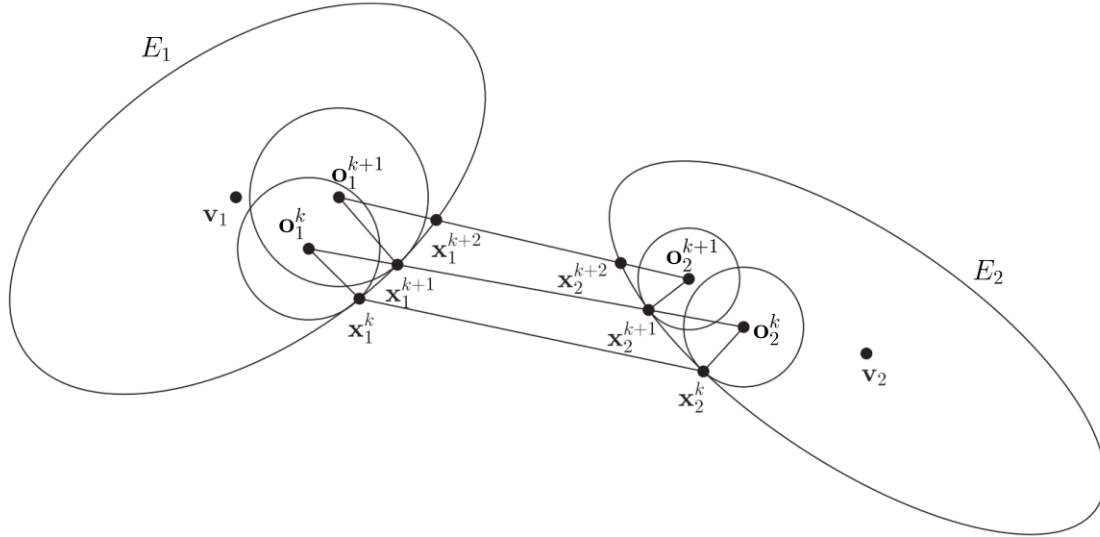


Figure 2.3: A schematic representation of the iterative algorithm for finding the minimum distance between two arbitrarily oriented ellipsoids. The picture has been taken from [Anoukou et al. \(2018\)](#) and has been modified according to our parameters.

The iterative process of computing the minimum distance between two ellipsoids is schematically displayed in Figure 2.3 and has been summarized in the following steps:

Initiation: We start by taking the sphere center point \mathbf{o}_1 and \mathbf{o}_2 as the centers \mathbf{v}_1 and \mathbf{v}_2 of the ellipsoids E_1 and E_2 , respectively.

step 1: We consider \mathbf{o}_1^k and \mathbf{o}_2^k as two spherical center points at the k th iteration. Next, we solve two one-dimensional quadratic equations to obtain the step sizes t_1 and t_2 .

$$t_i = \{t \in [0, 1] : A_i t^2 + B_i t + C_i = 0\}, \quad i = 1, 2 \quad (2.15)$$

with

$$\begin{aligned} A_i &= (\mathbf{o}_2^k - \mathbf{o}_1^k)^T \mathbb{Z}_i (\mathbf{o}_2^k - \mathbf{o}_1^k), \\ B_i &= (\mathbf{o}_1^k - \mathbf{v}_i)^T \mathbb{Z}_i (\mathbf{o}_2^k - \mathbf{o}_1^k), \\ C_i &= (\mathbf{o}_1^k - \mathbf{v}_i)^T \mathbb{Z}_i (\mathbf{o}_1^k - \mathbf{v}_i), \end{aligned} \quad (2.16)$$

Two ellipsoids E_1 and E_2 have a nonempty intersection if t_1 or t_2 have one of the following conditions:

$$E_1 \cap E_2 \neq 0 \quad \text{if:} \quad \begin{cases} t_2 \leq t_1 & \text{or} \\ t_1 \in (-\infty, 0) \cup (1, +\infty) & \text{or} \\ t_2 \in (-\infty, 0) \cup (1, +\infty) \end{cases} \quad (2.17)$$

If the intersection is nonempty then the minimum distance $d(E_1, E_2) = 0$, the process terminates, and the inclusion is not accepted. Otherwise, we proceed to the next step.

step 2: If the ellipsoids do not overlap, we compute two points \mathbf{x}_1^{k+1} and \mathbf{x}_2^{k+1} as the intersections of the center-to-center line of the tangent spheres $[\mathbf{o}_1^k, \mathbf{o}_2^k]$ with the ellipsoid surfaces, such that

$$\begin{aligned} \mathbf{x}_1^{k+1} &= \mathbf{c}_1^k + t_1(\mathbf{o}_2^k - \mathbf{o}_1^k), \\ \mathbf{x}_2^{k+1} &= \mathbf{c}_1^k + t_2(\mathbf{o}_2^k - \mathbf{o}_1^k), \end{aligned} \quad (2.18)$$

step 3: We now check whether the two points \mathbf{x}_1^{k+1} and \mathbf{x}_2^{k+1} are the closest points by computing the normal on the ellipsoid surfaces at these points i.e. \mathbf{N}_1^{k+1} and \mathbf{N}_2^{k+1} . If these normals and the vector $\mathbf{x}_2^{k+1} - \mathbf{x}_1^{k+1}$ are colinear, the minimum distance corresponds to $d(E_1, E_2) = \|\mathbf{x}_1^{k+1} - \mathbf{x}_2^{k+1}\|$. Collinearity is evaluated by determining whether the angles $\alpha_1 = \angle(\mathbf{N}_1^{k+1}, \mathbf{x}_2^{k+1} - \mathbf{x}_1^{k+1})$ and $\alpha_2 = \angle(\mathbf{N}_2^{k+1}, \mathbf{x}_2^{k+1} - \mathbf{x}_1^{k+1})$ are zero. In practice, we check $\alpha_1 \leq \epsilon$ and $\alpha_2 \leq \epsilon$ instead of $\alpha_1 = \alpha_2 = 0$, where ϵ is a small tolerance. If there is no collinearity, we proceed to the next step.

step 4: We generate two new balls with centers \mathbf{o}_1^{k+1} and \mathbf{o}_2^{k+1} , obtained from equation (2.13) as

$$\begin{aligned} \mathbf{c}_1^{k+1} &= \mathbf{x}_1^{k+1} - \frac{\gamma_1}{2} \mathbf{N}_1^{k+1}, \\ \mathbf{c}_2^{k+1} &= \mathbf{x}_2^{k+1} - \frac{\gamma_2}{2} \mathbf{N}_2^{k+1}. \end{aligned} \quad (2.19)$$

We start the new iteration with new tangent balls and return to the first step to repeat the process.

2.2.4 The minimum distance between an ellipsoid and a plane

In order to find the minimum distance between an arbitrarily oriented ellipsoid and a plane (defined as $d_{min}(E, P)$), we follow a similar collinearity condition that we presented in the previous section. In this case, we are solving a geometrical problem to find the closest point on the surface boundary of the ellipsoid E_i , in which the normal $\mathbf{N} = \nabla Q(\mathbf{x})$ is parallel with the normal of the plane.

We define the surface of the cuboidal unit-cell by the plane equation

$$P(\mathbf{n}, \xi) := \{\mathbf{x} : \mathbf{x} \cdot \mathbf{n} + \xi = 0\}, \quad (2.20)$$

where \mathbf{n} is the normal vector of the plane P , and ξ is a constant that can be evaluated by the scalar product of \mathbf{n} and a known point on the plane P . In a cuboidal unit-cell of dimensions L_1 , L_2 and L_3 , with a corner located at the origin, the normal \mathbf{n} and the constant ξ for six facing planes are defined as

$$\begin{aligned} \text{Face 1 : } \mathbf{n} &= (-1, 0, 0), & \xi &= 0, \\ \text{Face 2 : } \mathbf{n} &= (1, 0, 0), & \xi &= -L_1, \\ \text{Face 3 : } \mathbf{n} &= (0, -1, 0), & \xi &= 0, \\ \text{Face 4 : } \mathbf{n} &= (0, 1, 0), & \xi &= -L_2, \\ \text{Face 5 : } \mathbf{n} &= (0, 0, -1), & \xi &= 0, \\ \text{Face 6 : } \mathbf{n} &= (0, 0, 1), & \xi &= -L_3. \end{aligned} \quad (2.21)$$

Our task now is to find the solution to the following set of equations

$$\mathbf{N} \times \mathbf{n} = 0 \quad \text{and} \quad Q(\mathbf{x}) = 0. \quad (2.22)$$

There are two solutions to the above equations that correspond to the closest and farthest points of the ellipsoid from the plane. A closer point is chosen by calculating the distance between the two points from the plane P and keeping the smaller one

$$d(E, P) = \frac{|\mathbf{x} \cdot \mathbf{n} + \xi|}{\|\mathbf{n}\|}. \quad (2.23)$$

Therefore, \mathbf{x}_{min} is the solution of equation (2.22) which minimizes the distance $d(E, P)$. As a result, the minimum distance between the ellipsoid of the plane is defined as $d_{min}(E, P) = \mathbf{n} \cdot \mathbf{x}_{min} + \xi$.

2.2.5 The periodicity of the unit-cell

If periodicity is required, every accepted inclusion that intersects the unit-cell boundary faces has to be projected to the opposite faces. In order to determine whether the inclusions intersect the unit-cell boundaries, we use the following relations:

$$\begin{aligned} \forall j \in \{1, 3, 5\}, & \quad \text{if : } d_{min}(E, P) < 0 \implies \text{The inclusion intersects the face } j, \\ \forall j \in \{2, 4, 6\}, & \quad \text{if : } d_{min}(E, P) > 0 \implies \text{The inclusion intersects the face } j. \end{aligned}$$

We relocate the intersecting inclusions to the opposite faces by adding or subtracting the periodicity vectors \mathbf{h} to the center of the inclusion. If the inclusion intersects more than one face, one has to repeat the process in the other directions. The periodicity vectors

are a set of 26 vectors $\mathbf{h} = (h_1, h_2, h_3)$ where h_1 , h_2 and h_3 take the values $(0, -L_1, L_1)$, $(0, -L_2, L_2)$ and $(0, -L_3, L_3)$, respectively. We note that the intersection condition has also been used to create microstructures with no inclusions intersecting the boundaries. In this case, the intersecting inclusions are not accepted by the algorithm and a rigid bounding box with a minimum thickness of $tol2$ will cover the microstructure.

2.2.6 An extension of the RSA algorithm to achieve large volume fractions

Due to the irreversible nature of the sequential process in the RSA algorithm, achieving large volume fractions is more difficult than in the RCP algorithm. This drawback is more pronounced when we are interested in the monodisperse distribution of inclusions. There have been many numerical and experimental studies in the literature on the maximum volume fraction that can be achieved by RCP method for spheres of equal size (monodisperse distribution). However there is only one rigorous proof devised by Hales (1998) for *Kepler's conjecture*: the densest possible packing fraction c for identical spheres in three dimensions is $\pi/\sqrt{18} \approx 0.7405$, corresponding to the close-packed face-centered cubic (FCC) lattice or its stacking variants. For identical RSA spheres, the filling process reaches the saturation limit at a substantially lower value. It turns out that for a monodisperse distribution with RSA algorithm, the maximum volume fraction approximately corresponds to 0.38 and 0.55 for 3D and 2D RSA, respectively (Feder (1980), Cooper (1988)).

In order to overcome the volume fraction limitation, we create polydisperse distributions to fill the unit-cell with inclusions of smaller sizes. One can control the morphology of the microstructure by defining different families of inclusions to achieve the target volume fraction. However, finding the suitable set of parameters as described in the previous sections to obtain a microstructure with the target volume fraction c , could be long and difficult; especially if a large volume fraction is desired. Therefore, we use an automatic process to create an unlimited number of inclusion families by reducing the size of inclusions incrementally. Although there is not the same control over the morphology of the microstructure, one can define the limiting and regression parameters. Zerhouni (2019) have proposed another form of RSA algorithm to achieve large volume fractions. In this algorithm, he specifies the maximum and minimum sizes of the inclusions and the maximum iteration number for adding a new inclusion of the same size. When the maximum number of iterations is achieved, the algorithm reduces the size of inclusions by a regression number called g such that $R^{ref,new} = g R^{ref,old}$. This process continues until either the target volume fraction is reached or $R^{ref,new} = R^{min}$.

In this work, we use the method proposed by Zerhouni (2019) and modify it in our algorithm. In contrast to his work, we do not specify the maximum and minimum sizes of inclusions. Instead, the automatic regression process begins if the maximum number of iterations has been reached for each family of inclusions. This would lead the code to be more flexible in achieving the final volume fraction. This is due to the fact that, depending

Inputs		Outputs	
Parameters	Definition	Parameters	Definition
L_1, L_2, L_3	Unit-cell dimension	\mathbf{v}_i	Center of the inclusions
$N^p - 1$	Number of inclusion families	a_i, b_i, c_i	semi-axis lengths of the ellipsoids
N^{ref}	Number of inclusions	ϕ_i, θ_i, ψ_i	Euler angles of the ellipsoids orientation
c	Expected volume fraction of inclusions		
ω_1^r, ω_2^r	the aspect ratios of the ellipsoids		
χ^r	Size ratio of the families		
c^r/c	Volume fraction per inclusion family		
s_1, s_2	Offsets for adequate discretization		
g	Regression number		
nit	maximum iteration number for an inclusion		

Table 2.1: The inputs and Outputs of the 3D RSA algorithm.

on the characteristics of each family, there may not be sufficient space to accommodate new inclusions of the same size and shape. Therefore, automatic regression will assist the algorithm to fill the space and achieve the target porosity. The regression factor and the maximum iteration number are inputs and have to be specified by the user. In addition, the automatic regression process is optional and could be activated in the input file.

Finally, the input parameters are specified by the user and are listed in the table 2.1. In this table, r refers to the family number of inclusions and it is equal to $r = 1, \dots, N^p - 1$. The parameter i corresponds to the accepted inclusion number $i = 1, \dots, N$. The Output of the algorithm is a .geo file format readable in **Gmsh** or **Netgen** software.

2.3 RSA algorithm in two-dimensions

We established a 2D version of the RSA algorithm, which generates random distributions of random mono and polydisperse non-overlapping elliptical inclusions with arbitrary shape, size, and orientation in a 2D Unit-cell. Without losing generality, one can use the same 3D RSA algorithm and modify all the corresponding relations to the two-dimensional space. The same geometrical constraints described in Section 2.1.1 are applied to the 2D

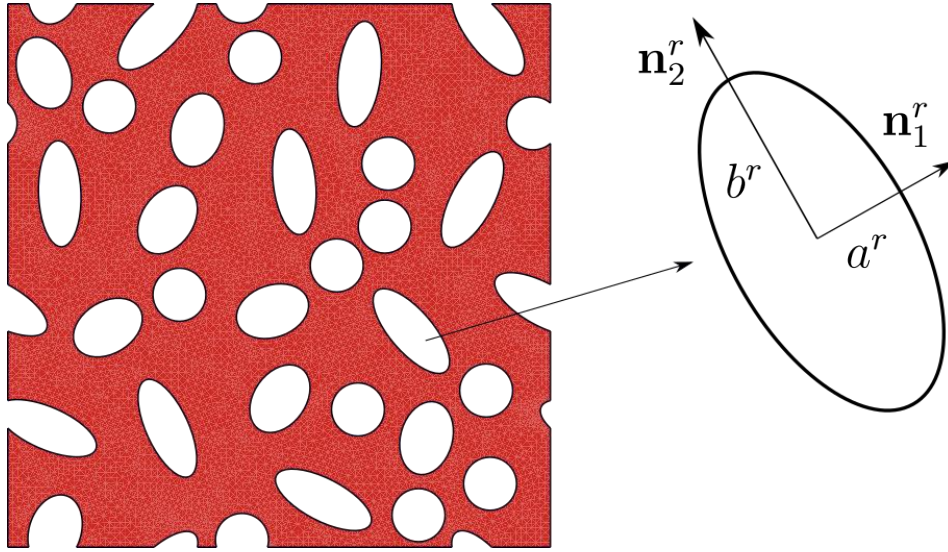


Figure 2.4: A rectangular RSA microstructure containing random 2D inclusions and the characteristics of an ellipse: the aspect ratio ω^r and the orthonormal vectors \mathbf{n}_1^r and \mathbf{n}_2^r .

RSA. However the microstructure parameters are different and are defined in the following section.

2.3.1 Microstructure parameters of the 2D RSA algorithm

We consider a rectangular unit-cell with dimensions L_1 and L_2 and a total surface S . The surface of every family r is S^r , such that $\sum_{r=1}^{N_p} S^r = S$ and the corresponding surface fractions are $c^r = S^r/S$ such that $\sum_{r=1}^{N_p} c^r = c$, where c is the total surface fraction of the inclusions. We note that the same parameter c is used to indicate the volume fraction in 3D and the surface fraction in 2D. In contrast to the ellipsoids in 3D space, an ellipse in 2D can be defined by two principal axes a^r and b^r and one aspect ratio $\omega^r = b^r/a^r$ ($r = 2, \dots, N_p$). In addition, the orientation of the ellipse is characterized by orthonormal basis vectors n_i^r ($i = 1, 2$). The characteristics of a random elliptical inclusion embedded in a 2D matrix are displayed in Figure 2.4.

Similar to the 3D RSA algorithm, we define a reference size of inclusions N^{ref} to calibrate the inclusion size and/or shape of every family. Again, in the most general case of polydispersity which is the polydispersity in size and shape, the reference inclusion is a circle of radius R^{ref} , from which all families are calibrated. Considering χ^r the size ratio of families, R^{ref} could be identified via the relation ⁵

$$c = \frac{S^{inc}}{S} = \frac{N^{ref} \pi R^{ref2}}{L_1 L_2}, \quad (2.24)$$

⁵We note that if the unit-cell is not rectangular, the total surface S does not have this form.

therefore

$$R^{ref} = \sqrt{\frac{c L_1 L_2}{\pi N^{ref}}}. \quad (2.25)$$

Subsequently, the characteristic length of each inclusion family is defined as

$$b^r = \chi^r \sqrt{\omega^r} R_{ref}, \quad a^r = \frac{b^r}{\omega^r}, \quad \text{where } \chi^r \leq 1. \quad (2.26)$$

2.3.2 The minimum distance between two ellipses

Following the 3D RSA code, the minimum distance between two 2D ellipses must exceed the minimum value s_1 , which corresponds to

$$s_1 = (\max(a_i^r, b_i^r) + \max(a_j^r, b_j^r)) tol_1, \quad (2.27)$$

where tol_1 is an input parameter. We follow the algorithm proposed by [Lin and Han \(2002\)](#) to check the intersection and compute the minimum distance, by transforming it into two-dimensional space. The equations (2.7) and (2.8) have also the general form of an arbitrarily oriented 2D ellipse $E(\mathbf{v}; \mathbb{Z})$, along with its corresponding 2D vectors. The \mathbb{Z}_i matrix is a positive definite square 2×2 matrix, where its eigenvalues are the semi-axis lengths of the ellipse (i.e., a_i, b_i) and its eigenvectors are the orthonormal basis of the ellipse $\mathbf{n}_1, \mathbf{n}_2$. Therefore, the matrix \mathbb{Z} in 2D space is defined as

$$\mathbb{Z}_i = \frac{1}{b_i^2} (\omega_i^2 \mathbf{n}_{i,1} \otimes \mathbf{n}_{i,1} + \mathbf{n}_{i,2} \otimes \mathbf{n}_{i,2}). \quad (2.28)$$

The orientation of the ellipse can be determined by one orientation angle θ_i such that the principal axes of the ellipse correspond to

$$\begin{aligned} \mathbf{n}_1 &= (\cos \theta, \sin \theta), \\ \mathbf{n}_2 &= (-\sin \theta, \cos \theta). \end{aligned} \quad (2.29)$$

By substitution of \mathbf{n}_1 and \mathbf{n}_2 into the equation (2.28), the expression for matrix \mathbb{Z}_i is given by

$$\mathbb{Z}_i = \frac{1}{a^2} \begin{bmatrix} \cos^2 \theta & \sin \theta \cos \theta \\ \sin \theta \cos \theta & \sin^2 \theta \end{bmatrix} + \frac{1}{b^2} \begin{bmatrix} \sin^2 \theta & -\sin \theta \cos \theta \\ -\sin \theta \cos \theta & \cos^2 \theta \end{bmatrix}. \quad (2.30)$$

We use the same algorithm to check the intersection and compute the minimum distance between two randomly oriented 2D ellipses E_1 and E_2 , defined by the equations (2.7), (2.8) and (2.28). However, in the iterative process, the 2D ellipse E_i is locally approximated by a 2D ball i.e., a circle that is tangent to the ellipse boundary line at a single point \mathbf{x}_i^k and marches along the internal boundary line of the ellipse (see Figure 2.3). All the vectors and equations are the same as the 3D algorithm, but with a 2D perspective, which means

all vectors contain two components and all matrices are 2×2 . For more discussion see Section 2.2.3.

2.3.3 The minimum distance between an ellipse and the unit-cell boundaries

The minimum distance between an ellipse and the boundary line of the unit-cell must exceed the minimum value s_2 , which corresponds to

$$s_2 = \max(a_i^r, b_i^r) \cdot tol_2, \quad (2.31)$$

where tol_2 is an input parameter. Similar to the 3D RSA, the minimum distance is obtained by solving a geometrical problem for finding the closest point on the boundary line of the ellipse E_i where the normal $\mathbf{N} = \nabla Q(\mathbf{x})$ is collinear with the normal of the plane \mathbf{n} . However, the unit-cell surfaces are transformed to unit-cell boundary lines in 2D and defined by

$$L(\mathbf{n}, \xi) := \{\mathbf{x} : \mathbf{x} \cdot \mathbf{n} + \xi = 0\}, \quad (2.32)$$

where \mathbf{n} is the normal vector of the line L , and ξ is a constant that can be evaluated by the scalar product of \mathbf{n} and a known point on the line L . In a rectangular unit-cell of dimensions L_1 and L_2 , with a corner located at the origin, the normal \mathbf{n} and the constant ξ for four boundary lines are defined as

$$\begin{aligned} \text{Line 1 : } \mathbf{n} &= (-1, 0), & \xi &= 0, \\ \text{Line 2 : } \mathbf{n} &= (1, 0), & \xi &= -L_1, \\ \text{Line 3 : } \mathbf{n} &= (0, -1), & \xi &= 0, \\ \text{Line 4 : } \mathbf{n} &= (0, 1), & \xi &= -L_2. \end{aligned} \quad (2.33)$$

Subsequently, we find the minimum distance $d_{min}(E, L)$ by solving the minimization problem in equation (2.22). If the unit-cell is not rectangular, one can define the corresponding normal vectors of the unit-cell boundary lines and follow the same procedure.

2.3.4 The periodicity of a 2D unit-cell

In order to determine periodic images of an inclusion intersecting the boundary lines, 8 vectors $\mathbf{h} = (h_1, h_2)$ are defined, where h_1 and h_2 take the values $(0, -L_1, L_1)$ and $(0, -L_2, L_2)$, respectively. In order to check the intersection of the inclusion with the boundary lines, we evaluate the sign of $d_{min} = \mathbf{n} \cdot \mathbf{x}_{min} + \xi$, such that:

$$\begin{aligned} \forall j \in \{1, 3\}, & \quad \text{if : } d_{min}(E, L) < 0 \implies \text{The inclusion intersects the face } j, \\ \forall j \in \{2, 4\}, & \quad \text{if : } d_{min}(E, L) > 0 \implies \text{The inclusion intersects the face } j. \end{aligned}$$

2.4 The eroded Voronoi (E-Voronoi) method

The Voronoi tessellation geometries are random geometries that are generated by the Laguerre-Voronoi diagram algorithm. In this algorithm, a 2D finite space is randomly divided into partitions of polygonal cells that are defined by a set of random seeds. The seeds are distributed randomly into the domain and they correspond to the center of circles which grow until connection occurs at the edges of circles in which the polygonal cell walls are defined. For each circle in this method, there is one cell, which is composed of all the points that lie within the circle such that their power distance is smaller than the power distance to the rest of the circles. The use of Voronoi geometries is very common in the simulation of polycrystalline microstructures which are modeled as composite materials. However, in this study, we are specifically interested in porous Voronoi geometries.

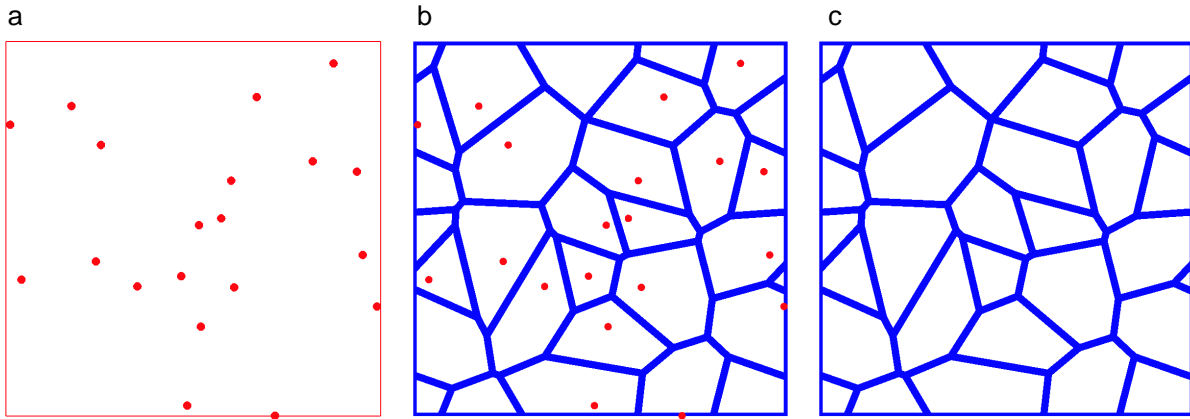


Figure 2.5: Generation of E-Voronoi geometries. (a) Random distribution of seeds. (b) To obtain the desired density, the cell walls are eroded and offset with a specific thickness. (c) The final E-Voronoi geometry with a surrounding solid box.

We follow the algorithm presented in [Spyrou et al. \(2019\)](#) for the modeling of human muscles to create these geometries. In that study, a standard Voronoi tessellation is first created by randomly distributed seeds and subsequently, the walls of each Voronoi inclusion are eroded in a uniform manner leading to constant-thickness intervoid ligaments. Therefore, we call them Eroded Voronoi (E-Voronoi) geometries. Figure 2.5 represents the generation process of E-Voronoi geometries with this algorithm. In Figure 2.5a the seeds of Voronoi are distributed randomly into the unit-cell by a random sequential addition algorithm [Torquato \(2002\)](#) such that they respect the defined minimum distance to ensure that the resulting Voronoi cells are not too small. Subsequently, the walls of each Voronoi cell are eroded to divide the domain into polygonal cells while applying a parallel offset to each Voronoi cell to generate a constant thickness area surrounding the cell (Figure 2.5b). The amplitude of erosion defines the final relative density of the unit-

cell. The erosion process has been performed by the Python Voronoi libraries `Qhull` and `Python/Scipy`. The geometric operations, such as applying an offset, are carried out by the `Python/Shapely` library. The periodicity condition has been applied to the geometries such that each seed is replicated in the neighboring cells. Nevertheless, the boundaries of the Voronoi geometry can be closed by a solid box if it is required. Closing the boundaries can be useful to avoid the collapse of the cells in the first rows when compression loading is applied to the unit-cell (see for example Section 4.5.3). In this case, the thickness of the surrounding box must be small enough to not affect the cell behavior and its thickness should be considered when calculating the volume fraction of the unit-cell.

The resulting structure of the Eroded-Voronoi algorithm is generated in the `Gmsh` format for mesh generation. The intervoid ligaments are meshed by two-dimensional elements to reach arbitrary density values (as opposed to earlier studies such as in [Tekoglu et al. \(2011\)](#) where beam elements were used). By construction, the E-Voronoi void boundaries exhibit sharp corners, while the process may lead to locally more elongated inclusions of large aspect ratio towards an arbitrary direction. The E-Voronoi geometries can span the entire range of practical relative densities from 0 to very low (e.g., 0.01) and are isotropic as a direct consequence of the random Voronoi tessellation process (but see the recent extension to anisotropic ones by [van Nuland et al. \(2021\)](#)).

2.5 Hexagonal lattices

Hexagonal lattices are a type of periodic cellular material that is certainly the most studied of all existing cellular materials. The term Hexagonal lattice is, in fact, a subgroup of honeycomb structures that contain also square or triangular cells. However, in this study, we will be specifically focusing on hexagonal lattices, and the honeycomb term wherever used refers to hexagonal lattices with six cell sides and three edge connectivity. Since centuries ago, this structure has been fascinating for mathematicians, physicists, and biologists ([Ashby and Gibson, 1997](#)). Particularly, in the mechanics community, there are countless studies on the properties of hexagonal lattices ([Papka and Kyriakides, 1994](#); [Ashby and Gibson, 1997](#); [Papka and Kyriakides, 1998](#); [Jiménez and Triantafyllidis, 2013](#)). Therefore, we do not discuss these studies, but instead, we study the process to create these lattices and will employ it in the studies in the next chapters.

In the literature, there are different formulations for the geometrical relations of hexagonal lattices insuring different morphological conditions such as variable beam length or thickness of the cell sides. Here, we assume that the geometry has a constant wall thickness and length. Furthermore, we consider that all cells in the geometry are closed and there are no open and incomplete cells at the edges of the lattice. This is a necessary condition to perform a compression test on these structures without having the first cell row collapsed. By imposing the mentioned constraints, we propose the following geometric formulation for hexagonal lattices. Figure 2.6a represents a considered single unit-cell in a honeycomb structure. This unit-cell will be repeated in the horizontal and vertical directions to construct the final lattice with the desired number of cells. Figure 2.6b shows

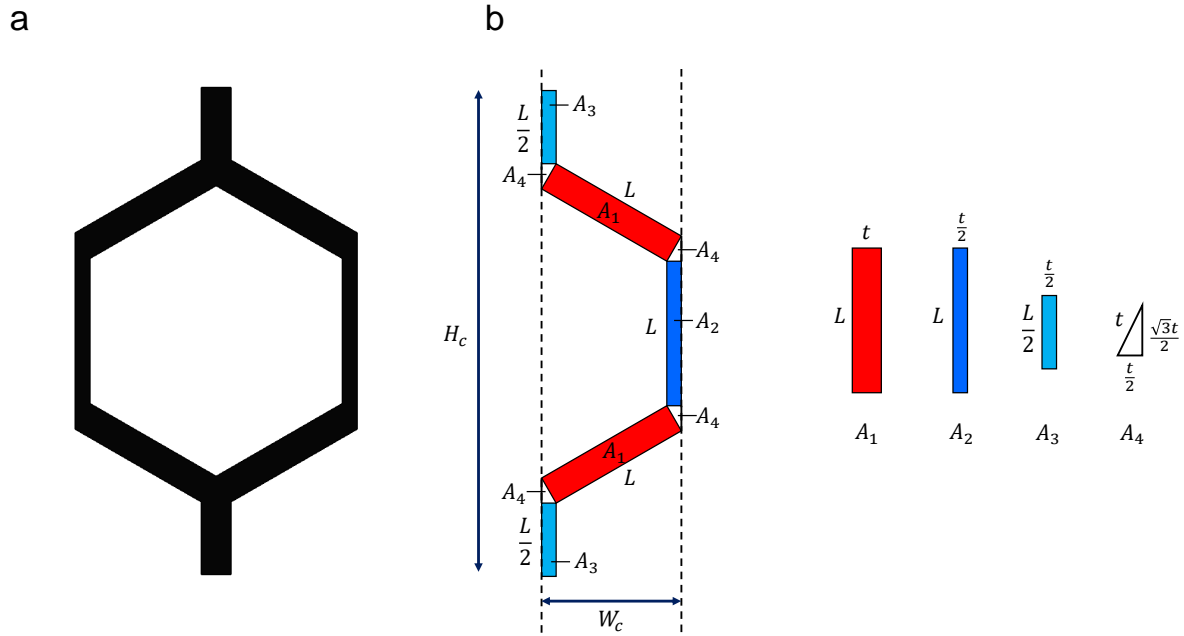


Figure 2.6: (a) A single unit-cell of the considered hexagonal lattice. (b) The geometrical parts of a half single hexagon unit-cell.

the geometric entities for half of the single hexagon unit-cell, where L corresponds to the constant length of the cell walls and t is their thickness. Moreover, H_c and W_c correspond to the height and width of the half unit-cell such that

$$H_c = 3L + \sqrt{3}t, \quad W_c = \frac{\sqrt{3}L}{2} + \frac{t}{2}. \quad (2.34)$$

This geometry consists of four different sub-geometries with the area of A_1 , A_2 , A_3 and A_4 . Therefore, the area occupied by the solid A_s constructing a half hexagon unit-cell can be obtained by

$$A_s = 2A_1 + A_2 + 2A_3 + 4A_4 = 3Lt + \frac{\sqrt{3}t^2}{2}. \quad (2.35)$$

Similarly, the total area occupied by the unit-cell A_c corresponds to

$$A_c = H_c W_c = (3L + \sqrt{3}t) \left(\frac{\sqrt{3}L + t}{2} \right). \quad (2.36)$$

Now, one can obtain the density of the unit-cell by

$$\rho_H = \frac{A_s}{A_c} = \frac{6Lt + \sqrt{3}t^2}{(3L + \sqrt{3}t)(\sqrt{3}L + t)}. \quad (2.37)$$

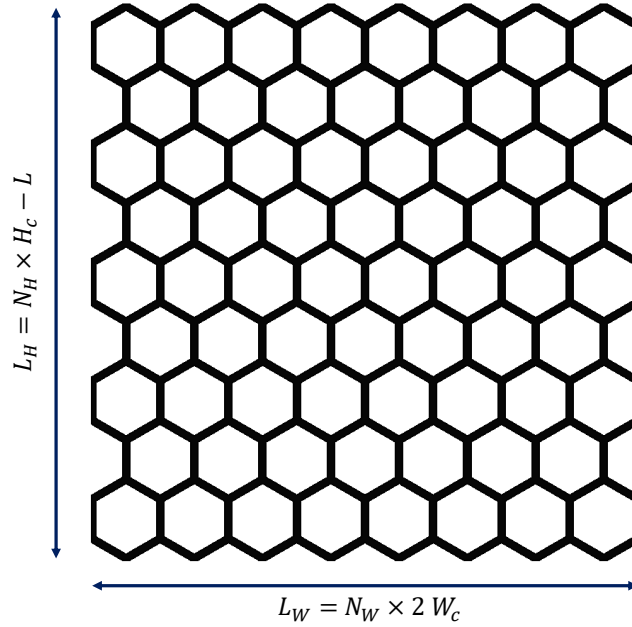


Figure 2.7: A honeycomb structure with horizontal length L_W and vertical length L_H , where $L_H \approx L_W$. The N_W and N_H denote the number of cells in the horizontal and vertical directions, respectively.

where ρ_H denotes the density of the hexagonal unit-cell. We consider that the parameters L and t are unknown while ρ_H is an input. Moreover, it is assumed that the number of cells in the horizontal and vertical directions is also defined by the user. However, if an almost square cell is desired, only one of the lengths is sufficient to design the lattice. Figure 2.7 shows a honeycomb structure with the horizontal length L_W and the vertical length L_H . N_W and N_H also denote the number of cells in the horizontal and vertical directions, respectively. In order to design this geometry, it has been assumed that the $L_H \approx L_W$ ⁶. As a result, assuming either N_W, L_W or N_H, L_H will result in the other parameters. Therefore, depending on the prescribed parameters two sets of formulations can be obtained. In the following, we discuss each of the formulations.

2.5.1 Prescribed L_W and N_W

If L_W and N_W are prescribed, the input parameters consist of L_W , N_W , and ρ_H , where again ρ_H is the density of the lattice. The outputs correspond to t , L , N_H , and L_H which can be obtained from a set of equations

⁶We note that the equality of L_H and L_W never happens if all cells are restricted to be close.

$$\begin{cases} W_c = \frac{L_W}{2N_W} = \frac{t}{2} + \frac{\sqrt{3}L}{2} \\ \rho_H = \frac{6Lt + \sqrt{3}t^2}{(3L + \sqrt{3}t)(\sqrt{3}L + t)} \end{cases} \quad (2.38)$$

There are two solutions to this set of equations such that one of them leads to a negative L which is not acceptable. Therefore, the accepted positive solution is

$$L = \frac{L_W \sqrt{1 - \rho_H}}{\sqrt{3}N_W}, \quad t = \frac{L_W(1 - \sqrt{1 - \rho_H})}{N_W}. \quad (2.39)$$

where N_H will be the integer part of the following approximate equation

$$N_H \approx \frac{L_W + L}{H_c}. \quad (2.40)$$

2.5.2 Prescribed L_H and N_H

Similar to the previous case, if L_H and N_H are prescribed, the input parameters consist of L_H , N_H , and ρ_H . The outputs correspond to t , L , N_W , and L_W which can be obtained from a set of equations

$$\begin{cases} H_c = \frac{L + L_H}{2N_H} = 3L + \sqrt{3}t \\ \rho_H = \frac{6Lt + \sqrt{3}t^2}{(3L + \sqrt{3}t)(\sqrt{3}L + t)} \end{cases} \quad (2.41)$$

Similarly, there is one acceptable positive solution, which corresponds to

$$\begin{aligned} L &= \frac{L_H(1 + 3N_H\sqrt{1 - \rho_H} - \rho_H)}{-1 + 9N_H^2 + \rho_H}, \\ t &= -\frac{\sqrt{3}L_H(1 - 3N_H + (-1 + 3N_H)\sqrt{1 - \rho_H} - \rho_H)}{-1 + 9N_H^2 + \rho_H}. \end{aligned} \quad (2.42)$$

where N_W will be the integer part of the following approximate equation

$$N_W \approx \frac{L_H}{2W_c}. \quad (2.43)$$

It is worth mentioning that the slenderness of the cell walls L/t in both equations (2.39) and (2.42) have the following relation which is independent of N_W and N_H and only depends on the density ρ_H .

$$\frac{L}{t} = \frac{\sqrt{1 - \rho_H}}{\sqrt{3}(1 - \sqrt{1 - \rho_H})}. \quad (2.44)$$

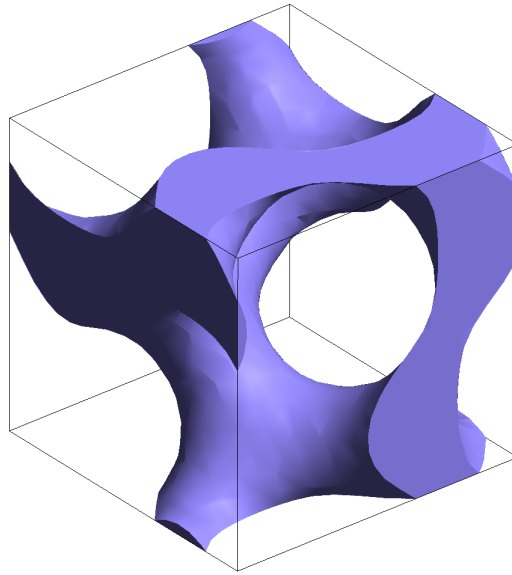


Figure 2.8: A 3D model of Gyroid minimal surface

The proposed set of equations have been implemented in `Gmsh` software to create the designed hexagonal lattices with the number of cells and porosity defined by the user.

2.6 Triply periodic minimal surfaces (TPMS) structures

The triply periodic minimal surfaces (TPMS) structures are a group of periodic cellular materials that are constructed based on the minimum surface condition. Mathematically, a minimal surface is one whose area is minimized locally which also corresponds to zero mean curvature. This type of geometry has been observed in various natural and biological systems such as butterfly wings ([Schröder-Turk et al., 2011](#)), beetle skin ([Galusha et al., 2008](#); [Al-Ketan and Abu Al-Rub, 2019](#)). The TPMS are frequently used to design structures with different crystalline symmetry groups. Due to their simple mathematical definitions, they are easy to design and can be created in very low volume fractions ([Soyarslan et al., 2019](#)). TPMS-based structures are interesting candidates for designing multifunctional materials with optimal properties due to their smooth curvature and capability to design functionally graded structures. Nevertheless, it should be noted that their properties are strongly direction dependent which could be considered as a drawback if the designed material is under multi-directional loading ([Bonatti and Mohr, 2019](#)).

The first study of TPMS originated from [Schwarz \(1972\)](#). Over the years, different types of TPMS structures have been discovered such as Schwarz-P, Schwarz-D, Diamond, Gyroid, etc. One of the most interesting geometries among them corresponds to the Gyroid surface introduced by [Schoen \(1970\)](#), which has been investigated extensively in

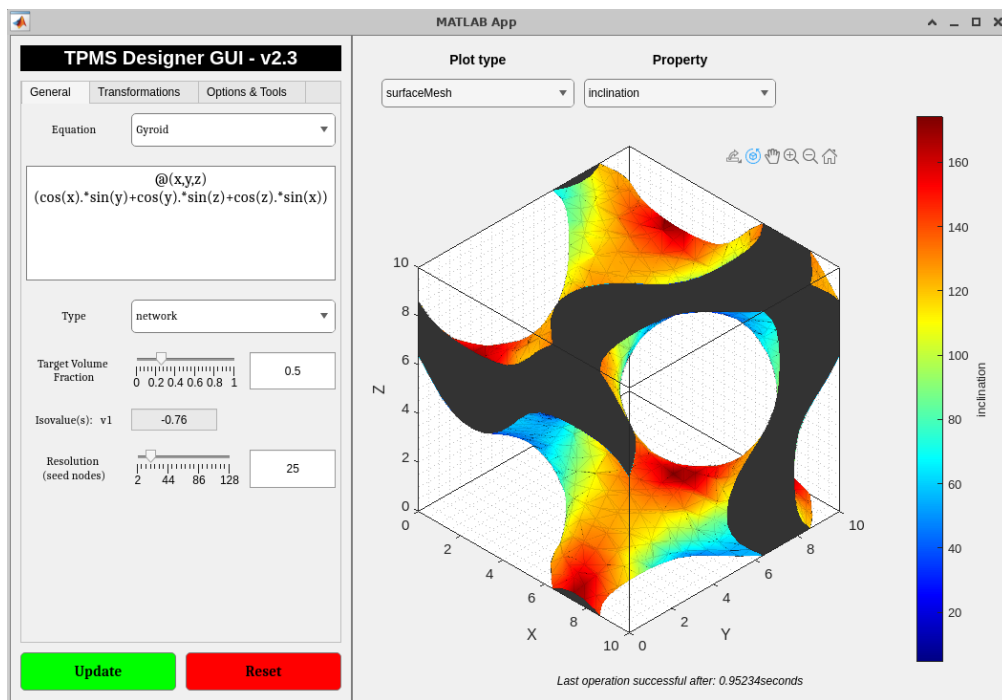


Figure 2.9: The TPMS Designer graphical user interface.

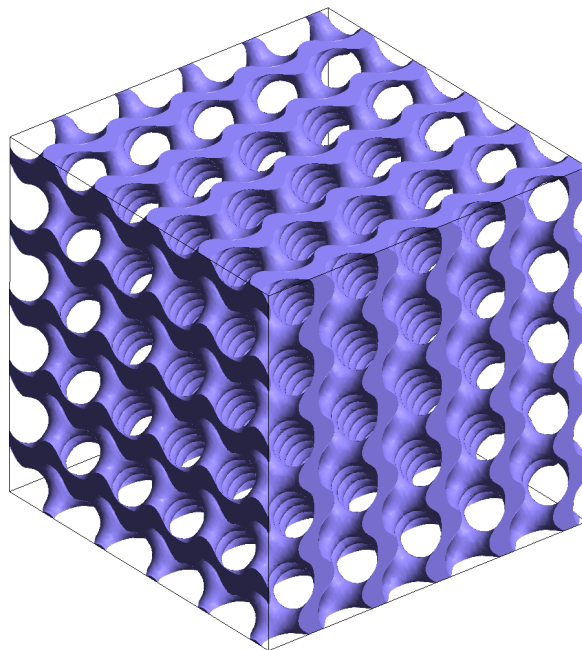


Figure 2.10: A Gyroid lattice with 50% solid volume fraction and $5 \times 5 \times 5$ cells.

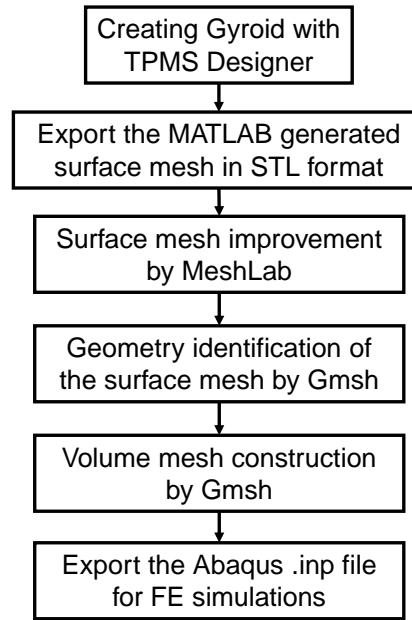


Figure 2.11: Flowchart of the steps for surface mesh quality improvement and conversion of the surface mesh to the volume mesh for numerical simulations.

different studies. In this thesis, we focus on the Gyroid structures and we will compare their properties with other cellular materials in Chapter 5. The Gyroid surface in the Euclidean space \mathbb{R}^3 is displayed in Figure 2.8 and can be approximated by the equation

$$\sin(x) \cos(y) + \sin(y) \cos(z) + \sin(z) \cos(x) = 0. \quad (2.45)$$

Using this equation, a Gyroid surface can be created in a variety of available software programs with graphical options. In this study, we have used TPMS Designer developed by Jones et al. (2021), which is a software package that runs within MATLAB⁷ and is used for designing and visualizing surface-based cellular structures. This software has a graphical user interface (Figure 2.9) and it not only contains different TPMS minimal surfaces but also it permits the user to define the arbitrary minimal surface function. The generated Gyroid could have a desired number of cells in a different direction. Figure 2.10, shows a Gyroid with 50% solid volume fraction and $5 \times 5 \times 5$ number of cells.

By using MATLAB mesh generator, the TPMS Designer software produces a Gyroid structure in STL format. The quality of the generated mesh is not acceptable and it is unnecessarily fine. Furthermore, for further numerical simulations, the surface mesh has to be converted into a volume mesh. Since the simulations in this study have been performed in the Abaqus software, the desired volume mesh format is the Abaqus input mesh format .inp. Several steps have been taken to obtain a good-quality volume mesh from a low-quality surface mesh. These steps are summarized in a flowchart in Figure 2.11. As

⁷TPMS Designer could also run within MATLAB Runtime which is a free MATLAB compiler.

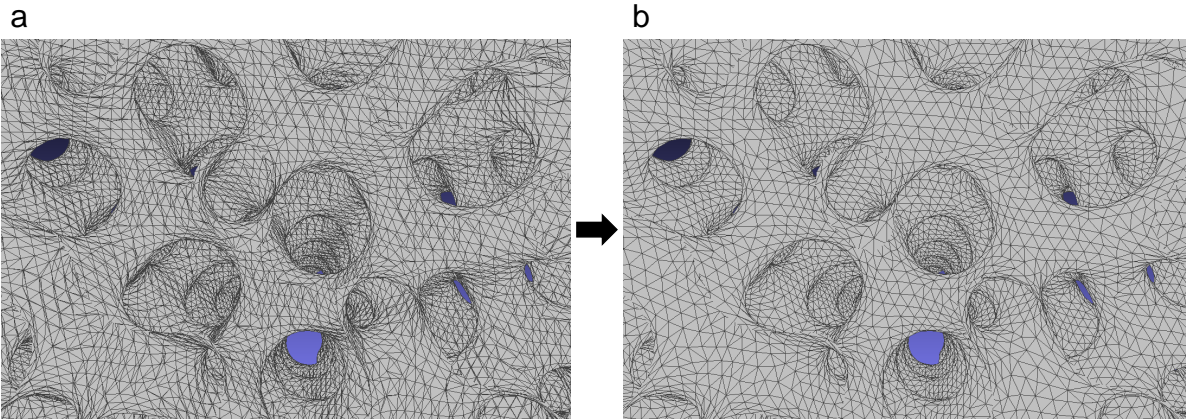


Figure 2.12: The improvement of the surface mesh quality by Meshlab in a MATLAB generated mesh. (a) A surface mesh generated by MATLAB with a low quality and large mesh size. (b) The same mesh with improved quality and smaller mesh size.

described, the generated low-quality surface mesh is improved by **MeshLab** which is mesh manipulation software. The improved surface mesh is then converted to a CAD geometry by **Gmsh** software. The generated geometry will construct a volume that can be simply meshed with 3D volume elements for further numerical analysis. Figure 2.12, illustrates the improvement in the surface mesh quality by **MeshLab**. Clearly, this procedure can be applied to cases requiring a good quality mesh with a low number of elements (Optimum quality mesh). Nevertheless, due to the incapability of the STL format to identify voids or the second phase, this method cannot be used in voided or multi-phase materials. A more general method for mesh reconstruction will be proposed in the Sections 3.3 for 2D and 5.2 for 3D mesh.

2.7 Concluding remarks

In summary, this chapter presents a review of a computer-aided design process for selected random and periodic geometries. The 3D RSA algorithm for generating randomly oriented ellipsoidal inclusions of arbitrary size, shape, and orientation (i.e. polydisperse) has been studied and we have shown the algorithm proposed by **Lin and Han (2002)** is sufficiently fast and effective to check the intersection and compute the minimum distance simultaneously. The modified 3D RSA algorithm is then converted to 2D space to create 2D random circular or elliptical inclusions. In addition, we note that the RSA algorithm is not able to obtain very large volume fractions due to the irreversibility of the sequential addition process.

The second random geometry corresponds to the Eroded Voronoi (E-Voronoi) geometries, which are created by a Voronoi tessellation method. Although this geometry is

random in cell shape and size, it has the constraint of a constant wall thickness. This will be shown later as a drawback of this class of random geometries. Subsequently, a brief review has been performed on hexagonal lattices while proposing two forms of geometry formulations based on the input parameters. These forms enable us to create hexagonal lattices with fully closed cell boundaries while keeping the horizontal and vertical lengths of the geometry very close. Finally, the process to create the Gyroid geometries which are a type of TPMS structures has been described. This generation process is within a MATLAB-based software proposed by [Jones et al. \(2021\)](#) and requires mesh quality improvement before numerical analysis on the geometries.

Chapter 3

The M-Voronoi

Chapter summary: This chapter deals with a novel computer-aided design process to create a new type of random Voronoi-type porous materials called M-Voronoi (from mechanically grown) with smooth void shapes and variable intervoid ligament sizes that can reach very low relative densities. This is achieved via a numerical, large strain, nonlinear elastic, void growth mechanical process. First, the general form of the morphogenesis process is described in different steps. Following that, we discuss the theoretical relations for controlling the final porosity and the growth of voids. We show that the final achieved relative density may be analytically estimated in terms of the determinant of the applied deformation gradient. Subsequently, we propose a new method to remesh an orphan mesh by constructing the deformed geometry that can be applied to any complex orphan mesh and is specifically useful for composite or porous materials. The proposed remeshing method has enabled us to reach low densities in M-Voronoi geometries. An extension of the M-Voronoi method has also been proposed to create M-Voronoi geometry at various convex cell domains. This has been further used to assemble the porous cells into a macroscopic structure. Furthermore, the method is employed to create anisotropic M-Voronoi which enables us to design random geometries with controllable properties.

Contents

3.1	M-Voronoi morphogenesis method	42
3.2	Relative density and porosity evolution	46
3.3	Geometry reconstruction and Remeshing	48
3.3.1	Description of 2D remeshing algorithm	51
3.3.2	Application of 2D remeshing algorithm in M-Voronoi	57
3.4	M-Voronoi in convex cell domains	58
3.5	Effect of initial volume fraction and attainable relative density	61
3.6	E-Voronoi and RSA versus M-Voronoi	63
3.7	Anisotropic M-Voronoi	64
3.8	The assembly of the porous cells into macroscopic structures	68

3.9	Concluding remarks	69
3.A	Appendix A. Equality between the applied and average deformation gradients	70
3.B	Appendix B. Algorithms for remeshing a 2D orphan mesh by constructing the geometry	71

3.1 M-Voronoi morphogenesis method

This section describes the computational morphogenesis process and its major steps to obtain the M-Voronoi porous materials. As a first attempt, we focus on voided materials that exhibit a two-dimensional random geometry. Those are then extruded in the third (out-of-plane) dimension for subsequent 3D-printing and mechanical experiments. The proposed process consists of four main steps, which are discussed in the following and are also summarized in Figure 3.1.

Step 1: Construction of the initial porous cell. The proposed void growth process begins with the construction of an initial porous unit-cell (Figure 3.1). We note that the unit dimensions of the cell are inconsequential and are only chosen for simplicity. It is noted here that the choice of the initial void distribution and cell geometry affects, in general, the final porous geometry obtained via this process, as it will be shown below. For illustration purposes at this stage, a square unit-cell occupying the volume \mathcal{V}_0 in the undeformed (reference) configuration is considered. The unit-cell comprises a random distribution of voids at initial volume fraction c_0 , or equivalently at initial relative density $\rho_0 \equiv 1 - c_0$ (see Section 3.2). The voids may be of any shape, size or orientation (e.g., ellipsoidal or even non-convex). Here, for simplicity and numerical efficiency, the random sequential absorption(RSA) algorithm described in Section 2.3 is used to embed, randomly and uniformly (in the sense of Torquato (1997, 2002)), circular holes of equal size in the square domain. Nevertheless, the proposed morphogenesis approach is general and thus any initial void geometry may be used to increase the final inclusion volume fraction (e.g. one may start with spinodal geometries at small volume fraction (Maskery et al., 2017; Portela et al., 2020; Zerhouni et al., 2021)).

Step 2: Uniform displacement boundary conditions. The unit-cell is subsequently subjected to uniform Dirichlet (affine) displacement boundary conditions over the entire cell boundary $\partial\mathcal{V}_0$ (Figure 3.1). For clarity, the most important finite strain kinematics and constitutive laws used in this work are hereinafter recalled. The deformable unit-cell occupies a volume \mathcal{V}_0 in the undeformed (Lagrangian) configuration with boundary $\partial\mathcal{V}_0$. We use $\mathbf{X} \in \mathcal{V}_0$ to denote the reference position vector of a material point in \mathcal{V}_0 . The deformed position vector $\mathbf{x}(\mathbf{X})$ of any material point is related to \mathbf{X} via $\mathbf{x}(\mathbf{X}) = \mathbf{X} + \mathbf{u}(\mathbf{X})$,

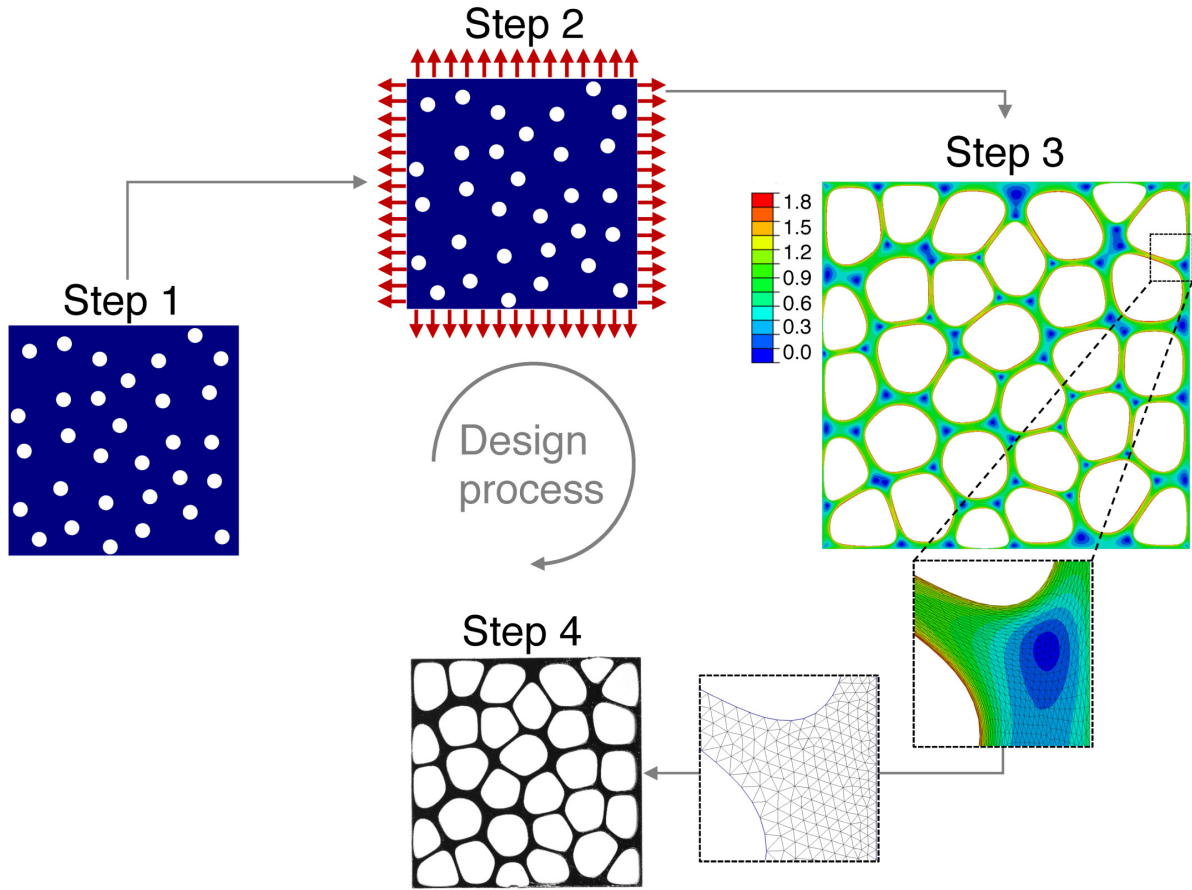


Figure 3.1: Computational process for the generation of the M-Voronoi material. For illustration purposes, the diagram shows the four steps required to obtain a virtual M-Voronoi geometry starting from a square unit cell containing a discrete number of mono-sized circular pores. **Step 1:** Random distribution of circular holes in a square domain. **Step 2:** Application of uniform displacement boundary conditions. **Step 3:** Numerical FE simulation at large strains using nonlinear elastic energy minimization and incompressible matrix behavior. The zoom image shows locally the deformed mesh. The color bar indicates the maximum principal logarithmic strain. **Step 4:** Uniform re-scaling of the deformed geometry to the desired size. Remeshing (as shown in the zoomed image), 3D extrusion and STL generation of the final geometry used for 3D-printing.

where $\mathbf{u}(\mathbf{X})$ denotes the displacement vector of any material point. The deformation gradient is defined then as $\mathbf{F} = \partial \mathbf{x} / \partial \mathbf{X} = \mathbf{I} + \text{Grad} \mathbf{u}$, where Grad denotes the gradient operator with respect to \mathbf{X} . We then impose the Dirichlet boundary conditions

$$\mathbf{u} = (\mathbf{F}^{\text{app}} - \mathbf{I}) \mathbf{X}, \quad \forall \mathbf{X} \in \partial \mathcal{V}_0, \quad (3.1)$$

where \mathbf{F}^{app} is a prescribed, constant, *non-symmetric* second-order tensor with four and nine independent components in 2D and 3D, respectively. By virtue of the divergence

theorem, one may easily show that \mathbf{F}^{app} corresponds to the average deformation gradient in the entire cell, i.e., $\mathbf{F}^{\text{app}} = |\mathcal{V}_0|^{-1} \int_{\mathcal{V}_0} \mathbf{F}(\mathbf{X}) d\mathbf{X}$ (The proof of this is provided in Appendix 3.A). It is further noted that the deformed volume of the unit-cell, \mathcal{V} , is entirely defined in terms of the average deformation gradient \mathbf{F}^{app} from the purely kinematic relation $\mathcal{V} = \det \mathbf{F}^{\text{app}} \mathcal{V}_0$ (see Section 3.2). Given that the initial unit-cell is porous and thus compressible, a $\det \mathbf{F}^{\text{app}} > 1$ readily leads to an increase of \mathcal{V} . A second condition for the growth of voids is provided next.

Step 3: Nonlinear elastic energy minimization. Subsequently, we trigger the mechanical growth of the voids by solving numerically a finite-strain (Figure 3.1), nonlinear elastic boundary value problem (BVP), whose geometry is defined in Step 1 and applied boundary conditions in Step 2. For this, we use the finite element (FE) method since the geometry is extremely complex and involves large deformations leading to a non-analytical BVP. In this study, the commercial FE solver ABAQUS (Dassault Systems) is used and finite strains are enabled by the option NLGEOM. Moreover, quadratic six-node, plane-strain (2D) hybrid elements (CPE6H) are used to deal with incompressibility.

Specifically, the void phase has zero energy density and thus is simply modeled as empty with traction-free boundaries and is not meshed, while the solid phase (blue in Figure 3.1) is assumed to follow an incompressible, neo-Hookean law described formally by the Helmholtz free energy density

$$W(\mathbf{F}) = \frac{\mu}{2}(\mathbf{F} \cdot \mathbf{F} - d), \quad \text{such that} \quad C(\mathbf{F}) = \det \mathbf{F} - 1 = 0, \quad (3.2)$$

with $d = 2, 3$ depending on the dimensionality of the problem. In this last expression, μ denotes the shear modulus and its value may be set equal to unity for the purposes of this study, while the incompressibility constraint $C(\mathbf{F})$ needs to be imposed everywhere in the solid phase. Then, the solution of the BVP is formally defined in terms of the optimization problem

$$\{\mathbf{u}, p\} = \arg \left\{ \min_{\mathbf{u}^* \in \mathcal{K}(\mathbf{F}^{\text{app}})} \max_{p^*} \int_{\mathcal{V}_0} W(\mathbf{F}(\mathbf{u}^*)) d\mathbf{X} \right\}, \quad (3.3)$$

where $\mathcal{K}(\mathbf{F}^{\text{app}}) = \{\mathbf{u} : \text{regular}, \mathbf{u} = (\mathbf{F}^{\text{app}} - \mathbf{I}) \mathbf{X}, \quad \forall \mathbf{X} \in \partial \mathcal{V}_0\}$ and p is a scalar pressure field (acting as a Lagrange multiplier to impose the incompressibility constraint $\det \mathbf{F} = 1$). The corresponding first Piola-Kirchhoff stress is given by

$$\mathbf{S} = \frac{\partial W}{\partial \mathbf{F}} - p \frac{\partial C}{\partial \mathbf{F}} = \mu \mathbf{F} - p \mathbf{F}^{-T}. \quad (3.4)$$

Even though the solid phase is incompressible, the embedded voids are fully compressible and can grow or shrink under large deformations. By prescribing $\det \mathbf{F}^{\text{app}} > 1$, the volume of the unit-cell is forced to grow, which can only occur via void growth. Specifically, using the incompressibility of the solid matrix phase, mass conservation and the applied Dirichlet boundary conditions, one may readily show that the current relative

density of the deformed unit-cell ρ is simply given in terms of the overall initial relative density ρ_0 via the purely kinematic relation (see Section 3.2)

$$\rho = \frac{\rho_0}{\det \mathbf{F}^{\text{app}}}. \quad (3.5)$$

Equivalently, this last relation allows to estimate directly the $\det \mathbf{F}^{\text{app}}$ that needs to be prescribed to the unit-cell to reach the desired final relative density ρ . Note that $\det \mathbf{F}^{\text{app}}$ does not define the entire tensor \mathbf{F}^{app} . Thus, one has countless choices for the remaining components allowing to obtain a multitude of void-grown geometries and deformed cell shapes. As can be easily observed in the example problem in Figure 3.1, the voids grow substantially exhibiting convex, polygonized but smooth shapes. Their exact growth rate and final shape are a complex outcome of interactions with neighboring voids and the boundary of the cell. The thickness of the intervoid ligaments is highly variable, while dense pockets of solid phase are observed across the cell, as shown by the blue spot regions in Step 3 of Figure 3.1. It is also important to note that at such large strains the underlying mesh may be significantly distorted at various regions (see the zoom image in Step 3 of Figure 3.1). In order to avoid such problems, one may remesh the geometry (see remeshed figure) without the need to transfer the stress and displacement fields and re-start the calculation from that point on (see Section 3.3.1). This is obviously allowed here since we are solely interested in the geometrical features and not in the calculated stresses themselves. Such an operation will allow us to reach very low relative densities as is discussed in Section 3.6.

Step 4: Void geometry extraction, rescaling, remeshing and 3D-printing. The deformed unit-cell is then *uniformly* rescaled back to any desired size (see Figure 3.1). By doing so, the relative density is preserved. For this re-scaling step and for subsequent accuracy in 3D-printing, the following strategy is proposed, without that being neither unique nor optimal in the sense of speed. Specifically, the nodal coordinates of the external and internal void boundaries of the unit-cell are first extracted and then rescaled uniformly. The deformed mesh is exported using an Abaqus python script and the geometrical entities, such as void boundaries and cell boundaries, are read by a custom made code. It is also remarked at this point that one could use an intermediate deformation state as the initial geometry. In this case, every rescaled geometry resulting from Step 4 could be plugged in back to Step 2 to apply a new deformation history. The various options are countless. The rescaled unit-cell obtained in Step 4 is then remeshed and extruded in the third dimension. This step is conducted using the open-source meshing software `Gmsh` (see Section 3.3.1). It is further noted that during the remeshing operation, we do not transfer the computed displacement and stress fields, instead only the deformed cell and void boundaries are retained. Finally, the extruded geometry is exported in stereolithography (STL) format for 3D-printing. The experimental methods used to fabricate and test the samples are discussed in detail in Section 4.3.

3.2 Relative density and porosity evolution

We discuss here the evolution of the porous volume fraction or equivalently of the relative density under prescribed uniform displacement (Dirichlet only) boundary conditions. We recall that the solid phase (matrix) is considered to be incompressible, and thus the volume of the cell changes under large deformation, due to void growth only. Therefore, \mathbf{F}^{app} can be cast in any form (provided of course that $\det \mathbf{F}^{\text{app}} > 0$ to satisfy material impenetrability), although the embedded voids may grow or shrink depending on the magnitude of $\det \mathbf{F}^{\text{app}}$. For the voids to grow, one needs $\det \mathbf{F}^{\text{app}} > 1$ and the contrary case to shrink ($0 < \det \mathbf{F}^{\text{app}} < 1$). Denote next the volumes of the matrix and voids in the reference (undeformed) configuration to be \mathcal{V}_0^m (\mathcal{V}^m) and \mathcal{V}_0^v (\mathcal{V}^v), respectively. Then, incompressibility in the matrix phase implies that

$$\mathcal{V}^m = \mathcal{V}_0^m, \quad (3.6)$$

while the total volumes in the reference and deformed configurations are given by

$$\mathcal{V}_0 = \mathcal{V}_0^m + \mathcal{V}_0^v, \quad \mathcal{V} = \mathcal{V}^m + \mathcal{V}^v. \quad (3.7)$$

We note further that the deformed volume of the cell, \mathcal{V} , is entirely defined in terms of the applied deformation gradient \mathbf{F}^{app} by the relation

$$\mathcal{V} = \det \mathbf{F}^{\text{app}} \mathcal{V}_0, \quad (3.8)$$

given that \mathbf{F}^{app} corresponds to the average deformation gradient in the cell. The proof of this is provided in Appendix 3.A.

Note further that the relative density in the reference, ρ_0 and deformed, ρ , configurations for a porous material are defined as

$$\rho_0 = \frac{\widehat{\rho}_0}{\widehat{\rho}_0^m}, \quad \rho = \frac{\widehat{\rho}}{\widehat{\rho}^m}. \quad (3.9)$$

Here, $\widehat{\rho}_0^m$ and $\widehat{\rho}^m$ indicate the density of the matrix phase in the reference and deformed configurations, respectively, and $\widehat{\rho}_0$ and $\widehat{\rho}$ the density of the cell in the reference and deformed configurations, respectively.

Moreover, in a porous material, the total mass in the cell, m , is equal to the mass of the matrix, m^m , i.e.,

$$m = \widehat{\rho}_0 \mathcal{V}_0 = \widehat{\rho} \mathcal{V}, \quad m^m = \widehat{\rho}_0^m \mathcal{V}_0^m = \widehat{\rho}^m \mathcal{V}^m. \quad (3.10)$$

and thus from mass conservation we have

$$m = m^m \quad \frac{\widehat{\rho}_0}{\widehat{\rho}_0^m} = \frac{\mathcal{V}_0^m}{\mathcal{V}_0} = \rho_0, \quad \Rightarrow \quad \frac{\widehat{\rho}}{\widehat{\rho}^m} = \frac{\mathcal{V}^m}{\mathcal{V}} = \rho. \quad (3.11)$$

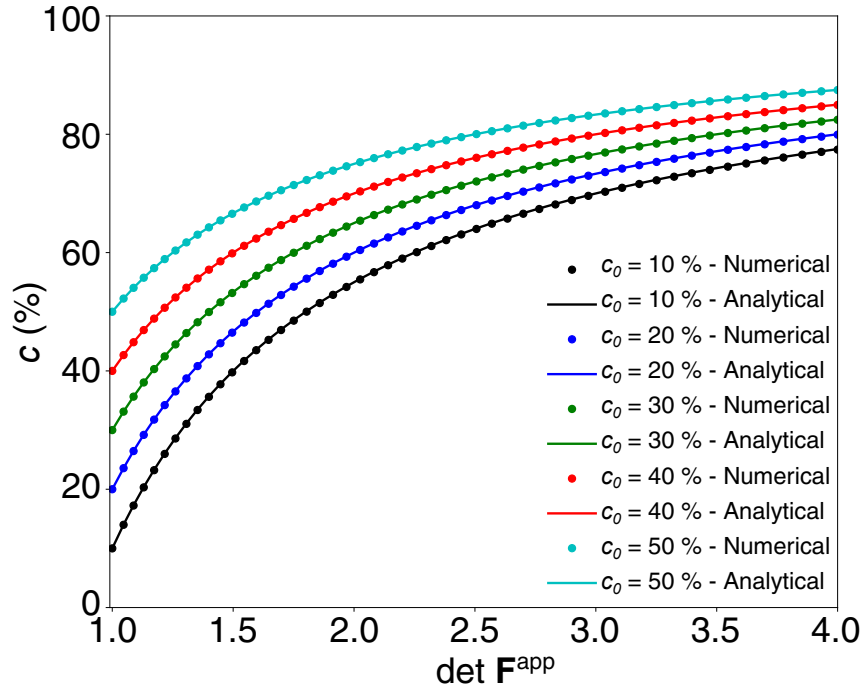


Figure 3.2: Evolution of porosity $c = 1 - \rho$ as a function of the applied determinant of the deformation gradient, as obtained by numerical simulations and the analytical expression (3.14).

Using the last definitions together with relations (3.6) and (3.8), we readily get

$$\frac{\mathcal{V}^m}{\mathcal{V}} = \frac{1}{\det \mathbf{F}^{\text{app}}} \frac{\mathcal{V}_0^m}{\mathcal{V}_0} \quad \text{or} \quad \rho = \frac{\rho_0}{\det \mathbf{F}^{\text{app}}}, \quad (3.12)$$

which corresponds to equation (3.5).

One may further define the void volume fraction in the reference, c_0 , and deformed configuration, c , as

$$c_0 = \frac{\mathcal{V}_0^v}{\mathcal{V}_0} = \frac{\mathcal{V}_0 - \mathcal{V}_0^m}{\mathcal{V}_0} = 1 - \rho_0, \quad c = \frac{\mathcal{V}^v}{\mathcal{V}} = \frac{\mathcal{V} - \mathcal{V}^m}{\mathcal{V}} = 1 - \rho. \quad (3.13)$$

Using the result (3.12), one readily gets

$$c = 1 - \frac{1 - c_0}{\det \mathbf{F}^{\text{app}}}. \quad (3.14)$$

It can be readily observed that the aforementioned relations are purely kinematic due to the incompressibility of the matrix phase as well as the application of the Dirichlet-only boundary conditions and consequently only \mathbf{F}^{app} controls the final porosity/relative density of the cell. In the case of mixed Neumann–Dirichlet boundary conditions and

incompressible matrix, still the void growth is controlled by the average deformation gradient in the cell but that does not correspond exactly to the partially applied deformation gradient imposed via the displacement field in a part of the boundary.

In Figure 3.2, we assess our numerical calculations by simulating RSA voided cells with different initial porosities c_0 applying equi-biaxial loads with $\det \mathbf{F}^{\text{app}} > 1$ and comparing the induced numerical porosity with that obtained by the analytical expression (3.14). The numerical simulation recovers to excellent accuracy the exact analytical result (3.14). In this figure, we observe that obtaining the desired porosity is easier with a larger initial porosity and requires less deformation. Furthermore, there is a nonlinear saturation type increase in the porosity with increasing $\det \mathbf{F}^{\text{app}}$. This saturated type response indicates that very large strains are, in general, necessary to reach very high porosities (or very low relative densities). This, in turn, leads to severe mesh distortion. In order to avoid numerical issues, a strategy consists in ceasing the simulation, extracting the geometry (but not the stress and strain fields), remeshing and restarting the simulation from the lastly obtained geometry. This allows for efficient and very accurate resolution at very low relative densities. The operation is discussed in detail in Section 3.3.1.

3.3 Geometry reconstruction and Remeshing

Well-shaped elements are crucial for the stability and efficiency of numerical computations. Large strain simulations often lead to severe mesh distortion, which is the main reason for terminating the simulation. Having a high-quality mesh not only improves the accuracy of the results but also might enable the simulation to proceed to larger strains. However, improving the initial mesh quality will increase computational costs and time. Furthermore, in complex geometries undergoing large strains, there might be regions that undergo larger deformations. Adaptive mesh techniques might lead to larger deformations, but still, mesh distortion is inevitable in such geometries. In order to achieve larger strains in a reasonable running time, it is essential to remesh the distorted mesh after termination of the simulation and resume it with/without mapping the fields to the new mesh.

Remeshing is a technique that automatically rebuilds the existing mesh (normally meshes containing ill-shaped elements) with a better-quality mesh. It can be done either by refining the existing mesh or reconstructing a new mesh with different approximative operations. Generally, refining the existing mesh will increase the mesh size and consequently the computational time and cost. Also, since the distorted elements are just refined to smaller sizes, the new refined mesh will not be sufficiently efficient for the simulation to go much further and avoid excessive distortion. In contrast, the mesh reconstruction technique consists of rebuilding a new mesh by approximating the current mesh to a uniform topology and remesh it. It can either add or remove the amount of topology depending on a defined resolution. In addition to being extensively studied in Computer Graphics, the technique of surface remeshing has also received considerable attention from other fields concerned with mesh generation, mainly Computational Fluid

Dynamics, Finite Element Methods, and Computational Geometry. However, the drawback of this technique consists of the accuracy of the approximated geometry and the computational time to rebuild the new mesh.

There are a variety of remeshing tools available in different commercial or open source software. For example, in open-source meshing software `Gmsh`, there is an option to remesh an STL file without an underlying CAD model. In this method, by employing the “classifySurfaces” option, the current surface mesh is classified based on the surface normal angle threshold in order to force splitting of the generated surfaces, resulting in the creation of new discrete entities and topologies. When the angle between two mesh element surfaces is above the threshold, the edge is considered a sharp angle. Then, a geometry for all the discrete curves and surfaces in the mesh is created, by computing a parametrization for each one. The latter is performed by the “CreateGeometry” command. The final parametrized geometry can be remeshed with higher-quality elements or an arbitrary element type. However, this method is highly dependent on the surface classification parameters and fails in complex geometries and especially in extremely distorted quadratic elements. In addition, it is unable to build a periodic or multi-phase mesh.

Another available remeshing tool is the `Meshlab` free software, which is based on improving the quality of the STL mesh, again without an underlying CAD model. In this method, the original topology of the geometry is preserved while the quality of the elements is improved by optimizing the node coordinates. Although this technique is an incredibly fast remeshing method, it is unable to create a periodic mesh. Also, the newly created surface mesh is exported in STL format, whereas in 3D, closed surface voids cannot be identified.

Additionally, Abaqus software can generate geometry from mesh files by using the Mesh to Geometry Plug-in. This plug-in converts .STL files and meshes back to geometry, allowing the structure to be remeshed and imported into a variety of CAD packages. Nevertheless, it fails to handle closed curves or surfaces, namely 2D and 3D voids. Furthermore, it is not able to deal with complex deformed voided geometries with large porosities, such as 3D M-Voronoi structures. Figure 3.3 shows the non-smooth imperfect 2D voided geometry created by Abaqus software when the mesh contains voids. Originally, the orphan mesh had no sharp corners at the edge of every void. Moreover, we note that there are adaptive meshing/remeshing techniques available in Abaqus software which improve the mesh during the simulation based on the evolving deformation applied to the mesh. However, they are limited to dealing only with first-order elements, whereas quadratic elements are more commonly used in large strain simulations.

In summary, the existing remeshing methods are incapable of taking into account voids and different element sets in multi-phase materials, especially in complex geometries when the elements are extremely distorted. Furthermore, none of the above methods are able to generate periodic meshes during the remeshing process. We present a new remeshing technique, both precise and efficient, for remeshing any orphan mesh in 2D and 3D. Using this technique, only an orphan mesh is required (i.e. no geometry information) and the

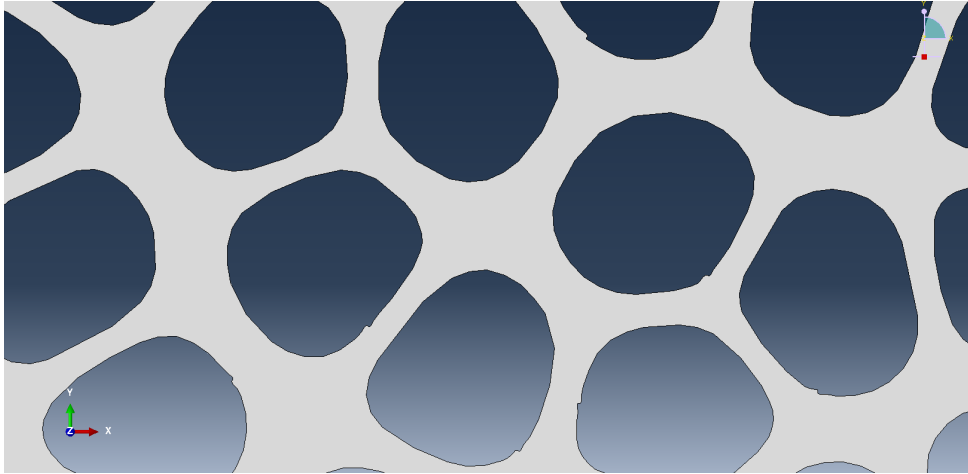


Figure 3.3: The geometry containing non-smooth void boundaries generated by Abaqus from orphan mesh.

surface elements are used to create the deformed geometry exactly as it appears on the surface. The generated geometry is subsequently remeshed with an arbitrary mesh size and algorithm (for example Delaunay triangulation). Unlike previous techniques, our remeshing technique has the following advantages:

- Producing the geometry of any orphan mesh.
- Preserving the exact geometry without any approximation.
- Constructing of regions with no elements i.e. voids. (Hollow structures)
- Considering different phases of multi-phase materials.
- Containing both 2D and 3D meshes.
- Dealing with different element types.

As a result, the proposed remeshing method is extremely versatile and general, enabling us to produce arbitrarily complex meshes with a variety of properties. The focus of our study is on the void construction feature of the developed remeshing algorithm, which is not found in commercial or open-source remeshing algorithms. This algorithm has been developed for both 2D and 3D meshes. In the following section, we discuss the details of the proposed remeshing algorithm for 2D geometries. Subsequently, the 3D remeshing technique will be described in Section 5.2.

3.3.1 Description of 2D remeshing algorithm

We developed a Fortran code and its corresponding Python version of the remeshing algorithm, which is based on Gmsh reconstruction process. The proposed remeshing algorithm consists of the following steps and is also summarized in Figure 3.4.

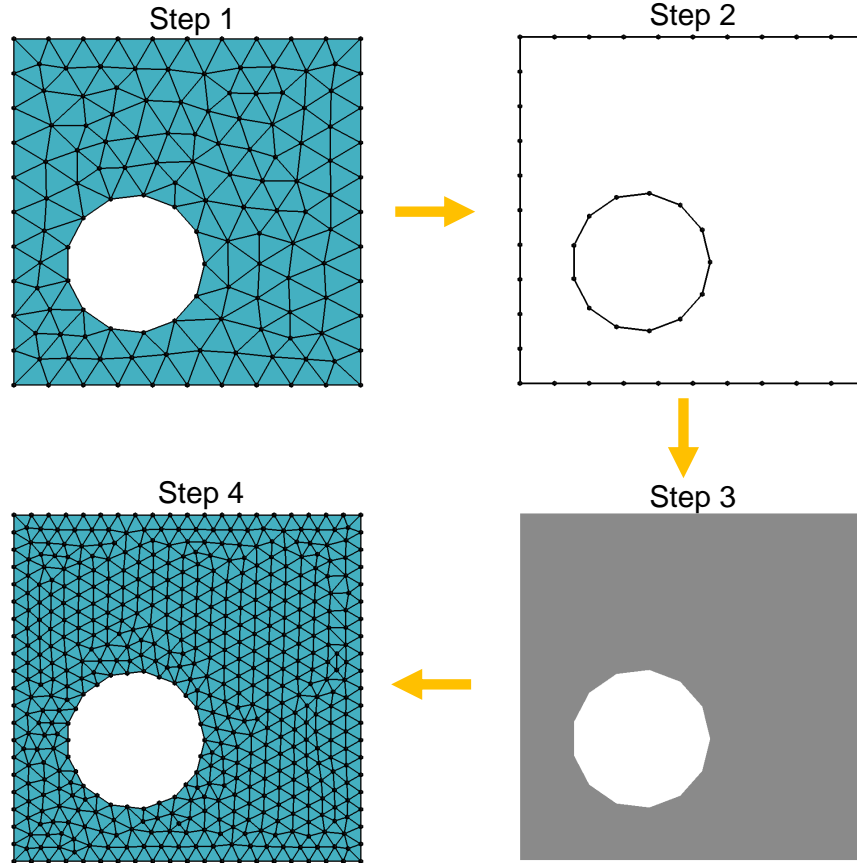


Figure 3.4: 2D remeshing algorithm for an orphan mesh based on geometry reconstruction. For illustration purposes, a simple orphan mesh containing a void is demonstrated. The diagram shows the four steps required to remesh an orphan mesh. **Step 1:** Reading the nodes and elements of the orphan mesh. **Step 2:** Finding the free sides of the elements. **Step 3:** Constructing the geometry of the orphan mesh. **Step 4:** Remeshing the new mesh with an arbitrary mesh algorithm.

Step 1: Importing the orphan mesh and reading the nodes and elements. Before the algorithm can be initiated, it is necessary to know the nodes and their connectivity. As soon as the orphan mesh file is imported, the nodes and elements are read, and stored in the corresponding matrices. We use this information to identify free lines/surfaces in the next step. We consider the mesh contains n nodes and each node i contains three

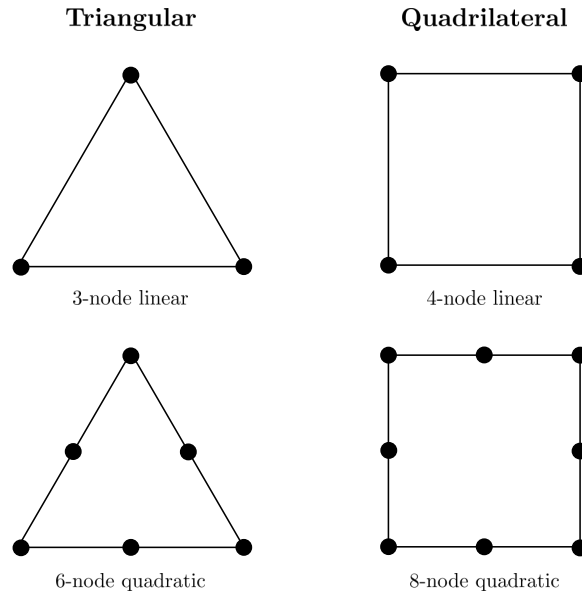


Figure 3.5: Different 2D element types and their number of nodes.

coordinate components x_i, y_i, z_i in 3D space. We define a matrix $\mathbb{N}_{n \times 3}$, containing the information of all nodes. Clearly, the row number corresponds to the nodes number. Similarly, we define a matrix $\mathbb{M}_{m \times h}$ to store the information of the elements. In this matrix, m is the number of elements and h denotes the number of nodes at each element. h will vary depending on the type and order of the elements. Figure 3.5 shows different 2D element types and their number of nodes. Therefore, h could be 3, 4, 6, 8.

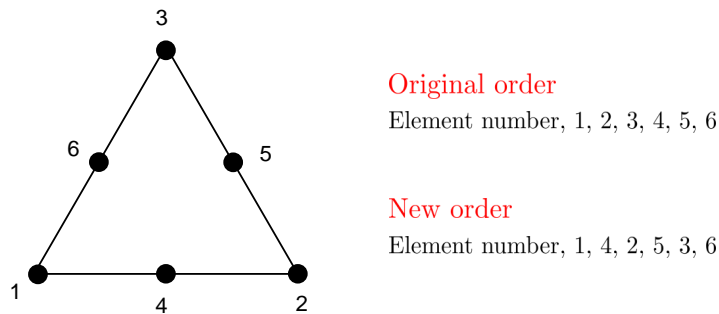


Figure 3.6: Reorganizing the order of the stored nodes for each quadratic element.

In the case of quadratic elements, one needs to reorganize the stored element nodes to provide proper connectivity between them as described in Figure 3.6. This reorganization

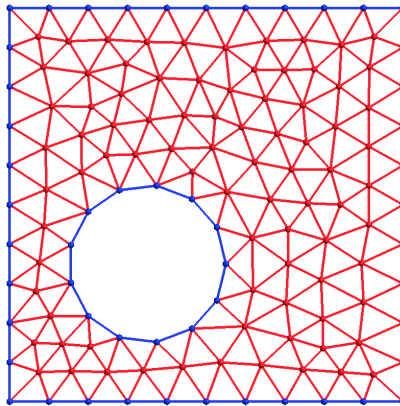


Figure 3.7: An illustrative example of a 2D orphan mesh containing free and shared lines corresponding to the blue and red colors, respectively.

has been performed to consider the displacement of the middle nodes after the deformation. This is because they would not stay on the same line as other two corner nodes. It is possible to ignore the middle nodes and let the geometry be constructed only by the corner nodes. However, this will affect the accuracy of the new geometry and mesh, depending on the geometry features and mesh size.

Step 2: Finding the free sides of the elements. Considering that we have a closed 2D object, the geometry can be constructed by connecting the free lines of the 2D elements, which make the exterior boundary of the object (see Figure 3.4). The free lines can be distinguished from other lines of a given element by their inherent feature, which is that they belong only to that element. A non-free side of an element, on the other hand, is shared by two elements at the same time. Figure 3.7 shows an illustrative example of a 2D orphan mesh containing free and shared lines corresponding to the blue and red colors, respectively. All free lines characterized by a couple of nodes will be stored in the matrix $\mathbb{L}_{f \times 2}$, where f denotes the total number of free lines. The algorithm for finding the free lines of an orphan mesh is described in Algorithm 1 in Appendix 3.B. This process consists of two main loops that compare each element's nodes with all other elements. To speed up the loops, we defined a matrix that contains the elements connected to each node in order to limit the search over all elements. It has resulted in a significant improvement in the algorithm's speed.

Step 3: Constructing the geometry from the free element sides. The free lines are then organized and connected to construct the geometry. The geometry is constructed using the geometry module of `Gmsh`. Generally, a geometry in `Gmsh` is defined using its Boundary Representation (BRep): a volume is bounded by a set of surfaces, a surface is bounded by a series of curves, and a curve is bounded by two endpoints (Geuzaine and Remacle, 2009). Geometry entities are built in a bottom-up manner (first points,

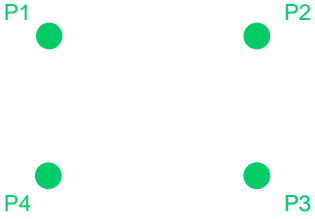
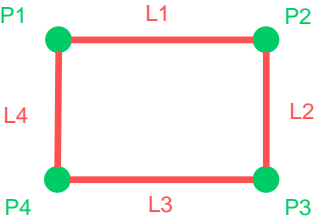
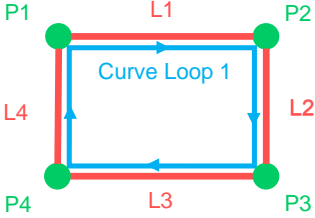
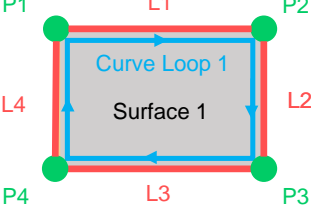

	Entity type	Geometry entities	Command examples
1	Points		$\text{Point}(1) = \{ x(1), y(1), z(1), \text{"mesh size factor"} \};$ $\text{Point}(2) = \{ x(2), y(2), z(2), \text{"mesh size factor"} \};$ $\text{Point}(3) = \{ x(3), y(3), z(3), \text{"mesh size factor"} \};$ $\text{Point}(4) = \{ x(4), y(4), z(4), \text{"mesh size factor"} \};$
2	Lines		$\text{Line}(1) = \{ 1, 2 \};$ $\text{Line}(2) = \{ 2, 3 \};$ $\text{Line}(3) = \{ 3, 4 \};$ $\text{Line}(4) = \{ 4, 1 \};$
3	Curve Loops		$\text{Curve Loop}(1) = \{ 1, 2, 3, 4 \};$
4	Plane Surface		$\text{Plane Surface}(1) = \{ 1 \};$
5	Physical Surface	 Physical Surface 1	$\text{Physical Surface}(1) = \{ 1 \};$

Figure 3.8: 2D geometry entities built in a bottom-up manner with the OpenCASCADE kernel in Gmsh: points, lines, curve loops, surfaces, and physical surfaces.

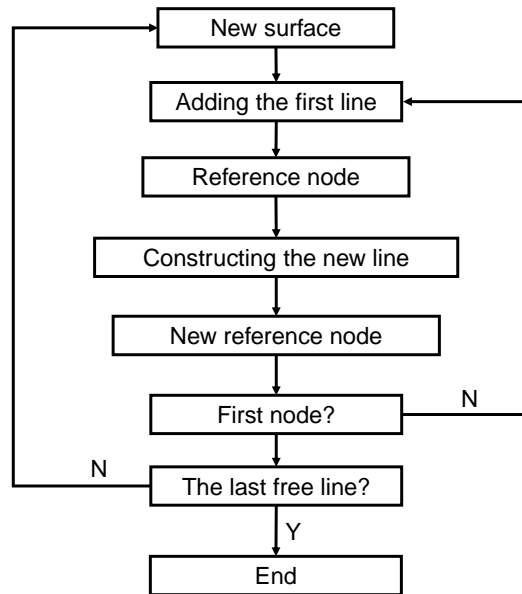


Figure 3.9: Flowchart of 2D geometry reconstruction from the identified free lines of an orphan mesh

then curves, surfaces, and volumes) with the built-in OpenCASCADE kernel. Figure 3.8 describes the bottom-up building process in `Gmsh` for a simple rectangle and the corresponding commands. Following this process, we construct the geometry surfaces by connecting the free points and lines. We propose an algorithm that consecutively connects the identified free lines. Initially, it starts with the first free line of the matrix $\mathbb{L}_{f \times 2}$ and then finds the second free line adjacent to it. This is determined by the node shared between the two lines. The process will continue to build a closed curve of the lines (Curve Loop in `Gmsh`), which happens when the current free line connects to the first free line. If all the free lines have been investigated, the process will terminate; otherwise, it will continue to build the next closed curve. This algorithm is summarized in Figure 3.9 and described in Algorithm 2 in Appendix 3.B.

Identifying multiple curve-loops/surfaces implies that the orphan mesh consists of a multi-phase material (i.e. there are either voids or particles or a combination of both).¹ To remove voids or create a mesh for particles, we must cut out the inclusion surfaces from the matrix surface. To do so, we use the `Boolean` operations available in `Gmsh` OpenCASCADE kernel. We apply the `BooleanDifference` operator to the matrix and void surfaces to create empty voids. On the other hand, if we want to have a multi-phase mesh for particles and matrix, we thus use `BooleanFragments` operator which intersects all volumes in a conformal manner (without creating duplicate interfaces). Figure 3.10 shows three different cases of the `Boolean` operator and their corresponding mesh. We consider

¹The number and type of phases can be assessed by the number of element sets in the orphan mesh. In particular, when the material is porous, there is only one element set for the matrix phase.

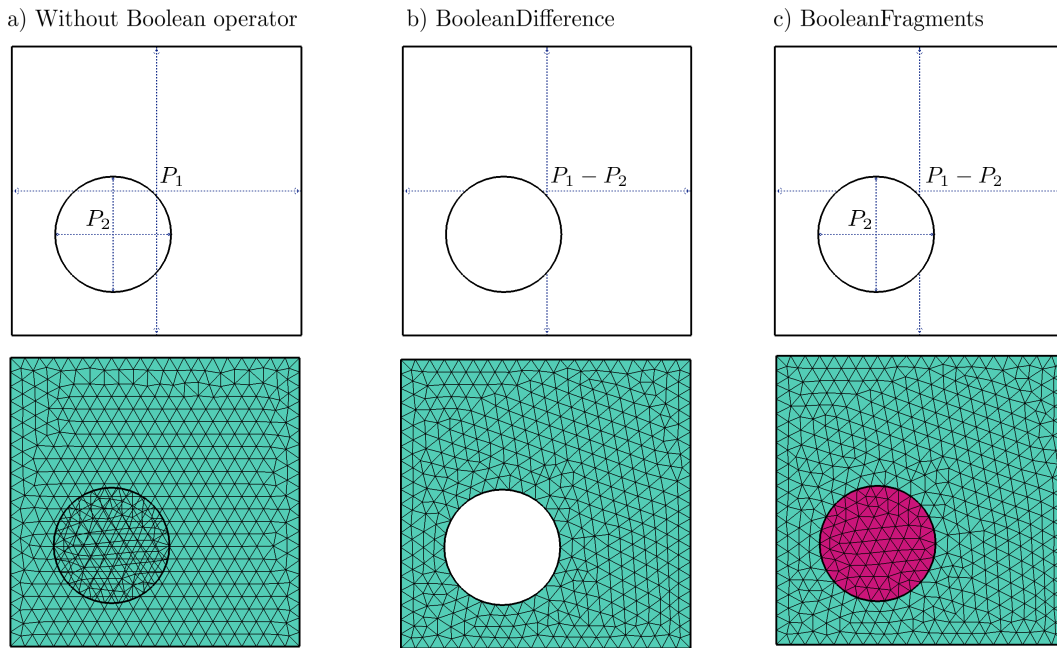


Figure 3.10: **Gmsh** Boolean operator. The surface P_1 is the rectangular matrix surface and P_2 is the inclusion surface. The first row displays the geometry and the second row corresponds to the meshed surfaces. (a) Without the Boolean operator, two surfaces are overlapping and are not distinguishable. (b) The **BooleanDifference** operator removes the inclusion surface. (c) The **BooleanFragments** operator preserves the inclusion surface and creates a conformal mesh at the interface between the inclusion and matrix

surface P_1 as the rectangular matrix surface and P_2 as the inclusion surface, which can be void or particle. In the absence of the Boolean operator in Figure 3.10a, two surfaces cannot be distinguished and the generated mesh is overlapping. With Boolean operators however, two surfaces become distinguishable. The **BooleanDifference** operator is applied to remove the inclusion surface when the second phase is an empty void (Figure 3.10b). Alternatively, one can apply **BooleanFragment** operator to preserve the inclusion surface and create a conformal mesh at the interface between the inclusion and matrix (Figure 3.10c). We note that in both Boolean operators, the largest surface must be determined to allocate the matrix phase to it. This is achieved by comparing the maximum or minimum coordinates of different surfaces when all surfaces are detected.

Step 4: Exporting the geometry, rescaling and remeshing. Once the geometry is constructed, it is possible to use it in CAD software or to generate a new mesh from it. By having the geometry, we have a high level of control over the output mesh and we can remesh it according to any meshing algorithm and element type that we desire. The

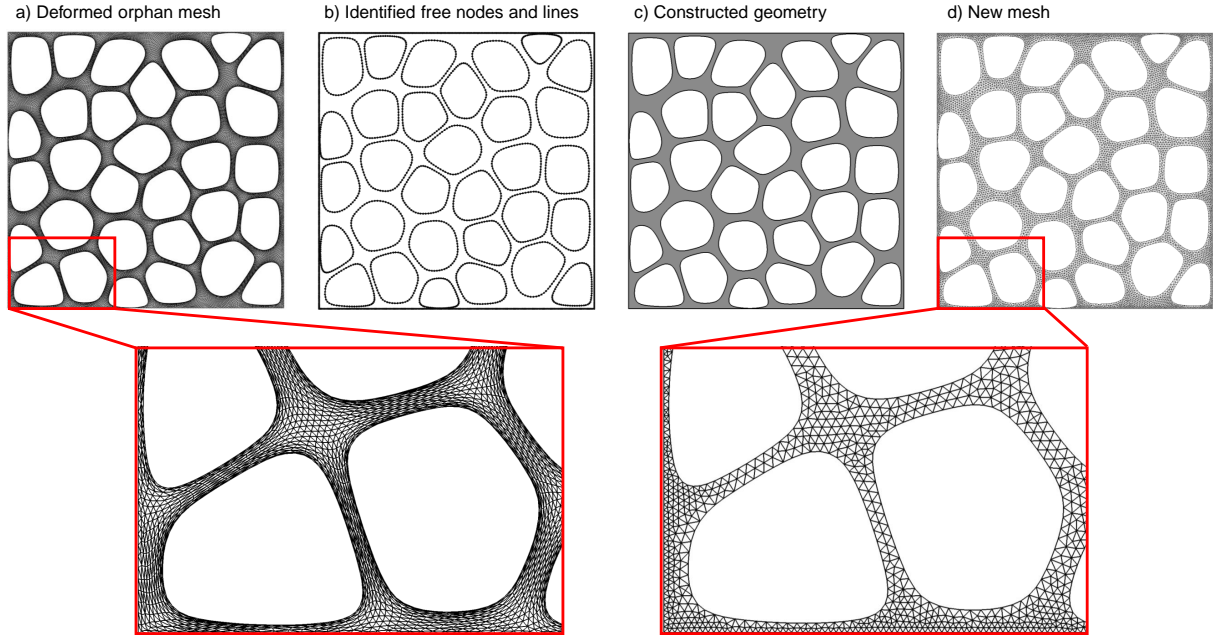


Figure 3.11: Remeshing steps applied to an orphan mesh of M-Voronoi containing extremely deformed elements and the corresponding new mesh with significantly higher quality.(as shown in the zoomed image)

geometry is written in `Gmsh` .geo format and is built based on a bottom-up manner (see Figure 3.8). Since remeshing is mostly applied to deformed structures, one might need to rescale the whole geometry to a specific size. By multiplying a fixed scaling number by all coordinate components of points in the geometry, a uniform scaling can be achieved. The scaling factor is normally an input parameter required from the user. The new mesh is created with `Gmsh` software and is exported as an Abaqus input file (.inp) for simulations. Various meshing options are available in `Gmsh`. If printing of 2D mesh is required, the mesh has to be extruded in an out-of-plane direction with a specific thickness. We have developed a Fortran code to extrude 2D meshes with a desired thickness and create the stereolithography (.stl) mesh file format, which is printable in 3D printers.

3.3.2 Application of 2D remeshing algorithm in M-Voronoi

As described in Section 3.1, the mechanical growth of the voids is triggered by applying large deformations to the unit-cell, which leads to severe mesh distortion. Generating a new mesh is therefore a fundamental step for further numerical simulation or 3D-printing of the final M-Voronoi geometries. Furthermore, due to the severe mesh distortion, the simulation might terminate before the target volume fraction of voids is achieved, which

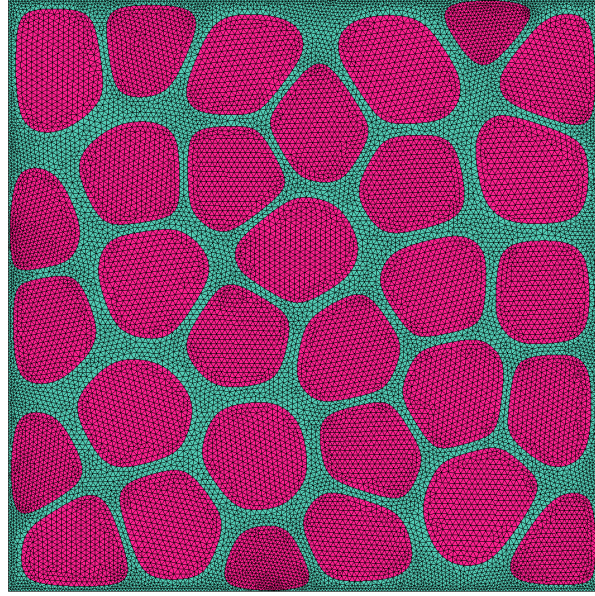


Figure 3.12: M-Voronoi containing particles instead of voids. The void regions can be meshed by applying the `BooleanFragments` operator.

happens especially when very low relative densities ($\rho \leq 0.05$) are required. In this case, one could use an intermediate deformation state as the initial geometry, remesh it and re-launch the simulation to proceed to larger strains. In Figure 3.11, we show the remeshing steps applied to an orphan mesh of M-Voronoi containing extremely deformed elements and the corresponding new mesh with significantly higher quality.

The proposed flexible remeshing technique also allows us to consider the voids in M-Voronoi as particles by applying the `BooleanFragments` operator and meshing the void regions. The same physical characteristics could be attributed by defining all particle surfaces as one physical group. The final mesh will contain two element/node sets: the matrix and the particles. Figure 3.12 illustrates the same M-Voronoi geometry containing particles instead of voids. We note that it is possible to create particles with different physical properties or a combination of voids and particles (i.e. materials with more than two phases).

3.4 M-Voronoi in convex cell domains

The discussed morphogenesis process is employed to obtain M-Voronoi geometries in rectangular, circular and triangular domains (Figure 3.13). For simplicity in presentation, we specialize to diagonal deformation loads, i.e., $\mathbf{F}^{\text{app}} = \text{diag}(\lambda_1^{\text{app}}, \lambda_2^{\text{app}})$ (with $\lambda_1^{\text{app}}, \lambda_2^{\text{app}}$ denoting the applied principal stretches).

In Figure 3.13a, we begin with a large number of initially circular voids ($\rho_0 = 0.9$), and subject the unit-cell to equi-biaxial tension with $\lambda_1^{\text{app}} = \lambda_2^{\text{app}} = \lambda^{\text{app}} > 1$. Three

rescaled contours show the maximum local principal logarithmic strain at current relative density $\rho = 0.7, 0.5, 0.3$ (Figures 3.13b-d). The circular voids gradually polygonize, albeit remaining smooth. This smoothness is a key feature of these newly obtained inclusion geometries. In particular, the complex interactions resulting from the disordered distributions of the voids and the underlying nonlinear large elastic deformations lead to convex and non-canonical Voronoi-type shapes. Most of these shapes resemble a pentagon and are of fairly similar size. By contrast, due to the random distance of the centers of the original circular voids, the deformed intervoid ligaments exhibit a rather random thickness variation. Pockets of almost *undeformed* solid regions (indicated by the blue spots in e.g., Figure 3.13c) are formed. Those pockets gradually shrink with further increase of the applied strains (Figure 3.13d). As a second representative example, the proposed morphogenesis process is employed to design M-Voronoi geometries with anisotropy. Specifically, as shown Figures 3.13e-h, we apply a biaxial tension with $2\lambda_2^{\text{app}} = \lambda_1^{\text{app}} = \lambda^{\text{app}} > 1$. Such a load transforms the initial square to a rectangle and the initially circular voids to *elongated* Voronoi-type shapes. Similar to the previous equi-biaxial case, the intervoid ligaments are again non-uniform. The possibilities for designing such M-Voronoi obviously are limitless since any combinations of the \mathbf{F}^{app} components can lead to different void formations and anisotropies. A selected set of such anisotropic M-Voronoi are discussed later in Section 3.7. This case of anisotropic M-Voronoi reveals the versatility of the method. This allows for a more tunable response by employing an inverse design protocol, albeit in a large nonlinear strain framework.

Finally, the simplicity of the process and the prescribed boundary conditions allows to grow M-Voronoi geometries in initially circular (Figures 3.13i,j), triangular (Figures 3.13k,l) or any other type of convex domain cells². The applied stretches may be chosen to be equi-biaxial retaining the original shape of the domain or simply biaxial leading to anisotropic responses. Interestingly, the grown voids exhibit similar polygonal (pentagon) type features except for a few ones that lie very close to the boundaries. For instance, the voids lying near the circle periphery or the corners of the triangle take a rather triangular shape (Figure 3.13l). The use of equi-biaxial loads tends to lead to a more isotropic growth even in anisotropic domains such as the triangular one. In turn, the use of non-equi-biaxial loads triggers a direction-dependent (i.e. anisotropic) void growth. In all cases, the only constraint that needs to be imposed for positive void growth is simply $\det \mathbf{F}^{\text{app}} > 1$, while the remaining components of \mathbf{F}^{app} may be arbitrarily chosen. It is important to note, that the randomness of void distributions allows to “fill” efficiently and uniformly those domains with voids/inclusions, a process that would be extremely difficult to achieve with periodic geometries (such as honeycombs, periodic lattices, etc.).

²Even though it is not shown rigorously, it is rather intuitive to see that a non-convex initial geometry of the unit-cell would lead to contact of the exterior faces of the cell and subsequent cease of the simulation under uniform affine loads. Thus a convex cell geometry, albeit of arbitrary shape is essential at the initial stage.

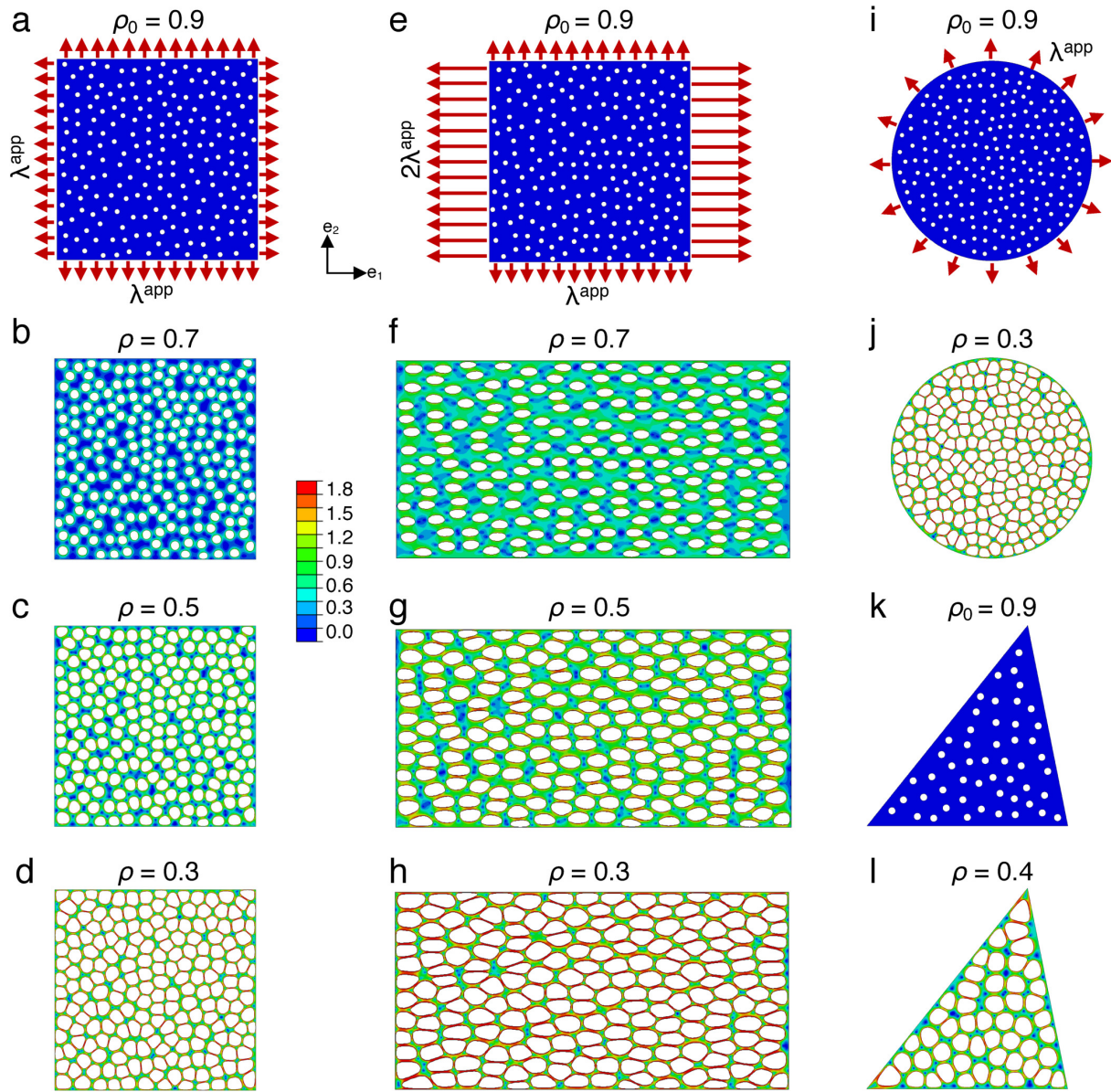


Figure 3.13: Representative M-Voronoi porous geometries for porous domains with different shapes: (a-d) isotropic geometries obtained using a rectangular cell subjected to equi-biaxial tension ($\lambda_1^{\text{app}} = \lambda_2^{\text{app}} = \lambda^{\text{app}} > 1$); (e-h) anisotropic geometries obtained using a rectangular cell subjected to biaxial tension ($2\lambda_2^{\text{app}} = \lambda_1^{\text{app}} = \lambda^{\text{app}} > 1$) and isotropic geometries obtained using respectively a (i-j) circular and a (k-l) triangular cell subjected to equi-biaxial load. The initial geometries in (a), (e), (i) and (k) are obtained using the RSA algorithm and monodisperse circular voids at relative density $\rho_0 = 0.9$. All deformed cells are scaled for visualization reasons.

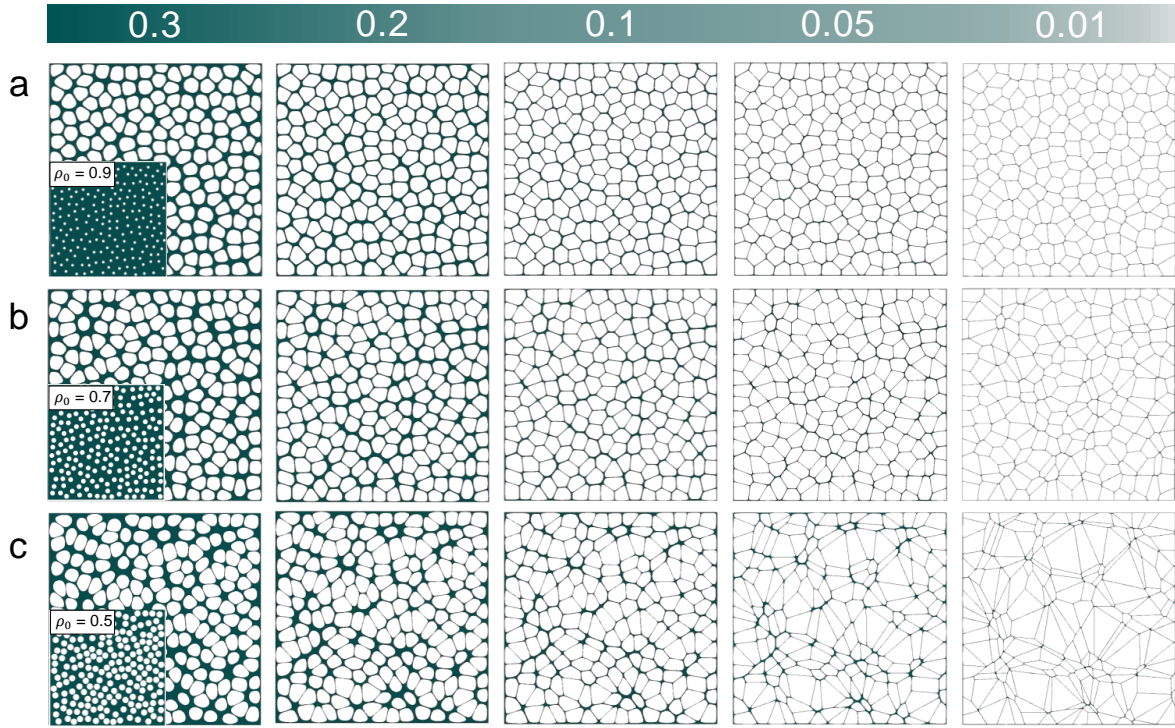


Figure 3.14: M-Voronoi obtained by using a RSA geometry with initial relative density (a) $\rho_0 = 0.9$, (b) $\rho_0 = 0.7$ and (c) $\rho_0 = 0.5$ as shown in the insets of the first row. The $\rho = 0.01$ geometries in, are obtained by using the corresponding $\rho = 0.1$ as an initial geometry after remeshing it. The top color bar indicates the final relative density ρ .

3.5 Effect of initial volume fraction and attainable relative density

The M-Voronoi geometries are numerically and experimentally realizable at solid densities spanning the full spectrum from 1 to very low (e.g., 0.01). Figure 3.14 represents M-Voronoi geometries with square unit-cell at different initial and final densities subjected to equi-biaxial loading which leads to an isotropic final geometry. We show that the initial relative density, ρ_0 , affects strongly the final M-Voronoi geometry. A higher initial $\rho_0 = 0.9$ (Figure 3.14a) leads to substantially more uniform and equi-sized Voronoi inclusions contrary to a lower initial $\rho_0 = 0.7, 0.5$ (Figures 3.14b,c). The latter tends to create disordered clustering of smaller and larger voids randomly distributed in the cell. It is important to note at this point that in order to achieve very low relative densities such as $\rho = 0.01$ while avoiding excessive mesh distortions, it is preferable to stop the simulation at an intermediate value of ρ , e.g. $\rho = 0.1$, extract the geometrical characteristics, remesh

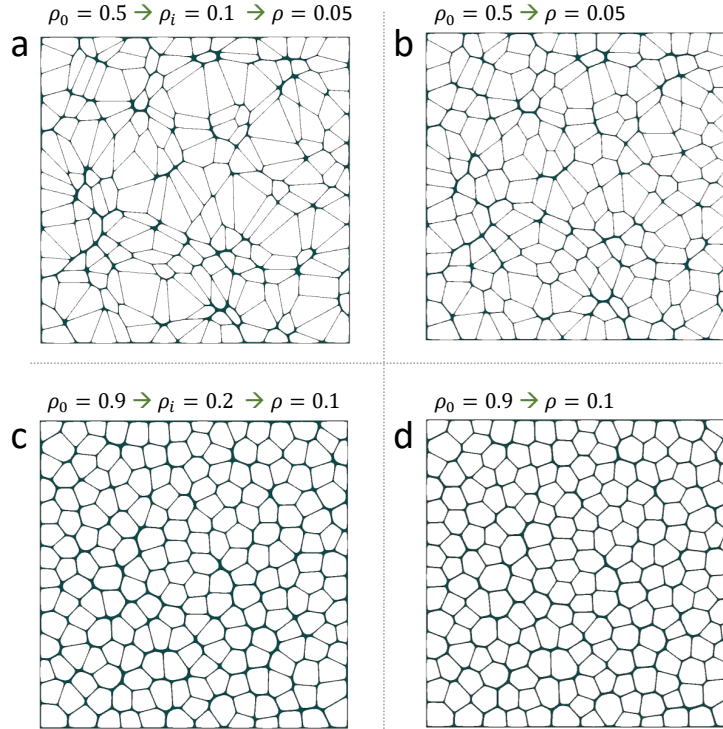


Figure 3.15: The effect of the intermediate re-launching step on M-Voronoi final geometries. The simulations have been stopped when the intermediate density ρ_i is achieved and the deformed geometry is extracted and remeshed. Then, the simulation is re-launched to obtain the final density ρ . (a),(b) M-Voronoi geometries of identical initial and final density ($\rho_0 = 0.5$ and $\rho = 0.05$), but with and without the intermediate M-Voronoi geometry, respectively. (c),(d) M-Voronoi geometries of identical initial and final density ($\rho_0 = 0.9$ and $\rho = 0.1$), but with and without the intermediate M-Voronoi geometry, respectively.

and re-launch the simulation to reach the final relative density desired. This last process implies re-launching **Steps 1-3** discussed in Figure 3.1, but using an intermediate M-Voronoi geometry as an initial one. Obviously, this process can be repeated whenever necessary to avoid severe mesh distortion or numerical convergence issues.

We note that if the intermediate re-launching step is performed without stress field mapping, the final geometry would be different from its counterpart without the intermediate step. This difference, however, is negligible when the initial density is higher ($\rho = 0.9$) and the size of the inclusions is more uniform and equi-sized contrary to a lower initial density ($\rho_0 = 0.7, 0.5$). In the latter, using an intermediate M-Voronoi geometry enhances the disorder size distribution of the inclusions. Figures 3.15a,b show the M-Voronoi geometries of identical final density, but with and without the intermediate M-Voronoi geometry, respectively. In the left side geometry, the simulation has stopped

when the intermediate density $\rho_i = 0.1$ is achieved. Then, the deformed geometry is extracted and remeshed without mapping the stress fields. The simulation is subsequently re-launched to obtain $\rho = 0.05$. In the right side geometry, the $\rho = 0.05$ is achieved directly from $\rho_0 = 0.5$ without the intermediate remeshed geometry. As a result of the intermediate step, the inclusions have become more polydisperse in size. Figures 3.15c,d show a similar comparison for the geometries with $\rho_0 = 0.9$ with and without the intermediate step. This step is performed at $\rho_i = 0.2$ for the left side geometry, while the final density $\rho = 0.1$ is identical. This process has a substantially lower effect on the more uniform size of the inclusions.

3.6 E-Voronoi and RSA versus M-Voronoi

For later use, we examine now the differences between the M-Voronoi geometries proposed in the present work versus the E-Voronoi and RSA polydisperse geometries (Figure 3.16). The (eroded) E-Voronoi geometries (Figure 3.16a) are constructed by use of the algorithms presented in [Spyrou et al. \(2019\)](#) for the modeling of human muscles. In that study, a standard Voronoi tessellation is first created and subsequently the walls of each Voronoi inclusion are eroded in a uniform manner leading to constant-thickness intervoid ligaments. The amplitude of erosion defines the final relative density, while the intervoid ligaments are meshed in two-dimensions to reach arbitrary values of ρ (as opposed to earlier studies such as in [Tekoglu et al. \(2011\)](#) where beam elements were used). By construction, the E-Voronoi void boundaries exhibit sharp corners, while the process may lead to locally more elongated inclusions of large aspect ratio towards an arbitrary direction. The E-Voronoi geometries can span the entire range of practical relative densities from 1 to very low (e.g., 0.01) and are isotropic as a direct consequence of the random Voronoi tessellation process (but see the recent extension to anisotropic ones by [van Nuland et al. \(2021\)](#)).

The random sequential adsorption algorithm (RSA) geometries ([Lopez-Pamies et al., 2013](#)) contain multiple sized (i.e. polydisperse) circular voids that are embedded randomly in the square domain (Figure 3.16b). Similar to the M-Voronoi, the RSA geometries exhibit non-uniform intervoid ligament thickness, while being extensively polydisperse with decreasing relative density. The main challenge in constructing the RSA geometries lies in the fact that it becomes increasingly difficult to reach representative specimens in the nonlinear finite-strain regime with very low relative densities (less than 0.2 in 2D and less than 0.3 in 3D) that are realizable numerically (for instance, no geometry has been achieved for $\rho < 0.05$ as shown in Figure 3.16b) as well as with 3D-printing technology. This is due to the extremely large difference between the largest and the smallest voids necessary to achieve such low densities. In turn, the RSA geometries may be isotropic or anisotropic depending on the void shapes ([Anoukou et al., 2018](#)) (e.g. ellipsoidal shape) and their distribution. In the present work, we focus on circular voids distributed randomly and uniformly in the square cell leading to a fairly isotropic response.

By contrast, the proposed M-Voronoi geometries are numerically and experimentally

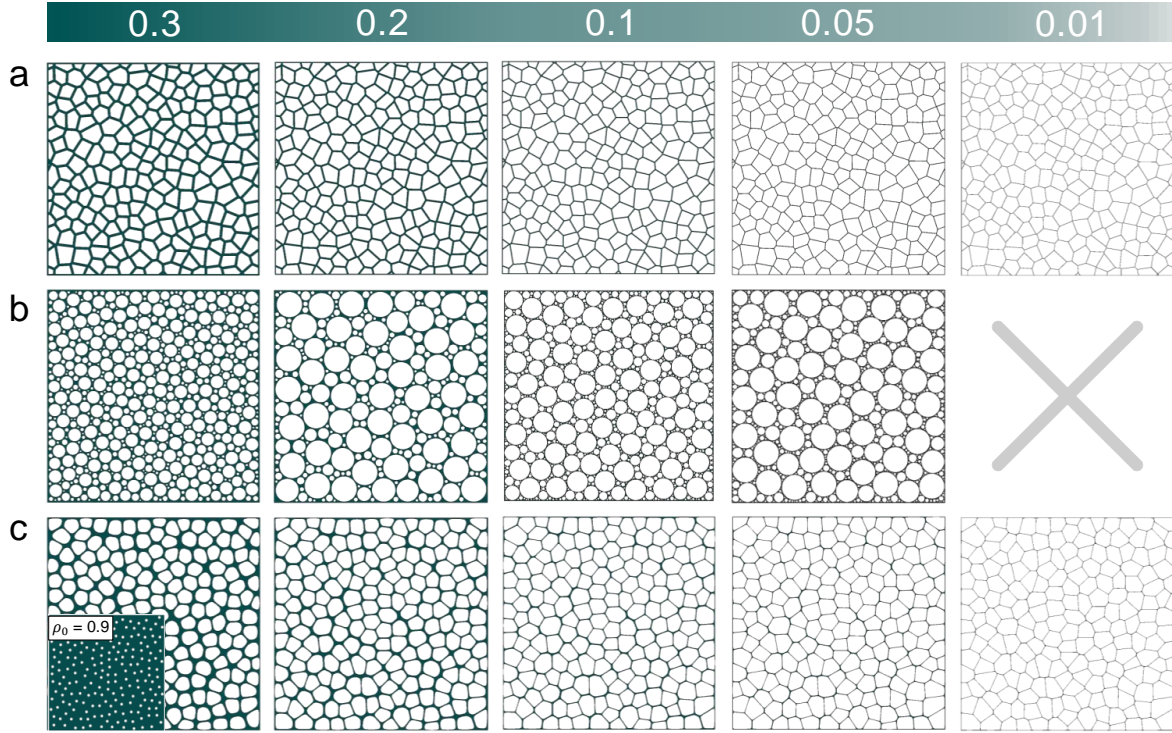


Figure 3.16: Random porous geometries: (a) E-Voronoi. (b) RSA polydisperse circles. (c) M-Voronoi obtained by using a RSA geometry with initial relative density $\rho_0 = 0.9$. The relative densities less than $\rho = 0.1$ are obtained by an intermediate remeshing step. The top color bar indicates the final relative density ρ .

realizable at solid densities spanning the full spectrum from 1 to very low (e.g., 0.01) (Figures 3.16c-e). For conciseness, we report M-Voronoi geometries obtained via an equibiaxial loading history applied to a RSA geometry with initial relative density $\rho_0 = 0.9$, which leads to an isotropic final geometry. The number of inclusions in M-Voronoi and E-Voronoi geometries is identical (=200) contrary to the RSA geometries where there is no control over the number of voids due to the polydispersity nature. In very low densities, the M-Voronoi and E-Voronoi are very similar. This is due to the uniform ligament thickness in the M-Voronoi allowing the voids to expand and fill the matrix.

3.7 Anisotropic M-Voronoi

The morphogenesis process for designing M-Voronoi geometries leads to macroscopic isotropy or anisotropy depending on the prescribed boundary conditions. As already shown in Figures 3.13e-h, anisotropic M-Voronoi geometries can be obtained using a

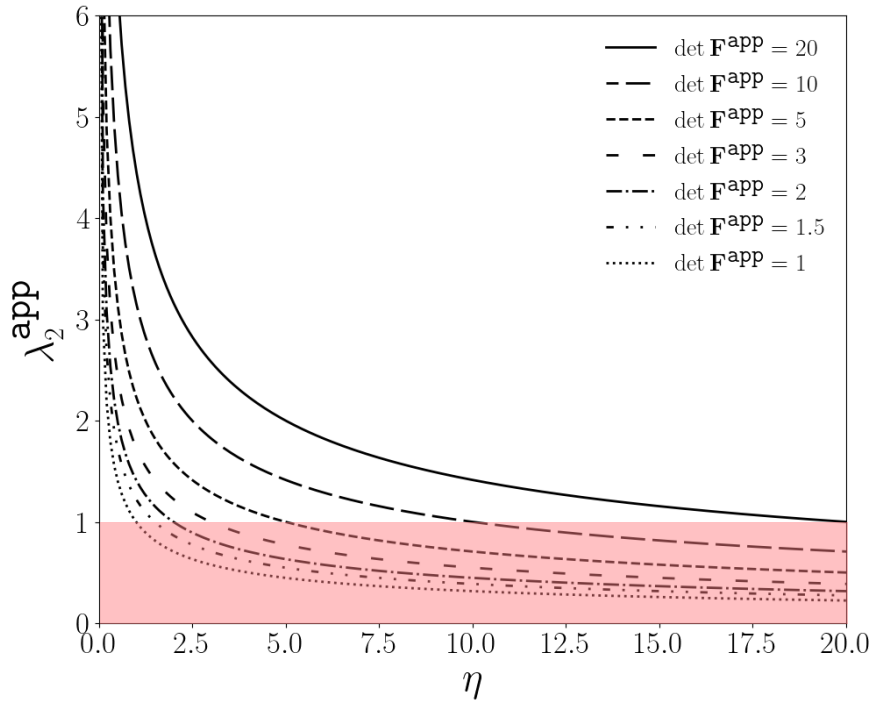


Figure 3.17: The variation of λ_2^{app} as a function of the anisotropy parameter η at different applied deformations $\det \mathbf{F}^{\text{app}}$. The red region shows the range of η and $\det \mathbf{F}^{\text{app}}$ leading to compressive deformations $\lambda_2^{\text{app}} < 1$ in the anisotropic generation process.

rectangular cell subjected to biaxial deformation $\mathbf{F}^{\text{app}} = \text{diag}(\lambda_1^{\text{app}}, \lambda_2^{\text{app}})$, where principal stretches are not equal $\lambda_1^{\text{app}} \neq \lambda_2^{\text{app}}$ and maintaining positive void growth via $\det \mathbf{F}^{\text{app}} > 1$.

However, one may readily employ an inverse design protocol to achieve a final square M-Voronoi cell with final dimensions $l_1 = l_2$ through a biaxial loading applied on an initially rectangular cell with dimensions $L_1 \neq L_2$. The latter imposes a geometrical constraint on the applied deformation to obtain the target porosity. The mechanical response of the final M-Voronoi with a specific porosity is tunable and depends on the applied deformation ratio $\eta = \lambda_1^{\text{app}}/\lambda_2^{\text{app}}$. By taking into account the geometrical constraint $l_1 = l_2$, one can readily show that the deformation ratio determines entirely the aspect ratio of the initial cell via the relation

$$\eta = \frac{\lambda_1^{\text{app}}}{\lambda_2^{\text{app}}} = \frac{L_2}{L_1}. \quad (3.15)$$

Here, η is an anisotropy parameter that leads to isotropic responses for $\eta = 1$ or anisotropic otherwise.

Using the last definitions together with (3.5), we readily obtain the following relations

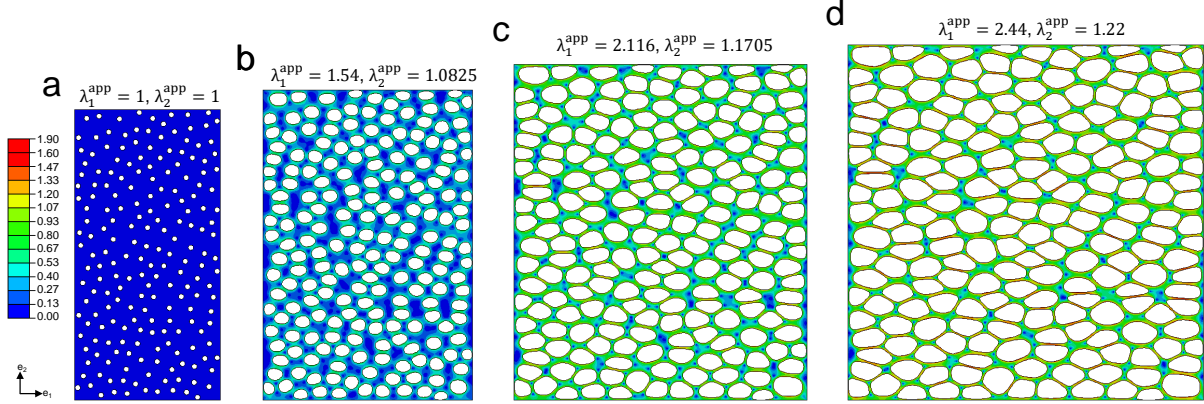


Figure 3.18: The generation process of an anisotropic M-Voronoi material with $\eta = 2$ obtained using a rectangular cell ($L_1 = 1$ and $L_2 = 2$) subjected to non equi-biaxial tension loading. The initial geometry in (a) is obtained using the RSA algorithm and monodisperse circular voids at the relative density $\rho_0 = 0.9$. (c) and (d) indicate the deformations at intermediate values of stretch. The final anisotropic geometry in (d) has a square shape with $l_1 = l_2 = 2.44$ and the relative density $\rho = 0.3$. The color bar indicates the maximum principal logarithmic strain.

for the applied deformation

$$\lambda_2^{\text{app}} = \sqrt{\frac{\rho_0}{\eta \rho}}, \quad \lambda_1^{\text{app}} = \eta \lambda_2^{\text{app}}, \quad (3.16)$$

where ρ_0 and ρ denote the initial and final relative density. It is important to note that void growth is achieved when $\det \mathbf{F}^{\text{app}} > 1$, which imposes the constraint $(\lambda_1^{\text{app}})^2 > \eta$, (or equivalently $(\lambda_2^{\text{app}})^2 > \eta^{-1}$). In spite of this, the void growth does not indicate tensile deformations in both directions, and both principal stretches are greater than one. In fact, even with $\det \mathbf{F}^{\text{app}} > 1$, compressive deformation might occur in either directions ($\lambda_1^{\text{app}} < 1$ or $\lambda_2^{\text{app}} < 1$). Following the relation (3.5), we denote ρ_0/ρ with $\det \mathbf{F}^{\text{app}}$. Figure 3.17 shows λ_2^{app} as a function of η for different values of $\det \mathbf{F}^{\text{app}} \geq 1$. There is obviously a compression in one direction for $\lambda_2^{\text{app}} < 1$, and that happens when $\eta > \det \mathbf{F}^{\text{app}}$ (red region in Figure 3.17). Therefore, in order to avoid such compressions one should consider the limit of aspect ratio η .

In practice, we create anisotropic M-Voronoi by prescribing the initial and final relative density, and the anisotropy parameter η . The initial RSA geometry is then constructed with $L_1 = 1$ and $L_2 = \eta$. Subsequently, the biaxial deformation $\mathbf{F}^{\text{app}} = \text{diag}(\lambda_1^{\text{app}}, \lambda_2^{\text{app}})$ is applied, where λ_1^{app} and λ_2^{app} are obtained from equation (3.16). The final deformed geometry has the dimension of $l_1 = \lambda_1^{\text{app}}$ and $l_2 = \lambda_2^{\text{app}} L_2$ where $l_1 = l_2$. This geometry is then remeshed and uniformly rescaled to 1×1 dimension with the remeshing algorithm.

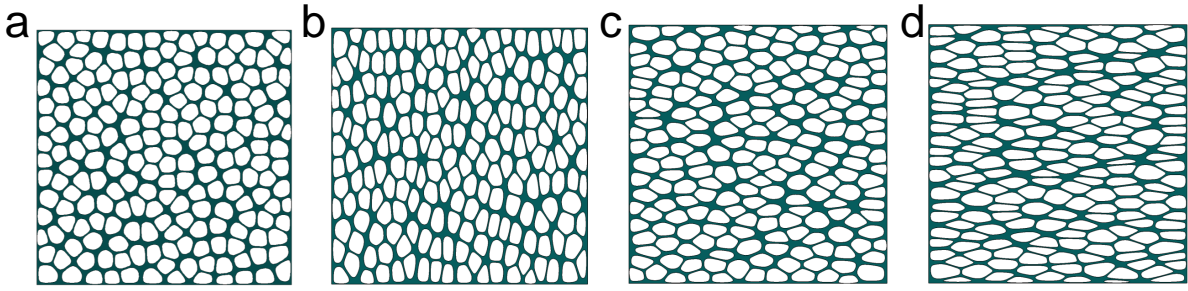


Figure 3.19: Isotropic and anisotropic M-Voronoi geometries with identical relative density $\rho = 0.3$ and different anisotropy parameters: (a) $\eta = 1$, isotropic M-Voronoi (b) $\eta = 0.5$, (c) $\eta = 2$, (d) $\eta = 4$.

In Figure 3.18, we show the generation process of an anisotropic M-Voronoi geometry with anisotropy parameter $\eta = 2$ and final density $\rho = 0.3$, constructed from a RSA geometry with initial density $\rho_0 = 0.9$ and dimensions $L_1 = 1$ and $L_2 = 2$. The initial unit-cell is subjected to a biaxial tension with $\lambda_1^{\text{app}} = 2.44$ and $\lambda_2^{\text{app}} = 1.22$. The contours show the maximum principal logarithmic strain at different current stretches until the final relative density is achieved. The final anisotropic M-Voronoi unit-cell has a square shape with $l_1 = l_2 = 2.44$ and it will be uniformly rescaled to 1×1 dimension for further studies. Similar to the isotropic M-Voronoi, the circular voids gradually polygonize, albeit remaining smooth and the intervoid ligaments are again non-uniform. However, the non equi-biaxial loads transform the circular voids to elongated voronoi-type shapes, resulting into a geometry with anisotropic properties. Such elongations in the horizontal direction are due to the strain field bonds created in the vertical direction, as a consequence of a larger deformation in the horizontal direction. These bonds are shown in Figure 3.18b with green color. Equivalently, dense pockets of solid phase are observed more in the horizontal intervoid ligaments. Finally the anisotropic M-Voronoi results in voids elongated two times more horizontally. The design process could be repeated for any arbitrary value of η to obtain an anisotropic M-Voronoi with controlled mechanical properties.

Following the same procedure, we created anisotropic M-Voronoi geometries with identical relative density $\rho = 0.3$ and different anisotropy parameters $\eta = 0.5, 1, 2, 4$, but identical relative densities $\rho = 0.3$ (Figure 3.19). For consistency, all geometries are uniformly rescaled to 1×1 dimension. The geometry with $\eta = 1$ corresponds to the isotropic M-Voronoi and we observe its difference from anisotropic geometries. Clearly, for $\eta > 1$ the voids are elongated horizontally, while for $\eta < 1$ the elongation is vertically. The possibilities for designing such an anisotropic M-Voronoi are countless since any combination of principal stretches λ_1^{app} and λ_2^{app} can lead to different anisotropies and properties. This reveals the versatility of the M-Voronoi method to design a geometries with tunable properties. A selected set of such anisotropic M-Voronoi are manufactured and studied

experimentally in Section 4.5.5.

3.8 The assembly of the porous cells into macroscopic structures

In this section, we take advantage of the M-Voronoi growth process over a variety of domains (Figure 3.13) to propose a novel modular assembly of the porous cells into macroscopic structures of arbitrary shape (Figure 3.20). As an example, we consider the logo of Ecole Polytechnique, which involves an X-shape with triangular curved ends (Figure 3.20a). The latter may be *discretized* in arbitrary finite volume elements (FVE) (similar to the finite elements in numerical methods) of triangular, trapezoidal and rectangular shape (Figure 3.20b). In addition, each FVE may be attributed a different relative density and be generated by applying a different deformation history (e.g., equi-biaxial, anisotropic biaxial, or shear plus biaxial, etc.). Once created, each FVE is assembled

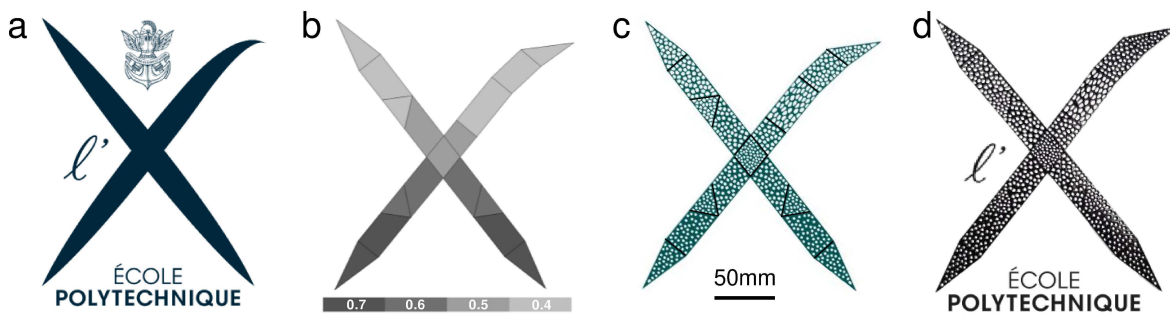


Figure 3.20: Assembly of individual M-Voronoi cells into a macroscopic geometry. (a) Ecole Polytechnique Logo. (b) Finite Volume Element (FVE) discretization with arbitrary porosity and anisotropy. (c) Numerical creation and assembly of the individual porous cells. (d) 3D-printed specimen.

numerically to reconstruct the original macroscopic X-shape geometry (Figure 3.20c). We recall that each FVE can be uniformly rescaled at will. The final X-shape is then transformed to STL format and 3D-printed (Figure 3.20d). We note that this modular assembly process is easily employed using the M-Voronoi geometries and at any relative density desired spatially. The advantage of such an assembly is that the FVEs have a versatile isotropic or anisotropic representative response with their relative density as an input. This relative density may be further optimized by use of the earlier homogenization-based methods proposed by Allaire (1992), allowing for a finite void volume fraction per FVE. Of course, an RSA geometry may also be considered, however, in the context of triangular or trapezoidal FVEs, the circles (and more generally the quadric objects) become highly non-conforming near the sharp corners of the triangles limiting even further the relative densities that can be reached. In turn, the E-Voronoi have the potential to

be implemented in such an assembly process (Martínez et al., 2018) recalling nonetheless the weaker mechanical resilience as compared to the M-Voronoi geometries at finite strains and buckling/fracture loads. One can further envisage a more uniform transition between the FVE boundaries by applying smoothing techniques (Martínez et al., 2016; Kumar et al., 2020). Obviously, the present assembly method is limited by the minimum 3D-printing feature capability, i.e., the minimum void size that can be properly realized in practice.

3.9 Concluding remarks

In the present chapter, we propose a versatile mechanically-grown morphogenesis method to obtain random geometries called M-Voronoi. This method is based on a nonlinear elastic finite strain computational strategy and creates random geometries with smooth void shapes and variable ligament thickness. We show that the final volume fraction of inclusions in M-Voronoi geometries can be controlled by a pure kinematic relation. Moreover, a full density range can be obtained by the proposed method. To achieve this, we propose a novel intermediate remeshing algorithm to improve mesh quality in the intermediate deformation steps. The developed algorithm is able to construct the deformed geometry of an orphan mesh with no information from the corresponding CAD model. It can then remesh it with improved mesh quality. This algorithm can also deal with arbitrary complex geometries containing either voids or multiphases. It is important to note that the discussed M-Voronoi method is general and can be applied to design random porous materials or particulate composites (Figure 3.12). In addition, random M-Voronoi can be constructed in various cell domain geometries (e.g. triangles, circles, trapezoids, rectangles, etc.), enabling us to assemble the porous cells (finite volume elements (FVEs)) into macroscopic structures. M-Voronoi geometries are also affected by the initial porous geometry. As an example, as we increase the porosity of the initial RSA domain, the final M-Voronoi geometry will become more polydisperse. We note that the choice of the initial geometry is countless and this method could be applied to any porous cell domain including irregular and periodic geometries. The comparison between the M-Voronoi, E-Voronoi and RSA geometries reveals that the M-Voronoi and E-Voronoi become very similar at large porosities, because of the saturation of the ligament thickness achieved in M-Voronoi geometries. Our study also indicated that RSA geometries are not able to cover the entire density range, especially with a representative microstructure. Therefore, at large porosities, one can use M-Voronoi geometries instead of random RSA materials. Finally, we note that anisotropic M-Voronoi geometries with tunable properties can be obtained by controlling the initial porous geometry dimension and the applied deformations.

3.A Appendix A. Equality between the applied and average deformation gradients

Using the finite strain kinematics definitions in Section 3.1, we show here that \mathbf{F}^{app} corresponds to the average deformation gradient in the cell, i.e., $\mathbf{F}^{\text{app}} = |\mathcal{V}_0|^{-1} \int_{\mathcal{V}_0} \mathbf{F}(\mathbf{X}) d\mathbf{X}$.

We start by noting

$$\frac{1}{|\mathcal{V}_0|} \int_{\mathcal{V}_0} \mathbf{F}(\mathbf{X}) d\mathbf{X} = \frac{1}{|\mathcal{V}_0|} \int_{\mathcal{V}_0} \text{Grad} \mathbf{x} d\mathbf{X}. \quad (\text{A.1})$$

Using the divergence theorem and the previous definitions, one gets

$$\frac{1}{|\mathcal{V}_0|} \int_{\mathcal{V}_0} \text{Grad} \mathbf{x} d\mathbf{X} = \frac{1}{|\mathcal{V}_0|} \int_{\mathcal{S}_0} \mathbf{x} \otimes \mathbf{n} d\mathcal{S}_0 = \frac{1}{|\mathcal{V}_0|} \int_{\mathcal{S}_0} (\mathbf{u} + \mathbf{X}) \otimes \mathbf{n} d\mathcal{S}_0 = \frac{1}{|\mathcal{V}_0|} \int_{\mathcal{S}_0} (\mathbf{F}^{\text{app}} \mathbf{X}) \otimes \mathbf{n} d\mathcal{S}_0 \quad (\text{A.2})$$

Since \mathbf{F}^{app} is a constant second order tensor, it may be taken outside of the integral, thus leading to

$$\frac{1}{|\mathcal{V}_0|} \int_{\mathcal{V}_0} \mathbf{F}(\mathbf{X}) d\mathbf{X} = \frac{1}{|\mathcal{V}_0|} \mathbf{F}^{\text{app}} \int_{\mathcal{S}_0} \mathbf{X} \otimes \mathbf{n} d\mathcal{S}_0 = \frac{1}{|\mathcal{V}_0|} \mathbf{F}^{\text{app}} \int_{\mathcal{V}_0} \text{Grad} \mathbf{X} d\mathcal{V}_0 = \mathbf{F}^{\text{app}}, \quad (\text{A.3})$$

since $\text{Grad} \mathbf{X} = \mathbf{I}$. This proof is due to Hill (Hill, 1963).

3.B Appendix B. Algorithms for remeshing a 2D orphan mesh by constructing the geometry

Nomenclature:

- n : total number of nodes in the orphan mesh
- m : total number of elements in the orphan mesh
- h : the number of nodes per element
- f : the number of free lines
- t : the reference node
- $\mathbb{N}_{n \times 3}$: matrix containing the nodes coordinates
- $\mathbb{M}_{m \times h}$: matrix containing the elements information
- $\mathbb{L}_{f \times 2}$: matrix containing the nodes of free lines

Algorithm 1 finding the free lines of a 2D orphan mesh

```

1: Initialize the algorithm with number of free lines  $f = 0$ 
2: for  $p = 1, m$  do
3:   for  $q = 1, h$  do
4:      $ref = [\mathbb{M}(p, q), \mathbb{M}(p, q + 1)]$ 
5:     for  $u = 1, m$  do
6:       for  $v = 1, h$  do
7:          $comp = [\mathbb{M}(u, v), \mathbb{M}(u, v + 1)]$ 
8:         if  $ref = comp$  then
9:           goto 3
10:        else
11:           $\mathbb{L}(f, :) = [\mathbb{M}(p, q), \mathbb{M}(p, q + 1)]$ 
12:           $f \leftarrow f + 1$ 
13:        end if
14:      end for
15:    end for
16:  end for
17: end for

```

Algorithm 2 Constructing the geometry by the free element sides

```

1: for  $i = 1, f$  do
2:   write new points  $\mathbb{L}(i, 1)$  and  $\mathbb{L}(i, 2)$ 
3:   write and store new line from point  $\mathbb{L}(i, 1)$  to point  $\mathbb{L}(i, 2)$ 
4:    $t = \mathbb{L}(i, 2)$   $\triangleright t$  is the temporary reference node which is in common between two
      consecutive lines.
5:   for  $j = 1, f$  do
6:      $w = 0$ 
7:     if  $\mathbb{L}(j, 1) = t$  then
8:       write next point  $\mathbb{L}(j, 2)$ 
9:       write and store new line from point  $t$  to point  $\mathbb{L}(j, 2)$ 
10:       $t \leftarrow \mathbb{L}(j, 2)$ 
11:       $w = 1$ 
12:      goto 5
13:     else if  $\mathbb{L}(j, 2) = t$  then
14:       write next point  $\mathbb{L}(j, 1)$ 
15:       write and store new line from point  $t$  to point  $\mathbb{L}(j, 1)$ 
16:       $t \leftarrow \mathbb{L}(j, 1)$ 
17:       $w = 1$ 
18:      goto 5
19:     end if
20:   end for
21:   if  $w=0$  then  $\triangleright$  The curve loop is closed.
22:     write Curve Loop of all lines of the loop
23:     write a Plane surface from the Curve Loop
24:   end if
25: end for

```

Chapter 4

3D-printing, experiments and numerical assessment for 2D M-Voronoi

Chapter summary: This chapter is focused on 3D printing, experiments and the numerical study of two-dimensional random and periodic geometries described in chapters 2 and 3. In the first part of this chapter, we study TangoBlack material which is a commercial polymer used in our 3D-printer and tested experimentally under uni-axial tension loading. Due to the brittle fracture of TangoBlack material, normal test specimen geometries like standard dog-bones are not suitable for identification of TangoBlack material properties. Instead, we propose a new specimen geometry to avoid early fracture of this material. When TangoBlack materials are tested under tensile, relaxation, and loading-unloading tests, they exhibit highly viscous and strain-rate dependent behavior. The material behavior of TangoBlack is then modeled by the rubber viscoelastic material model proposed by [Kumar and Lopez-Pamies \(2016\)](#) and the corresponding parameters are identified. We also show that the ultimate tensile properties of TangoBlack material can be characterized by a unique failure envelope.

The second part of this chapter deals with the fabrication process and uni-axial compression tests carried out on different two-dimensional random porous geometries. The M-Voronoi has shown remarkable ability in terms of energy absorption while being the most resilient porous geometry at certain porosities. The study of the representativity of M-Voronoi geometries has confirmed that with more than 200 voids the response is representative. Moreover, M-Voronoi has an isotropic response in both large and small strains which is in contrast to periodic 2D lattices such as hexagons. The experimental results are then simulated numerically by identifying material parameters and show a fairly reasonable response.

Contents

4.1 3D-printing method	74
--	----

4.2	Characterization and modeling of TangoBlack material	75
4.2.1	TangoBlack reported characteristics	75
4.2.2	The design of the specimen and experimental setup	75
4.2.3	Testing protocol	82
4.2.4	Optical strain measurement	84
4.2.5	Tensile test and high strain rates deformations	84
4.2.6	Loading-Unloading and cyclic tensile tests	88
4.2.7	Single-step Relaxation tests	90
4.2.8	Constitutive modeling of viscoelastic behavior of TangoBlack	94
4.2.9	Fracture and ultimate tensile properties of TangoBlack	99
4.2.10	Fracture in Relaxation tests	100
4.2.11	Neo-Hookean modeling at low strain rates	102
4.3	3D-printing method and limits for porous geometries	104
4.4	3D-printing interruption strategy	104
4.5	Experimental results and discussion	107
4.5.1	Testing protocol	107
4.5.2	Representativity and isotropy of M-Voronoi	108
4.5.3	Comparison among the three geometries	113
4.5.4	Comparison with Honeycombs	116
4.5.5	Anisotropic M-Voronoi	118
4.6	Numerical results and discussions	118
4.7	Concluding remarks	122

4.1 3D-printing method

In this study, the test specimens are 3D-printed via PolyJet technology, using an EDEN 260VS printer from Stratasys and a rubber-like UV-curable resin (commercial name TangoBlack FLX 973 from Stratasys). With PolyJet 3D Printing, layers of liquid photopolymer are jetted onto a build tray before being instantly cured by UV light. The fine layers with a resolution of 16 μm build up to create a precise 3D object with very fine feature details (more information: <http://www.stratasys.com>). After printing, the printed materials are ready to be handled without the need for post-curing. A support material is required in the 3D-printer to build a removable layer between the sample and tray, fill in the voided regions or cover the entire sample for a non-glossy resolution. The support material used in this study to print TangoBlack samples has the commercial name SUP705

and is removable with a waterjet. As this support material is not soluble in water, careful handling is required when using a waterjet.

4.2 Characterization and modeling of TangoBlack material

4.2.1 TangoBlack reported characteristics

The photopolymeric resin employed for 3D-printing has the commercial name TangoBlack FLX 973 and exhibits rubber-like qualities. Due to its flexible characteristics, it can be used in soft-touch coatings, non-slip surfaces, overmolding grips, shoe soles, and other applications (see [TangoBlack information](#)). The material properties of TangoBlack reported by Stratasys company are listed in Table 4.1. The reported values for tensile strength and elongation at break have shown a great discrepancy with our measured values. A reason for this is the viscous nature of TangoBlack, which is a rubber-like polymer. Therefore, the performance of this material is significantly affected by the loading rates and the temperature, and the reported values by Stratasys do not provide adequate information about the experimental conditions. Nevertheless, we confirm the reported value of the polymerized density by weighing a printed cuboid TangoBlack of the dimension $5 \times 5 \times 1 \text{ cm}^3$ (see Figure 4.1). The measured weight and density correspond to 28.644 g and 1.14576 g/cm^3 , respectively, which are in agreement with the reported value in table 4.1. Subsequently, one can characterize the non-linear viscous behavior of TangoBlack material by conducting uni-axial tensile and relaxation tests at different strain rates. In the following sections, the details of the experimental tests and the actual material properties are discussed.

	ASTM	METRIC	ENGLISH
Tensile Strength	D-412	1.8-2.4 MPa	115-220 psi
Elongation at Break	D-412	45-55%	45-55%
Compressive Set	D-395	0.5-1.5 %	0.5-1.5%
Shore Hardness (A)	D-2240	60-62 Scale A	60-62 Scale A
Tensile Tear Resistance	D-624	3-5 Kg/cm	18-24 lb/in
Polymerized Density	D-792	$1.14-1.15 \text{ g/cm}^3$	

Table 4.1: TangoBlack FLX973 material properties reported by [Stratasys](#).

4.2.2 The design of the specimen and experimental setup

Generally, the design of the specimen in a mechanical test is constrained by the type of required test, the material properties, the testing machine, and the grips that hold the sample. A sample design process for materials with exceptional properties may involve

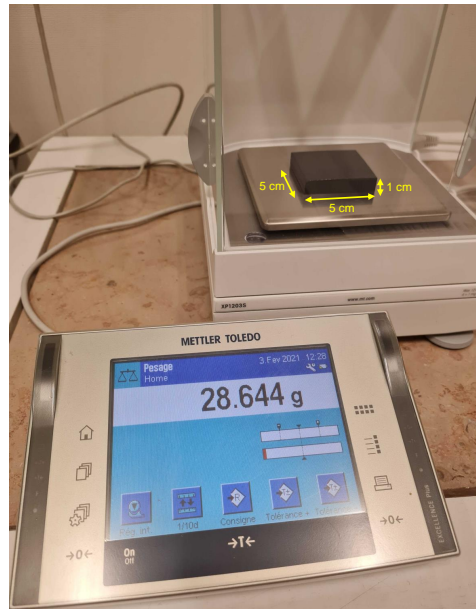


Figure 4.1: The density measurement of a polymerized TangoBlack FLX973 sample. The measured density corresponds to 1.14576 g/cm^3 .

different experimental trials and errors along with a preliminary numerical study in order to obtain a sample that performs as expected. We realized that it was particularly challenging to design a tensile test specimen for TangoBlack material due to its brittle fracture characteristics. Thus, we conducted several experiments and numerical analyses of different sample geometries in order to determine which geometry is best suited to deal properly with the brittle nature of the TangoBlack. The dog bone standard geometry is the first specimen option when a tensile test is required. Figure 4.2a shows the designed dog-bone specimen with a $12 \times 12 \text{ mm}^2$ cross-section. The geometry is subsequently 3D-printed with the TangoBlack material and stretched in a standard tensile test. We used a servo-hydraulic tensile test machine (Instron 5967) with hydraulic grips (Figure 4.2b). Several experiments have been conducted under displacement control with a constant strain rate of 0.0007 s^{-1} , while the deformations have been captured by a CCD camera with an optical strain measurement method (Figures 4.2b,c). The longitudinal and lateral strains are measured by means of the deformation of four white points that have been placed manually at the center of the specimen where the deformation is uniform. Choosing a white color ensures sufficient contrast in the deformation captured with the CCD camera. LED fiber lights have been used to enhance the contrast by focusing on the middle part of the specimen (Figure 4.2d). The experiments revealed that depending on the pressure applied by the grips, the dog-bone TangoBlack specimen would either slip off the grip surface or break at its edges. Figure 4.2d shows the TangoBlack dog-bone sample fractured at the edge of the top grip. It has been observed that the specimen will slip if the grip pressure is too low, and it will break if the pressure is too high. Moreover,

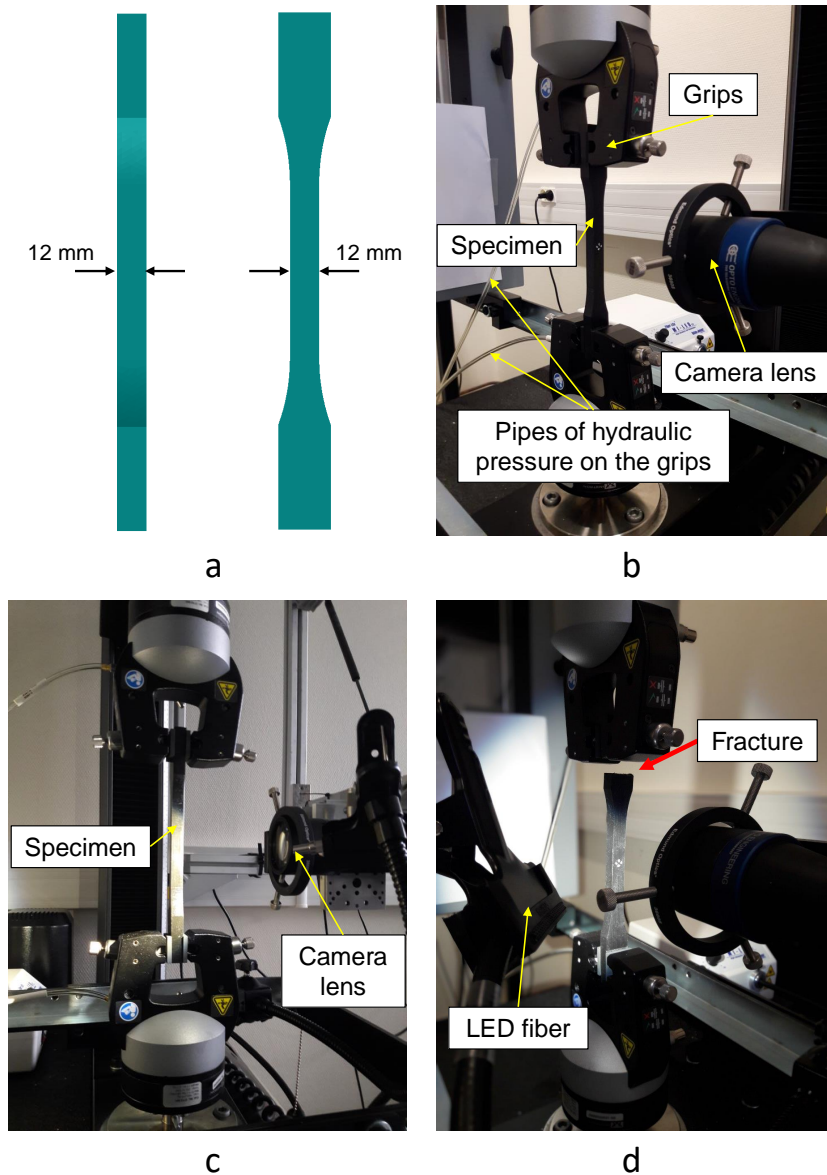


Figure 4.2: The TangoBlack dog-bone specimen. (a) The designed dog-bone geometry with a $12 \times 12 \text{ mm}^2$ cross-section. (b) The experimental setup for a tensile test on the specimen. (c) The lateral view of the sample held in the hydraulic grips. (d) The TangoBlack sample that was early broken at the edges of the top grip.

due to the incompressibility of TangoBlack and the change in cross-section, it is nearly impossible to determine the ideal pressure for the grips.

Consequently, we proposed a new specimen and grip geometry to apply tensile loading without transverse pressure. Initially, we proposed an I-shape geometry for the TangoBlack material, stretched by a surrounding box of the grips (Figure 4.3a). A harder mate-

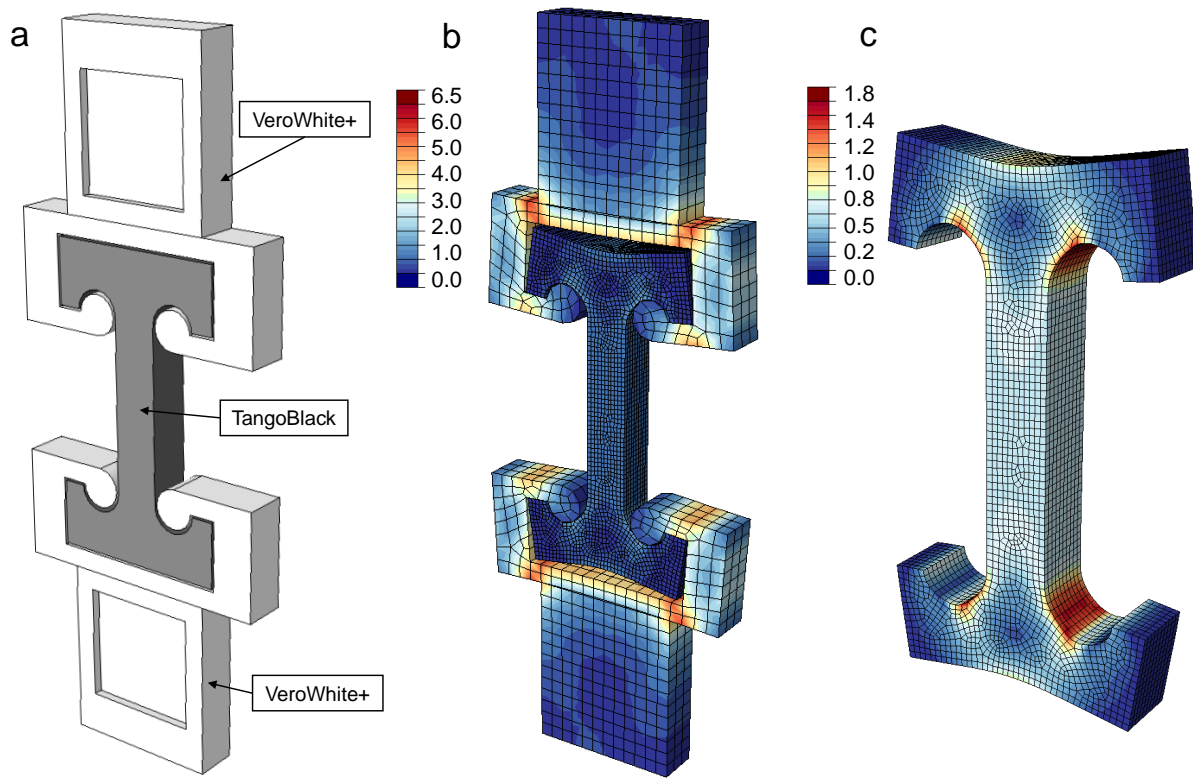


Figure 4.3: (a) I-shape design of TangoBlack specimen with VeroWhite Plus grips. (b) The stress field and deformation of the specimen under uni-axial tension. (c) The stress field in the deformed TangoBlack specimen is concentrated near the VeroWhite Plus contact region. The color bar indicates the von Mises stress field in MPa.

rial is obviously required for the grips so that they do not deform. We used VeroWhite Plus (RDG835) with Young's modulus of 1400 MPa to 3D-print the designed grips with a Stratasys 3D-printer. In order to ensure the designed specimen meets our expectations, we performed numerical simulations with Abaqus FE software. A hyperelastic Neo-Hookean material model has been used for TangoBlack with Young's modulus of 3.0 MPa and Poisson's ratio of 0.499 (almost incompressible). VeroWhite Plus is modeled as an elastic material with a Young modulus of 1400 MPa and Poisson's ratio of 0.42. Figure 4.3b illustrates the stress field and deformation of each part. The low thickness of VeroWhite Plus causes the grips to deform significantly, so reinforcement of the geometry is necessary due to the large deformation. Moreover, the stress fields in the TangoBlack sample are concentrated at the tangent point between the uniform length and the curvature where it comes into contact with VeroWhite Plus (Figure 4.3c). In real experiments, this would predict a fracture in this region. Therefore, both the TangoBlack and VeroWhite Plus parts must be reinforced geometrically.

We will next revise the proposed geometry by curving the structured regions to avoid

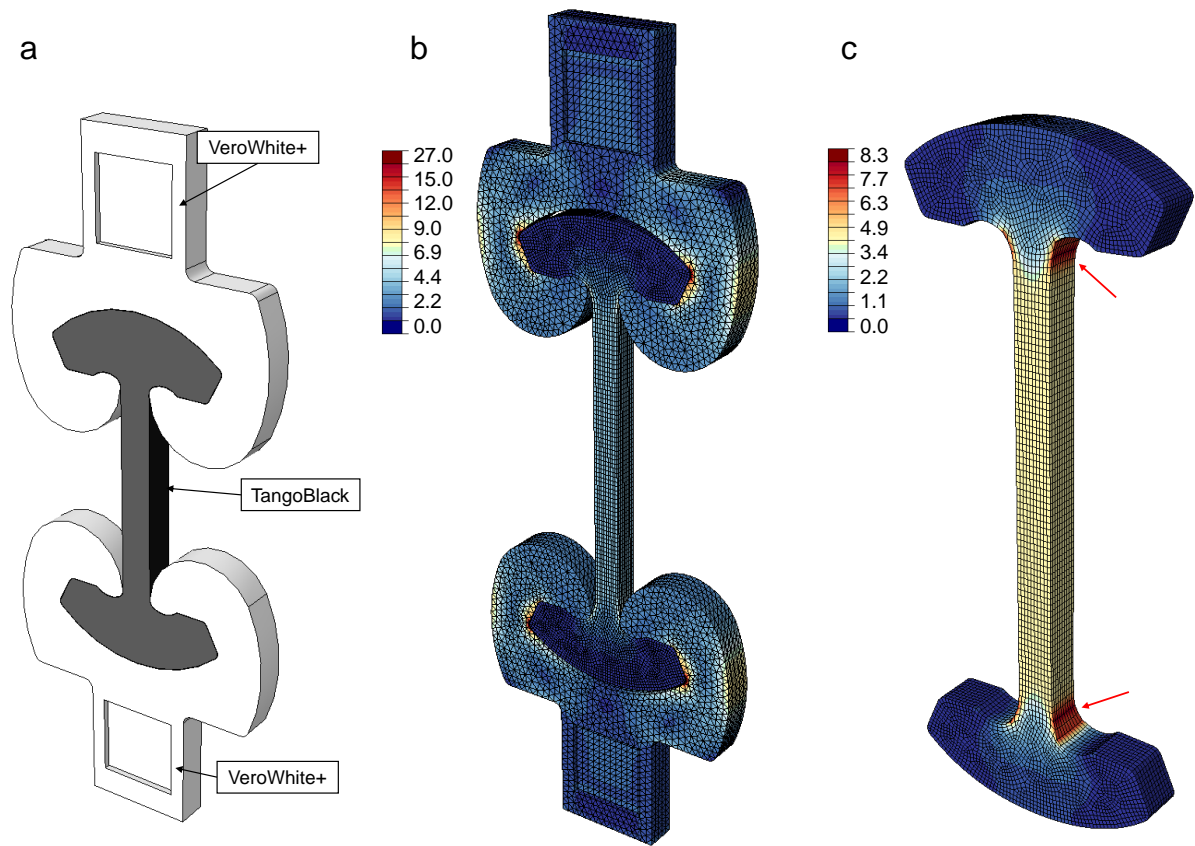


Figure 4.4: (a) The curved I-shape design of the TangoBlack specimen with geometrically reinforced VeroWhite Plus grips. (b) The stress field and deformation of the specimen under uni-axial tension. (c) The stress field in the deformed TangoBlack specimen is concentrated near the contact region with VeroWhite Plus. The color bar indicates the von Mises stress field in MPa.

large deformations in the grips while enhancing the thickness of the weak regions. Figure 4.4a shows the revised geometry with a curved shape and larger thickness. We note that the square notch on the VeroWhite parts is created to properly hold the grips on the tensile test machine (This is achieved by eliminating the risk of slipping). The geometry is subsequently evaluated numerically and experimentally to ensure its performance when dealing with the fracture of TangoBlack. A friction coefficient of 0.5 is employed in the contact regions for numerical convergence. Figure 4.4b illustrates the stress field in the specimen and grips stretched up to 100% strain. The deformation of the grips is now negligible with this geometry and they will sustain the applied load very well. Nevertheless, the stress field in the TangoBlack sample reveals once again a concentration near the VeroWhite Plus contact region (Figure 4.4c). The numerical tensile test has been conducted experimentally to assess the fracture point of the TangoBlack sample. Figure 4.5 shows the printed TangoBlack and VeroWhite parts under the tensile test. As

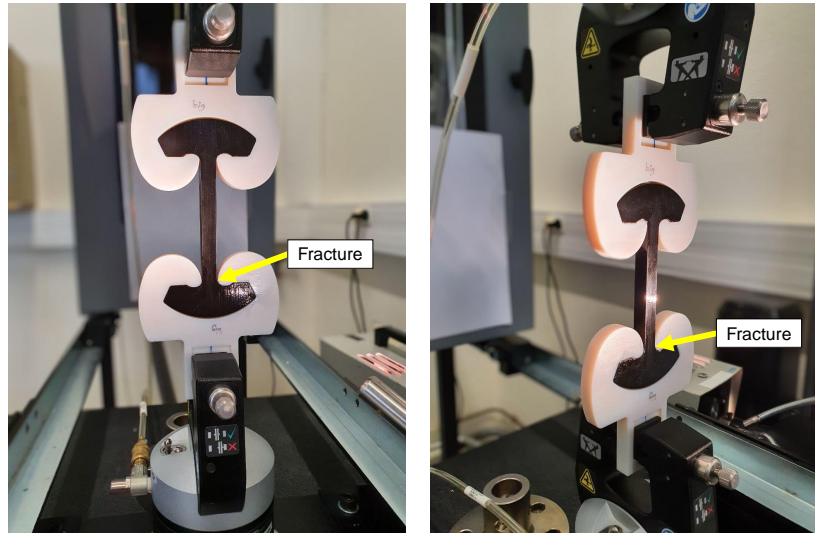


Figure 4.5: The tensile test on the second proposed geometry to assess the fracture point of the TangoBlack sample. The sample broke in the pointed section, where it gets in contact with the VeroWhite Plus grips.

predicted, the TangoBlack sample broke exactly at the line with the largest stress fields, indicated by yellow arrows. Consequently, one needs to revise the proposed geometry of TangoBlack in its middle part.

The discussed undesired fracture could be eliminated by avoiding a constant area cross-section. The stress concentration region of the TangoBlack sample must be moved from the contact point of VeroWhite Plus to the middle part of the specimen. The specimen geometry has subsequently been modified to incorporate a smooth curvature that gradually reduces the thickness of the sample to a constant value. However, this will result in an unavoidable increase in specimen length. Figures 4.6a,b represent the final virtually designed geometry and its corresponding 3D-printed part realized for the experiments. The geometry is subsequently simulated in Abaqus to assess the deformation and stress fields in the parts (Figure 4.6c). As expected, the smooth curvature has properly concentrated the stress in the middle, while the VeroWhite Plus grips exhibit minimal deformation. Additionally, the tensile test experiment verifies proper concentration at the middle part, where the specimen breaks (Figure 4.6d). This geometry is the final geometry configuration for all tensile test specimens throughout this study. The dimensions of the 3D-printed samples are provided in Figure 4.7. It is important to note that the length and the cross-section of the middle part of the specimen might differ depending on the experiment.¹ As a result, if a square cross-section is required, the out-of-plane thickness of the sample will also change. It is expected that out-of-plane deformation takes place in the top and bottom parts of small cross-sections if the thickness of the specimen is less than 6mm. For this reason, we have added two side plates that are screwed to

¹During this work, we will mention wherever there has been a change to the geometry.

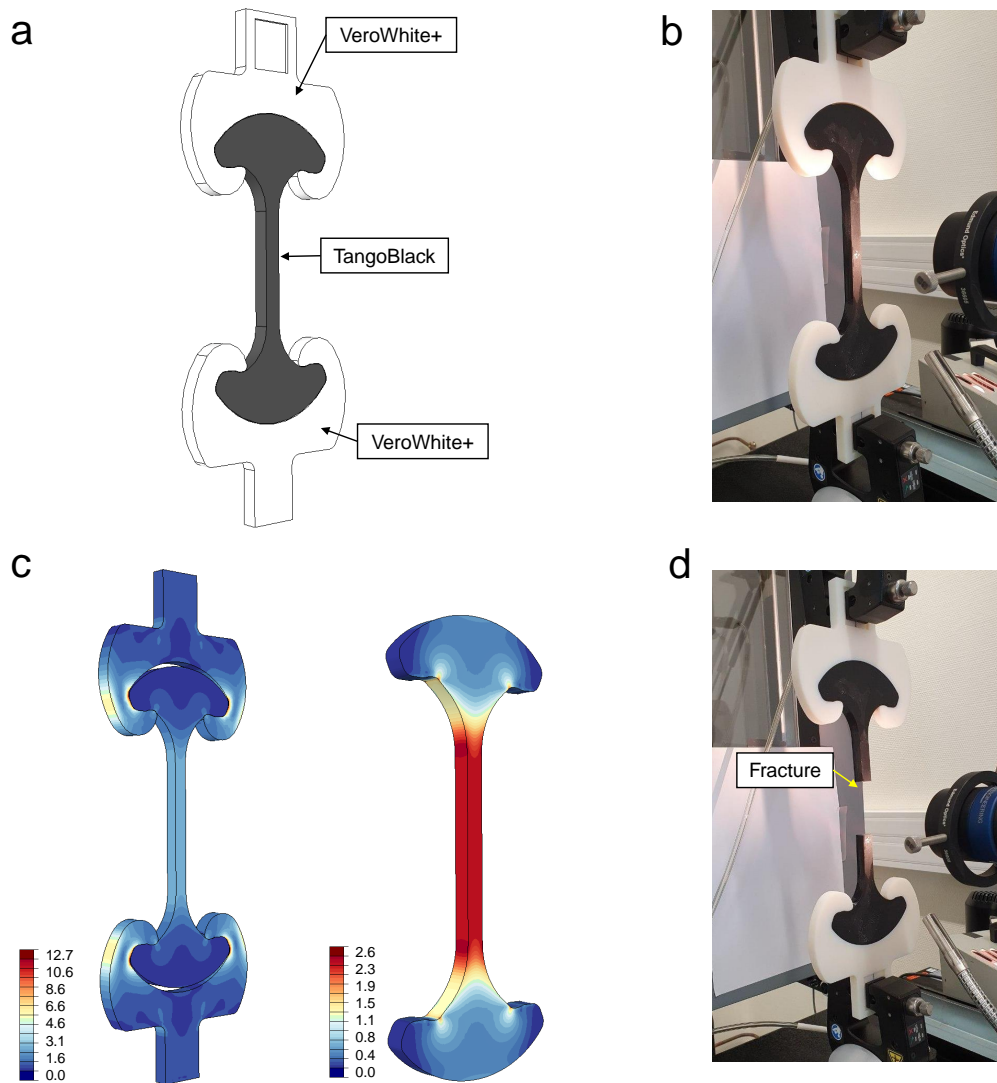


Figure 4.6: (a) The final I-shape design of the TangoBlack specimen with geometrically reinforced VeroWhite Plus grips. (b) The 3D-printed parts in the experimental setup. (c) The numerical simulation of the specimen under uni-axial tension and the corresponding stress field in the assembly of the parts and TangoBlack individually. (d) The TangoBlack specimen after the tensile test, broke in the middle part of the sample. The color bar indicates the von Mises stress field in MPa.

VeroWhite Plus parts in order to prevent the curved parts from buckling. Furthermore, this modification will reinforce VeroWhite Plus parts and prevent large deformations. It is worth mentioning that the thickness of the middle part of VeroWhite Plus will change depending on the thickness of the specimen. The entire assembly of the TangoBlack specimen and VeroWhite Plus parts is displayed in Figure 4.8. We note that the bottom plate can be in a different shape depending on the testing machine and loading cells.

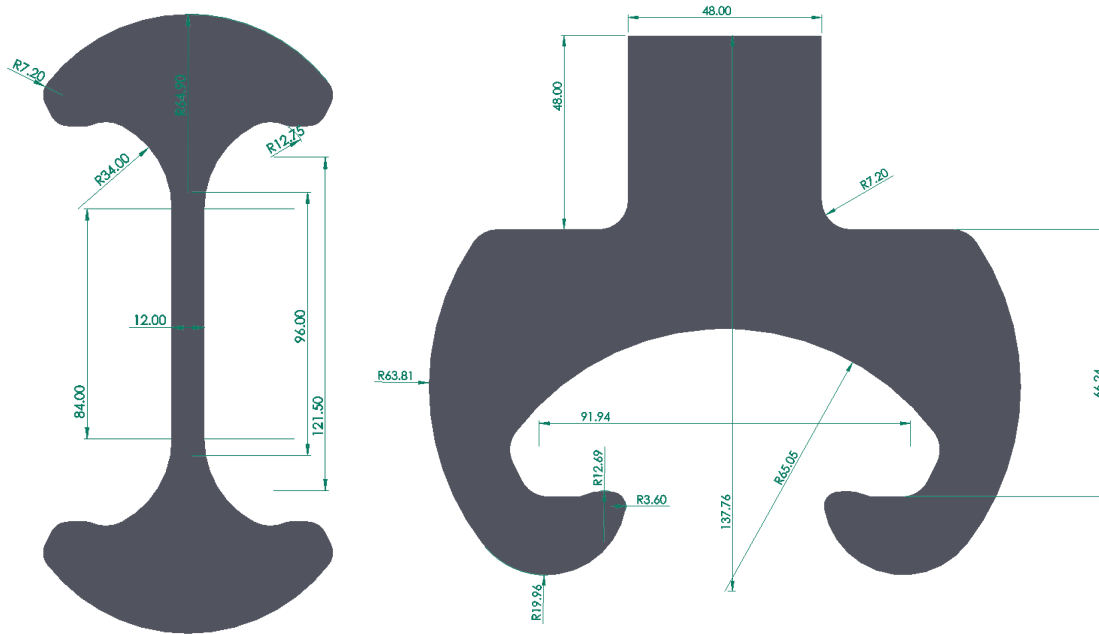


Figure 4.7: The dimensions of the 3D-printed TangoBlack and VeroWhite parts. All numbers are in mm units.

4.2.3 Testing protocol

The designed I-shape TangoBlack specimens are 3D-printed with TB FLX 973 and SUP705 as the main and support materials, respectively. Since SUP705 is not soluble in water, the 3D-printed samples have to be cleaned from the support material using a waterjet. This process requires careful handling to prevent material imperfections from causing early unexpected fractures in the test sample. As a result of these risks, we avoided cleaning the entire surface of several samples and left the support material intact in the uniform section of the sample. Subsequently, the 3D-printed I-shape TangoBlack specimens are subjected to uni-axial tension in a servo-hydraulic testing machine under displacement control. Depending on each test requirement, we used two different hydraulic tensile testing machines MTS 100kN and MTS 250kN. Their characteristics are listed in Table 4.2. As TangoBlack is a soft polymer, its load range is rather limited. Therefore, both machines are suitable in that aspect. However, there is a significant difference between the two machines, primarily due to the larger actuator maximum speed in MTS 100 kN, which is essential for testing specimens with large strain rates. Figure 4.9 shows the two tensile test machines and the details of the experimental setups. For the measurement of the force signal, two different load transducers with capacity 1500 ± 1.5 N and 200 ± 0.2 N are employed depending on the cross-section of the specimen. Specifically, the 200N transducer has been used in the relaxation testing, where the relaxed force is too small to be captured by a 1500N load cell.

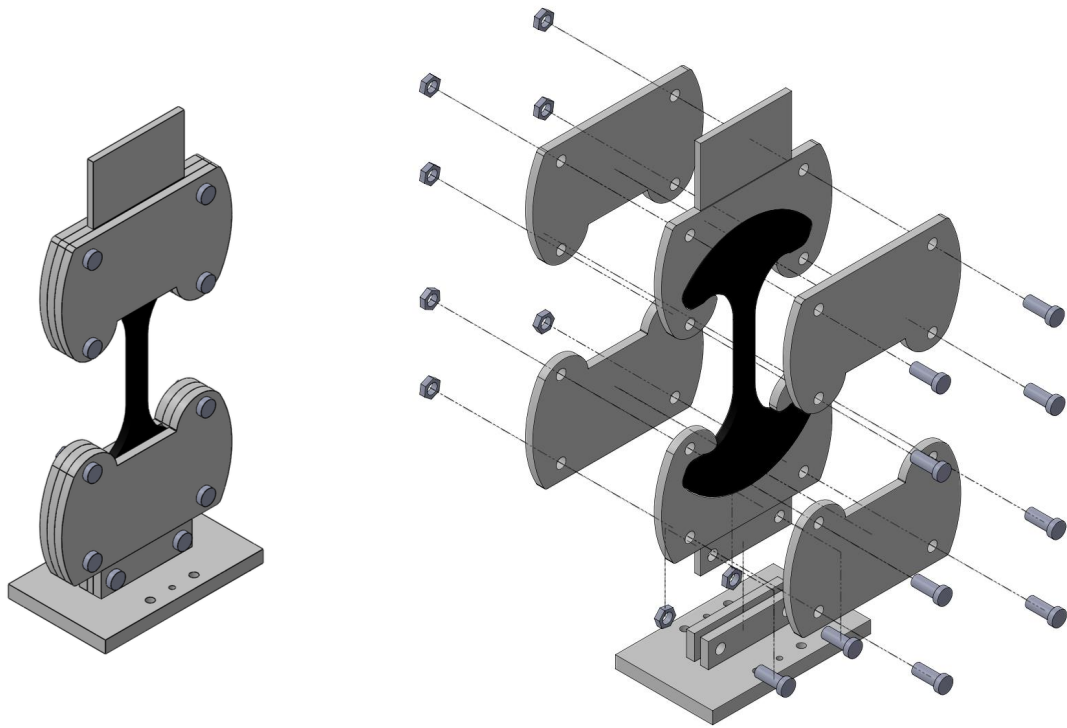


Figure 4.8: The assembly of the final experimental setup consisting of different parts. Two side plates are screwed to VeroWhite Plus parts in order to prevent the curved parts from buckling when the cross-section of the specimen is small.

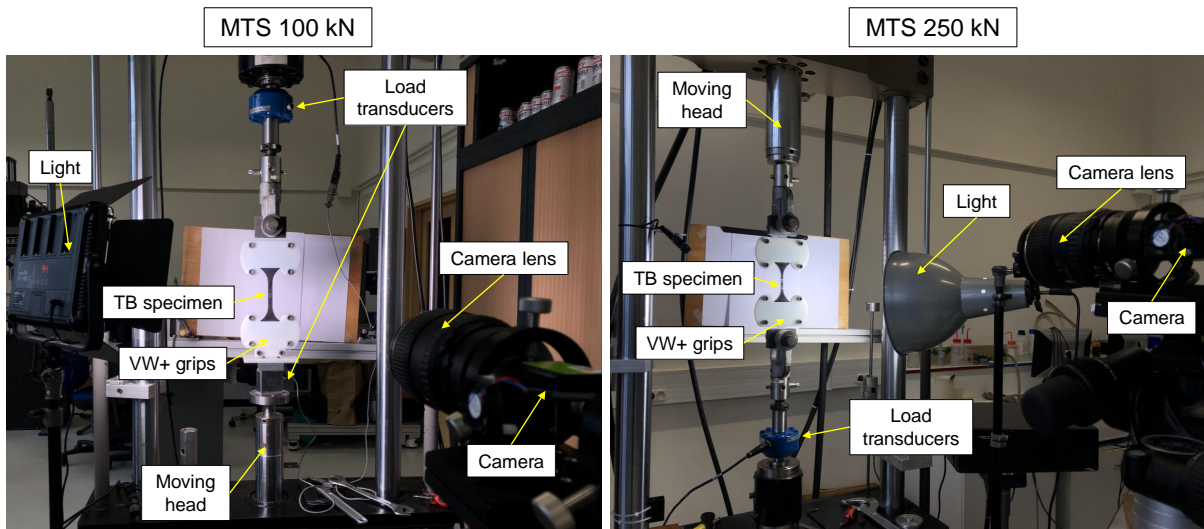


Figure 4.9: Tensile test setups with two different tensile testing machines MTS 100 kN (on the left side) and MTS 250 kN (on the right side).

	MTS 100kN	MTS 250kN
Load capacity	± 100 kN	± 250 kN
stroke range	± 100 mm	± 80 mm
Actuator maximum speed	± 100 mm \cdot s ⁻¹	± 30 mm \cdot s ⁻¹

Table 4.2: Characteristics of the MTS tensile testing machines.

4.2.4 Optical strain measurement

An optical strain measurement method by point tracking is employed to perform a complete strain measurement. In contrast to strain gages and extensometers, optical strain measurement reveals more details about deformation and is more suitable for materials that are soft, easy to deform, and tested at high strain rates. In this study, the deformation of the test specimen is tracked by a high-resolution camera (Figure 4.9), while a sequence of pictures is captured at a specific time interval that depends on the strain rate. The changes in the recorded pictures are then analyzed to accurately measure the local strain and displacement fields. The longitudinal and transverse strains are calculated by measuring the deformation of four white dots placed in the middle part of the uniform section. The white color on the black surface of TangoBlack provides sufficient contrast for tracking points. Also, a white background behind the test specimen is placed to assist image processing (Figure 4.9). Figure 4.10a shows the arrangement of the four dots in a real image of the test sample. The block of pixels in the red box is tracked during deformation and their distance is calculated by means of the Software *Sylvie IC*. When transverse strain is not required or the thickness of the sample is very thin, one can place only two points to measure only the longitudinal strain (Figure 4.10b). In some cases, however, tracking of the points may not succeed due to the large deformation of the specimen. This has also been observed at high strain rates, where the deformation is faster than the frequency of image capture. Therefore, we have used two parallel white lines called calipers, to measure the axial deformation of the sample (Figure 4.10c). This has significantly improved the range of image tracking. It should be noted that due to the rapid deformation of the specimen at high strain rates, automatic image tracking cannot be performed and it must be carried out manually.

4.2.5 Tensile test and high strain rates deformations

We conducted several tensile tests on 3D-printed TangoBlack I-shape geometry at different strain rates in order to characterize its dependence on strain rate. The tensile tests are conducted until the sample fails. A smaller cross-section 3×6 mm² is employed to further concentrate the stress in the middle part of the sample. Moreover, the length of the uniform section of the test specimen has been shortened to achieve higher strain rates. Figure 4.11 shows the modified I-shaped geometries with two different lengths used in the tensile tests. Due to the shape complexity of the tensile test specimens, obtaining the gage length is not straightforward. Therefore, the effective length of the specimens

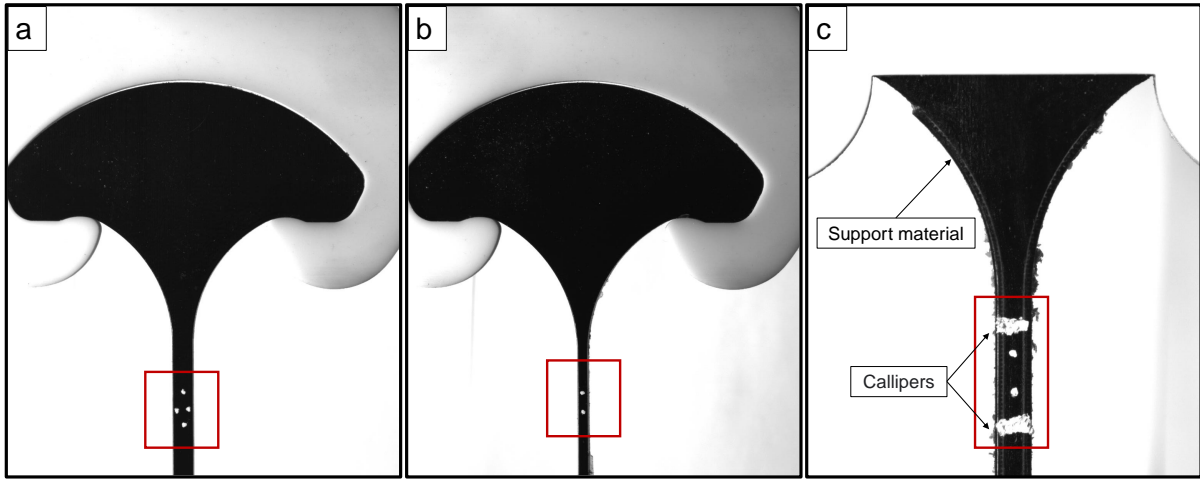


Figure 4.10: The optical strain measurement method by point tracking employed to measure the local strain fields. (a) The longitudinal and transverse strain measurements by means of four white dots. (b) The longitudinal strain measured by only two white dots. (c) Using the callipers to measure the strain in the large deformations and high strain rates, where the tracking by points becomes difficult.

has been determined by dividing the displacement rate by the measured strain rate. As a result, for each specimen geometry, a constant effective length has been obtained at all strain rates. The effective lengths of the tensile samples 1 and 2 in Figure 4.11 correspond to 78 mm and 45 mm.

Sample 1 was initially tested in the tensile test machine MTS 250 kN with a maximum strain rate of $0.4s^{-1}$. The same sample has been then tested in the MTS 100 kN tensile machine with a larger maximum displacement rate equivalent to 100 mm s^{-1} . As a result, the maximum strain rate has been increased to $1.3s^{-1}$. We have further increased the strain rate by reducing the effective length of sample 1 and modifying it to sample 2 with an effective length of 45 mm. This has enabled us to reach a strain rate of $2.2s^{-1}$, which is the limit of the strain rate that could be accomplished with our available equipment. Moreover, moving to larger strain values will lead to a nonlinear increase in the strain, due to the dynamic effects during the deformation process. A slight nonlinearity has also been observed in the large strain rates performed in this study.

Figure 4.12 shows the results of tensile tests at different strain rates until failure². Throughout this work, stress is defined as the reaction force divided by the unstressed cross-section area of the specimen (unless it is mentioned). In the same manner, strain is defined as the increase in the distance between two defined points in the optical strain measurement method divided by their initial distance when the specimen is unstressed. The stress-strain response and the elongation at break show a strong rate-dependent

²We note that for visualization reasons, all tested strain rates are not displayed in this figure. These results will be further used in the fracture analysis in Section 4.2.9.

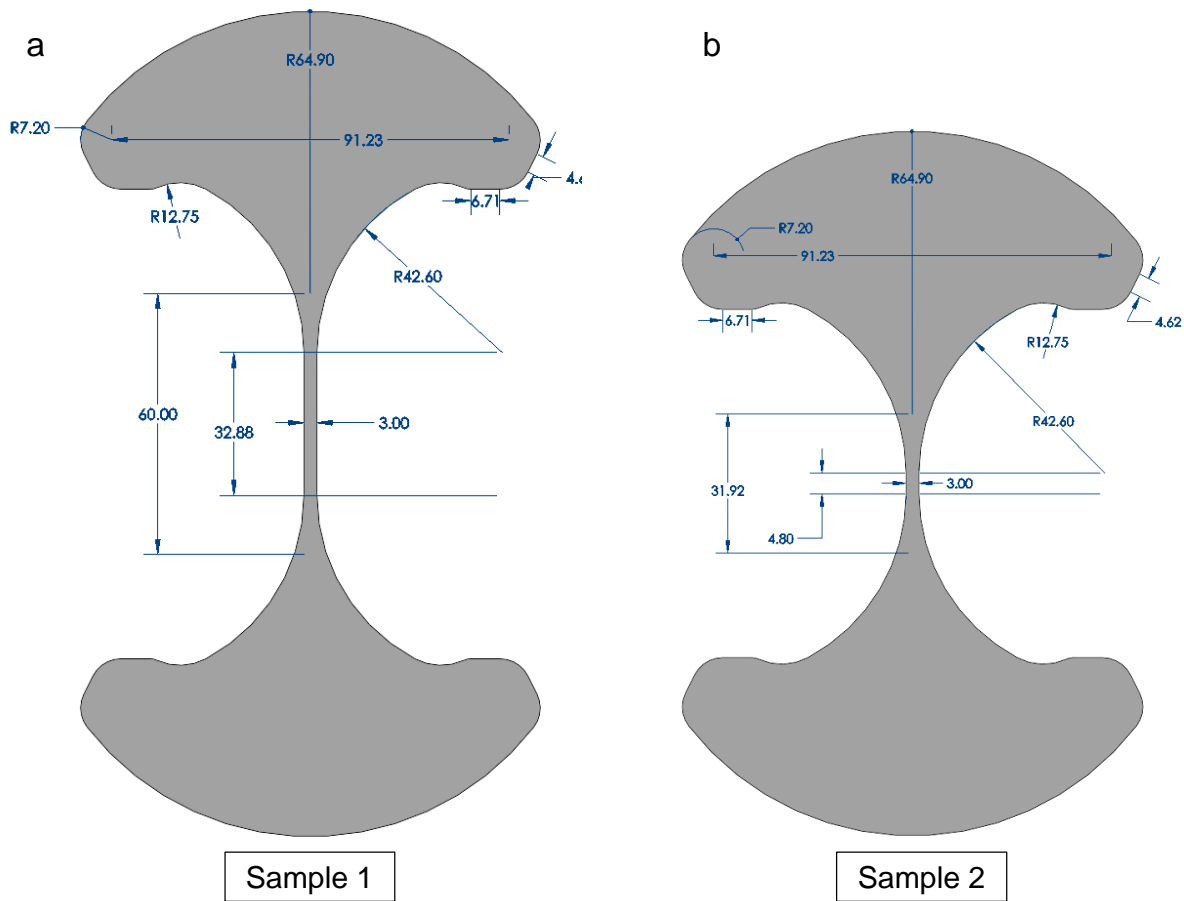


Figure 4.11: Dimensions of the specimens used in the tensile tests. The measured effective length of samples 1 and 2 corresponds to 78 mm and 45 mm, respectively. The out-of-plane thickness of both samples is 6mm.

behavior. From the inset of Figure 4.12, we observe that as the strain rate increases, the initial slope of the curves, which corresponds to material stiffness, increases at low strain rates (less than 1%). The Young's modulus of the material at different strain rates can now be assessed by calculating the initial slopes. Also, the Poisson's ratio can be obtained by the ratio of the transverse and axial strains. These values at different strain rates are listed in Table 4.3. It can be observed that the material tends to be more compressible as we increase the strain rates. In contrast, the material shows an almost incompressible behavior in very small strain rates $10^{-4} s^{-1}$. It should be noted that as the Young's modulus strongly depends on strain rates, one must be cautious when reporting the properties of this material and the loading rate must be taken into consideration. At large strains, the material response becomes non-linear with a similar dependency on the strain rate. However, due to the nonlinear behavior, the curves might overlap each other and might not necessarily show a stiffer response as the strain rate is increased in

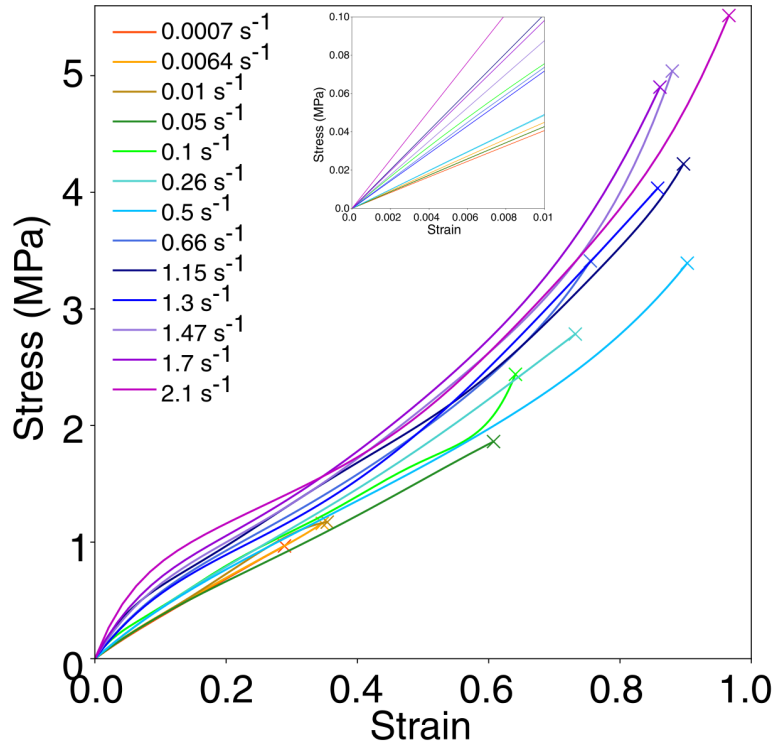


Figure 4.12: Tensile experiments results for TangoBlack at different strain rates 0.0007 - 2.1 s^{-1} until failure. The \times shows the breaking point of the sample. Inset shows the initial slope of the curves at different strain rates until 1% strain. Stress values correspond to engineering or first Piola-Kirchhoff stresses, and strain values correspond to engineering strains.

a consecutive manner. Instead, the global tenacity of the response indicates that higher strain rates result in greater stiffness and elongation at break.

Strain rate (s^{-1})	Young's modulus (MPa)	Poisson's ratio
10^{-1}	4.1	0.46
10^{-2}	4.007	0.4766
10^{-3}	3.914	0.4879
10^{-4}	3.818	0.4956

Table 4.3: The Young's modulus and Poisson's ratio of TangoBlack FLX 973 at different strain rates.

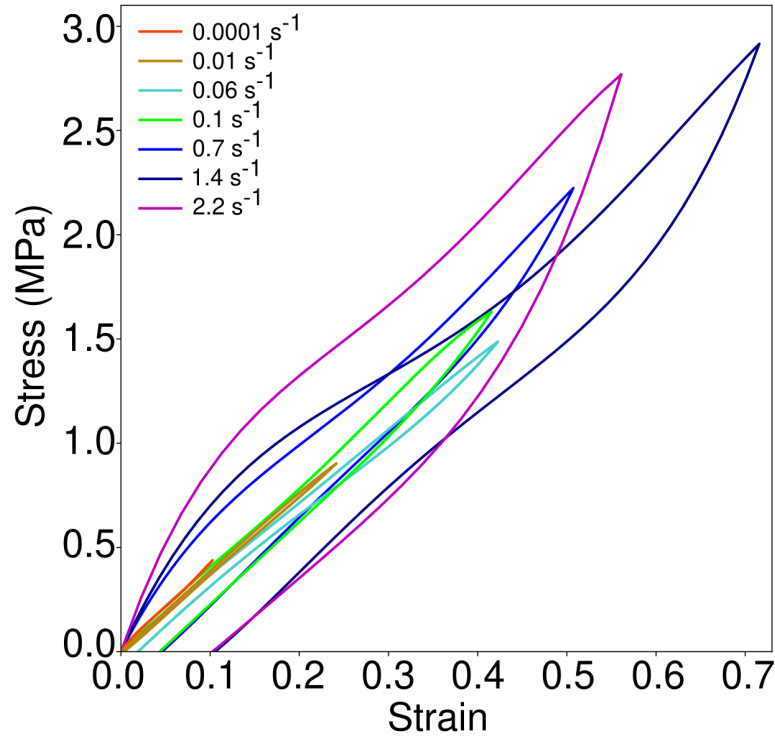


Figure 4.13: Loading-unloading tests at various strain rates: 0.0001 s^{-1} , 0.01 s^{-1} , 0.06 s^{-1} , 0.1 s^{-1} , 0.7 s^{-1} , 1.4 s^{-1} , 2.2 s^{-1} . The specimen is unloaded just before the ultimate stress at each strain rate is reached. Stress values correspond to engineering or first Piola-Kirchhoff stresses, and strain values correspond to engineering strains.

4.2.6 Loading-Unloading and cyclic tensile tests

The ultimate tensile stress at the break of a material at each strain rate represents the maximum stress that it can withstand at a given strain rate. Based on this data, we have performed loading-unloading and cyclic tests at constant strain rates so that unloading occurs just before the ultimate tensile stress is reached. The results of these tests are essential to characterize the viscoelastic properties of TangoBlack since they represent the rate-dependent behavior of the material. Figure 4.13 shows the results of the loading-unloading tests in terms of nominal stress as a function of nominal strain. The tests have been carried out on TangoBlack specimens with the geometry of sample 2 (Figure 4.11) at different strain rates ranging from 0.0001 s^{-1} to 2.2 s^{-1} . The results demonstrate a clear rate-dependent highly nonlinear behavior of the material where the nonlinearity increases at higher strain rates. Although TangoBlack material is considered a soft polymer, rather high strain rates (greater than 0.1 s^{-1}) are required to reveal its dissipative behavior. The results of the strain rates in this range clearly indicate the presence of a hysteresis loop as well as a permanent unrecovered deformation after full unloading. The

results of low strain rates (0.0001 s^{-1} and 0.01 s^{-1}) on the other hand, show almost no dissipation and residual strain. Furthermore, as the strain rate increases, the amount of dissipated energy corresponding to the hysteresis curve area increases. We note that some of these experimental data will be used in Section 4.2.8 to identify the material modeling of TangoBlack.

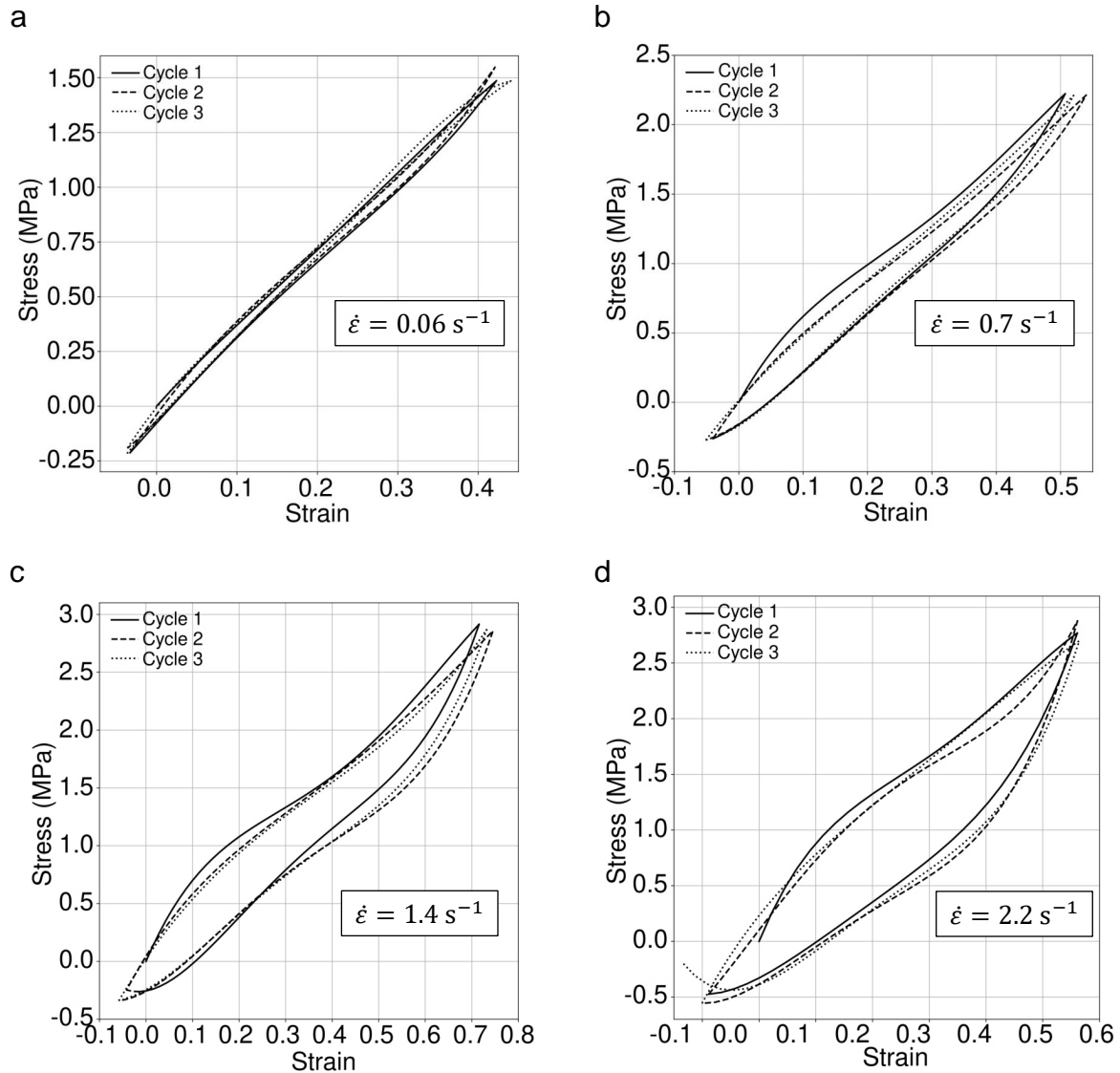


Figure 4.14: Cyclic loading-unloading tests with three cycles at various strain rates: (a) 0.06 s^{-1} , (b) 0.7 s^{-1} , (c) 1.4 s^{-1} , (d) 2.2 s^{-1} . The specimen is unloaded just before the ultimate stress of each strain rate is reached, whereas the re-loading started upon achieving zero displacement. Stress values correspond to engineering or first Piola-Kirchhoff stresses, and strain values correspond to engineering strains.

In order to further investigate the dissipative behavior of TangoBlack, we conducted cyclic loading-unloading tests with three cycles at a constant strain rate such that the unloading occurred prior to the ultimate tensile stress being reached and the re-loading started upon achieving zero displacements. Figures 4.14a-d represent the results of the cyclic loading with three cycles at four different strain rates 0.06 s^{-1} , 0.7 s^{-1} , 1.4 s^{-1} and 2.2 s^{-1} . Clearly, as the strain rate increases, the hysteresis loop area increases, which is consistent with the loading-unloading results. The hysteresis loop at strain rate 0.06 s^{-1} indicates very small dissipation and almost 2% residual strain with a more linear-like behavior (Figure 4.14). Contrary to this, as we increase the strain rate, a more non-linear dissipative loop is obtained with a larger residual strain. Specifically, at a constant strain rate, the area of the hysteresis loop slightly increases with the number of loading-unloading cycles. Nonetheless, the amount of the residual strain remained almost unchanged as we repeated the cycles. It is important to note that there exists a compressive strain corresponding to the negative of the residual strain as we unload the specimen to the zero displacement position. This also indicates that the specimen in a stress-free state is significantly elongated.

4.2.7 Single-step Relaxation tests

In order to observe the time-dependent viscous behavior of TangoBlack, we conducted single-step relaxation tests at various strain rates and levels. Initially, the experiments were performed on sample 2 in Figure 4.11 with an effective length of 45 mm. However, due to its small cross-section, the detected force after relaxation contains a significant amount of noise, which makes the data difficult to interpret. Therefore, we first used a more sensitive load transducer with a capacity of $200 \pm 0.2N$. Then, we modified the uniform section of the specimen geometry to enlarge the cross-section area from $3 \times 6 \text{ mm}^2$ to $12 \times 6 \text{ mm}^2$ (Sample 3 in Figure 4.15). Although this modification has notably cleaned the detected force data, the measured local strain of the sample reveals a slight nonlinear deviation upon relaxation initiation, where the strain is assumed to be constant. Figure 4.16 shows the experimentally measured strain at a relaxation test performed at 20% strain level on the specimen with sample 3 geometry that is primarily stretched with a constant strain rate 0.83 s^{-1} . It can be observed that there is an initial small increase followed by an immediate decay toward the imposed strain value. Such a deviation could be either due to the sample configuration, the movement of the grips, or the inertial effect because of the large size and mass of the specimen. Nevertheless, it will vanish as we move to lower strain rates and it has never exceeded 1% of the strain. In order to eliminate the deviation, we modified the specimen geometry to a dog-bone configuration with ASTM D638 Type IV standard dimensions. In this case, it is permissible to use this geometry since we are only concerned with the relaxation properties and not the ultimate properties. Thus, the range of force and deformation remains rather small and the specimen will not be exposed to the risk of unexpected fracture or slip. Figure 4.15b shows the dimension of the specimen denoted with Sample 4 with an effective length of 55

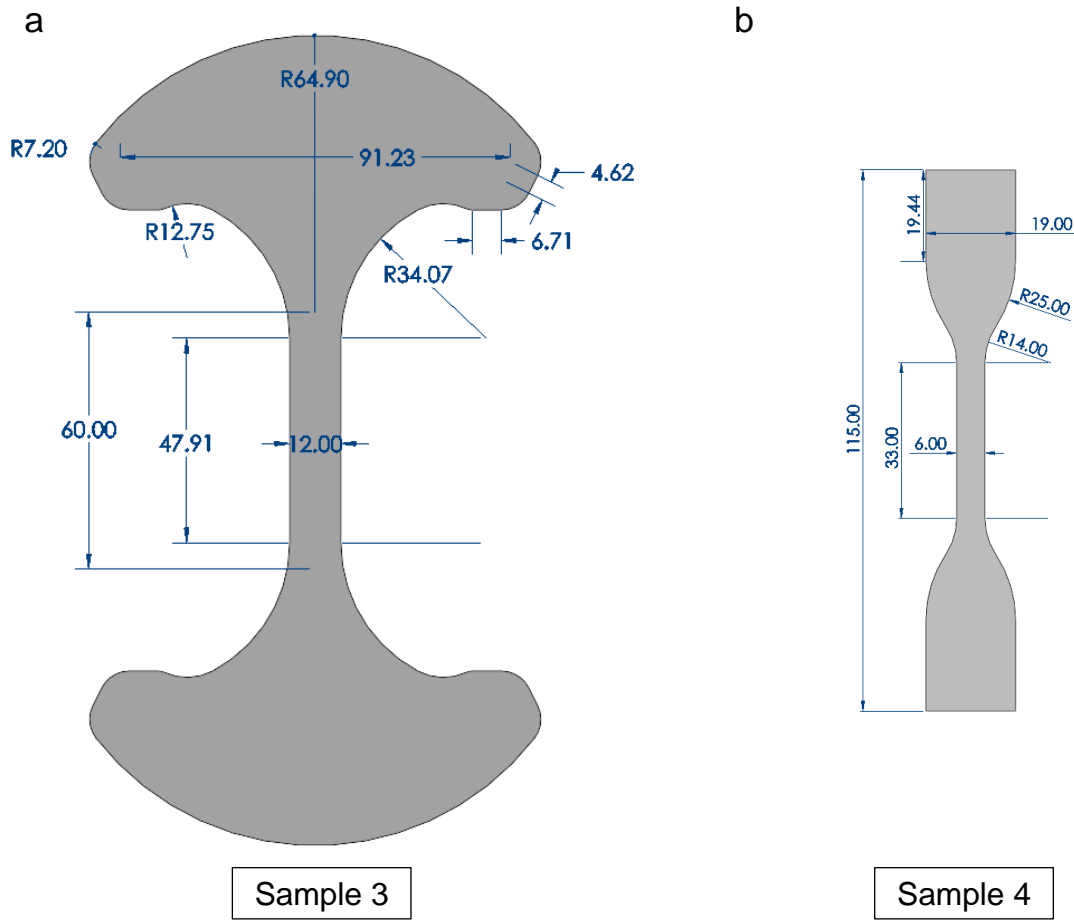


Figure 4.15: The dimensions of the specimens used in the relaxation tests. The measured effective length of samples 3 and 4 corresponds to 120 mm and 55 mm, respectively. In sample 3, the out of plane thickness is 6mm, whereas in sample 4, it is 3.3mm.

mm and an out-of-plane thickness of 3.3 mm. In order to perform the experimental test, the sample has been held between two parallel gripes with a distance of 3 mm to ensure the same fixation force was applied to both sides of the sample. As a result of several relaxation tests carried out on this geometry, we observed that either there is no deviation or that it is of a very small magnitude. In Figure 4.16, the dashed line corresponds to the typical strain curve obtained in the relaxation test on sample 4.

The discussed geometries have been subsequently subjected to relaxation tests at different strain rates and values. In relaxation tests, the specimen was initially deformed at a constant strain rate and subsequently held at a constant strain value until the equilibrium or time-independent stress was achieved. Figures 4.17a-d show the results of the relaxation tests at different loading strain rates 0.02 s^{-1} , 0.1 s^{-1} , 0.83 s^{-1} and 2.2 s^{-1} . For all performed tests, we measured the stress values for 30 minutes after relaxation initiation.

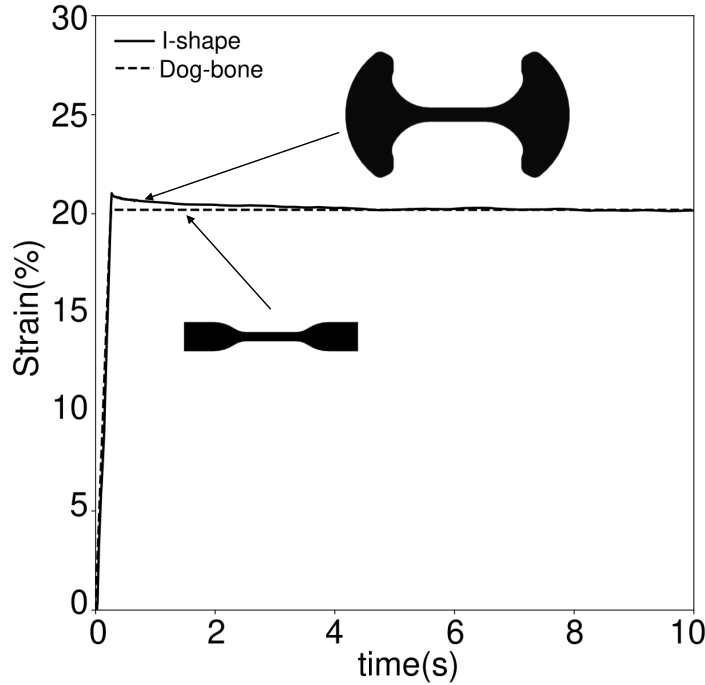


Figure 4.16: Nominal strain as a function of time during the relaxation test performed on a TangoBlack specimen with the geometry of sample 3. The dashed line indicates the expected strain curve from the dog-bone geometry with the dimension of sample 4.

However, the stress value converges rapidly before almost 50 seconds, which is a considerably short time compared to other existing viscous polymers and has added difficulties to the experimental measurements. Here, for illustrative reasons, we present the results for the first 350 or 400 seconds. At each strain rate, the specimen is tested at different strain levels. The inset figures indicate the variation in strain values over time for each strain rate. We note that the time in the inset figure differs from the relaxation time, which corresponds to the time after the strain is kept constant. Defining the overstress as the difference between the current and equilibrium stresses (Hossain et al., 2012), we observe that higher strain rates result in larger overstresses as compared to those at lower strain rates. As an example, a very small overstress of less than 20 kPa is observed at the strain rate 0.02 s^{-1} (Figure 4.17a), whereas at 2.2 s^{-1} , the maximum overstresses correspond to 100 kPa (Figure 4.17d). Furthermore, as expected from the material viscosity, the comparison between the results at a constant strain rate and various strain values indicates that higher strain values lead to larger overstress and equilibrium stress. Finally, the occurrence of fracture in the relaxation tests will be discussed in Section 4.2.10.

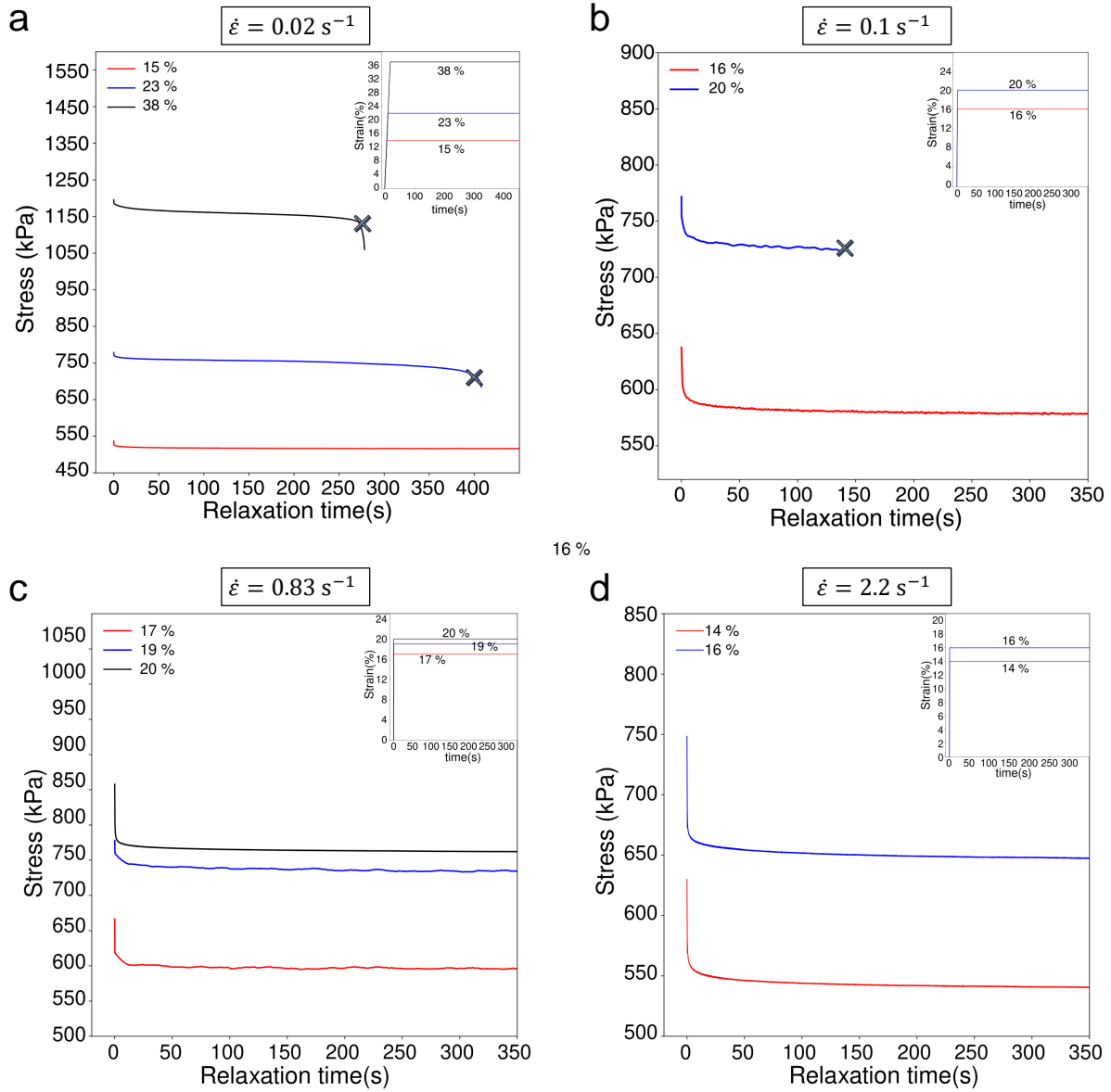


Figure 4.17: Single-step relaxation tests at different strain rates and levels: (a) Strain rate= 0.02s^{-1} tested at 14%, 22% and 37% strain levels. (b) Strain rate= 0.1s^{-1} tested at 15% and 19.6% strain levels. (c) Strain rate= 0.83s^{-1} tested at 17%, 19% and 20% strain levels. (d) Strain rate= 2.2s^{-1} tested at 14% and 16% strain levels. The \times shows the break point of the sample. Stress values correspond to engineering or first Piola-Kirchhoff stresses, and strain values correspond to engineering strains.

4.2.8 Constitutive modeling of viscoelastic behavior of TangoBlack

By using the experimental data obtained in the previous sections, this section characterizes the TangoBlack material using viscous hyperelastic models. Since TangoBlack exhibits almost incompressible behavior, it can be identified using incompressible hyperelastic models. However, due to the nonlinearity of the TangoBlack response (especially at large strain rates), simple hyperelastic models such as the incompressible Neo-Hookean model are unable to model its response. Specifically, we observed that the Neo-Hookean incompressible model fails to model the strong nonlinearity of TangoBlack, especially when there is a hardening in the material response. Consequently, higher-order energy functions are necessary to be employed in material modeling.

General constitutive relations

We have used the rubber viscoelastic model for incompressible isotropic elastomers that is proposed by [Kumar and Lopez-Pamies \(2016\)](#) and is obtained by using the two-potential constitutive framework. In the following, we provide a brief overview of the main equations in the model that they proposed. Considering that \mathbf{F} denotes the deformation gradient tensor as described in Section 3.1, the total deformation \mathbf{F} can be decomposed into the dissipative part of the deformation \mathbf{F}^v and the elastic/non-dissipative part of the deformation \mathbf{F}^e such that $\mathbf{F} = \mathbf{F}^e \mathbf{F}^v$. Subsequently, based on the two-potential framework, the stored and dissipated energy of the material are described using the free energy function ψ and the dissipation potential ϕ , respectively. The free energy function ψ is decomposed into the equilibrium ψ^{Eq} and non-equilibrium ψ^{NEq} parts, where the equilibrium part is associated with the thermodynamic equilibrium states, while the non-equilibrium part serves to provide additional energy storage at non-equilibrium states. Representing these terms as a function of the deformation gradient tensor provides the following form

$$\psi = \psi^{\text{Eq}}(\mathbf{F}) + \psi^{\text{NEq}}(\mathbf{F}\mathbf{F}^{v-1}) \quad \text{and} \quad \phi = \phi(\mathbf{F}, \mathbf{F}^v, \dot{\mathbf{F}}^v), \quad (4.1)$$

which implies that the dependence of ψ^{NEq} on \mathbf{F}^v is only through $\mathbf{F}^e = \mathbf{F}\mathbf{F}^{v-1}$. Following these expressions, we can obtain the constitutive relation implied by these potentials as shown in the following two coupled equations

$$\mathbf{S} = \frac{\partial \psi^{\text{Eq}}}{\partial \mathbf{F}}(\mathbf{F}) + \frac{\partial \psi^{\text{NEq}}}{\partial \mathbf{F}}(\mathbf{F}\mathbf{F}^{v-1}) \quad \text{and} \quad \frac{\partial \psi^{\text{NEq}}}{\partial \mathbf{F}^v}(\mathbf{F}\mathbf{F}^{v-1}) + \frac{\partial \phi}{\partial \dot{\mathbf{F}}^v}(\mathbf{F}, \mathbf{F}^v, \dot{\mathbf{F}}^v) = 0, \quad (4.2)$$

where \mathbf{S} represent the first Piola-Kirchhoff stress tensor. [Kumar and Lopez-Pamies \(2016\)](#) characterized the equilibrium and non-equilibrium free energy functions for isotropic incompressible elastomers in the following form.

$$\psi^{\text{Eq}}(\mathbf{F}) = \begin{cases} \frac{3^{1-\alpha_1}}{2\alpha_1}\mu_1[I_1^{\alpha_1} - 3^{\alpha_1}] + \frac{3^{1-\alpha_2}}{2\alpha_2}\mu_2[I_1^{\alpha_2} - 3^{\alpha_2}] & \text{if } J = 1 \\ +\infty & \text{otherwise} \end{cases} \quad (4.3)$$

$$\psi^{\text{NEq}}(\mathbf{F}^e) = \begin{cases} \frac{3^{1-a_1}}{2a_1}m_1[I_1^{a_1} - 3^{a_1}] + \frac{3^{1-a_2}}{2a_2}m_2[I_1^{a_2} - 3^{a_2}] & \text{if } J = 1 \\ +\infty & \text{otherwise} \end{cases} \quad (4.4)$$

where $I_1 = \text{tr}\mathbf{C}$ and $J = \sqrt{\det\mathbf{C}} = \det\mathbf{F}$ are the first and third principal invariants of the right Cauchy-Green deformation tensor $\mathbf{C} = \mathbf{F}^T\mathbf{F}$. In addition, $\mu_r, \alpha_r, m_r, a_r$ ($r = 1, 2$) are the material parameters to be identified. Using the equation (4.2), the Piola-Kirchhoff stress tensor is

$$\mathbf{S} = \left[\sum_{r=1}^2 3^{1-\alpha_r} \mu_r I_1^{\alpha_r-1} \right] \mathbf{F} + \left[\sum_{r=1}^2 3^{1-a_r} m_r (\mathbf{C} \cdot \mathbf{C}^{\mathbf{v}-1})^{a_r-1} \right] \mathbf{F}\mathbf{C}^{\mathbf{v}-1} - p\mathbf{F}^{-T}, \quad (4.5)$$

where $\mathbf{C}^{\mathbf{v}} = \mathbf{F}^{\mathbf{v}T}\mathbf{F}^{\mathbf{v}}$ and p is the hydrostatic pressure associated with the incompressibility constraint $J = \det\mathbf{F} = 1$. Subsequently, since the dissipation potential ϕ is a non-negative function and convex in $\dot{\mathbf{F}}^{\mathbf{v}}$, it could be written as

$$\phi(\mathbf{F}, \mathbf{F}^{\mathbf{v}}, \dot{\mathbf{F}}^{\mathbf{v}}) = \frac{1}{2} \tilde{\Gamma}^{\mathbf{v}} \cdot \mathcal{A}(\mathbf{F}, \mathbf{F}^e) \tilde{\Gamma}^{\mathbf{v}}, \quad (4.6)$$

where $\tilde{\Gamma}^{\mathbf{v}}$ and $\mathcal{A}_{ijkl}(\mathbf{F}, \mathbf{F}^e)$ are

$$\tilde{\Gamma}^{\mathbf{v}} = \mathbf{F}^e \Gamma^{\mathbf{v}} \mathbf{F}^{e-1}, \quad \Gamma^{\mathbf{v}} = \dot{\mathbf{F}}^{\mathbf{v}} \mathbf{F}^{\mathbf{v}-1}, \quad (4.7)$$

$$\mathcal{A}_{ijkl}(\mathbf{F}, \mathbf{F}^e) = \eta_K [\mathcal{K}_{ijkl} + \mathcal{K}_{ijmn} \mathbf{F}_{mp}^e \mathbf{F}_{lp}^e \mathbf{F}_{qn}^{e-1} \mathbf{F}_{qk}^{e-1}] + 3\eta_J \mathcal{J}_{ijkl}. \quad (4.8)$$

It should be noted that \mathcal{A} has been represented by the isotropy and material frame indifference conditions. The \mathcal{K} and \mathcal{J} are the orthogonal projection tensors. The parameters η_k and η_J are defined by the following relations

$$\eta_K(I_1^e, I_2^e, I_1^{\mathbf{v}}) = \eta_\infty + \frac{\eta_0 - \eta_\infty + K_1 [I_1^{\mathbf{v}\beta_1} - 3^{\beta_1}]}{1 + (K_2 J_2^{NEq})^{\beta_2}}, \quad (4.9)$$

$$J_2^{NEq} = \left(\frac{I_1^e}{3} - I_2^e \right) \left(\sum_{r=1}^2 3^{1-a_r} m_r I_1^{e a_r - 1} \right)^2, \quad (4.10)$$

where $I_1^e = \text{tr} \mathbf{C}^e$, $I_2^e = 1/2[(\text{tr} \mathbf{C}^e)^2 - \text{tr} \mathbf{C}^{e2}]$ and $I_1^v = \text{tr} \mathbf{B}^v$. Here \mathbf{B}^v is the left Cauchy-Green viscous deformation tensor defined as $\mathbf{B}^v = \mathbf{F}^v \mathbf{F}^{vT}$. The parameters $\eta_\infty, \eta_0, K_1, K_2, \beta_1, \beta_2$ are also the material parameters to be identified by the experimental data. Substituting the above relations into the evolution equation on the right hand side of (4.2) leads to the following ODE equation.

$$\dot{\mathbf{C}}^v = \frac{\sum_{r=1}^2 3^{1-a_r} m_r (\mathbf{C} \cdot \mathbf{C}^{v-1})^{a_r - 1}}{\eta_k} \left(\mathbf{C} - \frac{1}{3} (\mathbf{C} \cdot \mathbf{C}^{v-1}) \mathbf{C}^v \right). \quad (4.11)$$

Constitutive relations for a uni-axial tensile test

Since all the tests performed on TangoBlack in this study are of uni-axial type, we focus our attention on the uni-axial boundary conditions. The developed constitutive relations now can be formulated for one-dimensional loading. A uni-axial tension test is characterized by the specimen elongating only in one direction, whereas the other two directions are free to move. In this case, the principal stretches λ_1, λ_2 and λ_3 are related by the incompressibility constraint $\det \mathbf{F} = \lambda_1 \lambda_2 \lambda_3 = 1$. Considering that the loading is applied in the $\lambda_3 = \lambda$ direction, the deformation gradient tensors \mathbf{F} and \mathbf{F}^v then become

$$\mathbf{F} = \begin{bmatrix} \lambda^{-1/2} & 0 & 0 \\ 0 & \lambda^{-1/2} & 0 \\ 0 & 0 & \lambda \end{bmatrix}, \quad \mathbf{F}^v = \begin{bmatrix} \lambda_v^{-1/2} & 0 & 0 \\ 0 & \lambda_v^{-1/2} & 0 \\ 0 & 0 & \lambda_v \end{bmatrix}. \quad (4.12)$$

We note that, in the case of uni-axial tension, all the components of the stress tensor \mathbf{S} except S_{33} are zero. By substituting the tensors \mathbf{F} and \mathbf{F}^v into the equations (4.5) and (4.11), the following relations are obtained for the first Piola-Kirchhoff stress tensor and the differential equation.

$$S_{33} = \left[\sum_{r=1}^2 3^{1-a_r} \mu_r \left(\frac{2}{\lambda} + \lambda^2 \right)^{a_r - 1} \right] \left[\lambda - \frac{1}{\lambda^2} \right] + \left[\sum_{r=1}^2 3^{1-a_r} m_r \left(\frac{2\lambda_v}{\lambda} + \frac{\lambda^2}{\lambda_v^2} \right)^{a_r - 1} \right] \left[\frac{\lambda}{\lambda_v^2} - \frac{\lambda_v}{\lambda^2} \right], \quad (4.13)$$

$$\dot{\lambda}_{\mathbf{v}} = \frac{\sum_{r=1}^2 3^{1-a_r} m_r \left(\frac{2\lambda_{\mathbf{v}}}{\lambda} + \frac{\lambda^2}{\lambda_{\mathbf{v}}^2} \right)^{a_r-1}}{3\eta_k} \left[\frac{\lambda^2}{\lambda_{\mathbf{v}}} - \frac{\lambda_{\mathbf{v}}^2}{\lambda} \right], \quad (4.14)$$

where

$$\eta_k = \eta_{\infty} + \frac{\eta_0 - \eta_{\infty} + K_1 \left[\left(\frac{2}{\lambda_{\mathbf{v}}} + \lambda_{\mathbf{v}}^2 \right)^{\beta_1} - 3^{\beta_1} \right]}{1 + \left[K_2 J_2^{NEq} \right]^{\beta_2}}, \quad (4.15)$$

and

$$J_2^{NEq} = \frac{1}{3} \left[\frac{\lambda_{\mathbf{v}}}{\lambda} - \frac{\lambda^2}{\lambda_{\mathbf{v}}^2} \right]^2 \left[\sum_{r=1}^2 3^{1-a_r} m_r \left(\frac{2\lambda_{\mathbf{v}}}{\lambda} + \frac{\lambda^2}{\lambda_{\mathbf{v}}^2} \right)^{a_r-1} \right]^2. \quad (4.16)$$

$\mu_1(\text{MPa})$	$\mu_2(\text{MPa})$	α_1	α_2	$m_1(\text{MPa})$	$m_2(\text{MPa})$	a_1
0.6258	0.6258	2.3664	2.3668	0.3628	0.3627	-1.3595
a_2	$\eta_0(\text{MPa.s})$	$\eta_{\infty}(\text{MPa.s})$	β_1	β_2	$K_1(\text{MPa.s})$	$K_2(\text{MPa}^{-2})$
-1.3600	0.2740	0.0047	0.0000	26.7236	0.0000	18.9752

Table 4.4: Material parameters of TangoBlack FLX 973.

The last four equations imply that in order to model the material behavior, there are 14 parameters to be characterized: $\mu_r, \alpha_r, m_r, a_r, \beta_r, K_r$ ($r = 1, 2$), η_0 and η_{∞} . We used the experimental data of the loading-unloading tests at three different strain rates of 0.06, 0.7, and 1.4 s^{-1} and a relaxation test at $\lambda = 1.155$ initially stretched with 0.02 s^{-1} (Figure 4.18). The parameters are fitted by a self-developed Matlab code to solve the ODE equation (4.14) by numerical Runge-Kutta method given an initial value for the parameters. The initial value is iteratively updated to converge to optimized parameters that minimize the squared difference value between the experimental data and the modeling. Figure 4.18 represents the comparison between the experimental data and the model of Kumar and Lopez-Pamies (2016) with the optimized material parameters in Table 4.4. The model shows its good capability to deal with the nonlinearity of the material. We note that the optimized parameter values denote no dependence on the parameters K_1 and β_1 . Therefore, 12 parameters are sufficient to model the behavior of TangoBlack under uni-axial loading. We have performed several model validation to ensure the validity of the parameters and the employed model has predicted well the experimental data. These results however have not been presented here.

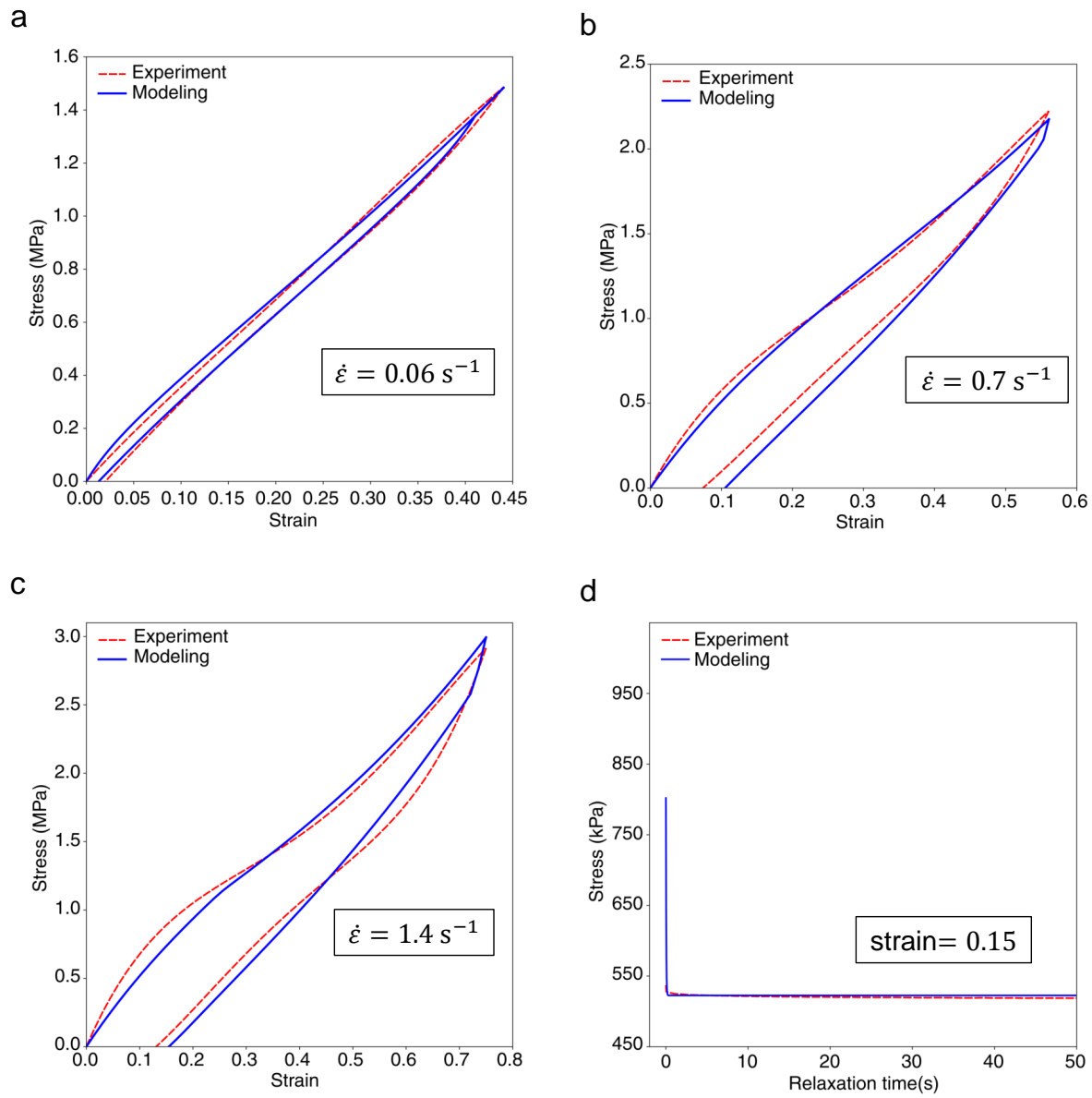


Figure 4.18: The modeling of the experimental data of TangoBlack with the viscoelastic incompressible model proposed by [Kumar and Lopez-Pamies \(2016\)](#) and the material parameters in the table 4.4. TangoBlack is subjected to uni-axial tension loading-unloading at different constant strain rates: (a) 0.06 s^{-1} , (b) 0.7 s^{-1} , (c) 1.4 s^{-1} . (d) Single-step relaxation test with the strain held at 0.15 and the primary strain rate 0.02 s^{-1} . Stress values correspond to engineering or first Piola-Kirchhoff stresses, and strain values correspond to engineering strains.

4.2.9 Fracture and ultimate tensile properties of TangoBlack

TangoBlack as a viscous rubbery elastomer exhibits a semi-brittle fracture when the ultimate stress is reached. In a uni-axial tensile test, the ultimate stress value corresponds to the tensile stress at break S_{uni}^b ; likewise, the associated ultimate strain corresponds to the strain at break ε^b which is equal to $\varepsilon^b = \lambda^b - 1$, where S_{uni} represents the first Piola-Kirchhoff stress³ component in the uni-axial direction and λ^b is the principal stretch at the break. The corresponding Cauchy stress component of the ultimate stress can be obtained by $\sigma_{uni}^b = S_{uni}^b \lambda^b$ ⁴. The elongation at break (ε^b) reported by the manufacturing company of TangoBlack is equal to 45-50% (Table 4.1). Our experiments, however, show an extensive range of ε^b from 13 to 100%, highly dependent on the strain rate (see the ultimate points of the stress-strain curves in Figure 4.12). The higher the strain rate, the higher the ultimate strain can be achieved.

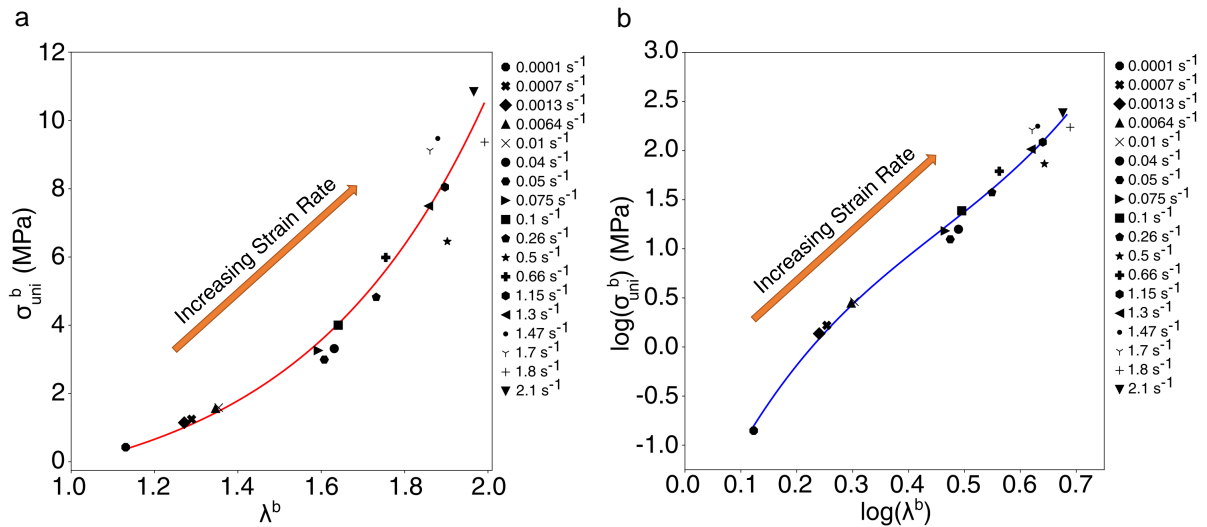


Figure 4.19: Failure envelope for TangoBlack FLX 973 from data obtained at various strain rates. (a) The Cauchy stress at break σ_{uni}^b as a function of the principal stretch at break λ^b at different strain rates. (b) The logarithmic values of the Cauchy stress at break $\log(\sigma_{uni}^b)$ as a function of the logarithmic values of the principal stretch at break $\log(\lambda^b)$ at different strain rates.

It is often possible to characterize the ultimate tensile properties of polymers by defining a *failure envelope* based on the values of ultimate stress and strain (σ_{uni}^b and ε^b) measured at various strain rates. A unique failure envelope is a characteristic of each

³Nominal or engineering stress

⁴The Cauchy stress tensor $\boldsymbol{\sigma}$ can be obtained from the first Piola-Kirchhoff stress \mathbf{S} by this relation $\boldsymbol{\sigma} = J^{-1}\mathbf{S}\mathbf{F}^T$, where $J = 1$ for incompressible TangoBlack material.

elastomer regardless of the test conditions and is distinct from that of other elastomers. For example, [Smith \(1963\)](#) showed in his work that there is a unique failure envelope for SBR-II whether it is tested at different strain rates or temperatures. [Figure 4.19a](#) shows the ultimate Cauchy stress and engineering strain of TangoBlack at various strain rates. The ultimate values obtained from the results of the uni-axial tensile tests are reported in [Figure 4.12](#). [Figure 4.19b](#) shows the corresponding logarithmic values of the ultimate Cauchy stress and strain. The failure envelope is subsequently obtained by fitting a third-order polynomial function $y = 14.04x^3 - 19.02x^2 + 13.05x - 2.15$ where $y = \log(\sigma_{uni}^b)$ and $x = \log(\lambda^b)$. It can be observed that the failure envelope fitted with logarithmic values shows a smaller deviation as opposed to the left figure. The obtained failure envelope indicates that for each value of σ_{uni}^b there exists a unique value of λ^b independent of the test conditions. The value of the unique ultimate stress and strain is determined by the strain rate. By increasing the strain rate, the fracture point moves across the envelope in the counterclockwise direction. Moreover, these results have enabled us to predict the occurrence of rupture in TangoBlack specimens subjected to a variety of tests and under a variety of conditions. One can confirm the obtained failure envelope by performing tensile tests at different temperatures subjected to a constant strain rate. Although more test data is required to determine the exact failure envelope, it remains a relatively good approximation of fracture behavior.

4.2.10 Fracture in Relaxation tests

The occurrence of fracture in a few seconds after relaxation initiation is one of the major challenges of performing relaxation tests on the Tango Black material. On the one hand, high strain levels are essential for observing stress relaxation, while on the other hand, strain levels above approximately 20% lead to the sample breaking before equilibrium stress is achieved. [Figure 4.17a](#) displays the occurrence of fracture when the sample has been relaxed at 22% and 37% strain levels. It shows that fracture occurs more quickly as the strain level increases. A similar fracture has been observed in [Figure 4.17b](#) at 150 s in the specimen loaded to 19.6% strain level with a constant strain rate of 0.1 s^{-1} . Comparing the time when the fracture occurs between the strain levels 0.02 s^{-1} and 0.1 s^{-1} also reveals that higher strain rates are associated with earlier fractures.

The observed fracture in the relaxation test at high strain levels can be justified by a similar fracture envelope presented by [Smith \(1963\)](#). He illustrated a schematic representation of the stress-strain curves at different strain levels and the corresponding fracture envelope. Inspired by his work, we have shown the fracture envelope of the TangoBlack material in [Figure 4.20](#). In this figure, we particularly show the stress-strain curves at 1.3 s^{-1} strain rate by a black line originating from the diagram's origin, while the fracture points are connected by the envelope with the red line. The important remark in this figure is the dotted lines originating from points A and B, which represent the stress relaxation at a constant strain. The line from point A shows that if the strain level in the relaxation test is below the initial point of the envelope, the stress will reach

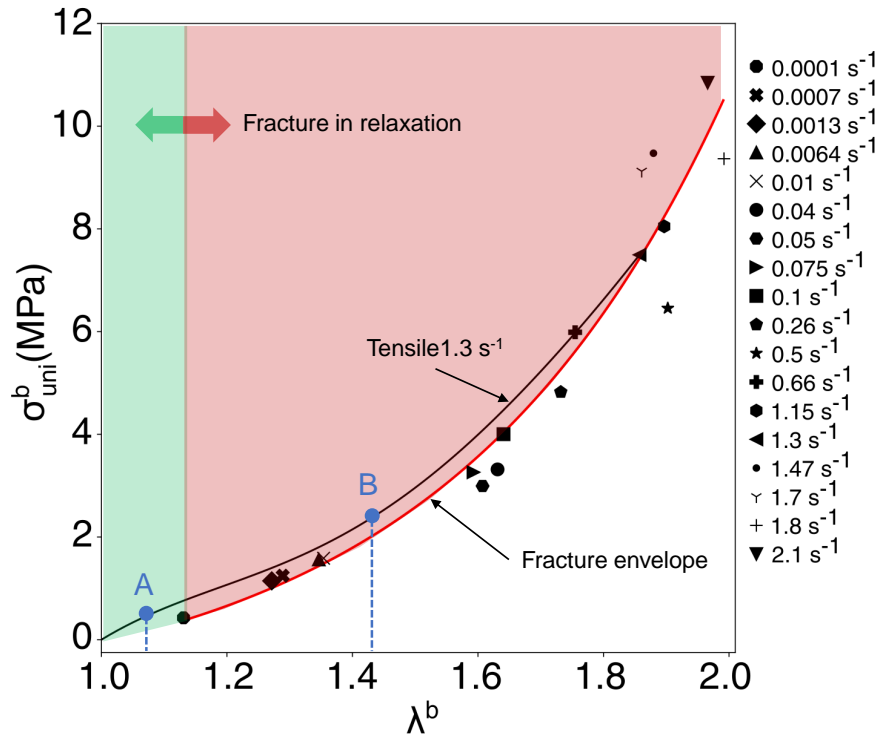


Figure 4.20: The failure envelope of the TangoBlack material and the result of the tensile test at 1.3 s^{-1} strain rate. Points A and B indicate the initiation of the relaxation. The red region represents the stress and strain values where the fracture occurs during the relaxation process. In contrast, the green region shows stress and strain values without fracture when relaxed.

equilibrium without any fracture occurring in the specimen. This region is indicated by green color, assuming that the specimen will not reach the fracture envelope before the relaxation. On the other hand, if the relaxation initiates from point B which has a strain level above the initial point of the envelope, the stress will be relaxed followed by a fracture occurring when the fracture envelope is reached (red color region). We note here that the results of [Smith \(1963\)](#) and [Ferry \(1980\)](#) have indicated that the determination of the exact initial point of the fracture envelope might not be possible and a sharp corner at the beginning of the fracture envelope does not exist. Nevertheless, it provides a rough approximation of the range of failures occurring. Particularly, the dotted line from point B shows qualitatively why a fracture is observed in the TangoBlack material when it goes under relaxation at large strain levels. From this figure, we also realize that the

stress equilibrium line for the TangoBlack sample is very short and the strain level at the beginning of the fracture envelope corresponds to approximately 19% to 20%. Hence, it is necessary to apply high strain rates to the specimen until the strain level falls below 20% to properly observe stress relaxation in the TangoBlack material.

4.2.11 Neo-Hookean modeling at low strain rates

The experimental results of the TangoBlack materials indicate that the material nonlinearity is observed at large strain rates approximately greater than 0.01 s^{-1} . This is due to the fact that at low strain rates, the TangoBlack material breaks at smaller strain values before nonlinearity appears. Therefore, at strain rates below 0.01 s^{-1} one may use a simpler material viscoelastic model. As an example, we modeled the TangoBlack material with a Neo-Hookean viscous incompressible model for hyperelastic materials. A similar approach to the previous constitutive modeling has been followed. The equilibrium and non-equilibrium energy functions associated with the Neo-Hookean incompressible hyperelastic viscous model are

$$\psi^{\text{Eq}}(\mathbf{F}) = \frac{\mu_1}{2}(\mathbf{F} \cdot \mathbf{F} - 3), \quad (4.17)$$

$$\psi^{\text{NEq}}(\mathbf{F}^e) = \frac{\mu_2}{2}(\mathbf{F}^e \cdot \mathbf{F}^e - 3), \quad (4.18)$$

where \mathbf{F} and \mathbf{F}^e are defined similar to the previous constitutive model and μ_1 and μ_2 are the material parameters. The dissipation potential ϕ could be written in the following form

$$\phi(\mathbf{F}^v) = \frac{1}{2}\mathbf{\Gamma}^v \cdot (2\eta_K \mathbf{K} + 3\eta_J \mathbf{J})\mathbf{\Gamma}^v, \quad (4.19)$$

where η_K and η_J are the material parameters and $\eta_J \rightarrow \infty$ due to the material incompressibility. Also, $\mathbf{\Gamma}^v$ is defined by equation (4.7). By imposing the similar uni-axial boundary conditions defined in equation (4.12) and using the evolution equation (4.2), we obtain the first Piola-Kirchhoff stress component.

$$S_{33} = \mu_1\left(\lambda - \frac{1}{\lambda^2}\right) + \mu_2\left(\frac{\lambda}{\lambda_v^2} - \frac{\lambda_v}{\lambda^2}\right), \quad (4.20)$$

and the following differential equation for λ_v

$$\dot{\lambda}_v = \frac{\mu_2}{3\eta_K}\left(\frac{\lambda^3 - \lambda_v^3}{\lambda\lambda_v}\right). \quad (4.21)$$

The last couple of equations implies that in order to model the material behavior, there are 3 parameters to be characterized: μ_1 , μ_2 , and η_K . We used the experimental results to identify the parameters. Figure 4.21 shows the comparison between the experimental data and the Neo-Hookean modeling at two strain rates 0.66 s^{-1} and 0.0007 s^{-1} . We observe that this model fails to fit the hardening part of the curve at large strains. It implies that we would need some power in the energy functions to fit the increase in stress. Therefore, at large strains, we must use the rubber viscoelastic model proposed by [Kumar and Lopez-Pamies \(2016\)](#). However, at low strain rates, the TangoBlack material breaks at below 30% strain and it is not able to reach high strain values. One may conclude that the simple Neo-Hookean model can be used either at low strain rates (for TangoBlack material below 0.01 s^{-1}), or at small strains, when large strain rate deformations are applied.

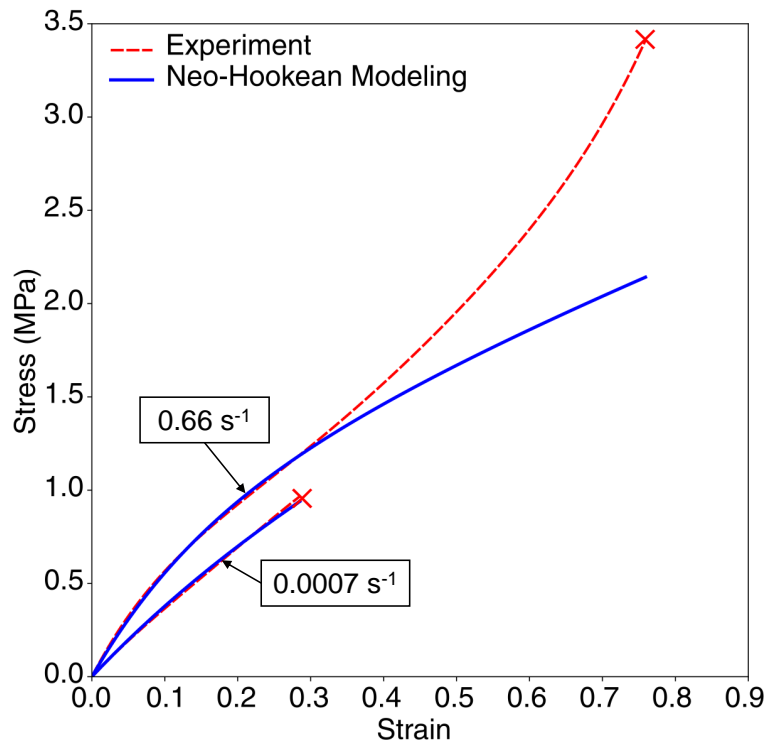


Figure 4.21: The modeling of the experimental data of TangoBlack at two strain rates 0.66 s^{-1} and 0.0007 s^{-1} with Neo-Hookean viscous incompressible model for hyperelastic materials. The \times shows the breaking point of the sample. Stress values correspond to engineering or first Piola-Kirchhoff stresses, and strain values correspond to engineering strains.

During this study, we use the TangoBlack material as the base polymer matrix to

manufacture the designed random porous geometries for experimental testing. However, we apply very low strain rates 10^{-4} s^{-1} at all performed experiments and we expect to observe a fracture at less than 20% strain. Therefore, for the modeling of deformation in porous geometries, we will use the simple Neo-Hookean model with the identified parameters. Consequently, the ligaments will break when their local strain values reach almost 15%.

4.3 3D-printing method and limits for porous geometries

In this study, the designed porous test specimens at different porosities are 3D-printed by the Stratasys 3D-printer and TangoBlack material. The 3D-printer specifications and the Tangoblack material properties are discussed in Sections 4.1 and 4.2, respectively. Prior to the manufacturing of the porous specimens, a straightforward 3D-printing test using isolated and closely packed aligned circular and rectangular voids was conducted to quantify the size of the pore features that could be manufactured with sufficient geometrical accuracy (Figure 4.22). The equal-sized rectangular and circular voids are printed with a variety of intervoid ligament thicknesses to evaluate the minimum printing thickness of the 3D-printer. Circular voids of different sizes also determine the minimum size of a printable empty void. Therein, we have found that the minimum pore diameter and intervoid thickness ligament that may be 3D-printed once-off with acceptable accuracy are respectively, $\sim 300 \mu\text{m}$ and $\sim 600 \mu\text{m}$. These numbers are slightly larger than those reported in a study considering RSA geometries with VeroWhite material (Tarantino et al., 2019) and imply that TangoBlack has an actual lower resolution.

4.4 3D-printing interruption strategy

For the experimental study, and in order to attain with our 3D-printer the minimum ligament thicknesses required for representativity of the results discussed in detail in Section 4.5.2, we consider porous test specimens with in-plane dimensions $100 \times 100 \text{ mm}^2$ and out-of-plane thickness 10 mm. In the M-Voronoi materials, we do not control entirely the thickness of the intervoid ligaments. In fact, those are highly variable at different positions. As a result, as one reaches lower relative densities, the intervoid ligament thickness may become less than the minimum that can be accurately 3D-printed (i.e., $< 300 \mu\text{m}$) resulting to a rather low quality reproduction of the numerically obtained geometrical features, especially along the out-of-plane direction, as shown in Figure 4.23a. In order to improve further upon this limitation directly related to the specific 3D-printing technology used, we propose here an interruption strategy. In the present case of a commercial 3D-printer, this simply consists in manually interrupting the 3D-printing process for a few minutes thus allowing the existing polymer layer to solidify partially before additional

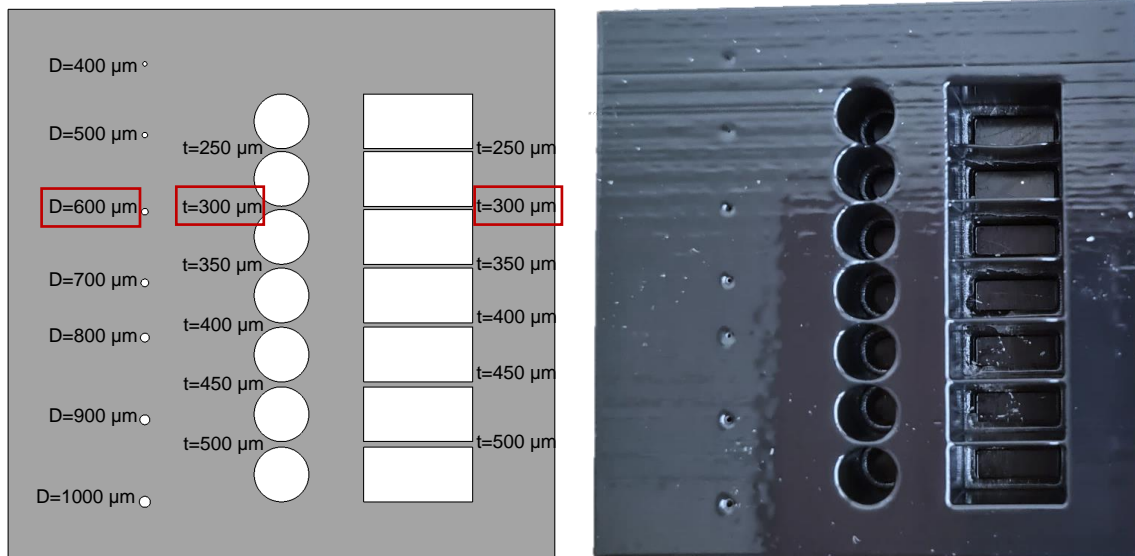


Figure 4.22: 3D-printing accuracy test of TangoBlack material with circular and rectangular voids. The minimum pore diameter and intervoid thickness ligament that may be 3D-printed once-off with acceptable accuracy are $\sim 300 \mu\text{m}$ and $\sim 600 \mu\text{m}$ respectively.

layers with additional weight are positioned atop. As clearly shown in Figure 4.23b, this interruption strategy allows to improve substantially on the quality of the 3D-printed specimen, even though some imperfections are still present in these extreme relative densities. For completeness, we also include in Figures 4.23c,d, corresponding E-Voronoi geometries. Even in this case of uniform intervoid ligament thickness, we observe that an once-off 3D-printing approach still leads to imperfections, albeit of smaller amplitude than those observed for the M-Voronoi geometries.

More precisely, the interruption period depends on the in-plane dimensions of the specimen and the number of specimens laid on the 3D-printer tray. The reason for this is simply related to the time that the 3D-printer heads require to return to exactly the same printing point. As a rule of thumb in our work, we use the following time steps. For one specimen of in-plane dimensions $100 \times 100 \text{ mm}^2$, we 3D-print for 10 min and interrupt for another 10 min. Given that the total estimated time for a single-step 3D-printing of the given specimen with an out-of-plane thickness of 10 mm is about 1 hour, the interruption delay time is taking place every about 10/6 mm intermediate layers. If additional specimens are added to the tray, the 3D-printing time before applying an interruption should be calculated accordingly. Obviously, the proposed time scales do not constitute a universal protocol expected to work for any arbitrary geometry. Nevertheless, the idea itself of interruption clearly allowed us to improve the quality of the 3D-printed specimens, especially at low relative densities. Finally, Figure 4.24 illustrates more clearly

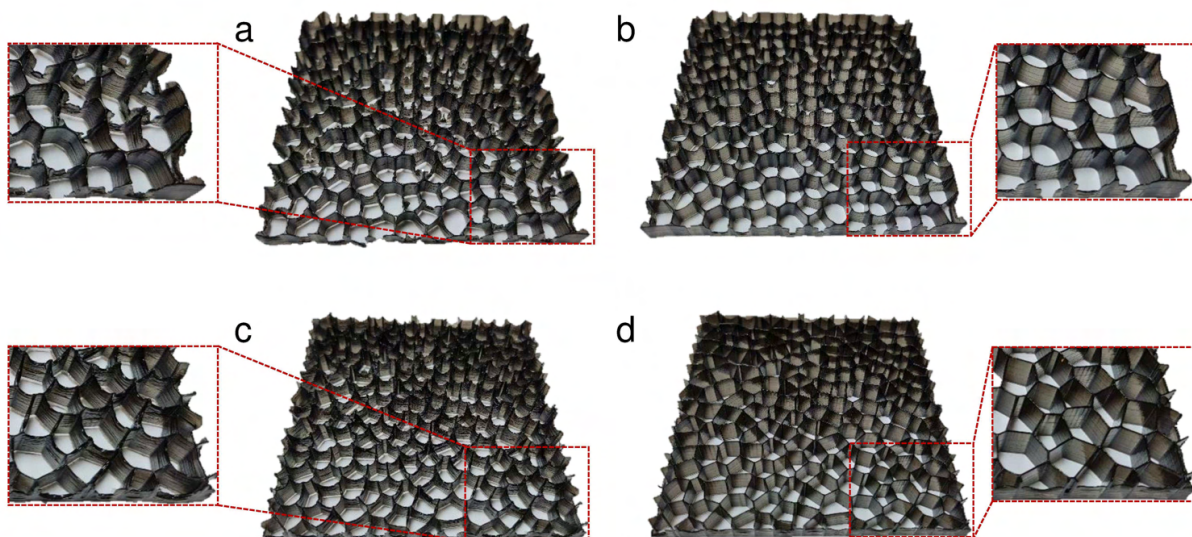


Figure 4.23: (a,b) M-Voronoi and (c,d) E-Voronoi 3D-printed specimens with relative density $\rho = 0.1$. The specimens are obtained in (a,c) without and (b,d) with the interruption strategy.

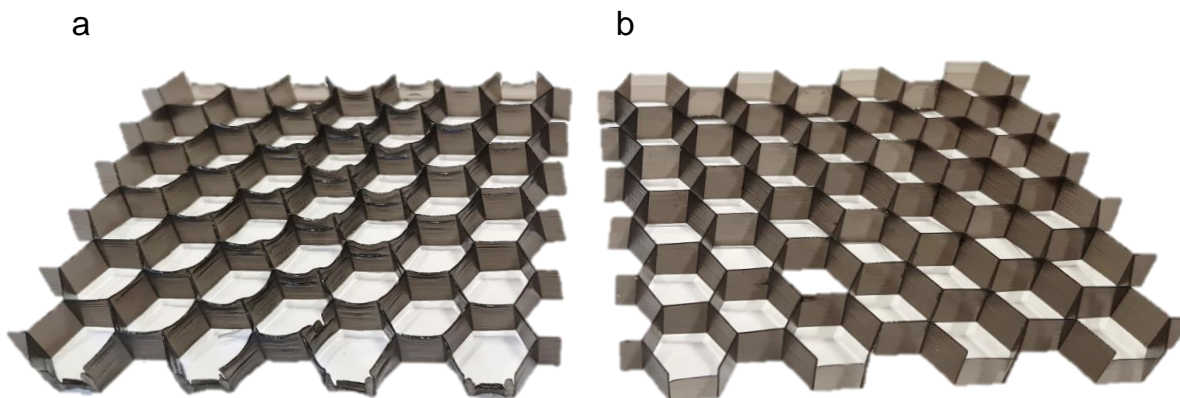


Figure 4.24: The effect of interruption method on hexagons with a constant intervoid ligament thickness that are 3D-printed a) without interruption method, and b) with interruption method. The relative density of the geometry corresponds to $\rho = 0.05$.

how the interruption method affects hexagonal lattices with a constant thickness.

For completeness, we show in Figure 4.25, 3D-printed specimens for $\rho = 0.2$ for all three geometries, i.e., (a) M-Voronoi, (b) E-Voronoi and (c) RSA. In this case, no interruption during the 3D-printing is necessary to achieve sufficient specimen quality. Even so, one may observe at the boundaries of the cell a few regions where the 3D-printing has not been entirely complete. Nevertheless, those regions are only a very minor propor-

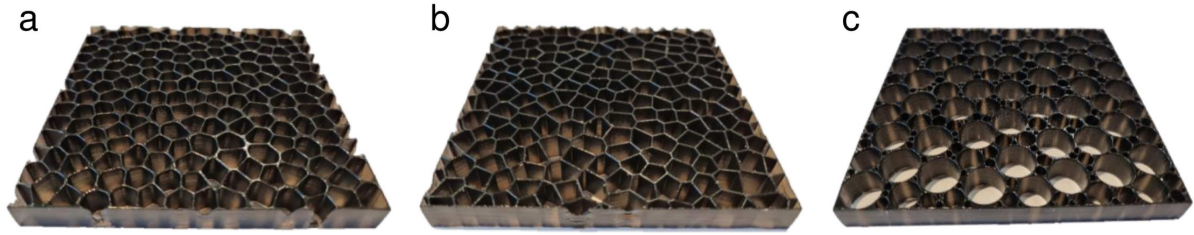


Figure 4.25: (a) M-Voronoi, (b) E-Voronoi and (c) RSA 3D-printed specimens with no interruption strategy and $\rho = 0.2$.

tion of the specimen and they do not affect the overall response, as we will show in the representativity study in Section 4.5.2.

4.5 Experimental results and discussion

In this section, we quantify experimentally the response of the M-Voronoi, E-Voronoi and RSA geometries when subjected to uni-axial compression loads. First, we study the representativity and isotropy of response of the M-Voronoi (the E-Voronoi have a similar response to the M-Voronoi in terms of representativity) and RSA specimens in terms of number of voids as well as direction of loading (in order to probe isotropy even partially). Subsequently, we carry out a comparison analysis between the M-Voronoi, E-Voronoi and RSA geometries for isotropic and anisotropic geometries.

4.5.1 Testing protocol

The 3D-printed test specimens are subjected to quasi-static uni-axial compression using a servo-hydraulic testing machine and their deformation history is tracked by means of a CCD camera. Experiments have been carried out under displacement control with a constant strain rate of 0.001 s^{-1} . For the measurement of the force signal, two different load transducers with capacity $200 \pm 0.2 \text{ N}$ and $10 \pm 0.01 \text{ N}$ are employed depending on the relative density of the test specimen. Specifically, the 200 N transducer was mounted onto the fixed platen of the testing machine, whereas the 10 N transducer (mounted onto the movable platen of the crosshead) is designed to double as a piston. To this end, a dedicated testing set-up proposed by [Tarantino and Danas \(2019\)](#) is re-adapted and used. Finally, during experiments all specimens are enclosed between two transparent PMMA plates of 10 mm thickness in order to avoid out-of-plane-buckling of the test specimens. The two plates are lubricated with teflon at the inner side to reduce contact friction with the test specimen.

4.5.2 Representativity and isotropy of M-Voronoi

Considering the previously-mentioned fabrication constraints, we choose the overall size to be $100 \times 100 \times 10 \text{ mm}^3$ for all 3D-printed specimens. These dimensions allow to reach a large enough number of voids (~ 250) leading to a sufficiently representative response (i.e., scattering of the response as a function of realization and number of voids) and low relative density realizability⁵. By considering 200 voids (or ~ 14 per each direction) in the M-Voronoi, we obtain a minimum void diameter size of $\sim 5 \text{ mm}$. Note that since the void distribution and size are random, these numbers should only be considered in an average sense. Decreasing the number of voids leads gradually to a more “structural” (i.e. with larger scatter) response that is strongly dependent on realization. In order to assess the effect of the number of voids in the cell (or equivalently void size) effect on the representativity of the response, we have carried out experiments for six different numbers of voids, $N_p = 30, 50, 100, 150, 200, 250$ with $\rho = 0.3$ in M-Voronoi specimens, as shown in Figure 4.26.

Specifically, Figure 4.26a shows the overall “engineering” stress-strain response of the relevant M-Voronoi geometries. At this stage, only one realization is considered. As easily observed in Figure 4.26a, convergence of the stress-strain response is achieved as we increase $N_p \geq 200$ voids⁶. The cross-plot in Figure 4.26b shows the engineering stress as a function of N_p at different levels of the strain. We conclude that beyond $N_p \geq 200$ a sufficiently converged response is obtained, as this is revealed by the saturation of the stress measures with increasing N_p . This average number of voids is used in the next sections to compare the various geometries. It is further pointed out that even in fully periodic systems such an analysis is necessary to assess the representativity of the results as a function of the specimen size. Such an analysis is even more critical at large strains where nonlinear phenomena such as buckling or fracture are involved (Michel et al., 2007).

In order to complete the study of representativity as well as obtain a *rough* measure of the isotropy of the M-Voronoi geometries, we analyze in Figure 4.27 the scatter in the stress-strain response due to different realizations but for a fixed number of voids. Figures 4.27a,b correspond to $N_p = 30$ and 200 with $\rho = 0.3$. For each N_p , we consider two different realizations subjected to two different loading directions thus effectively studying four realizations, as shown in Figures 4.27c,d. One readily observes that increasing the number of N_p leads to a decrease of the apparent scatter. The rough convergence of the results for $N_p \geq 200$ indicates that the M-Voronoi geometries behave similarly in the two main directions of the square cell. This invariance to directionality is a strong evidence of isotropy at large strains, albeit not entirely complete. Nevertheless, a more complete isotropy analysis is not possible with our current experimental setup. Yet, considering

⁵It is noted here that experimental realizability of the geometries is directly tight to the accuracy of the 3D-printer. The resulting representative geometries are, in turn, scalable and independent of the size of the specimen itself.

⁶Convergence should be thought in a less strict manner here given that in experiments scatter is also due to small fabrication variations as discussed already in Section 4.4 as well as small testing uncertainties ranging from one experiment to the other.

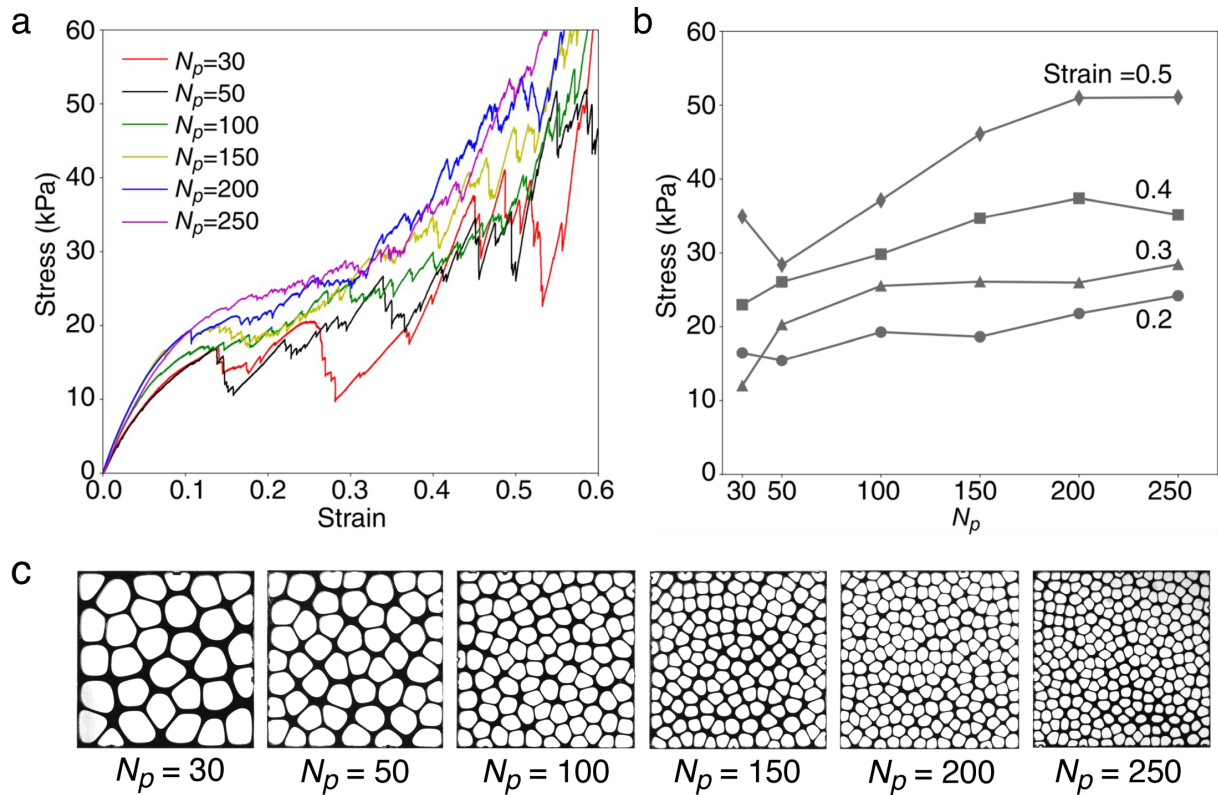


Figure 4.26: Experimental representativity study for M-Voronoi with $\rho = 0.3$ in terms of number of voids N_p . (a) Stress-strain response of the M-Voronoi with different number of voids and (b) engineering stress as a function of N_p for different levels of the overall strain. (c) Optical images of the corresponding realizations for different N_p . The values of stress and strain correspond to their nominal or engineering values.

the randomness of the geometry and the different realizations, the present results imply a sufficient isotropic response even at *large strains*, a feature usually ignored in many recent studies of plates, trusses and more generally periodic cellular materials. We recall here that isotropy in linear elasticity and small strains does not imply⁷ isotropy at large strains as we show clearly in Section 4.5.4. It is also noted that additional geometries (not shown here for brevity) and tests were performed with open voids reaching the lateral boundaries. The latter did not change the converged response observed in Figure 4.27b.

By contrast, for $N_p = 30$, while at small strains all four realizations exhibit very similar response (up to an acceptable scatter discussed in the following), their scatter increases substantially leading to a different initial buckling as well as post-bifurcated response. This observation reveals the extremely complex local mechanisms that enter

⁷Perhaps the most straightforward example is that of two-dimensional hexagonal trusses which are studied further below. At small strains, they are exactly isotropic (Francfort and Murat, 1986), but become highly anisotropic in the post-buckling regime and finite strains (Spyrou et al., 2019).

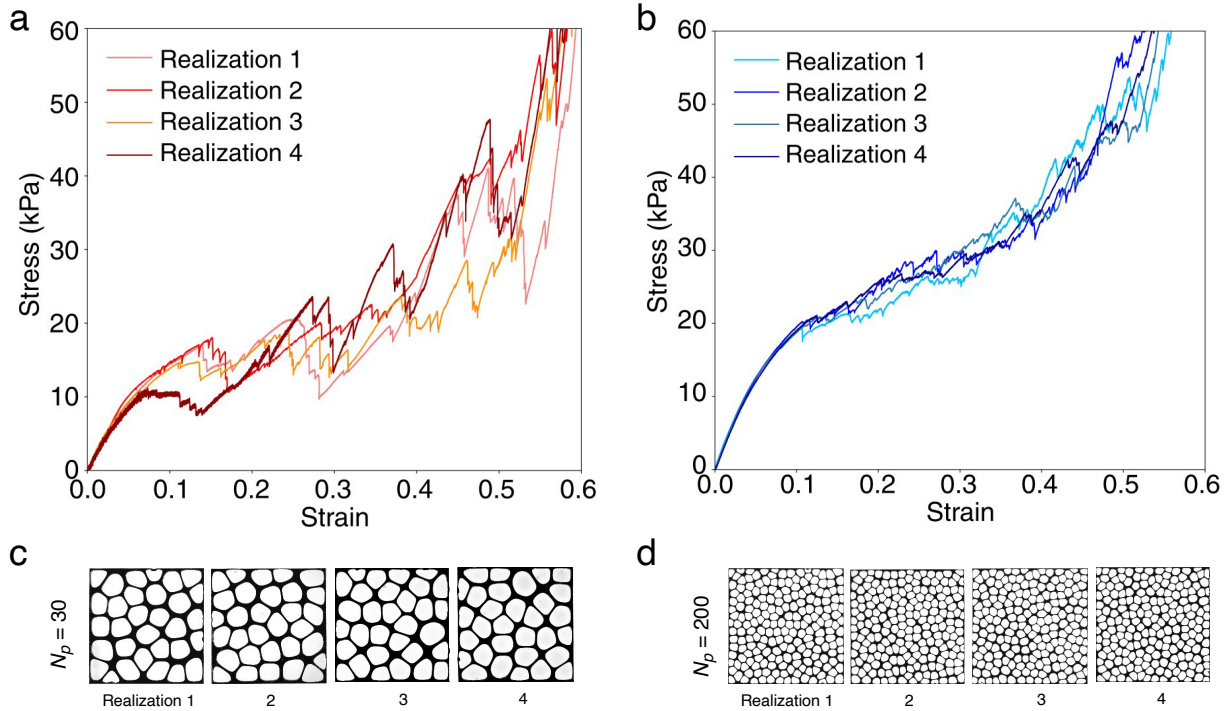


Figure 4.27: Experimental representativity study for M-Voronoi with $\rho = 0.3$ in terms of number of realizations and number of voids. Stress-strain response for four different realizations for (a) $N_p = 30$ and (b) $N_p = 200$. Corresponding optical images of the realizations for (c) $N_p = 30$ and (d) $N_p = 200$. The values of stress and strain correspond to their nominal or engineering values.

in the response of the post-bifurcation regime, as well as the fact that representativity of response is strongly dependent on realization, void sizes as well as the consideration or not of large strains.

Next, we analyze the scatter induced by the different realizations discussed previously. The scatter of a quantity A is defined as

$$\text{Realization scatter } \% = \frac{A_{max} - A_{min}}{A_{ave}} \times 100, \quad (4.22)$$

where A_{max} , A_{min} and A_{ave} correspond to the maximum, minimum and average value of the quantity among different realizations.

In Table 4.5, we show the average and scatter values for the apparent Young's modulus obtained at very small strains ($0 - 0.2\%$). We observe that increase of N_p leads effectively to a stiffer and less scattered response as expected.

In turn, in Figure 4.28, we show the scatter of the stress values in the strain range $0.05 - 0.6$. Therein, the M-Voronoi with $N_p = 30$ are found to be highly dependent upon realization exhibiting a large scatter in the order of 40% (reaching a maximum of 90% and a minimum of 10%) while the ones for $N_p = 200$ are substantially more

N_p	E_{ave} (kPa)	Scatter (%)
30	206	11.2
200	267	5

Table 4.5: Average and scatter values of the Young's modulus.

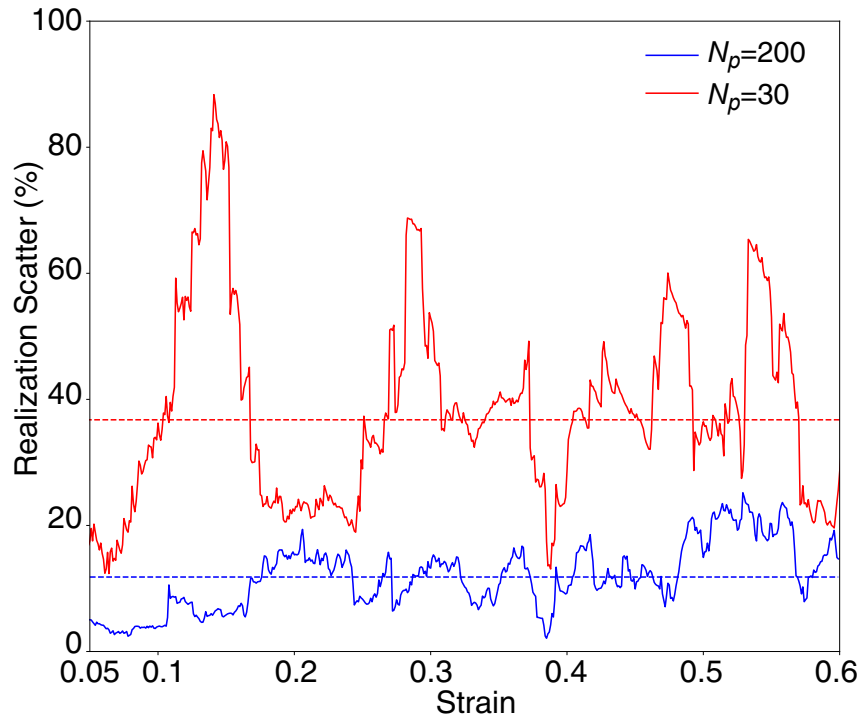


Figure 4.28: The scatter in the stress-strain response induced by four different realizations of M-Voronoi geometries with $\rho = 0.3$ and number of voids $N_p = 30, 200$. The straight dotted lines indicate the average value over the strain range considered in the figure.

representative showing an average scatter in the order of 10% (reaching a maximum of 20% and a minimum of 1%) throughout the entire strain history. We should mention here that fabrication imperfections (see Section 4.4) as well as uncontrollable experimental uncertainties always lead to a certain level of scatter from sample to sample. It is clear, however, that the scatter substantially decreases with increasing number of N_p .

We close this section by noting that the RSA and E-Voronoi geometries exhibit similar behavior in terms of representativity with the M-Voronoi ones at relative densities $\rho = 0.3, 0.4$. Nevertheless, it is substantially more difficult to reach low relative densities ($\rho \leq 0.2$) and simultaneously representative responses at large strains with the RSA approach. This is a direct consequence of the necessity for a very large polydispersity

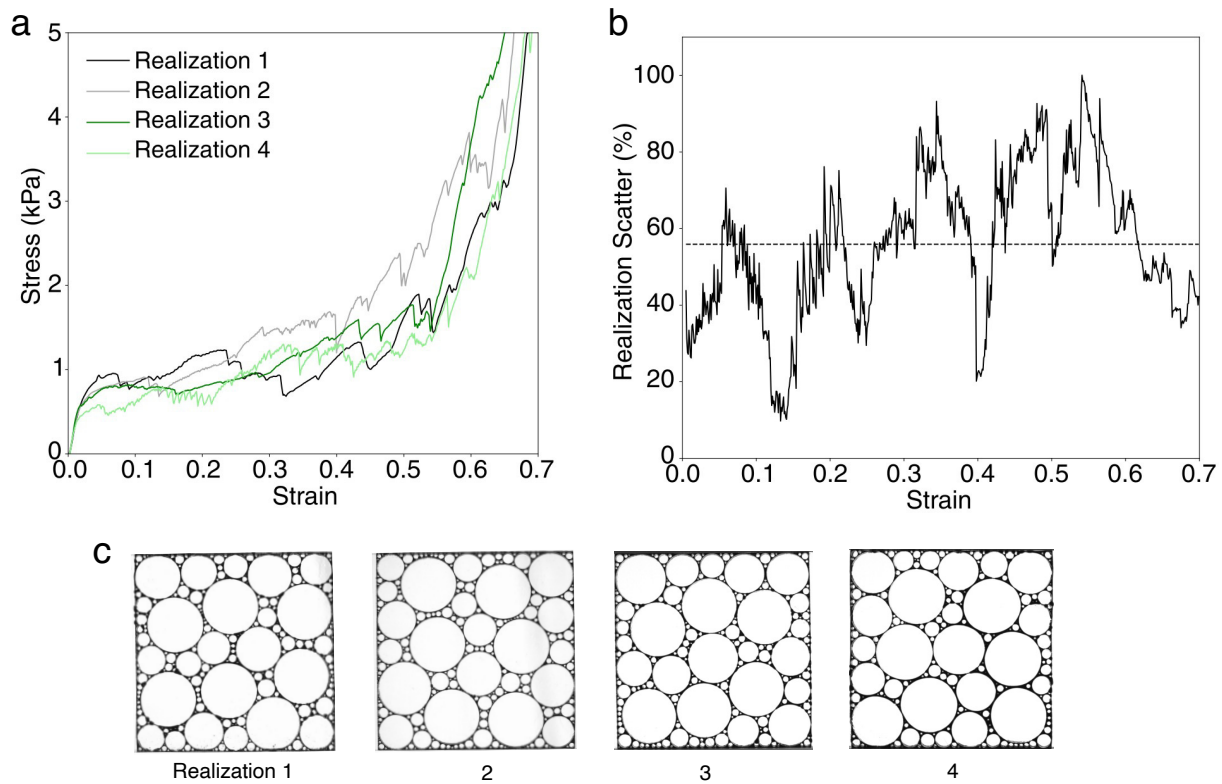


Figure 4.29: Experimental representativity study for RSA with $\rho = 0.1$ in terms of number of realizations. (a) Stress-strain response for four different realizations. (b) Stress-strain realization scatter. The straight dotted line indicates the average value over the strain range considered in the figure. (c) Corresponding optical images of the realizations considered. The values of stress and strain correspond to their nominal or engineering values.

ratio (i.e. difference between the largest and smallest void added in the cell) to reach low densities below $\rho = 0.2$. The difficulty is mainly linked to the limitations of our 3D-printer (e.g. the minimum ligament size that can be printed) and less of the numerical scheme itself.

In order to show this clearly, Figures 4.29a,b show compression tests for RSA geometries with $\rho = 0.1$ using two different realizations subjected to two different loading directions (see Figure 4.29c). Given the 3D-printing and realization constraints discussed in the previous section, we can only reach low relative densities by considering 3-4 “large” voids per-direction (with approximate size $\sim 15 - 20$ mm) and many smaller ones with a polydispersity ratio in the order of $\sim 50/1$ (Tarantino et al., 2019). Figure 4.29a represents the engineering stress-strain response, while the corresponding realization scatter is shown in Figure 4.29b. In agreement with earlier studies by Zerhouni et al. (2018), Zerhouni et al. (2019) and Tarantino et al. (2019), at small strains, the response is rather converged and representative. Nonetheless, the initial buckling and post-buckling response becomes

highly scattered at large strains. It can be observed in Figure 4.29b that the amplitude of this scatter reaches very large values ($\sim 100\%$ at maximum). Similar representativity limitations are in general true for $\rho \leq 0.2$, and therefore their use in the next section is only done for completeness purposes.

4.5.3 Comparison among the three geometries

In order to compare the three geometries considered in this study, we show in Figures 4.30 and 4.31 quasi-static, uni-axial compression experiments for relative densities $\rho = 0.4, 0.3, 0.2, 0.1$. The representativity analysis carried out in the previous section allows to consider only one realization for the M-Voronoi geometries. In order for the comparison to be meaningful, the corresponding E-Voronoi geometries also contain a similar number of voids with the corresponding M-Voronoi ones. For a better understanding, we also include optical images of the three geometries selected at three intermediate strains levels, denoted with (1), (2) and (3).

In Figure 4.30 corresponding to relative densities $\rho = 0.3, 0.4$, the initial response for all tested geometries has a net linear behavior. The range of the initial linearity decreases with decreasing relative density, as shown in Figure 4.31 corresponding to $\rho = 0.1, 0.2$. In all cases however, this initial linear response remains free of oscillations. After this initial smooth behavior, initial buckling, deformation localization and fracture occur at different regions in the specimen (see green lines on the optical images). Since the tested samples are random, ligaments bend, buckle and rupture at different positions inducing an oscillatory overall response. Rather remarkably, the M-Voronoi exhibit the strongest hardening response with no apparent *major peak-stress* up to complete densification and for all relative densities considered here. This leads to overall the stiffest response at large strains, even if initially the M-Voronoi may exhibit a lower modulus than the corresponding RSA geometries in some cases (e.g., $\rho = 0.3$). In particular, for $\rho = 0.3$, the RSA geometries show an initially stiffer response than the M-Voronoi which however becomes softer at larger strains leading to a lower hardening modulus than that of the M-Voronoi at moderate and large strains. Note that in general, the RSA geometries exhibit similar trends with the M-Voronoi ones, except at lower $\rho = 0.1, 0.2$ (Figure 4.31), where the response becomes non-representative for the reasons discussed in Section 4.5.2. As consequence, at low densities $\rho = 0.1, 0.2$, the RSA depict a more flat, plateau-type, response beyond the occurrence of the first peak-stress. Such plateau type responses are very usual in lattice, truss and plate-type models (Symons and Fleck, 2008) as well as in stochastic porous composites (Jang et al., 2008; Gong and Kyriakides, 2005). A few exceptions have been reported for random foams produced by replication processing (San Marchi and Mortensen, 2001) though.

By contrast, the E-Voronoi, even though they exhibit no major peak-stress, their stress-strain response and overall hardening rate lies always lower than that of the M-Voronoi for all relative densities considered here. To explain this further, we focus on the corresponding optical images. It is clear that the non-uniform intervoid ligament

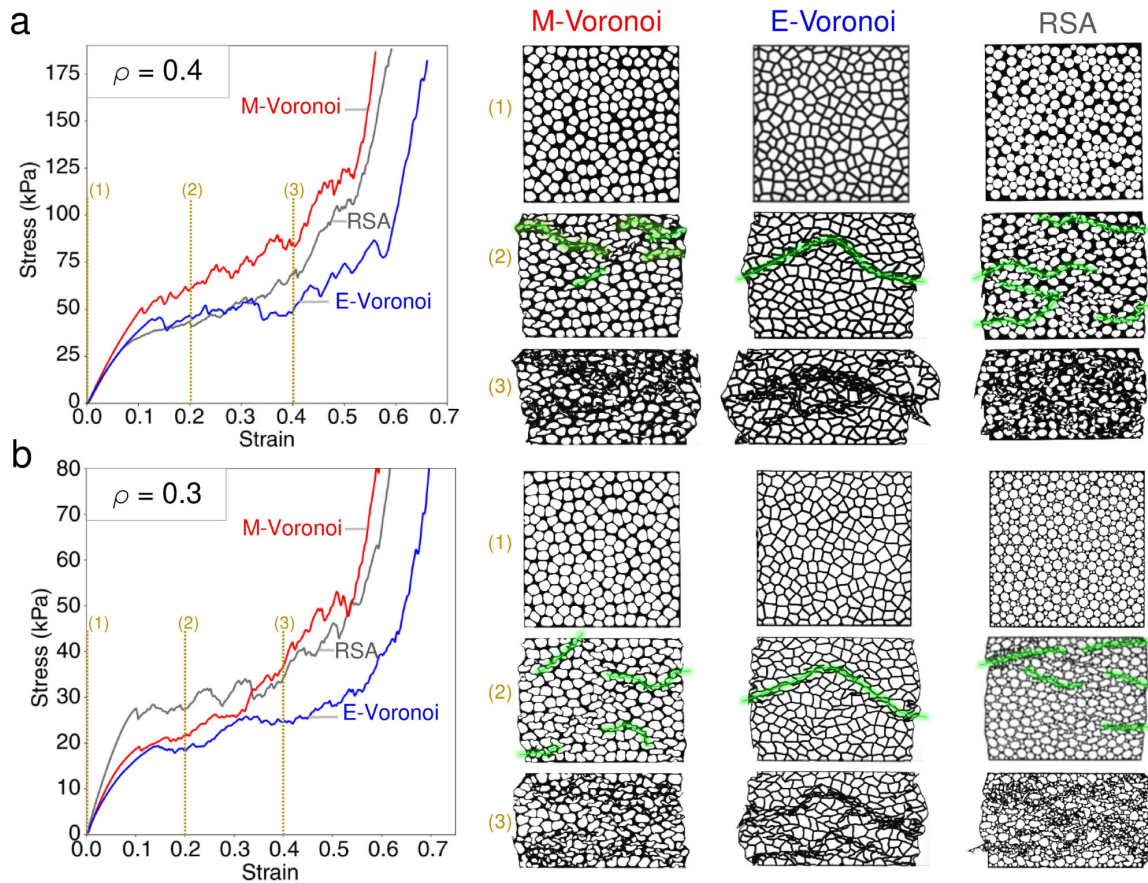


Figure 4.30: Compression experiments and corresponding optical images for the M-Voronoi, E-Voronoi and RSA geometries for relative densities (a) $\rho = 0.4$ and (b) $\rho = 0.3$. For all cases, snapshots are shown of the three geometries selected at three intermediate strains levels, denoted with (1), (2) and (3). The green lines indicate zones of strong localization and fracturing of the intervoid ligaments. The in-plane dimensions of the undeformed specimens are $100 \times 100 \text{ mm}^2$. The values of stress and strain correspond to their nominal or engineering values.

thickness of the M-Voronoi geometry leads to a diffuse distribution of buckled, bended and fractured unconnected zones throughout the entire specimen (see for instance the corresponding image in Figure 4.30b for the M-Voronoi). The RSA exhibit a similar distribution of disordered and disconnected pockets of localized deformation. By contrast, the E-Voronoi cells, despite being random too, very early form a localization/fracture band that spans the entire specimen for all relative densities considered here. This is a direct consequence of the *uniform* intervoid ligament thickness. Again, such responses are also representative in periodic geometries including trusses, lattices and plate-based

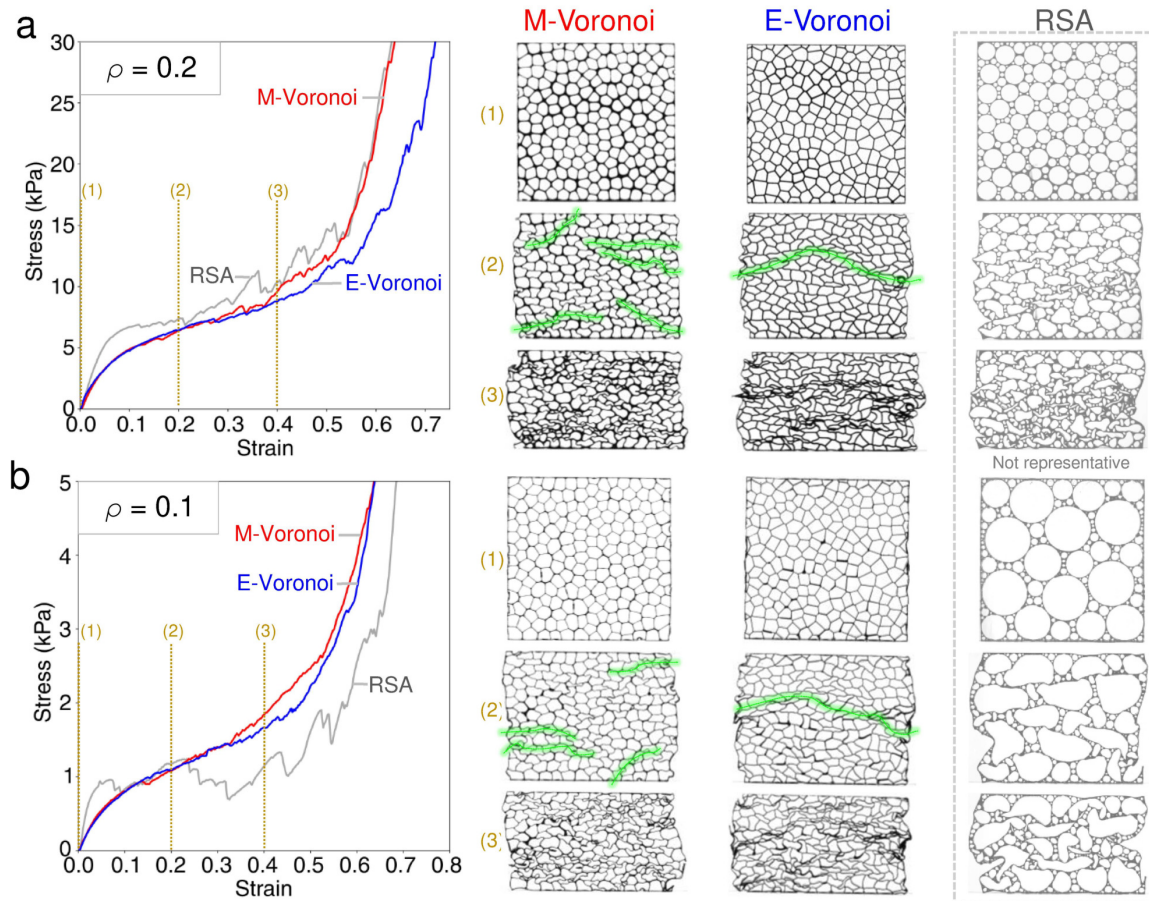


Figure 4.31: Compression experiments and corresponding optical images for the M-Voronoi, E-Voronoi and RSA geometries for different relative densities (a) $\rho = 0.2$ and (b) $\rho = 0.1$. For all cases, snapshots are shown of the three geometries selected at three intermediate strains levels, denoted with (1), (2) and (3). The green lines indicate zones of strong localization and fracturing of the intervoid ligaments. The RSA for $\rho = 0.2, 0.1$ are non-representative due to fabrication limitations. The in-plane dimensions of the undeformed specimens are $100 \times 100 \text{ mm}^2$. The values of stress and strain correspond to their nominal or engineering values.

architected materials (Symons and Fleck, 2008). Interestingly, the E-Voronoi response approaches the M-Voronoi one at lower relative density $\rho = 0.1$. This is somehow expected since at such low relative densities the M-Voronoi samples exhibit a gradually more uniform intervoid ligament thickness, but somehow the M-Voronoi still remains superior, especially at larger strains. Note however, that at such low densities, the differences are in the order of the realization scatter. We note further that as ρ decreases, fracture be-

comes less dominant and the thin ligaments mainly deform by bending and stretching and less by shearing. Even so, the long-wavelength localization bands in E-Voronoi persist for all ρ considered here, while the M-Voronoi continue to exhibit more disconnected and diffuse deformation modes. Finally, it is important to note that overall the higher hardening modulus of the M-Voronoi leads to a lower densification strain than the corresponding E-Voronoi one.

4.5.4 Comparison with Honeycombs

In this section, we compare the M-Voronoi geometries with the widely used honeycomb or hexagonal void geometries. While honeycombs are *exactly* isotropic in the linear elastic regime, they become highly anisotropic beyond buckling exhibiting a peak-stress, a pronounced plateau and subsequent densification. For this reason, the honeycombs constitute a perfect case study in the present work allowing to clarify whether the corresponding M-Voronoi hardening response at large strains is due to geometry or is strongly affected by the constitutive response of the 3D-printed polymer itself.

In Figure 4.32a, corresponding to relative density $\rho = 0.4$, we observe that both the longitudinal and transverse response of the hexagonal geometries is initially linear. This linearity changes abruptly at strains of about 0.15 where the longitudinal geometry exhibits a clear peak-stress and subsequent softening due to the appearance of a localization band spanning the entire specimen (see the corresponding optical image). Beyond that peak-stress the response is oscillatory due to fracturing and the occurrence of additional localization bands. As a result, the longitudinal honeycomb response exhibits no apparent hardening, except much later near the densification regime. By contrast, the response of the transverse honeycomb sample does not exhibit a clear peak-stress but still shows a much lower apparent hardening than the corresponding M-Voronoi geometry. Interestingly, the transverse hexagon geometry shows localization at larger strains and overall exhibits a stiffer response and hence better absorption properties than the longitudinal geometry since they both exhibit very similar densification strains. The results are qualitatively similar for $\rho = 0.3$, not shown here for brevity. Therefore, one may conclude, that for moderate relative densities $\rho \geq 0.3$, the hardening exhibited by the M-Voronoi is mainly due to its geometrical characteristics—i.e., randomness in both void and ligament size as well as the rounding of the void surfaces—and not a result of the base material hardening.

In Figure 4.32b, we compare M-Voronoi with honeycombs for a lower relative density $\rho = 0.1$. The main observations made for $\rho = 0.4$ remain valid here too except for the fact that all geometries now exhibit a clear hardening less or more pronounced depending on the loading direction. A main difference between $\rho = 0.1$ and 0.4 is that at low relative densities the intervoid ligaments mainly buckle or bend but very little fracture is observed in all geometries considered here. This change of deformation mode (i.e. from shear fracturing to bending) leads to a much smoother response throughout the entire process for both the M-Voronoi and the hexagons. Rather interestingly, the longitudinal hexagonal

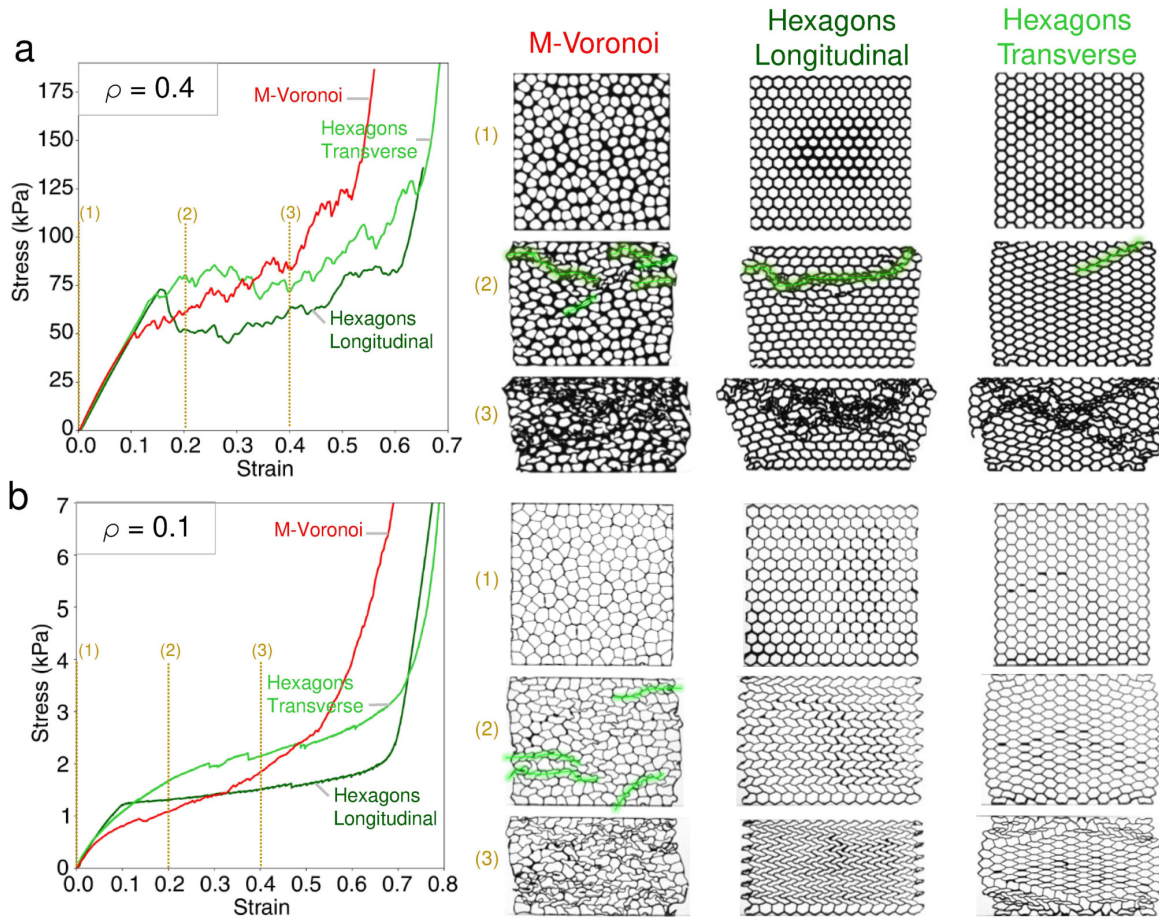


Figure 4.32: Compression experiments and corresponding optical images for the M-Voronoi, Honeycombs along the longitudinal and transverse direction for two relative densities (a) $\rho = 0.4$ and (b) $\rho = 0.1$. For all cases, snapshots are shown of the three relevant geometries selected at three intermediate strains levels, denoted with (1), (2) and (3). The green lines indicate zones of strong localization and fracturing of the intervoid ligaments. The in-plane dimensions of the undeformed specimens are $100 \times 100 \text{ mm}^2$. The values of stress and strain correspond to their nominal or engineering values.

geometry exhibits a remarkably uniform local bifurcated pattern up to very large strains showing no apparent localization band (see also [Ohno et al. \(2002\)](#) for corresponding theoretical results). Obviously this response is strongly related to the use of a base polymer material instead of a metallic one. In the latter case, the longitudinal hexagon geometry only shows such local bifurcated patterns in a fairly short region of straining before plastification beyond which localization bands and crushing appears ([Papka and Kyriakides, 1994](#); [Ashby and Gibson, 1997](#); [Papka and Kyriakides, 1998](#)). In turn, the

transverse hexagon geometry exhibits localization bands originating from the boundaries in the present case.

In closing, we observe that the M-Voronoi geometry, although softer initially, overcomes both the longitudinal and transverse honeycomb curves as a result of its strong hardening. In this lower density case, as expected from the early studies of [Ashby and Gibson \(1997\)](#), the hardening of the polymer material leads to a slight hardening of the hexagonal geometries (see Figure 4.2 in that reference). Yet, that mild hardening, which is a direct result of the stable post-buckling response of the honeycombs, remains substantially lower than that exhibited by the M-Voronoi. At this point, one may also comment on the possible imperfection sensitivity of the random *versus* periodic geometries. The M-Voronoi, RSA and E-Voronoi geometries are expected to be relatively insensitive to small imperfections owing to their intrinsic randomness, while it is intuitively straightforward to assume that the very uniform deformation process of the longitudinal hexagonal material in Figure 4.32b may be lost under the presence of fabrication imperfections (such as missing or of varying thickness ligaments) or leading to an even less pronounced hardening response. Nonetheless, such claims need to be further confirmed by experiments along such directions. Such an analysis is beyond the scope of the present study.

4.5.5 Anisotropic M-Voronoi

As already discussed in Section 3.7, anisotropic M-Voronoi geometries can be obtained using a rectangular cell subjected to biaxial deformation where principal stretches are not equal $\lambda_1^{\text{app}} \neq \lambda_2^{\text{app}}$ and the deformation ratio (anisotropy parameter) is defined as $\eta = \lambda_1^{\text{app}}/\lambda_2^{\text{app}}$. We assess the effect of anisotropy by designing two anisotropic M-Voronoi with $\eta = 2, 4$ and $\rho = 0.3$. In Figure 4.33, we observe that the initial linear response of the anisotropic M-Voronoi geometries in the longitudinal direction becomes stiffer with increasing η as compared to the the corresponding transverse direction as well as the isotropic one (shown again here for completeness). Subsequently, the anisotropic M-Voronoi exhibit buckling at lower stresses with increasing η in both directions but maintain a hardening response at large strains, even though the hardening slope tends to decrease with increasing η . Interestingly, one can observe that significant fracturing occurs in the longitudinal direction but substantially less in the transverse direction which is rather soft. We conclude this discussion by the most important observation in the context of this figure which is that the isotropic response, although slightly more compliant in the initial linear regime, leads to the larger buckling stress loads as well as overall the stiffest and with largest hardening rate response throughout the deformation process.

4.6 Numerical results and discussions

In this section, we study numerically the designed random geometries under large strain compression loading and try to simulate the experimental results. We use the commercial FE solver ABAQUS (Dassault system) to deal with nonlinear finite strain simulations.

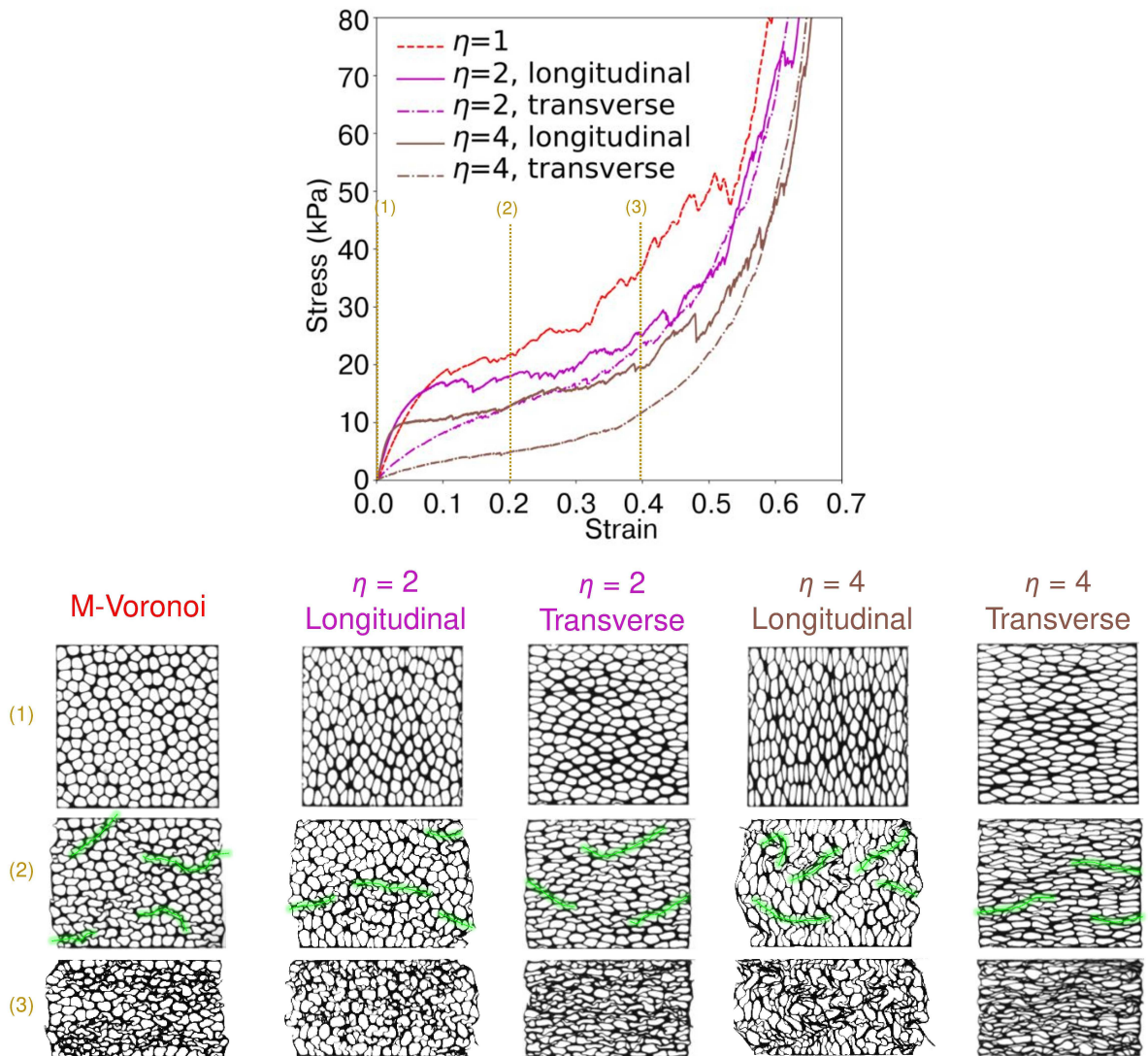


Figure 4.33: Compression experiments and corresponding optical images for the isotropic and anisotropic M-Voronoi along the longitudinal and transverse direction for $\rho = 0.3$. For all cases, snapshots are shown of the three relevant geometries selected at three intermediate strains levels, denoted with (1), (2) and (3). The green lines indicate zones of strong localization and fracturing of the intervold ligaments. The in-plane dimensions of the undeformed specimens are $100 \times 100 \text{ mm}^2$. The values of stress and strain correspond to their nominal or engineering values.

Due to the complexity of the geometry, large compressive deformations, and contact between the cells, Abaqus/Standard (Implicit) solver is unable to simulate the deformations and it stops as soon as the first cell collapses and the cell walls contact. Consequently,

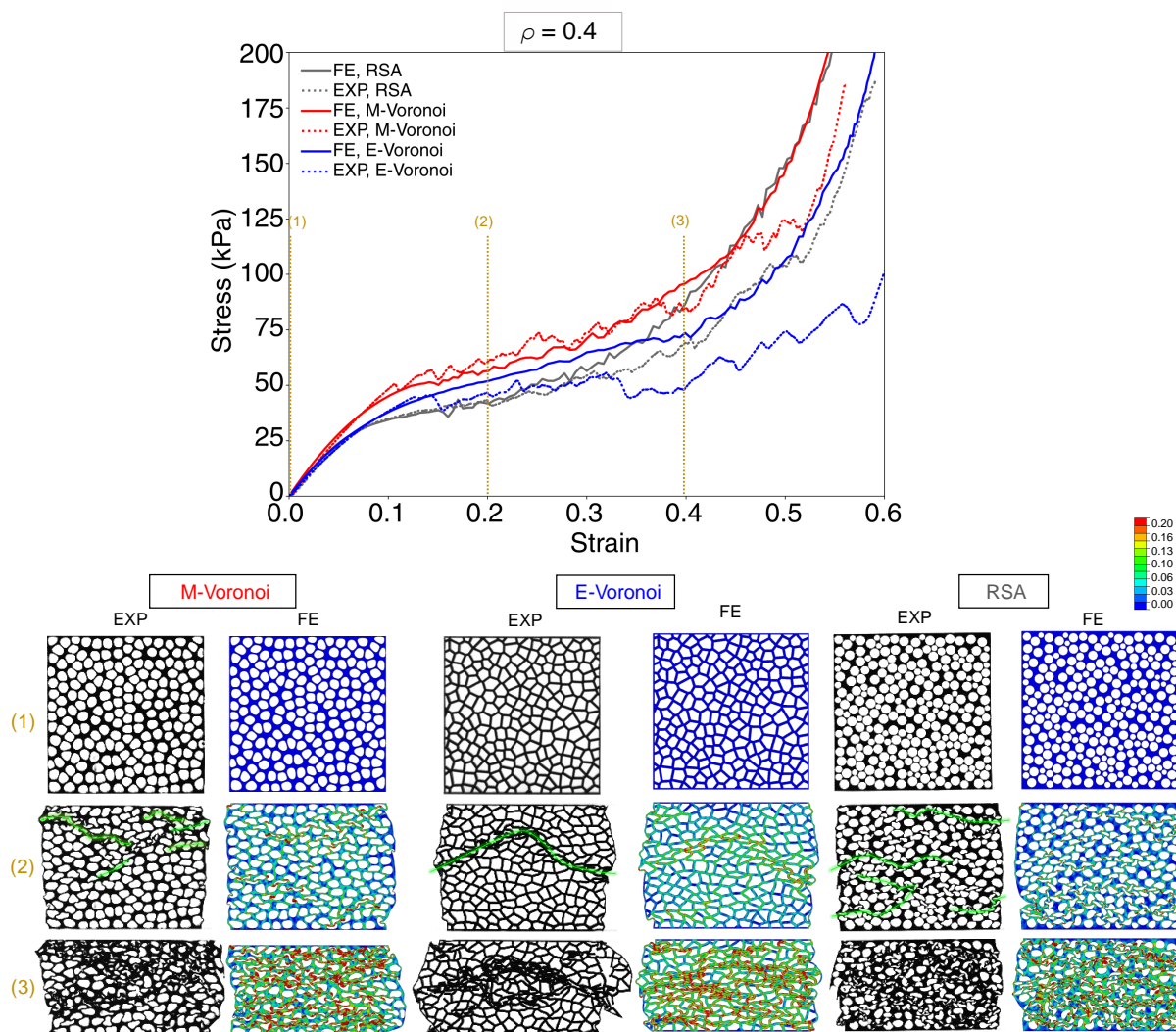


Figure 4.34: Comparison between the compression experimental and numerical results for the M-Voronoi, E-Voronoi and RSA geometries for relative density 0.4. For all cases, snapshots of the experimental samples and numerical geometries are shown of the three geometries selected at three intermediate strain levels, denoted with (1), (2) and (3). The legend indicates the maximum principal logarithmic strain values. The green lines indicate zones of strong localization and fracturing of the intervoid ligaments. The values of stress and strain correspond to their nominal or engineering values.

we use the Abaqus/Explicit solver to simulate the deformations and material behavior (see Section 5.4 for more discussion). Nevertheless, the Abaqus/Explicit solver requires three-dimensional elements to deal with the contact between the cells by activating the

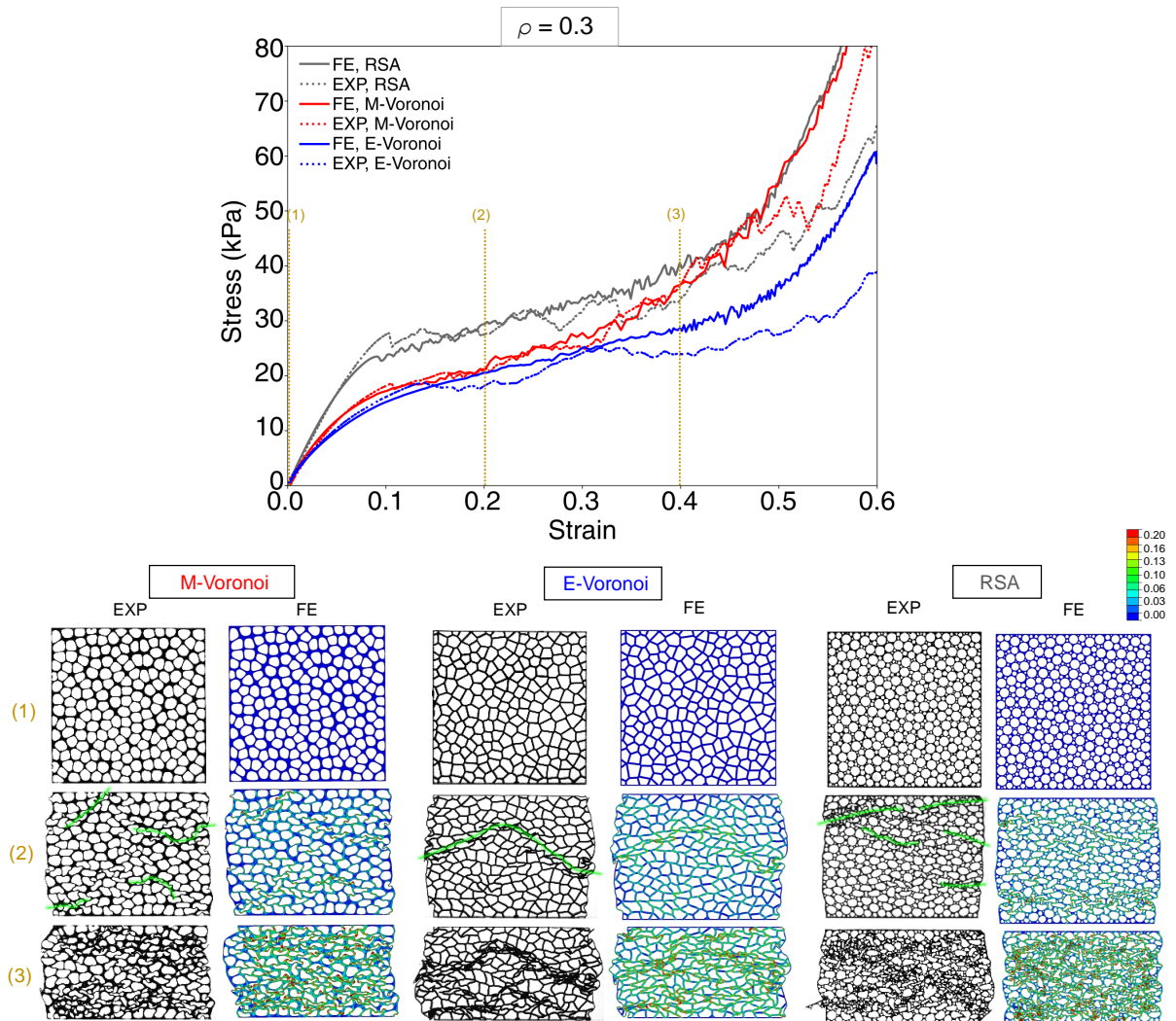


Figure 4.35: Comparison between the compression experimental and numerical results for the M-Voronoi, E-Voronoi and RSA geometries for relative density 0.3. For all cases, snapshots of the experimental samples and numerical geometries are shown of the three geometries selected at three intermediate strain levels, denoted with (1), (2) and (3). The legend indicates the maximum principal logarithmic strain values. The green lines indicate zones of strong localization and fracturing of the intervold ligaments. The values of stress and strain correspond to their nominal or engineering values.

command Contact inclusions, All exterior. We developed an algorithm to extrude the two-dimensional meshes in an out-of-plane direction. A sufficient number of brick elements C3D8 are used to mesh the domain. Due to the small strain rate, TangoBlack is considered

an incompressible Neo-Hookean material with Young's modulus of 3.92 MPa and Poisson's ratio of 0.49 (see Section 4.2.11 for more discussion on material modeling). It has been determined that the time increment is sufficiently small to guarantee compliance with the quasi-static requirement while running within an acceptable time frame. As an example, a mesh containing brick elements and 360 000 nodes (DOF) requires approximately 60 hours of running time with 40 cores in parallel.

During real compression tests, random geometries encounter a variety of phenomena, including buckling, contact, fracture, and shear. In addition, every ligament within a random porous geometry is subjected to a complex set of stresses. Therefore, modeling the fractures occurring in TangoBlack ligaments is not an easy task. Although in our simulation, neither fracture nor buckling criteria are defined, the comparison between the experimental and numerical results shows a fairly good agreement. Figures 4.34 and 4.35 represent the stress-strain results obtained from the numerical and experimental studies at $\rho = 0.4, 0.3$. Moreover, a side-by-side comparison is performed between the deformations of the real test sample and the simulated random geometry. Generally, we observe great consistency between the numerical and experimental stress-strain results for M-Voronoi and RSA geometries. However, there is a larger deviation for E-Voronoi geometries. E-Voronoi simulations at large strains show a stiffer response at both densities. This discrepancy might be due to two factors. First the imperfections during 3D-printing process create a non-uniform ligament thickness, leading to early cell collapse. Secondly, the deformation of the E-Voronoi is fracture dominant and there is a collapsed row of broken cells at intermediate strain values. Consequently, the absence of fracture modeling may result in a numerically stiffer response. It is interesting to note that when comparing the deformation patterns in side-by-side numerical and experimental deformed geometries, there is a remarkable consistency in the localized deformation, especially at moderate strain levels. At both densities, a localized collapsed cell row (green lines) is observed in E-Voronoi geometries. Moreover, an identical deformation distribution is observed in the numerical results of the M-Voronoi and RSA geometries. In spite of this, we note that due to the absence of fracture modeling, the deformation patterns at larger strains deviate from those observed in experiments since more fracture is involved.

4.7 Concluding remarks

We characterize the viscoelastic behavior of a brittle soft polymer material called TangoBlack by performing different mechanical tests such as tensile, loading-unloading and relaxation tests. In contrast to the reported material properties provided by the manufacturing company, who do not provide strain rate information, we observed highly rate dependent mechanical properties in the TangoBlack materials. We used the rubber viscous incompressible hyperelastic model proposed by Kumar and Lopez-Pamies (2016), to characterize the mechanical behavior of the TangoBlack material. The study of the ultimate tensile properties of the TangoBlack material shows a short equilibrium stress response at small strains followed by a fracture envelope spanning 90% strain ranges.

We showed that TangoBlack can be characterized by simple incompressible Neo-Hookean material modeling at low strain rates or small strain values.

The TangoBlack material is used as a base polymer matrix to manufacture porous polymer materials. In order to achieve sufficient specimen quality, we propose an interruption program during 3D-printing which consists in alternate additive manufacturing and interruption time increments. The resulting porous specimens are then experimentally tested under uni-axial compression. In particular, the newly proposed M-Voronoi materials exhibit a strong hardening behavior under compressive loads as compared to RSA and E-Voronoi geometries, which tend to exhibit either a peak stress and a plateau or only weak hardening for most of the deformation process before final densification. This hardening response is mainly a consequence of three geometrical characteristics: (i) the randomness of the void geometries, (ii) the non-uniformity of the intervoid ligaments and (iii) the smooth void geometry reducing efficiently stress localization. In addition, the randomness of the M-Voronoi geometry makes these materials less sensitive to imperfections and realization variations. Nevertheless, a more detailed study is required along this direction perhaps including additional loading conditions such as tensile and hydrostatic ones ([Tankasala et al., 2017](#)).

Chapter 5

M-Voronoi in 3D

Chapter summary: In this chapter, the 2D M-Voronoi morphogenesis process is extended into 3D space to obtain random smooth polygonal inclusions. A similar procedure has been followed in order to create 3D M-Voronoi geometries. However, in order to create periodic M-Voronoi, periodic boundary conditions have been applied. To achieve the full density range, an intermediate remeshing step is required to improve the mesh quality. This has been performed by generalizing the developed 2D remeshing algorithm into 3D space. We investigate numerically the random 3D M-Voronoi, RSA, and Gyroid geometries under large compressive deformations while considering the matrix as an elastic-perfectly plastic material without hardening. We observe delayed yield stress and enhanced plastic response in structures with random voids.

Contents

5.1	The M-Voronoi morphogenesis method in 3D	126
5.2	Geometry reconstruction and Remeshing in 3D	129
5.2.1	Description of 3D remeshing algorithm	129
5.2.2	The span of the 3D remeshing technique	133
5.3	Attainable relative density in 3D M-Voronoi	135
5.4	Large strain simulation of 3D M-Voronoi	137
5.4.1	Plasticity in random and periodic structures	138
5.5	Concluding remarks	145
5.A	Appendix A. Algorithms for remeshing a 3D orphan mesh by constructing the geometry	146

5.1 The M-Voronoi morphogenesis method in 3D

This section describes the computational morphogenesis process and its steps to obtain 3D M-Voronoi porous materials. The M-Voronoi morphogenesis process in 3D is an extension of 2D M-Voronoi process described in Section 3.1 by prescribing the 3D objects. The main steps are identical with minor differences discussed in the following.

Step 1: Construction of the initial porous cell. Similar to the 2D morphogenesis method of M-Voronoi geometries, the void growth process begins with the construction of an initial porous unit-cell (Figure 5.1). We remind that the choice of the unit-cell shape and size is arbitrary and will affect the final porous geometry. Furthermore, the unit-cell can comprise voids with any shape, size, or orientation. Once again, it should be noted that the initial volume fraction of the voids is denoted as c_0 which is related to the initial density $\rho_0 \equiv 1 - c_0$. For illustration purposes, we consider a simple case where the voids are equal-sized spheres and randomly distributed in the matrix. Here, the 3D random sequential absorption (RSA) algorithm (Section 2.2) is employed to create 3D random porous unit-cells. Also, for simplicity, a cubic unit-cell with $1 \times 1 \times 1$ dimension is considered and all deformed geometries will be rescaled to this dimension. We note again that the unit dimensions of the cell are inconsequential and are only chosen for simplicity.

Step 2: Periodic displacement boundary conditions. In order to ensure the periodicity of the final geometry, the unit-cell is subsequently subjected to periodic displacement boundary conditions (PBC) over the entire cell boundary $\partial\mathcal{V}_0$ (Figure 3.1). All finite strain kinematics and constitutive laws are identical with 2D M-Voronoi method and the deformation gradient tensor is again defined as $\mathbf{F} = \partial\mathbf{x}/\partial\mathbf{X} = \mathbf{I} + \text{Grad}\mathbf{u}$, where $\mathbf{u}(\mathbf{X})$ denotes the displacement vector of any material point between the reference and deformed configurations. The definition of periodic displacement boundary conditions implies that the displacement field is periodic about an average strain field. Therefore, the displacement field can be split into the average strain field and a correction $\mathbf{u}^*(\mathbf{X})$ which accounts for the presence of heterogeneities (see Michel et al. (1999) and Mbiakop et al. (2015)). We then impose the periodic boundary conditions

$$\mathbf{u}(\mathbf{X}) = (\mathbf{F}^{\text{app}} - \mathbf{I})\mathbf{X} + \mathbf{u}^*(\mathbf{X}), \quad \forall \mathbf{X} \in \partial\mathcal{V}_0, \quad (5.1)$$

where $\mathbf{u}^*(\mathbf{X})$ represents an L-periodic displacement field that accounts for the field fluctuations and has volume average equal to zero such that $|\mathcal{V}_0|^{-1} \int_{\mathcal{V}_0} \mathbf{u}^*(\mathbf{X}) d\mathbf{X} = 0$. Evidently, the components of $\mathbf{u}^*(\mathbf{X})$ have identical values at points on the opposite faces of the unit-cell. In order to eliminate rigid body motion in the FE calculations, it is further necessary to fix a corner node of the unit-cell (Danas, 2017). Moreover, to prevent the wavy boundaries of the unit-cell, the LEFT, BOTTOM, and BACK sides have no deformation in e_1 , e_2 , and e_3 directions, respectively. Similar to Section 3.1, \mathbf{F}^{app} is a prescribed, constant, *non-symmetric* second-order tensor with nine independent components in 3D. Also,

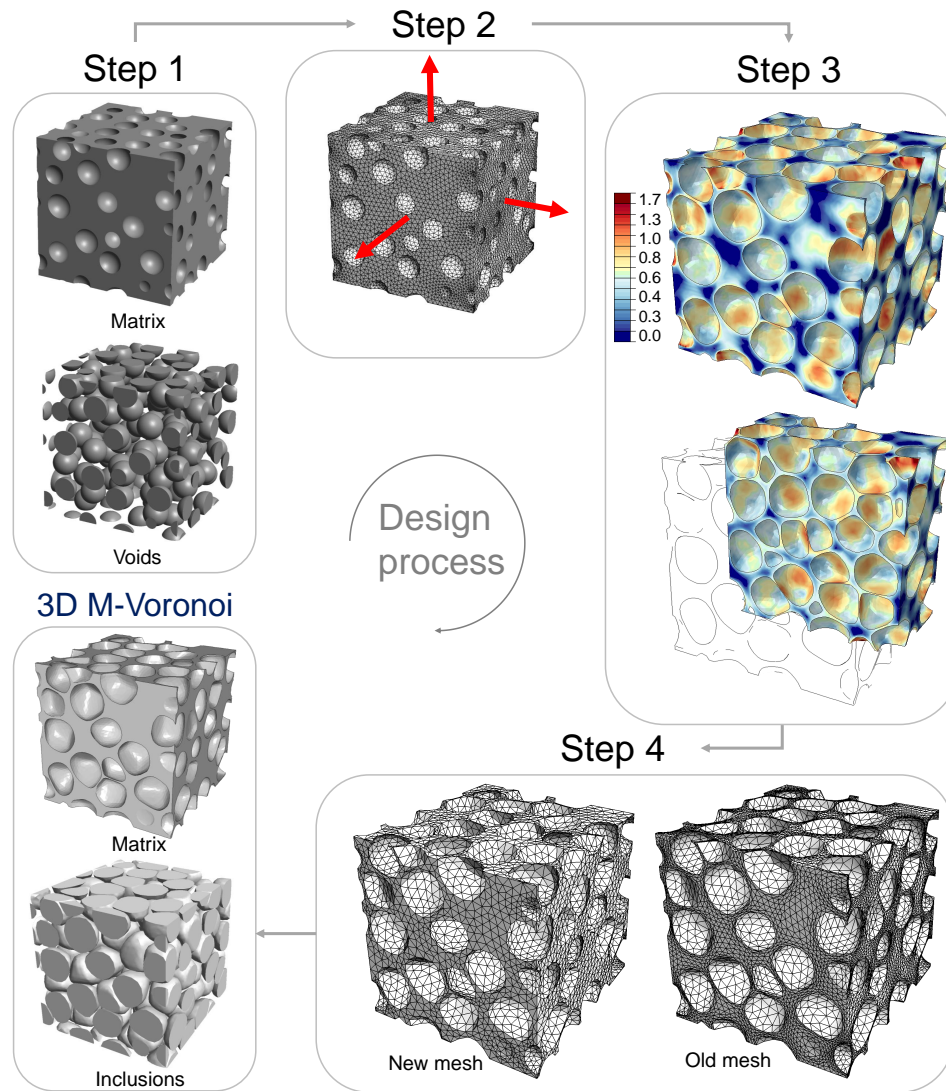


Figure 5.1: Computational process for the generation of the 3D M-Voronoi material. For illustration purposes, the diagram shows the four steps required to obtain a virtual M-Voronoi geometry starting from a cubic unit cell containing a discrete number of mono-sized spherical voids. **Step 1:** Random distribution of spherical voids in a cubic domain with initial relative density $\rho = 0.7$. **Step 2:** Application of displacement boundary conditions. **Step 3:** Numerical FE simulation at large strains using nonlinear elastic energy minimization and incompressible matrix behavior. The final relative density corresponds to $\rho = 0.3$. The cut image shows inside of the deformed geometry. The color bar indicates the maximum principal logarithmic strain. **Step 4:** Remeshing and uniform re-scaling of the deformed geometry to the desired size. The final 3D M-Voronoi and its containing inclusions are uniformly re-scaled to the size of the initial geometry.

$\det \mathbf{F}^{\text{app}} > 1$ is the first void growth condition of the voids. The second condition for the growth of voids is provided by the material characteristics described in the next step.

We note that one can prescribe the uniform Dirichlet(affine) boundary conditions to have the same void growth as described in Section 3.1. Such deformations lead to non-periodic M-Voronoi geometries and are especially applicable to non-periodic unit-cell shapes such as: triangular and quadrilateral in 2D and cylindrical or others in 3D.

Step 3: Nonlinear elastic energy minimization. We trigger the mechanical growth of the voids by solving numerically a finite-strain (Figure 5.1), nonlinear elastic boundary value problem (BVP), whose geometry is defined in Step 1 and applied boundary conditions in Step 2. For this, we use the finite element (FE) method with commercial ABAQUS software and material properties described in Step 3 of Section 3.1. In contrast to the 2D M-Voronoi method, we apply periodic boundary conditions to solve the minimization problem such that $\mathcal{K}(\mathbf{F}^{\text{app}}) = \{\mathbf{u} : \text{regular}, \mathbf{u} = (\mathbf{F}^{\text{app}} - \mathbf{I}) \mathbf{X} + \mathbf{u}^*, \forall \mathbf{X} \in \partial \mathcal{V}_0\}$. Moreover, quadratic 10-node, three-dimensional (3D) hybrid elements (C3D10H) are used to deal with incompressibility. Similarly, given the incompressibility of the solid phase, the purely kinematic relation 3.5 is governed between the initial ρ_0 and final relative density ρ of the unit-cell (see 3.2).

As can be easily observed in the example problem in Figure 5.1, the voids grow substantially exhibiting 3D convex, polyhedralized but smooth shapes. Their exact growth rate and final shape are a complex outcome of interactions with neighboring voids and the boundary of the cell. The thickness of the intervoid ligaments is highly variable, while dense pockets of solid phase are observed across the cell, as shown by the blue spot regions in Step 3 of Figure 5.1. The same dense pockets have been observed while studying the 2D M-Voronoi morphogenesis process in Step 3 of Figure 3.1. The cut view of the deformed M-Voronoi in Figure 5.1 also demonstrate that the deformation at a plane of the 3D geometry is similar to 2D M-Voronoi geometries.

Step 4: Void geometry extraction, rescaling and remeshing. The large strain simulations may lead to significant mesh distortion at various regions (see the right image in Step 4 of Figure 5.1). A final distorted mesh cannot be used for further numerical study or 3D-printing. Therefore, one may remesh the geometry (see remeshed figure on the left side of Step 4) without modifying the deformed geometry features. Also, severe mesh distortion might stop the simulation and prevent the final relative density to be achieved. In such cases, we need to extract the deformed mesh from the stopping point, remesh it, and re-start the calculation from that point on. Such an operation will allow us to reach very low relative densities even in 3D M-Voronoi as is discussed in Section 5.3.

The main strategy to remesh the distorted mesh is similar to the 2D remeshing method described in Section 3.3.1. In this strategy, the deformed mesh is exported using an Abaqus python script and the geometrical entities, such as void boundaries and cell boundaries, are read by a custom-made code. However, the algorithm to reconstruct the deformed geometry and remesh is substantially different in 3D geometries. The new

mesh is subsequently *uniformly* rescaled back to any desired size while preserving the relative density (see the re-scaled 3D M-Voronoi in Figure 5.1). The remeshing algorithm employed in this step is discussed in Section 5.2.

5.2 Geometry reconstruction and Remeshing in 3D

In this section, we extend the 2D remeshing algorithm in Section 3.3.1 to 3D mesh and geometries. The main steps of the algorithm are identical to those of the 2D method, and here we are only discussing the differences. The main difference involves the shape of 3D elements and the construction of 3D objects. Particularly, the free surfaces of polyhedral element shapes are identified rather than the free edges of polygonal elements. Similar to the 2D method, we developed a Fortran code for the remeshing algorithm, which is based on the open-source meshing software `Gmsh`. The corresponding Python version follows a slightly different algorithm to connect the free surfaces and will be discussed later. The advantages of the proposed remeshing algorithm over the existing tools are discussed in Section 3.3.

5.2.1 Description of 3D remeshing algorithm

In the following, we summarize the steps of the algorithm focusing on the differences with the 2D method (Hooshmand-Ahoor et al., 2022). The steps are also summarized in Figure 5.2. For illustrative purposes, we consider a simple 3D geometry containing a single spherical void in the middle.

Step 1: Importing the orphan mesh and reading the nodes and elements. Similarly, we read the nodes and elements data of the orphan mesh and store them to the corresponding matrices. We define matrices $\mathbb{N}_{n \times 3}$ and $\mathbb{M}_{m \times h}$, containing all nodes coordinates and element connectivity information, respectively. Here n denotes the number of nodes, m is the number of elements and h is the number of nodes at each element which will vary depending on the type and order of the elements. In addition, we have considered tetrahedron and brick element types with linear or quadratic element orders. Therefore, $h = 4, 8, 10, 20$. One can extend this method to the triangular prism element type. It should be noted that unlike the 2D remeshing algorithm described in Figure 3.6, here we do not reorganize the quadratic element orders. Step 1 in Figure 5.2 represents an orphan mesh of a matrix containing one spherical void, where the right side image shows a cut view of the mesh.

Step 2: Finding the free surfaces of the elements. The resulting geometry from the remeshing algorithm will be written in `Gmsh` format and can be further converted to various CAD versions. `Gmsh` allows building a complex 3D closed volume by connecting a series of planes, which are the surface planes that make the exterior boundary of the volume.

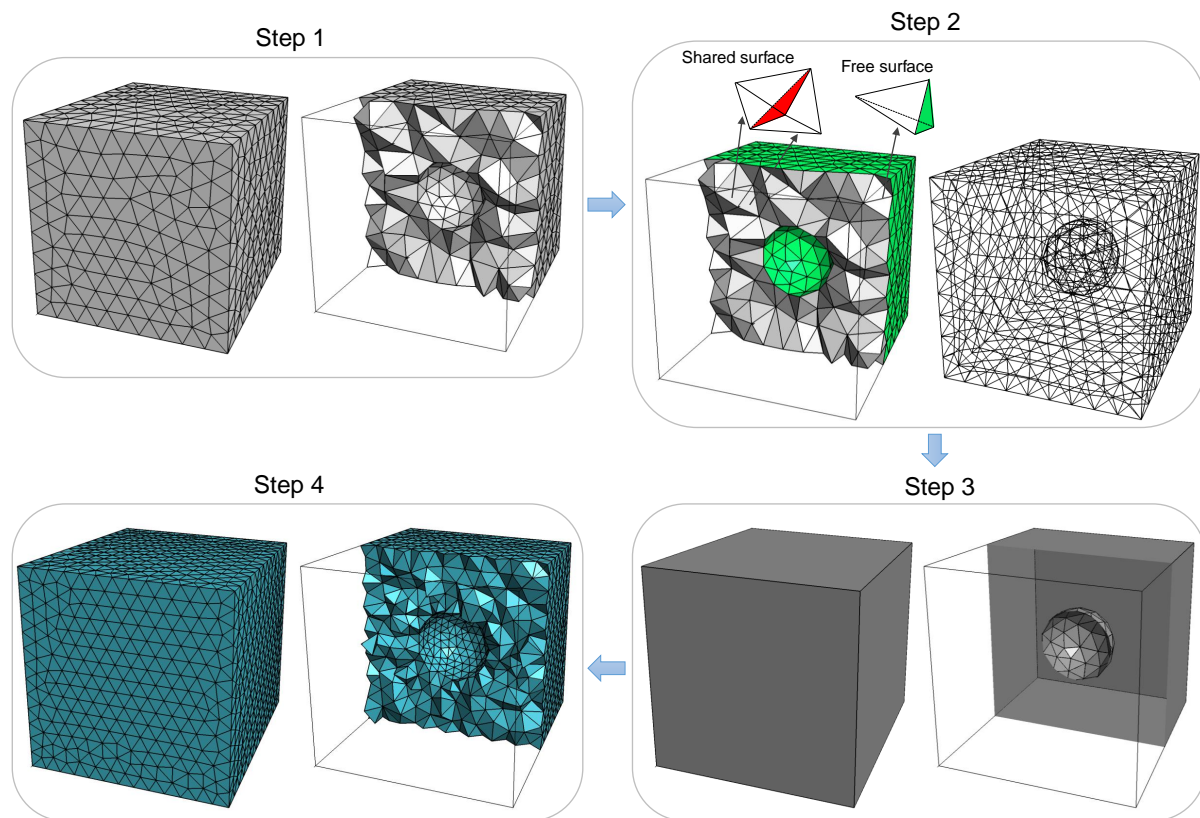


Figure 5.2: 3D remeshing algorithm for an orphan mesh based on geometry reconstruction. For illustration purposes, a simple 3D orphan mesh containing a spherical void is demonstrated. The diagram shows the four steps required to remesh an orphan mesh. **Step 1:** Reading the nodes and elements of the orphan mesh. **Step 2:** Finding the free surfaces of the elements. The green color corresponds to accepted free surfaces, whereas the red regions are rejected shared surfaces. **Step 3:** Constructing the geometry of the orphan mesh. **Step 4:** Remeshing the new mesh with an arbitrary mesh algorithm.

The free surfaces of an orphan mesh can be distinguished from the shared surfaces of a given element by their inherent feature, which is that they belong only to that element. A shared surface of an element, on the other hand, is shared by two elements at the same time. The left image of the **Step 2** in Figure 5.2 displays the identification process of the free surfaces. The green surfaces correspond to the free sides of the individual elements and the red surfaces denote the shared side of tetrahedron elements. The right image of **Step 2** shows all identified free points (nodes) and element surfaces of the orphan mesh. These surfaces will construct the geometry in the next step.

The algorithm for finding the free surfaces of an orphan mesh is described in Algorithm 3 in Appendix 5.A. This process consists of two main loops that compare the nodes at

each surface of an element with all other elements. Consequently, the surfaces that are not in common between two different elements are identified and stored as free surfaces. We consider that each surface of an element contains 3 or 4 nodes for the tetrahedron or brick element type. In the case of quadratic elements, the middle nodes are identified according to the corner nodes. To speed up the loops, we defined a matrix that contains the elements connected to each node in order to limit the search over all elements, which results in a significant improvement in the speed of the algorithm. Similar to the 2D remeshing algorithm, the free surfaces are stored in the matrix $\mathbb{S}_{f \times r}$, where f denotes the total number of free surfaces and $r = 3, 4, 6, 8$ corresponds to the number of nodes on every side of elements and will vary depending on the element type and order. It is noted that the type and order of the elements are determined as input by the user.

Step 3: Constructing the 3D geometry by the free element sides. Once the free surfaces have been identified in **Step 2**, they must be organized and connected in order to construct the closed volumes of the 3D geometry. Similar to 2D geometry reconstruction, geometry entities are built in a bottom-up manner (first points, then curves, surfaces, and volumes) with the built-in OpenCASCADE kernel of the geometry module in the open source software **Gmsh** (see Figure 3.8). Following a similar approach, we construct the geometry volumes by connecting the free surfaces built up from the free points and curves. The algorithm is implemented in the Fortran and Python languages, where the Python version follows a different approach to the geometry construction step. Different methods are employed specifically to reduce the running time required to construct the geometry, which has been found to be much longer in the Python format with an almost identical algorithm. Here, we will be focused on the algorithm used in the Fortran version and will discuss briefly the differences with the Python algorithm.

In contrast to the 2D method, geometry reconstruction in 3D requires a different approach. In the former case, each free line is connected to only two lines, whereas in 3D, each surface is surrounded by more than two surfaces. Initially, the Fortran algorithm starts with the first free surface $s_1 \in \{s_1, s_2, \dots, s_f\}$ ¹ and then finds the second free surface connected to it, which is determined by the line in common between the two neighboring surfaces. As a result, there are three possible scenarios when a second free surface is identified. Figure 5.3 represents an example of three different cases of newly identified free surfaces displayed in red color. In this figure, the previously constructed surfaces are shown in gray. We consider **Noderef 1** and **Noderef 2** to be two reference nodes, from which the new red surface is constructed. The third node of the newly added surface corresponds to **Noderef 3**, which is connected to the reference nodes by **Line 23** and **Line 13**. Depending on the repetition of the new geometry entities **Noderef 3**, **Line 23**, and **Line 13**, three different cases exist. In the first case, all new entities are not previously constructed and have to be newly added to the geometry. In the second case, only one line will be added to the geometry and finally, in the last case, all entities are already constructed and one needs to only add a new surface from the constructed entities. The process will

¹ $s_i = \mathbb{S}(i, r)$

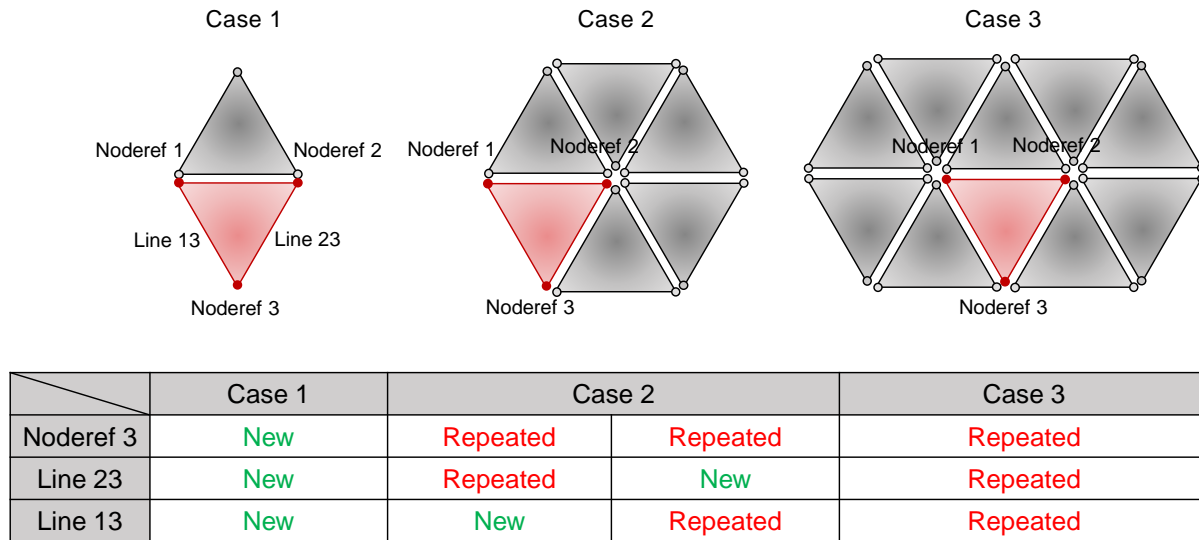


Figure 5.3: Three possible scenarios in the geometry construction method of the Fortran algorithm. New and old identified free surfaces are shown in red and gray, respectively. Noderef 1 and Noderef 2 are two reference nodes, from which the new red surface is constructed. The new surface is characterized by three geometry entities, Noderef 3, Line 23 and Line 13. The table shows the conditions in each case. **Case 1:** All three entities are new. **Case 2:** only one line of the new surface is new. **Case 3:** All three entities were previously added.

continue until all free surfaces have been investigated. The distinction between different closed volumes $v_i \in \{v_1, v_2, \dots, v_N\}$ of the geometry is performed by checking whether all lines of the free surfaces are investigated. If no free line remains, the volume will be closed and the process continues to construct a new volume until all N volumes are identified. We note that this method requires all data of previously existing entities of the geometry and thus might be time-consuming. However, to speed up the process, we have limited the search over all elements by looping over the defined matrix in **Step 2**, which contains the elements connected to each node. Therefore, the construction process even with extremely complex geometry will not exceed a few seconds. This algorithm is summarized in Figure 5.4 and described in Algorithm 4 in Appendix 5.A.

Similar to the 2D remeshing method, multiphases can be identified when there are either voids or particles or a combination of both. We apply `Boolean` operators (from `Gmsh` OpenCASCADE kernel) to the 3D geometry volumes to distinguish or remove them. Similarly, we use `BooleanDifference` and `BooleanFragments` operators to create empty voids or particles, respectively (see Figure 3.10). We note that the largest volume must be determined to allocate the matrix phase to it. This has been done by evaluating the coordinates of different volumes when all volumes are detected.

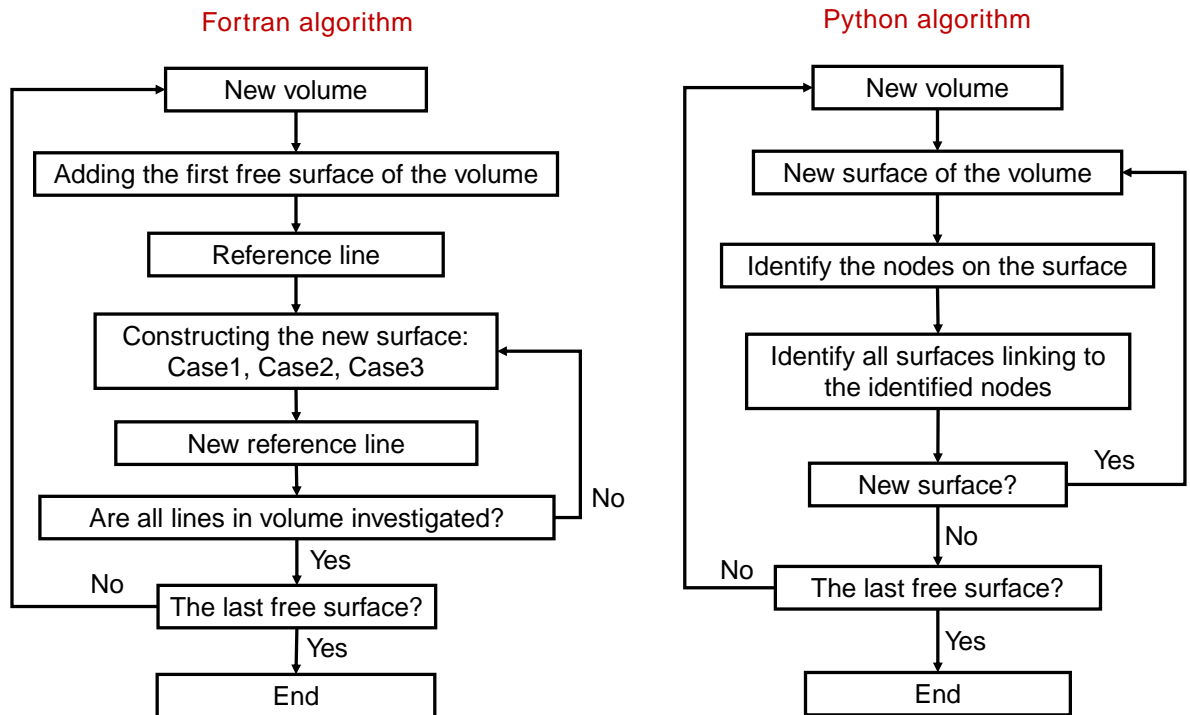


Figure 5.4: Flowchart of 3D geometry reconstruction from the identified free surfaces of an orphan mesh with Fortran and Python versions of the algorithm

Step 4: Exporting the geometry, rescaling and remeshing. The constructed 3D geometry is written in Gmsh .geo format and is built based on the bottom-up manner (see Figure 3.8). It can be subsequently converted into any CAD version or meshed with an arbitrary method. Specifically, in contrast to the other existing remeshing methods, having the geometry gives a high level of control over the output mesh type. Either the final geometry or new mesh can be uniformly rescaled back to a specific size by multiplying a fixed calculated scaling number by all coordinate components of points created in the geometry. In our study of 3D geometries, the new mesh is created with Gmsh software and is exported as an Abaqus input file (.inp) for simulations with different element types and orders.

5.2.2 The span of the 3D remeshing technique

In spite of the flexibility of the proposed remeshing method, here we state the limitations of this approach. The proposed remeshing method is applicable to all element types with linear order. Also in practice, one can approximate the quadratic elements with the corresponding linear type, by connecting the corner nodes and ignoring the middle nodes. However, this will lead to a minor difference ($< 3\%$ depending on the mesh size) between

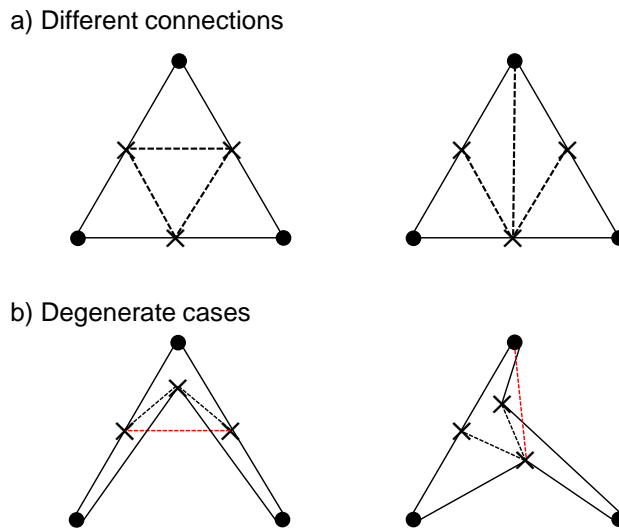


Figure 5.5: The limitations of the 3D remeshing algorithm in the case of quadratic elements. (a) The possible node connection methods for a free surface of a quadratic tetrahedral element type. We note that the nodes are not in the same plane. (b) The degenerate cases of each connection method when excessive element distortion exists. In both cases, the red line overlaps the neighboring elements.

the actual volume fraction of different phases. In general, the reconstruction algorithm is found to have limitations when dealing with quadratic elements under very large deformations. Such limitations persist even with linear approximations of the elements. In contrast to linear elements, the points of a surface in a deformed 3D quadratic element are not in the same plane. One can construct the deformed surface by connecting the triangular planes built up of three nodes. Therefore, the middle nodes of quadratic elements must be connected properly to construct the 3D element surface.

In Figure 5.5a, two possible connection methods for points on a free element surface are shown, where the corner and middle nodes are represented by solid circles and crosses, respectively. It is important to note that the points are not on the same surface. The 3D surface is then constructed by connecting four triangular surfaces. It has been observed that both of the proposed connection methods can accurately (without any approximation of volume fraction) construct the deformed geometry up to excessive distortions of the elements. Large deformations in the geometry, whether local or global, may cause the elements to be distorted such that both approaches will not work. Figure 5.5b represents the degenerate cases of each approach. In both cases, the red line is overlapping the neighboring elements and subsequently, the geometry construction will be unsuccessful. Such distortions are mainly present at low densities $\rho < 0.2$. In order to avoid such limitations, two approaches can be followed: 1-the simulation can be stopped before

excessive element distortion and the deformed mesh can be remeshed (with or without stress mapping) to improve the quality of the elements. 2-the quadratic elements can be approximated by linear type. We note that the second approach will add a small error to the final volume fraction and might not work if the elements are highly distorted.

Subsequently, we discuss the required time and feasibility of the proposed algorithm. In practice, both of the `Fortran` and `Python` construction methods will take less than two minutes to read the orphan mesh, rebuild the geometry and write it to the `Gmsh` format. When there are quadratic elements or degrees of freedom (DOF) greater than 500 000, this time may increase to five or ten minutes, depending on the mesh size. Therefore, we consider the algorithm processing time reasonably fast and feasible for practical use. However, the time required for `Gmsh` to read and construct the geometry is substantially larger and in some cases not feasible. As an example, the required time for the geometry to be built corresponds to approximately two hours for DOF 200 000. This time will vary depending on computer power or the number of voids/particles in the mesh. One can reduce the required time considerably by approximating the quadratic elements in linear order. Moreover, we have realized that the intermediate remeshing step will also reduce the DOF and, thus, the time required to complete the remeshing process.

5.3 Attainable relative density in 3D M-Voronoi

In this study, we apply the discussed 3D morphogenesis process to obtain 3D M-Voronoi geometries in a cubic domain. It is important to note that the geometry choice for unit-cells is generally not limited to the cubic shape. Nevertheless, due to the periodicity requirement, we specialize in cubic unit-cells with diagonal deformation loads, i.e., $\mathbf{F}^{\text{app}} = \text{diag}(\lambda_1^{\text{app}}, \lambda_2^{\text{app}}, \lambda_3^{\text{app}})$ (with $\lambda_1^{\text{app}}, \lambda_2^{\text{app}}, \lambda_3^{\text{app}}$ denoting the applied principal stretch). In order to ensure void growth, one has to apply deformation such that $\det \mathbf{F}^{\text{app}} > 1$, where $\lambda_1^{\text{app}}, \lambda_2^{\text{app}}, \lambda_3^{\text{app}} \geq 1$ to have tensile deformation in all directions.

Similar to the 2D M-Voronoi geometries, the 3D M-Voronoi geometries are numerically and experimentally realizable at solid densities spanning the full spectrum from 1 to very low (e.g., 0.01). However, in order to obtain very low relative densities $\rho < 0.2$, it is required to perform intermediate remeshing to assist the simulation going to final relative densities. As we discussed previously in Section 3.3, the excessive distortion of elements is the main reason for the early termination of simulation in large strain calculations. Such deformations prevent the 3D M-Voronoi morphogenesis process to achieve the target porosity especially when large porosities are required. Initially, a good-quality mesh will facilitate the process, but very fine meshes are not suitable for large deformations that occur locally in complex geometries under large strains. This is due to the fact that they will be distorted and collapsed more quickly. Instead, a good quality mesh in large strain simulations refers to a smooth medium size mesh that is fine enough in thin regions. To do so, we use the Delaunay optimization algorithm in `Gmsh`, which automatically optimizes the quality of tetrahedra elements. Furthermore, a uniform mesh size distribution is performed over the curvature of sphere surfaces in the initial RSA geometry. Despite the

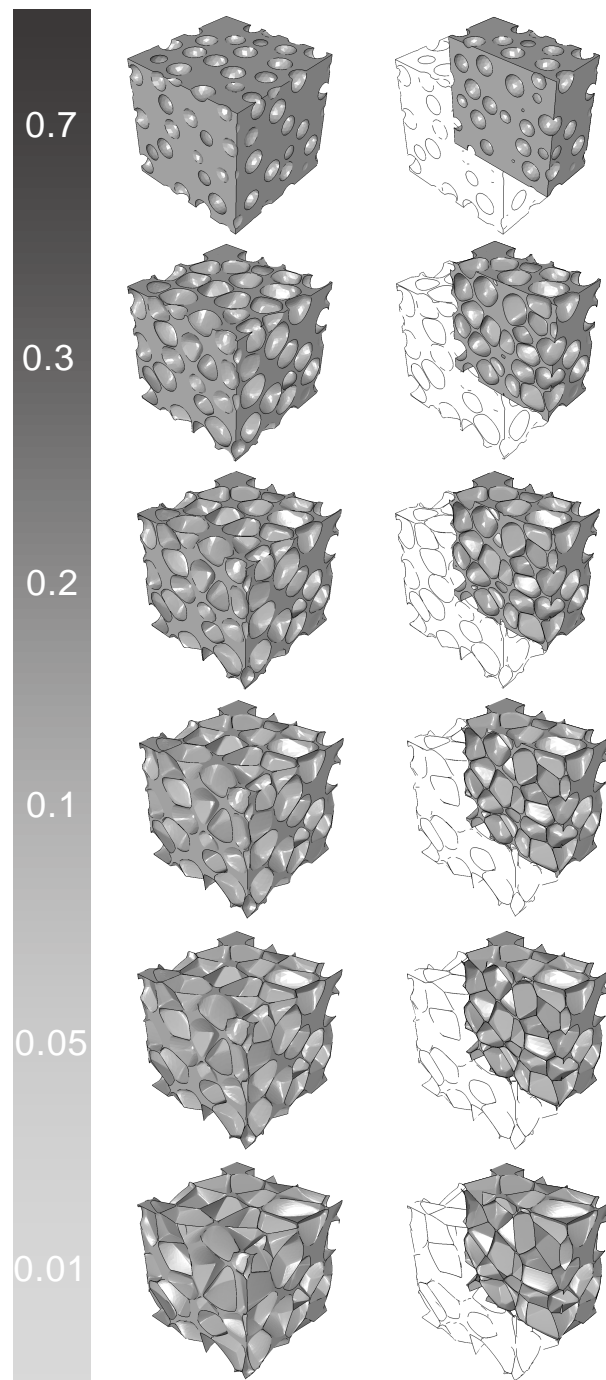


Figure 5.6: 3D M-Voronoi obtained by using RSA geometry with initial relative density $\rho_0 = 0.7$ (The first geometry). The color bar indicates the final relative density ρ and the right images represent the void shapes inside of the geometry. The densities $\rho > 0.2$ are obtained by using the corresponding $\rho = 0.3$ as an initial geometry after remeshing it.

significant assistance of the initial mesh quality, the simulation might stop under very large deformations. In this case, it is required to remesh the deformed geometry and resume the simulation with or without mapping the existing fields. Since we are solely interested in the geometric features and not in the calculated stresses, we remesh the deformed geometry without stress mapping. Such an operation has allowed us to reach very low relative densities as shown in Figure 5.6. This figure represents 3D M-Voronoi geometries obtained with tensile deformations $\lambda_1^{\text{app}} = \lambda_2^{\text{app}} = \lambda_3^{\text{app}}$. The initial relative density of the RSA geometry corresponds to $\rho_0 = 0.7$. Evidently, the 3D M-Voronoi geometries are numerically realizable at solid densities spanning the full spectrum from 1 to very low (e.g., 0.01).² In order to achieve the M-Voronoi with relative densities $\rho = 0.2, 0.1$, we have performed a remeshing on the M-Voronoi with $\rho = 0.3$ and resumed the process without mapping the stress fields. For lower relative densities i.e., $\rho = 0.05, 0.01$ a second remeshing is required on M-Voronoi with $\rho = 0.1$. As a result of the limitations of the remeshing algorithm for severely distorted quadratic elements (see Section 5.2.2), the new mesh is generated in linear order with C3D4H, so that the final geometry can be constructed accurately after remeshing in large porosities.

5.4 Large strain simulation of 3D M-Voronoi

In this section, we study 3D M-Voronoi geometries under large deformations with different material models. In general, the numerical simulation of a material/structure undergoing large strains is a challenging task that requires a specific effort in the choice between the element types and the solving method. These choices largely depend on the nature of the problem. In this study, the commercial FE solver ABAQUS (Dassault system) is used to deal with finite strain simulations, while enabling the option NLGEOM. For such simulations, there are two solvers available in Abaqus: Abaqus/Explicit and Abaqus/Standard (Implicit), which are based on explicit and implicit approaches in FEM analysis. It is possible to understand which solver is to be used by identifying the distinction between the two approaches. In the implicit method, at each solution step, equilibrium is ensured between the external load and the reaction forces generated by the internal load. Therefore, iteration and convergence checking are required. In the case of the explicit method, neither iteration nor convergence checking are required. At each solution step, the unknown values are obtained from information already known in the previous step. As a result, the time increment has to be small enough in order to accurately predict the results. In applications, Abaqus/Standard is very good at solving linear to moderately nonlinear problems quickly on large time scales, while it may be slower or unable to solve extremely nonlinear problems at all. Abaqus/Explicit, on the other hand, is more beneficial for high-speed dynamic problems and non-linear analyses. In addition, it has capabilities that make it easy to simulate quasi-static problems involving nonlinearity such as crash analyses of structural members, post-buckling and collapse simulations, and

²Similar density range has been observed for 2D M-Voronoi geometries in Section 3.5.

changes in contact in complex geometries. Specifically, the contact between surfaces has extremely nonlinear behavior that typically requires many iterations to be resolved by the implicit method. Abaqus/Explicit method, on the other hand, can effectively handle such severely nonlinear behavior, due to its incremental schema.

The present study focuses specifically on large strain compressive loadings on porous geometries, in which contact is actively involved. Therefore, we employed the Abaqus/Explicit solver with sufficiently small time increments to preserve quasi-static conditions. The element type has been chosen depending on the considered material properties. Due to the small time increment in Abaqus/Explicit, the total time required to finish the calculation can be very long taking several days. One needs to retain the data at the end of each increment to protect the data if the system crashes or the CPU time limit is exceeded. Therefore, we use `RESTART`, `WRITE` option to store the data and subsequently resume the process from the termination point. However, restoring the data at the end of each increment can create big size files and is not efficient. We employ option `OVERLAY`, which stores the data in the most recent increment and removes the previously stored data. Thus, it minimizes the space required to store the restart files, while retaining the information of the last increment for a later resume. Subsequently, Abaqus Explicit uses `RECOVER` analysis option in the execution command to resume the simulation from the last stored increment. In this work, the `OVERLAY` and `RECOVER` options have been implemented in all Abaqus/Explicit simulations regardless of material properties.

5.4.1 Plasticity in random and periodic structures

Constitutive relations for elastic-perfectly plastic materials

In this section, we briefly review the constitutive equations for materials with elastic-perfectly plastic properties. Generally, these materials are capable of irreversible deformation without increasing their stresses or loads. Perfect plasticity is characterized by a constant yield stress regardless of the plastic strain. Here, we employ the Mises yield function with the associated flow rule in plasticity. The formulation follows an incremental plastic strain approach that facilitates numerical implementations ([McMeeking and Rice, 1975](#)). We begin by additive decomposition of the total strain increment into elastic and plastic parts as

$$d\boldsymbol{\varepsilon} = d\boldsymbol{\varepsilon}^e + d\boldsymbol{\varepsilon}^p. \quad (5.2)$$

Furthermore, the Cauchy stress (true stress) tensor $\boldsymbol{\sigma}$ can be similarly decomposed into the volumetric and deviatoric stresses, such that the deviatoric stress $\boldsymbol{\sigma}_d$ can be obtained by the following relation:

$$\boldsymbol{\sigma}_d = \boldsymbol{\sigma} - \frac{1}{3}(\sigma_{kk})\mathbf{I}, \quad (5.3)$$

where \mathbf{I} is the identity tensor.

The yield function $\phi(\boldsymbol{\sigma}_d)$ determines the yielding surfaces of a material and depends on the deviatoric stress. For an isotropic material, the yield function can be defined by the principal invariants of the deviatoric stress $\boldsymbol{\sigma}_d$. The von Mises yield criterion states that yielding begins when the second invariant of the deviatoric stress reaches a critical value. Moreover, in this criterion, there is no volumetric plastic strain and the plastic strain consists of only the deviatoric term. Therefore, the yield function is defined as

$$\phi(\boldsymbol{\sigma}_d) = \sigma_{eq}^2 - \sigma_Y^2, \quad (5.4)$$

where σ_Y is the tensile yield strength of the material and σ_{eq}^2 is

$$\sigma_{eq}^2 = \frac{3}{2} \boldsymbol{\sigma}_d : \boldsymbol{\sigma}_d. \quad (5.5)$$

Next, by considering the flow rule assumption, the plastic strain increment is directly proportional to the gradient of the yield surface, which means that it is normal to the yield surface. As a result of the normality rule and from Hill (1998), the flow rule takes the following form

$$d\boldsymbol{\varepsilon}^p = d\lambda \frac{\partial \phi}{\partial \boldsymbol{\sigma}}, \quad (5.6)$$

where the $d\lambda$ is a plastic multiplier and is a positive scalar. In order to determine the magnitude of the plastic strain increment $d\boldsymbol{\varepsilon}^p$, it is necessary to obtain the value of $d\lambda$. To do so, we solve the full set of equations (5.4) and (5.6). The defined equations characterize the material behavior such that in any increment when the plastic flow is occurring (after the yield surface is reached), the equations should be integrated and solved to obtain the state at the end of the increment. In Abaqus FE solver, the integration is done by applying the backward Euler method to the flow rule. For more discussion on the numerical implementation of the incremental set of equations, see Smith (2009).

Numerical results

The elastic-perfectly plastic material model has been employed into Abaqus FE software to simulate different porous materials under large strains compression loading by considering that the matrix phase is an elastic-perfectly plastic material. We examine the differences between three different geometries M-Voronoi, RSA, Gyroid with the same volume fraction. Figure 5.7a shows the Gyroid lattices at four different densities $\rho = 0.4, 0.3, 0.2$ and 0.1 , with $5 \times 5 \times 5$ unit-cells created by the method described in Section 2.6. The M-Voronoi geometries with 110 voids are generated by deforming a 3D RSA with initial density $\rho_0 = 0.7$ (Figure 5.7b). The corresponding RSA geometries with the same porosities as the M-Voronoi and Gyroid are generated by 3D RSA algorithm discussed in Section 2.2. In order to have good mesh quality, the voids should keep a minimum distance. This constraint result in uncontrolled number of voids and a more polydisperse RSA geometry as we go to the lower densities. Consequently, the RSA geometry with a

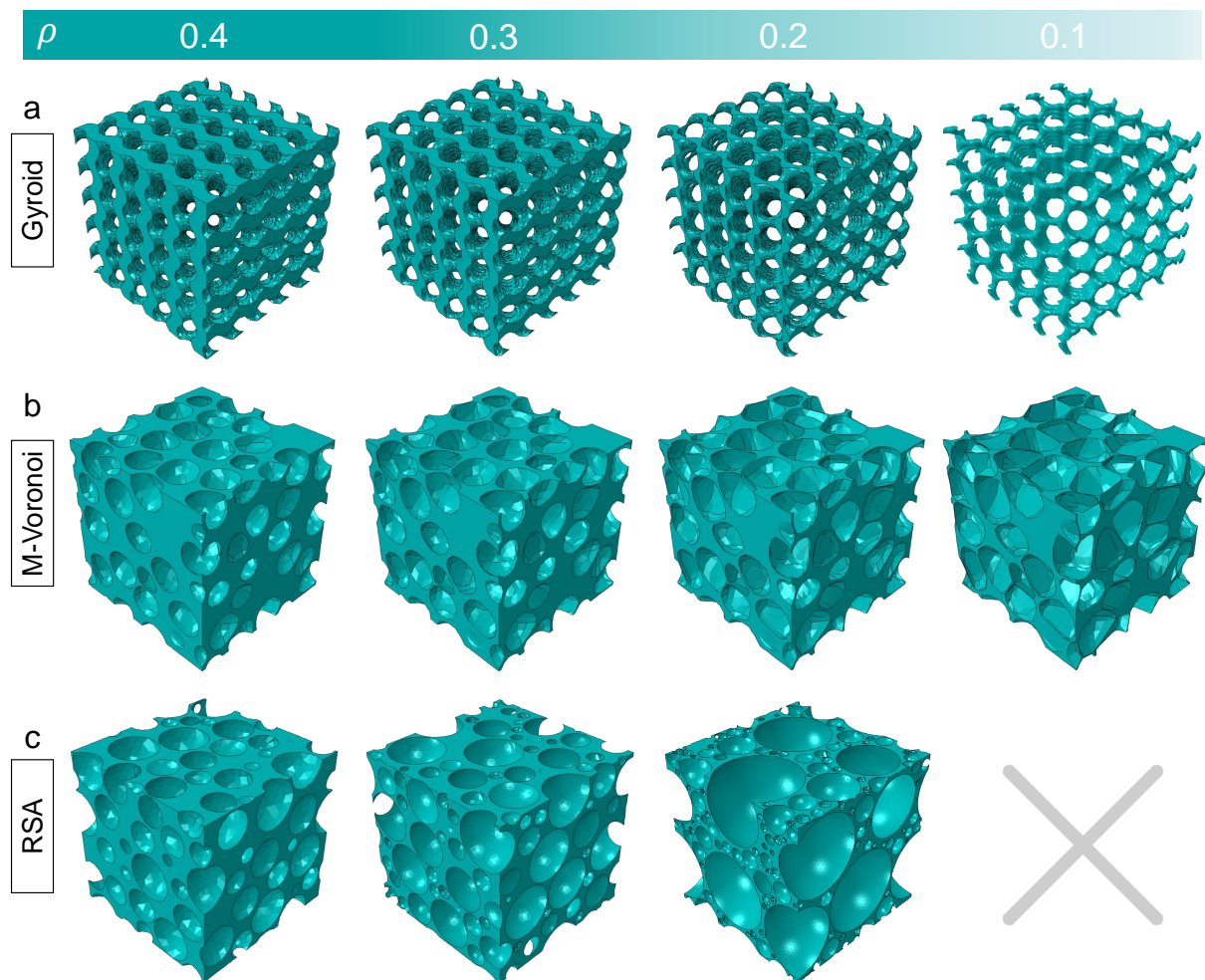


Figure 5.7: (a) Gyroid lattices created by the method described in Section 2.6 with $5 \times 5 \times 5$ unit-cells. (b) M-Voronoi with 110 voids obtained by using a RSA geometry with initial relative density $\rho_0 = 0.7$. (c) Polydisperse RSA geometries with various sphere sizes. All geometries are created at four different porosities $\rho = 0.4, 0.3, 0.2$ and 0.1 , except RSA that is not realizable at relative density $\rho = 0.1$.

relative density $\rho = 0.1$ is not numerically and experimentally realizable. Therefore, only M-Voronoi as a random and Gyroid as a periodic geometry can achieve very low densities.

As discussed in Section 5.4, for large strain simulations, Abaqus/Explicit has to be implemented to solve the numerical problem without encountering convergence issues. Our study of the mesh element type has shown that brick elements are the best element type for compression with plasticity. Moreover, by using brick elements with reduced integration C3D8R, the number of integration points will be reduced from four to one. There has been a significant reduction in computation time as a result of this modification.

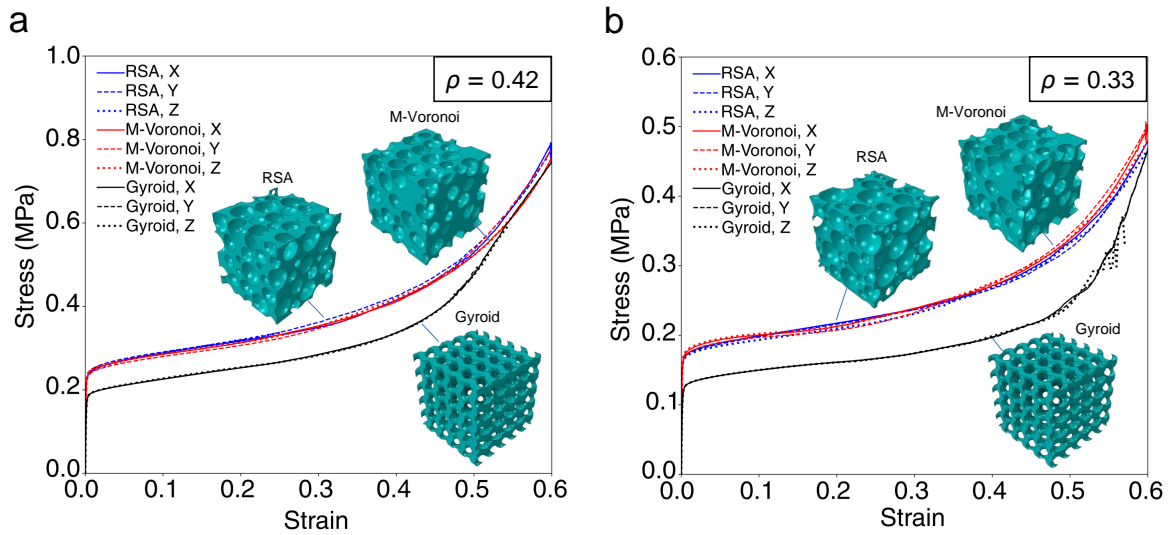


Figure 5.8: Large strains compression simulations for M-Voronoi, RSA and Gyroid geometries at three different directions for relative densities (a) $\rho = 0.42$ and (b) $\rho = 0.33$. The values of stress and strain correspond to their nominal or engineering values.

The three-dimensional mesh in all geometries is created with **Gmsh** software using the hexagonal subdivision algorithm. The computation time for a brick element type mesh with 870 000 nodes (DOF) corresponds to approximately 103 hours when running on 40 cores in parallel. To achieve this, the **OVERLAY** option in Abaqus/Explicit has been activated to restore the last increment and enable the computation to continue for several days with multiple restarts. The matrix phase is considered an elastic-perfectly plastic material with Young's modulus of 1000 MPa, Poisson's ratio of 0.3, and yield stress of 1 MPa. The choice of this material model has been made to ensure no presence of the material hardening. Therefore, any observed material hardening would be a direct consequence of the geometry characteristics.

In order to compare the three geometries, we show in Figures 5.8a,b uni-axial compression simulations for relative densities $\rho = 0.42, 0.33$. All geometries have been tested in three different directions. The M-Voronoi and RSA geometries represent an isotropic response at small and large strains. For the Gyroid geometry, although it represents an isotropic response in three different directions, it is known to have a cubic anisotropy. Interestingly, the yield stress and large strain plastic response of the M-Voronoi and RSA geometries are very close and much higher than the Gyroid geometries. This result shows that materials with random smooth geometries represent an enhanced plastic response as compared to periodic geometries. For a better understanding, we also include the deformations of three geometries at three different strain levels, denoted with (1), (2), and (3) in Figures 5.9 and 5.10. By looking at the locations of the plastic strain equivalent (PEEQ) of the deformed geometries, we observe that the random features of the

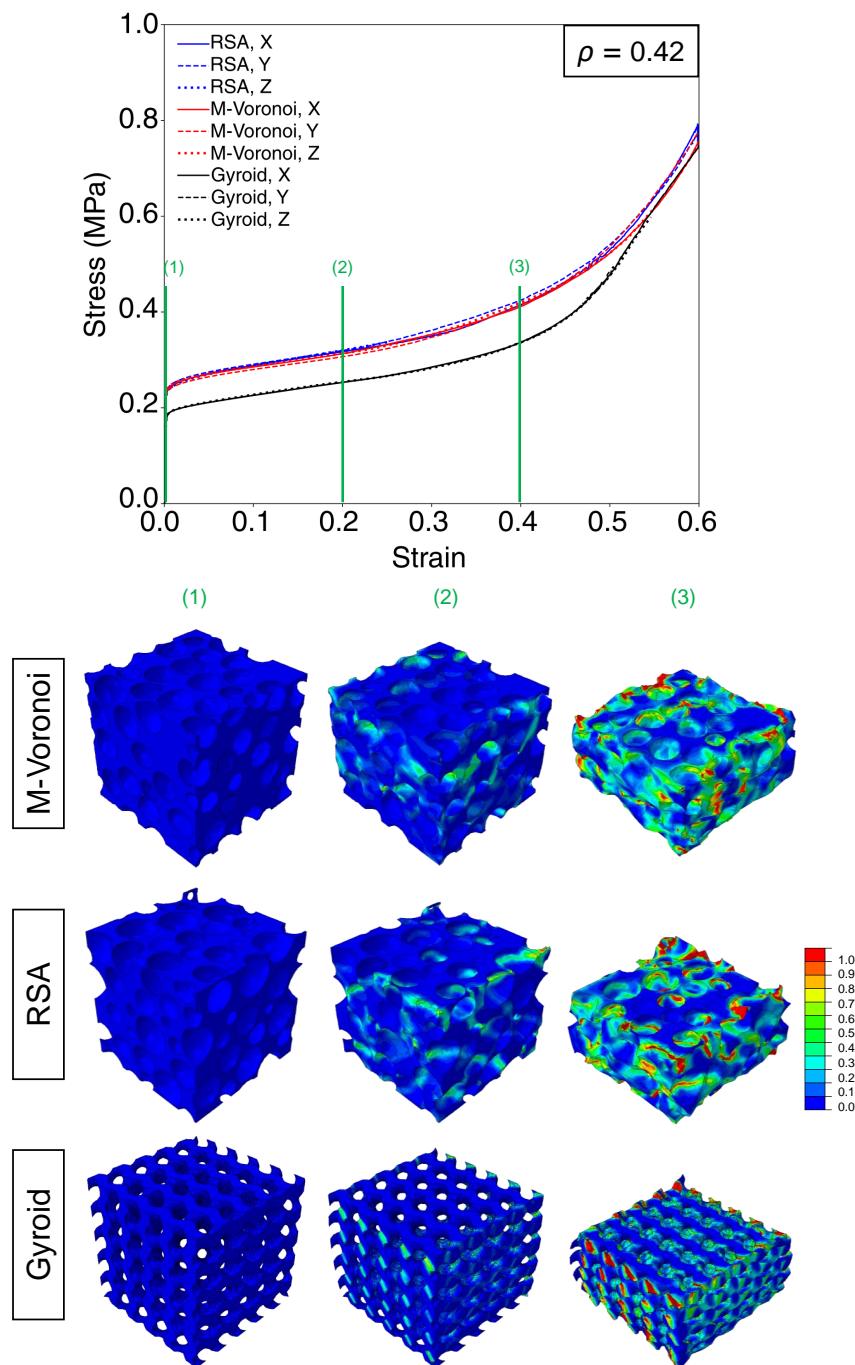


Figure 5.9: Deformations of M-Voronoi, RSA and Gyroid geometries with the relative density $\rho = 0.42$ at three different strain levels, denoted with (1), (2) and (3). The legend indicates the plastic strain equivalent (PEEQ) values. The values of stress and strain correspond to their nominal or engineering values.

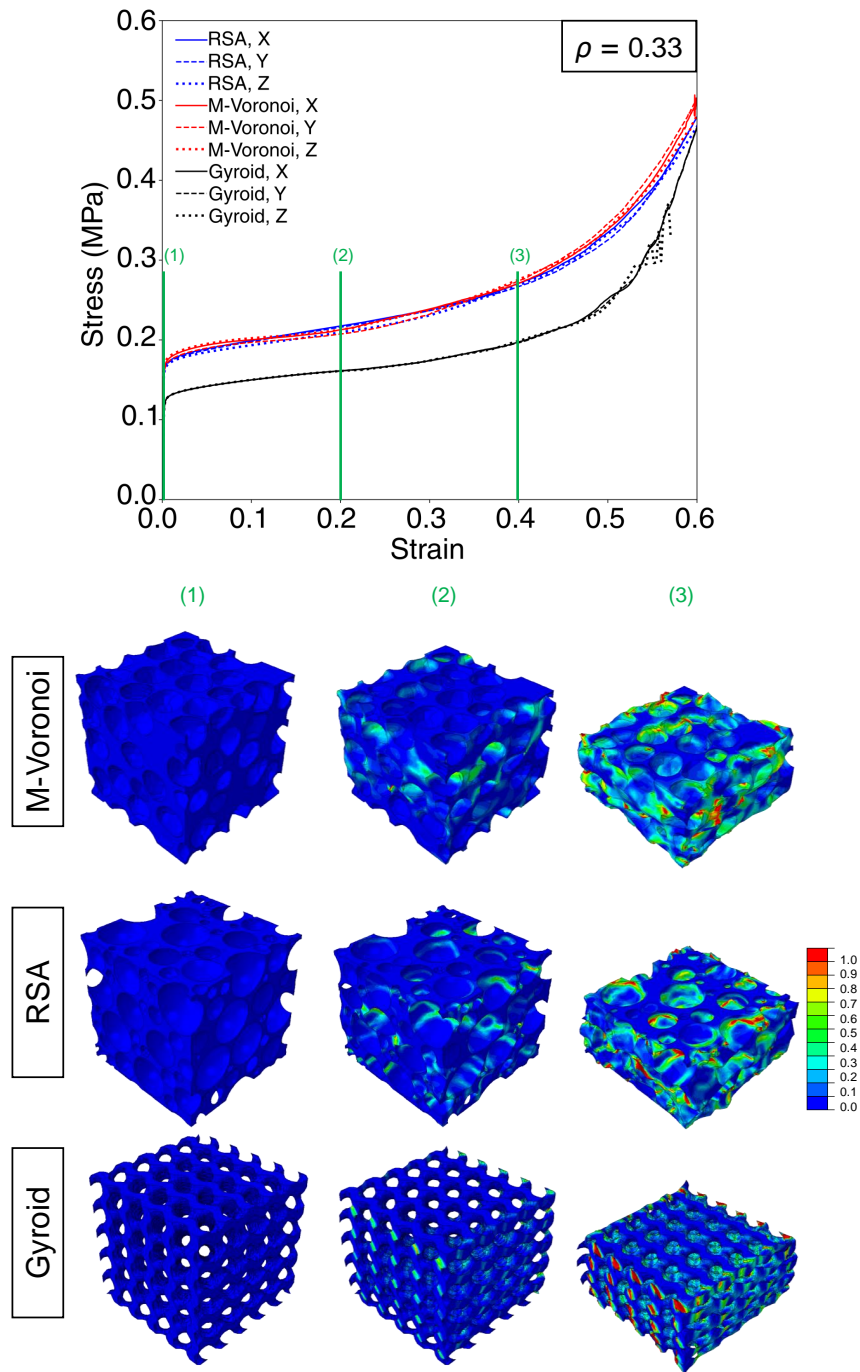


Figure 5.10: Deformations of M-Voronoi, RSA and Gyroid geometries with the relative density $\rho = 0.33$ at three different strain levels, denoted with (1), (2) and (3). The legend indicates the plastic strain equivalent (PEEQ) values. The values of stress and strain correspond to their nominal or engineering values.

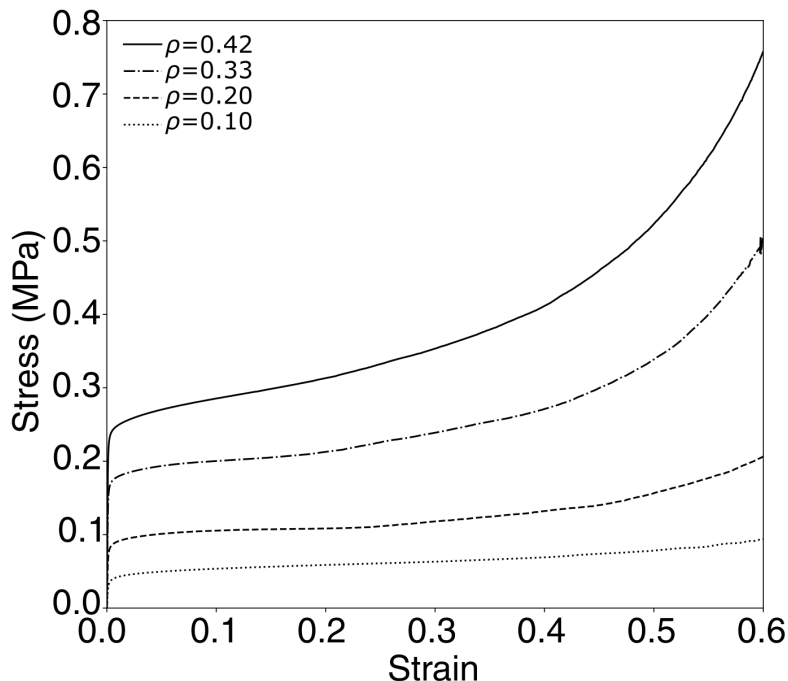


Figure 5.11: Large strains compression simulations for M-Voronoi geometries at four different relative densities $\rho = 0.42, 0.33, 0.20,$ and 0.1 . The values of stress and strain correspond to their nominal or engineering values.

M-Voronoi and RSA geometries such as random void size, shape, position, and ligament thickness, lead to a diffuse distribution of unconnected zones of localized plastic strain throughout the entire specimens. We note however, that the RSA geometries are not realizable at low densities and only the M-Voronoi geometry can span the full density range. In contrast to the random geometries, the Gyroid lattices, being one of the stiffest periodic geometries, display a periodic localized deformation pattern spanning the cell rows for both relative densities. This behavior is a consequence of the periodic geometry features. Such responses are also expected in other periodic geometries including trusses, lattices, and plate-based architected materials. It is also important to note that the stress-strain curves converge after densification occurs in the geometries.

The M-Voronoi geometries are the easiest realizable geometry among the three studied geometries. The proposed remeshing technique in Section 5.2, has enabled us to create high-quality meshes with a less number of elements. As a result, the computation time for the M-Voronoi geometries is significantly less than for the RSA and Gyroid lattices. In particular, the large number of voids in the RSA geometries requires a very careful fine mesh to perfectly capture the smallest voids and this will increase the computation time. Figure 5.11, represents the stress-strain response of the M-Voronoi geometries at

four different relative densities $\rho = 0.42, 0.33, 0.20, 0.10$. In accordance with expectations, the larger the density, the stiffer the plastic response and the higher the yield stress will be. A rather remarkable observation is that the hardening of the stress-strain response decreases with decreasing relative densities. The reason for this can be explained by the fact that at higher relative densities, the cell walls are able to establish contact earlier than at lower densities.

5.5 Concluding remarks

In this chapter, we developed the mechanically-grown morphogenesis method to create the three-dimensional random M-Voronoi geometries. In order to create periodic random 3D M-Voronoi geometries with straight boundary faces, we generalized the assumed boundary conditions to those of periodic ones. Moreover, the novel remeshing algorithm that had been proposed for two-dimensional meshes in Section 3.3.1 is developed for arbitrary three-dimensional orphan meshes. The span of the proposed method and the technical challenges have also been discussed. With the new remeshing technique, we demonstrated that it is possible to achieve a full density range of the 3D M-Voronoi geometries. The mechanical properties of the 3D M-Voronoi geometries have been examined numerically at large compressive strains by considering the matrix as an elastic-perfectly plastic material without hardening. For comparison, we also study the Gyroid and RSA geometries under the identical conditions and the same porosity as the M-Voronoi geometries. We observe an enhanced yield stress and plastic flow in the geometries with random topologies as opposed to the TPMS periodic structures. This behavior is explained by noting that deformation localizes in geometries with periodic pattern, contrary to the random geometries which exhibit a rather diffused localization. Nevertheless, achieving very low densities with random geometry is possible only with M-Voronoi materials. Further studies are required to compare other random geometries such as Spinodoid ones or 3D Voronoi tessellation with the M-Voronoi. In addition, the geometries can be examined in other loading conditions and material properties. We note that the flexibility of the M-Voronoi method enables us to also create 3D anisotropic M-Voronoi geometries. The study on such materials is left for in the future.

5.A Appendix A. Algorithms for remeshing a 3D orphan mesh by constructing the geometry

Nomenclature:

- n : total number of nodes in the orphan mesh
- m : total number of elements in the orphan mesh
- h : the number of nodes per element
- r : the number of nodes per element surface
- f : the number of free surfaces
- t : the reference node
- $\mathbb{N}_{n \times 3}$: matrix containing the nodes coordinates
- $\mathbb{M}_{m \times h}$: matrix containing the elements information
- $\mathbb{S}_{f \times p}$: matrix containing the nodes of free lines
- \mathbb{B} : matrix containing the list of investigated lines

Algorithm 3 finding the free surfaces of a 3D orphan mesh

```

1: Initialize the algorithm with number of free surfaces  $f = 0$ 
2: for  $p = 1, m$  do
3:   for  $q = 1, h$  do
4:      $ref = [\mathbb{M}(p, q), \mathbb{M}(p, q + 1), \mathbb{M}(p, q + 2)]$ 
5:     for  $u = 1, m$  do
6:       for  $v = 1, h$  do
7:          $comp = [\mathbb{M}(u, v), \mathbb{M}(u, v + 1), \mathbb{M}(u, v + 2)]$ 
8:         if  $ref = comp$  then
9:           goto 3
10:        else
11:          if  $h=4$  then ▷ Linear tetrahedron element
12:             $\mathbb{S}(f, :) = [\mathbb{M}(p, q), \mathbb{M}(p, q + 1), \mathbb{M}(p, q + 2)]$ 
13:             $f \leftarrow f + 1$ 
14:          else if  $h=10$  then ▷ Quadratic tetrahedron element
15:             $\mathbb{S}(f, :) = [\mathbb{M}(p, q), \mathbb{M}(p, q + 1), \mathbb{M}(p, q + 2), \text{midnode12},$ 
midnode23, midnode31 ]
16:             $f \leftarrow f + 1$ 
17:          end if
18:        end if
19:      end for
20:    end for
21:  end for
22: end for

```

Algorithm 4 Fortran algorithm for constructing 3D geometry by the free element sides

```

1: Initialize the algorithm with number of identified volumes  $N = 0$ 
2: for  $i = 1, f$  do ▷ Searching over all free surfaces
3:   Construct the reference surface from three corner nodes  $\mathbb{S}(i, 1)$ ,  $\mathbb{S}(i, 2)$  and  $\mathbb{S}(i, 3)$ 
4:   Add three lines of the surface to  $\mathbb{B}$ 
5:   Noderef 1=  $\mathbb{S}(i, 1)$  ▷ Noderef 1 and Noderef 2 are the temporary reference nodes
6:   Noderef 2=  $\mathbb{S}(i, 2)$  ▷ which are in common between two consecutive surfaces.
7:   for  $j = 1, f$  do
8:      $w = 0$ 
9:     if Noderef 1 and Noderef 2  $\in \mathbb{S}(j, :)$  then
10:      Noderef 3  $\in \mathbb{S}(j, :)$ 
11:       $w = 1$ 
12:      if Noderef 3 and Noderef 1  $\in \mathbb{B}$  then
13:        if Noderef 3 and Noderef 2  $\in \mathbb{B}$  then
14:          Case 3
15:        else
16:          Case 2
17:        end if
18:      else if Noderef 3 and Noderef 2  $\in \mathbb{B}$  then
19:        Case 2
20:      else
21:        Case 1
22:      end if
23:      if Case 1 then
24:        Construct the surface by adding new point Noderef 3 and new lines
25:        Noderef 2 $\leftarrow$  Noderef 3
26:        Add new two lines of the surface to  $\mathbb{B}$ 
27:      else if Case 2 then
28:        Construct the new surface by adding one new line
29:        Noderef 2 $\leftarrow$  Noderef 3
30:        Add new line of the surface to  $\mathbb{B}$ 
31:      else if Case 3 then
32:        Close the existing surface
33:      end if
34:    end if
35:  end for
36:  if  $w=0$  then ▷ The surface loop is closed.
37:     $N \leftarrow N + 1$  ▷ A new volume is identified
38:    write Surface Loop of all surfaces of the loop
39:    write a volume from the Surface Loop
40:    goto 2
41:  end if
42: end for

```

Chapter 6

Conclusion

Contents

6.1 Concluding remarks	149
6.2 Perspectives	152

6.1 Concluding remarks

In this work, we study the mechanical response of random topologies with a focus on porous materials. We assess the behavior of random porous materials at large strain by numerical simulations and comparing with several random and periodic porous geometries. We investigate the computer-aided design process of a variety of existing random and periodic porous topologies including the random sequential adsorption (RSA) algorithm for ellipsoidal inclusions, standard Voronoi geometries, hexagonal honeycombs and TPMS geometries. We also propose a versatile mechanically-grown morphogenesis method to obtain high-to-low density *isotropic* and *anisotropic* random porous and more generally composite materials, called M-Voronoi. The method is based on a nonlinear elastic finite strain computational strategy. It has been comprehensively developed to generate both 2D and 3D M-Voronoi geometries in a variety of unit-cell geometry. In both cases, due to large deformations, remeshing is required on the final deformed mesh for further numerical or experimental investigations. We developed an algorithm that remeshes a highly deformed orphan mesh in 2D and 3D by constructing the exact geometry of the deformed mesh. The proposed algorithm is extremely versatile and general, enabling us to remesh arbitrarily complex orphan meshes with a variety of properties containing multi-phase or voids. In addition, it has assisted us in obtaining very large porosities by performing an intermediate remeshing step either with or without stress field mapping.

The designed geometries have been 3D-printed using a soft polymer called TangoB-lack material and subsequently have been tested under uni-axial compression. We have

performed first a mechanical characterization to identify the material parameters of the TangoBlack. This material shows a rate-dependent and highly viscous response under relaxation and loading-unloading uni-axial tensile tests. It is then modeled by the rubber viscoelastic model proposed by [Kumar and Lopez-Pamies \(2016\)](#) and the corresponding parameters are identified. This material at ultimate stress limits shows a brittle fracture that can be characterized by a unique failure envelope ([Smith, 1963](#)) which is independent of the test conditions and is characterized by the break stress and strain values. The fracture of the TangoBlack material during the relaxation can also be justified by obtained failure envelope.

The extruded 2D M-Voronoi geometries have been 3D-printed with TangoBlack with four different densities: 0.4, 0.3, 0.2, 0.1. For comparison, we have also printed the RSA and E-Voronoi porous extruded 2D geometries with the same porosities as M-Voronoi, while keeping the almost same number of voids. In order to achieve sufficient specimen quality (especially at low-densities), we propose an interruption program during 3D-printing which consists of alternate additive manufacturing and interruption time increments. The resulting porous specimens have then been experimentally tested under in-plane uni-axial compression. In particular, the newly proposed M-Voronoi materials exhibit a strong hardening behavior under compressive loads as compared to a number of available voided and random cellular materials such as RSA and E-Voronoi, which tend to exhibit either peak stress and a plateau or only weak hardening for most of the deformation process before final densification. This hardening response is mainly a consequence of three geometrical characteristics: (i) the randomness of the void geometries, (ii) the non-uniformity of the intervoid ligaments, and (iii) the smooth void geometry reducing efficiently stress localization. In addition, the randomness of the M-Voronoi geometry makes these materials less sensitive to imperfections and realization variations. Nevertheless, a more detailed study is required along this direction perhaps including additional loading conditions such as tensile and hydrostatic ones ([Tankasala et al., 2017](#)).

The study on the representativity of the M-Voronoi materials shows that at small strains for almost 30 voids, there is a converged representative response, while in order to achieve convergence in large strains, at least 200 voids are required (see [Figures 4.26 and 4.27](#)). Most of the studies on the RVE size determination and representativity of heterogeneous materials are developed for small strains ([Tarantino et al., 2019](#); [Dirrenberger et al., 2014](#)). However, these materials under general loading conditions might be subjected to large deformations, in which the small strain representative microstructure might not be converged. Moreover, it is also important to consider loading conditions when determining the convergence limit. In our study, the large strain representative range is proposed solely under compression loading. Therefore, further studies with different loading conditions are required to obtain the exact representative range of the geometry. Accordingly, the results of our study indicate that careful consideration of the deformation scale and loading conditions is necessary when discussing representativity.

In the next approach, the M-Voronoi morphogenesis method is also applied to three-dimensional geometries. The heart of the method which is the nonlinear elastic finite

strain computations remains identical to the 2D M-Voronoi process. However in order to create the 3D periodic M-Voronoi geometries, we applied periodic boundary conditions, while keeping the edges straight. The resulting geometry is a periodic cubic unit-cell. Of course, one can apply Dirichlet uniform boundary conditions to create non-periodic M-Voronoi geometries with arbitrary unit-cell geometry. The proposed morphogenesis method in 3D creates 3D smooth polygonal shape inclusions that are observed in many natural and synthetic porous and composites such as metal foams, magnetorheological elastomers (MREs), skeletal muscles, etc. Similar to the 2D M-Voronoi, an algorithm is developed to remesh the extremely deformed 3D mesh, by constructing the geometry of the orphan mesh. By performing intermediate remeshing steps, this algorithm enables us to span a full density range from 0 to 1 with 3D M-Voronoi geometries.

Finally, the 3D M-Voronoi materials are numerically studied using a metallic material with an elastic-perfectly plastic material model while subjected to uni-axial large strain compression loading. The M-Voronoi materials show an enhancement in the plastic response in both the yield stress and the stress plateau as compared to periodic cellular Gyroid lattices. Nevertheless, their response remains very close to the random RSA geometries due to their random smooth void shape. Despite this, in contrast to the M-Voronoi, the RSA geometries are unable to reach low densities (less than 0.2). Therefore, in order to obtain an enhanced plastic response, one needs to use the M-Voronoi geometries when low densities are required.

In summary, the random features of the proposed M-Voronoi geometries enhance the mechanical response both in hyperelastic and elastoplastic materials i.e. polymers and metals. These features consist of the random smooth shape, position, size, and orientation of the inclusions as well as the random ligament thickness. The M-Voronoi geometries are also able to span the full density range, which is a great advantage over the existing random RSA geometries with a limited density range. The high randomness of the M-Voronoi materials enables them to have a representative response (given a sufficient number of voids) in both small and large strains. Moreover, the M-Voronoi method is capable to create both isotropic and anisotropic materials depending on the applied deformations. Contrary to this, anisotropic geometries cannot be obtained by void-growth methods that use internal gas pressures in the voids (Dabo et al., 2019; Bargmann et al., 2018). Remarkably, the anisotropy in M-Voronoi materials is tunable by the designed parameters. Interestingly, the induced anisotropy can stiffen up the material response in small strains, while in large strains the isotropic M-Voronoi remains the stiffest microstructure. This is in contrast to the conventional view that anisotropy enhances material response. Furthermore, the results are in good agreement with those observed when comparing the M-Voronoi with periodic lattices such as hexagons, which are isotropic in small strain regimes and highly anisotropic (thus softer) in large deformation regimes. It is important to note that since M-Voronoi materials have inherent randomness, they are less sensitive to imperfections, whereas periodic geometries are not only intrinsically unstable, but they are also highly vulnerable to any imperfections that may occur during the manufacturing process. As a result, the random M-Voronoi material is the most resilient material under both small

and large strains, exhibiting an isotropic representative response, and being less sensitive to imperfections.

6.2 Perspectives

The versatility and generality of the M-Voronoi morphogenesis method, which is numerical and is based on solving a nonlinear elastic problem subjected to only Dirichlet boundary conditions, and unlike more classical periodic cells, allows to grow uniformly such M-Voronoi geometries in arbitrary shaped domains or as called in this study, finite volume elements (FVEs) (e.g. triangles, circles, trapezoids, rectangles, etc.). This allows for their easy subsequent assembly into complex macroscopic geometries. A potential implication of such processes is the future use of well-known (Allaire, 1992) as well as more recent optimization techniques (Wang and Sigmund, 2021) to design lightweight structures that behave optimally for a large number of loading states, since the proposed materials can vary from isotropic to anisotropic at different regions in these structures.

On a different note, one could apply more complex non-shape-preserving Dirichlet boundary conditions leading a non-trivial final domain shape. Such a process is beyond the scope of the present study, however, the same design idea presented here is directly applicable to such a case. Note, however, that such non-uniform Dirichlet boundary conditions may lead to boundary inter-penetrations as well as non-uniform inclusion/void concentrations throughout the domain. Yet, it may allow to reach a pre-designed domain shape and thus deserves further study in the future.

The method proposed here is directly applicable to any type of composite which may be created by simply replacing at the final stage the void phase with any inclusion(s) type that may be required (see Figure 3.12 as an example of M-Voronoi materials). A composite obtained in this way can be used either as a model for existing composites or for the design of new composite materials with random particles and tunable properties. In the latter case, 3D-printing enables us to manufacture the designed composite materials with high precision. Our first attempt to visualize such a composite was made by 3D-printing a two-phase composite RSA geometry with TangoBlack Plus matrix and VeroWhite Plus spherical inclusions using a multi-material Stratasys 3D printer (Figure 6.1). In this composite, the volume fraction of the inclusions corresponds to 0.25, which has a significant impact on the stiffness of the composite. Further investigations are required for such composite materials, especially the study on the debonding of the matrix and inclusions under tensile loading. It is also important to note that as a result of the multi-material 3D-printing, the properties of the constituents may differ from those of the constituents printed individually. Such effects also require more studies.

The designed random geometries may also be used to model the existing composites with random particles. Figures 1.2a,d,g,h represent such composites. For example in the study of Spyrou et al. (2019), they employed 2D random E-Voronoi geometries to model the human muscles consisting of two phases: the fibers and the extra-cellular matrix (see Figure 1.2g). Such approaches can be further improved by using the M-Voronoi

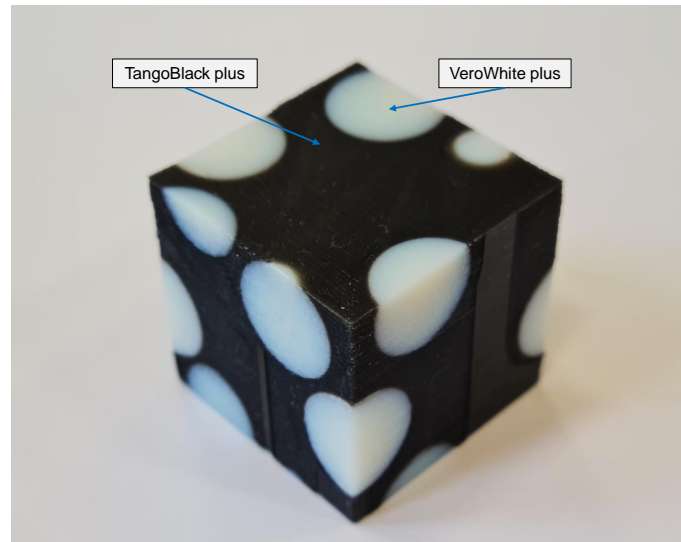


Figure 6.1: A 3D-printed two-phase composite with random RSA geometry consisting of TangoBlack plus matrix and VeroWhite plus spherical inclusions.

geometries which resemble more the real microstructure and contain all random features. Furthermore, in the studies of magnetorheological elastomers (MREs), random composite geometries (such as RSA) are employed to model the MREs (Mukherjee et al., 2021). These materials are essentially two-phase composites with metallic magneto-active particles randomly distributed in a non-magnetic and mechanically soft elastomer matrix (see Figures 1.2d,h). Figure 6.2 represents an example of the hard MREs¹ model created with RSA random geometries by considering the perfectly rounded shape of the particles. Figure 6.2a shows the magnetization in the pre-magnetized hard magnetic particles dispersed in a passive soft matrix. To study the variation of the magnetization and other mechanical or coupled properties of the magnetized material, mechanical tensile loading is applied. Figure 6.2b shows the change in the magnetization while Figure 6.2c represents the magnetic induction field and the interaction between the magnetic particles. Generally, the manufactured MREs contain a moderate range of the magnetic particles volume fraction up to approximately 30%. In this range of volume fraction, the RSA model is capable of dealing with the randomness of the particles (see Figures 1.2d,h) and predicts very well the response of the MREs. Recently, new 3D-printing techniques have been developed to 3D-print magnetoactive polymers, which by definition can be referred to as 4D-printing (Falahati et al., 2020; Brusa da Costa Linn et al., 2022). With these techniques, we are able to design and manufacture active composites or 3D surface patterns (Moreno-Mateos et al., 2022) with a controlled regular or irregular morphology. As a result, one can take a multi-scale design approach to embed MREs with random geometries as particles in

¹Depending on the magnetic coercivity of the particle phase, the MREs are classified into two categories: hard and soft MREs. The hard MREs are capable of being permanently magnetized, while the soft MREs have a small coercivity and are not able to preserve the magnetization.

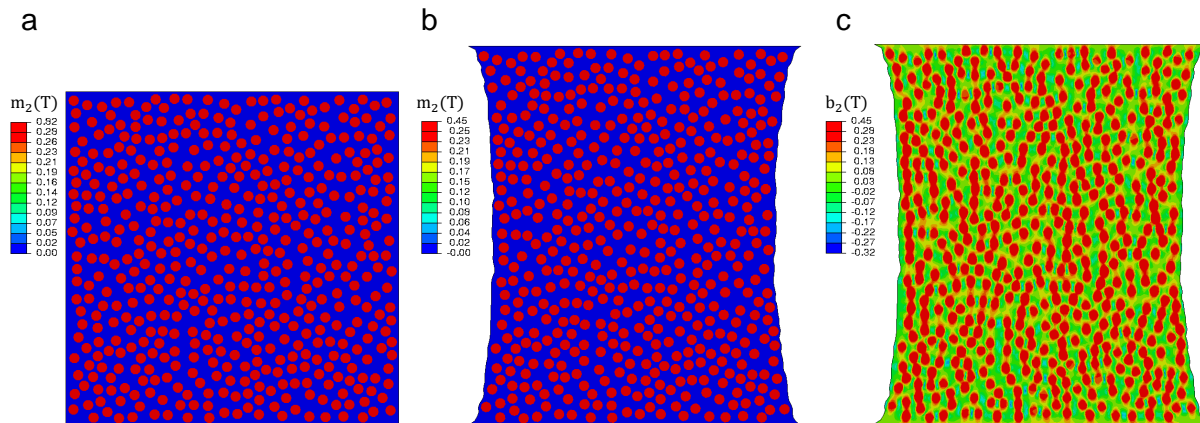


Figure 6.2: An example of the application of random geometries in coupled magneto-mechanical problems. The geometry contains 500 particles with a 0.4 volume fraction and is proposed to model hard magnetorheological elastomers (h-MREs). (a) The pre-magnetized microstructure. m_2 denotes the magnetization in the vertical direction. (b) The deformation of the permanently magnetized microstructure under mechanical tensile loading. (c) The magnetic induction field b_2 in the deformed microstructure. The contours illustrate particle interactions.

magnetically inactive polymers as a matrix. If a large volume fraction of MREs is required, a random M-Voronoi geometry can be used to design a random active particulate composite. We note here again that in contrast to the RSA, M-Voronoi geometries are capable of spanning a full density range and therefore they can be used to model materials with large volume fractions.

In the future, a machine learning inverse approach (Kumar et al., 2020) could potentially be extended to the nonlinear response to obtain a targeted family of M-Voronoi and RSA materials with “tunable” an-isotropy, since the latter allow for a limitless number of geometries that may be achieved via complex applied mechanical loads. We also note at this point that the void growth mechanism via incompressible nonlinear elasticity may be directly applied to porous solids with or without connectivity and with moderate relative density in order to reach much lower relative densities (such as the spinodal geometries in Portela et al. (2020) and Zerhouni et al. (2021)).

Bibliography

- Aage, N., Andreassen, E., Lazarov, B.S., Sigmund, O., 2017. Giga-voxel computational morphogenesis for structural design. [Nature](#) 550, 84–86.
- Adams, D., Matheson, A., 1972. Computation of dense random packings of hard spheres. [The Journal of Chemical Physics](#) 56, 1989–1994.
- Al-Ketan, O., Abu Al-Rub, R.K., 2019. Multifunctional mechanical metamaterials based on triply periodic minimal surface lattices. [Advanced Engineering Materials](#) 21, 1900524.
- Al-Ketan, O., Lee, D.W., Abu Al-Rub, R.K., 2021. Mechanical properties of additively-manufactured sheet-based gyroidal stochastic cellular materials. [Additive Manufacturing](#) 48, 102418.
- Allaire, G., 1992. Homogenization and two-scale convergence. [SIAM Journal on Mathematical Analysis](#) 23, 1482–1518.
- Andrew, J.J., Alhashmi, H., Schiffer, A., Kumar, S., Deshpande, V.S., 2021. Energy absorption and self-sensing performance of 3d printed cf/peek cellular composites. [Materials & Design](#) 208, 109863.
- Anoukou, K., Brenner, R., Hong, F., Pellerin, M., Danas, K., 2018. Random distribution of polydisperse ellipsoidal inclusions and homogenization estimates for porous elastic materials. [Computers & Structures](#) 210, 87–101.
- Ashby, M.F., Gibson, L.J., 1997. Cellular solids: structure and properties. [Press Syndicate of the University of Cambridge, Cambridge, UK](#) , 175–231.
- Baandrup, M., Sigmund, O., Polk, H., Aage, N., 2020. Closing the gap towards super-long suspension bridges using computational morphogenesis. [Nature communications](#) 11, 1–7.
- Balit, Y., Margerit, P., Charkaluk, E., Constantinescu, A., 2021. Crushing of additively manufactured thin-walled metallic lattices: Two-scale strain localization analysis. [Mechanics of Materials](#) 160, 103915.

-
- Bargmann, S., Klusemann, B., Markmann, J., Schnabel, J.E., Schneider, K., Soyarslan, C., Wilmers, J., 2018. Generation of 3d representative volume elements for heterogeneous materials: A review. [Progress in Materials Science](#) 96, 322–384.
- Benedetti, M., Du Plessis, A., Ritchie, R., Dallago, M., Razavi, S.M.J., Berto, F., 2021. Architected cellular materials: A review on their mechanical properties towards fatigue-tolerant design and fabrication. [Materials Science and Engineering: R: Reports](#) 144, 100606.
- Bi, S., Chen, E., Gaitanaros, S., 2020. Additive manufacturing and characterization of brittle foams. [Mechanics of Materials](#) 145, 103368.
- Bonatti, C., Mohr, D., 2019. Mechanical performance of additively-manufactured anisotropic and isotropic smooth shell-lattice materials: Simulations & experiments. [Journal of the Mechanics and Physics of Solids](#) 122, 1–26.
- Chen, X.D., Yong, J.H., Zheng, G.Q., Paul, J.C., Sun, J.G., 2006. Computing minimum distance between two implicit algebraic surfaces. [Computer-Aided Design](#) 38, 1053–1061.
- Combescure, C., Elliott, R.S., Triantafyllidis, N., 2020. Deformation patterns and their stability in finitely strained circular cell honeycombs. [Journal of the Mechanics and Physics of Solids](#) 142, 103976.
- Combescure, C., Henry, P., Elliott, R.S., 2016. Post-bifurcation and stability of a finitely strained hexagonal honeycomb subjected to equi-biaxial in-plane loading. [International Journal of Solids and Structures](#) 88, 296–318.
- Cooper, D.W., 1988. Random-sequential-packing simulations in three dimensions for spheres. [Physical Review A](#) 38, 522.
- Corson, F., Hamant, O., Bohn, S., Traas, J., Boudaoud, A., Couder, Y., 2009. Turning a plant tissue into a living cell froth through isotropic growth. [Proceedings of the National Academy of Sciences](#) 106, 8453–8458.
- Brusa da Costa Linn, L., Danas, K., Bodelot, L., 2022. Towards 4d printing of very soft heterogeneous magnetoactive layers for morphing surface applications via liquid additive manufacturing. [Polymers](#) 14, 1684.
- Crossland, E.J.W., Kamperman, M., Nedelcu, M., Ducati, C., Wiesner, U., Smilgies, D.M., Toombes, G.E.S., Hillmyer, M.A., Ludwigs, S., Steiner, U., Snaith, H.J., 2008. A bicontinuous double gyroid hybrid solar cell. [Nano Letters](#) 9, 2807–2812.
- Dabo, M., Roland, T., Dalongeville, G., Gauthier, C., Kékicheff, P., 2019. Ad-hoc modeling of closed-cell foam microstructures for structure-properties relationships. [European Journal of Mechanics-A/Solids](#) 75, 128–141.

- Danas, K., 2017. Effective response of classical, auxetic and chiral magnetoelastic materials by use of a new variational principle. [Journal of the Mechanics and Physics of Solids](#) 105, 25–53.
- De Angelo, M., Spagnuolo, M., D’annibale, F., Pfaff, A., Hoschke, K., Misra, A., Dupuy, C., Peyre, P., Dirrenberger, J., Pawlikowski, M., 2019. The macroscopic behavior of pantographic sheets depends mainly on their microstructure: experimental evidence and qualitative analysis of damage in metallic specimens. [Continuum Mechanics and Thermodynamics](#) 31, 1181–1203.
- Deshpande, V., Fleck, N., 2000. Isotropic constitutive models for metallic foams. [Journal of the Mechanics and Physics of Solids](#) 48, 1253–1283.
- Deshpande, V., Fleck, N., Ashby, M., 2001. Effective properties of the octet-truss lattice material. [Journal of the Mechanics and Physics of Solids](#) 49, 1747–1769.
- Dirrenberger, J., Forest, S., Jeulin, D., 2013. Effective elastic properties of auxetic microstructures: anisotropy and structural applications. [International Journal of Mechanics and Materials in Design](#) 9, 21–33.
- Dirrenberger, J., Forest, S., Jeulin, D., 2014. Towards gigantic rve sizes for 3d stochastic fibrous networks. [International Journal of Solids and Structures](#) 51, 359–376.
- Dong, L., Deshpande, V., Wadley, H., 2015. Mechanical response of ti-6al-4v octet-truss lattice structures. [International Journal of Solids and Structures](#) 60, 107–124.
- Faisal, T.R., Hristozov, N., Rey, A.D., Western, T.L., Pasini, D., 2012. Experimental determination of philodendron melinonii and arabidopsis thaliana tissue microstructure and geometric modeling via finite-edge centroidal voronoi tessellation. [Physical Review E](#) 86, 031921.
- Falahati, M., Ahmadvand, P., Safaee, S., Chang, Y.C., Lyu, Z., Chen, R., Li, L., Lin, Y., 2020. Smart polymers and nanocomposites for 3d and 4d printing. [Materials today](#) 40, 215–245.
- Feder, J., 1980. Random sequential adsorption. [Journal of Theoretical Biology](#) 87, 237–254.
- Ferry, J.D., 1980. Viscoelastic properties of polymers. [John Wiley & Sons](#).
- Francfort, G., Murat, F., 1986. Homogenization and optimal bounds in linear elasticity. [Archive for Rational mechanics and Analysis](#) 94, 307–334.
- Fritzen, F., Forest, S., Böhlke, T., Kondo, D., Kanit, T., 2012. Computational homogenization of elasto-plastic porous metals. [International journal of plasticity](#) 29, 102–119.

-
- Galusha, J.W., Richey, L.R., Gardner, J.S., Cha, J.N., Bartl, M.H., 2008. Discovery of a diamond-based photonic crystal structure in beetle scales. [Physical Review E](#) 77, 050904.
- Geuzaine, C., Remacle, J.F., 2009. Gmsh: A 3-d finite element mesh generator with built-in pre-and post-processing facilities. [International journal for numerical methods in engineering](#) 79, 1309–1331.
- Ghazi, A., Berke, P., Tiago, C., Massart, T., 2020. Computed tomography based modelling of the behaviour of closed cell metallic foams using a shell approximation. [Materials & Design](#) 194, 108866.
- Gibson, L., 2000. Mechanical behavior of metallic foams. [Annual review of materials science](#) 30, 191–227.
- Gibson, L.J., Ashby, M.F., Harley, B.A., 2010. Cellular materials in nature and medicine. [Cambridge University Press](#).
- Gong, L., Kyriakides, S., 2005. Compressive response of open cell foams part ii: Initiation and evolution of crushing. [International Journal of Solids and Structures](#) 42, 1381–1399.
- Grenestedt, J.L., 1998. Influence of wavy imperfections in cell walls on elastic stiffness of cellular solids. [Journal of the Mechanics and Physics of Solids](#) 46, 29–50.
- Grenestedt, J.L., Tanaka, K., 1998. Influence of cell shape variations on elastic stiffness of closed cell cellular solids. [Scripta Materialia](#) 40, 71–77.
- Hales, T.C., 1998. The kepler conjecture. [arXiv preprint math.MG/9811078](#) .
- Hashin, Z., Shtrikman, S., 1963. A variational approach to the theory of the elastic behaviour of multiphase materials. [Journal of the Mechanics and Physics of Solids](#) 11, 127 – 140.
- Heinl, P., Rottmair, A., Körner, C., Singer, R.F., 2007. Cellular titanium by selective electron beam melting. [Advanced Engineering Materials](#) 9, 360–364.
- Hengsbach, S., Lantada, A.D., 2014. Direct laser writing of auxetic structures: present capabilities and challenges. [Smart materials and structures](#) 23, 085033.
- Hill, R., 1963. Elastic properties of reinforced solids: Some theoretical principles. [Journal of the Mechanics and Physics of Solids](#) 11, 357 – 372.
- Hill, R., 1998. The mathematical theory of plasticity. volume 11. [Oxford university press](#).
- Hooshmand-Ahooor, Z., Tarantino, M., Danas, K., 2022. Mechanically-grown morphogenesis of voronoi-type materials: Computer design, 3d-printing and experiments. [Mechanics of Materials](#) 173, 104432.

- Hossain, M., Vu, D.K., Steinmann, P., 2012. Experimental study and numerical modelling of vhb 4910 polymer. [Computational Materials Science](#) 59, 65–74.
- Hsieh, M.T., Endo, B., Zhang, Y., Bauer, J., Valdevit, L., 2019. The mechanical response of cellular materials with spinodal topologies. [Journal of the Mechanics and Physics of Solids](#) 125, 401–419.
- Jang, W.Y., Kraynik, A.M., Kyriakides, S., 2008. On the microstructure of open-cell foams and its effect on elastic properties. [International Journal of Solids and Structures](#) 45, 1845–1875.
- Jiménez, F.L., Triantafyllidis, N., 2013. Buckling of rectangular and hexagonal honeycomb under combined axial compression and transverse shear. [International Journal of Solids and Structures](#) 50, 3934–3946.
- Jones, A., Leary, M., Bateman, S., Easton, M., 2021. Tpms designer: A tool for generating and analyzing triply periodic minimal surfaces. [Software Impacts](#) 10, 100167.
- Kairyte, A., Kremensas, A., Balčiūnas, G., Członka, S., Strkowska, A., 2020. Closed cell rigid polyurethane foams based on low functionality polyols: Research of dimensional stability and standardised performance properties. [Materials](#) 13, 1438.
- Kasza, K., Farrell, D., Zallen, J., 2014. Spatiotemporal control of epithelial remodeling by regulated myosin phosphorylation. [PNAS; Proceedings of the National Academy of Sciences](#) 111, 11732–11737.
- Khristenko, U., Constantinescu, A., Tallec, P.L., Oden, J.T., Wohlmuth, B., 2020. A statistical framework for generating microstructures of two-phase random materials: Application to fatigue analysis. [Multiscale Modeling & Simulation](#) 18, 21–43.
- Kumar, A., Lopez-Pamies, O., 2016. On the two-potential constitutive modeling of rubber viscoelastic materials. [Comptes Rendus Mecanique](#) 344, 102–112.
- Kumar, S., Tan, S., Zheng, L., Kochmann, D.M., 2020. Inverse-designed spinodoid meta-materials. [npj Computational Materials](#) 6, 1–10.
- Kurzanski, A., Vályi, I., 1997. Ellipsoidal calculus for estimation and control. [Springer](#).
- Lin, A., Han, S.P., 2002. On the distance between two ellipsoids. [SIAM Journal on Optimization](#) 13, 298–308.
- Linke, J.M., Borin, D.Y., Odenbach, S., 2016. First-order reversal curve analysis of magnetoactive elastomers. [RSC advances](#) 6, 100407–100416.

-
- Liu, L., Kamm, P., Garcia-Moreno, F., Banhart, J., Pasini, D., 2017. Elastic and failure response of imperfect three-dimensional metallic lattices: the role of geometric defects induced by selective laser melting. [Journal of the Mechanics and Physics of Solids](#) 107, 160–184.
- Liu, Z., Tan, J., Cohen, D., Yang, M., Sniadecki, N., Ruiz, S., Nelson, C., Chen, C., 2010. Mechanical tugging force regulates the size of cell–cell junctions. [PNAS; Proceedings of the National Academy of Sciences](#) 107, 9944–9949.
- Lopez-Pamies, O., Gouzarzi, T., Danas, K., 2013. The nonlinear elastic response of suspensions of rigid inclusions in rubber: II—a simple explicit approximation for finite-concentration suspensions. [Journal of the Mechanics and Physics of Solids](#) 61, 19 – 37.
- Luan, S., Kraynik, A.M., Gaitanaros, S., 2022. Microscopic and macroscopic instabilities in elastomeric foams. [Mechanics of Materials](#) 164, 104124.
- Lubachevsky, B.D., Stillinger, F.H., 1990. Geometric properties of random disk packings. [Journal of statistical Physics](#) 60, 561–583.
- Lubachevsky, B.D., Stillinger, F.H., Pinson, E.N., 1991. Disks vs. spheres: Contrasting properties of random packings. [Journal of Statistical Physics](#) 64, 501–524.
- Ma, J., Zhao, Z.L., Lin, S., Xie, Y.M., 2021. Topology of leaf veins: Experimental observation and computational morphogenesis. [Journal of the Mechanical Behavior of Biomedical Materials](#) 123, 104788.
- Martínez, J., Dumas, J., Lefebvre, S., 2016. Procedural voronoi foams for additive manufacturing. [ACM Transactions on Graphics \(TOG\)](#) 35, 1–12.
- Martínez, J., Hornus, S., Song, H., Lefebvre, S., 2018. Polyhedral voronoi diagrams for additive manufacturing. [ACM Transactions on Graphics \(TOG\)](#) 37, 1–15.
- Maskery, I., Aboulkhair, N., Aremu, A., Tuck, C., Ashcroft, I., 2017. Compressive failure modes and energy absorption in additively manufactured double gyroid lattices. [Additive Manufacturing](#) 16, 24–29.
- Mason, G., Beresford, R.H., Walkley, J., Hillier, I.H., Collins, R., Everett, D.H., Finney, J., Domb, C., Smith, B.L., 1967. General discussion. [Discuss. Faraday Soc.](#) 43, 75–88.
- Mbiakop, A., Constantinescu, A., Danas, K., 2015. An analytical model for porous single crystals with ellipsoidal voids. [Journal of the Mechanics and Physics of Solids](#) 84, 436–467.
- McMeeking, R.M., Rice, J., 1975. Finite-element formulations for problems of large elastic-plastic deformation. [International Journal of Solids and Structures](#) 11, 601–616.

- Menges, A., 2012. Biomimetic design processes in architecture: morphogenetic and evolutionary computational design. [Bioinspiration & biomimetics](#) 7, 015003.
- Michel, J., Lopez-Pamies, O., Ponte Castañeda, P., Triantafyllidis, N., 2007. Microscopic and macroscopic instabilities in finitely strained porous elastomers. [Journal of the Mechanics and Physics of Solids](#) 55, 900–938.
- Michel, J.C., Moulinec, H., Suquet, P., 1999. Effective properties of composite materials with periodic microstructure: a computational approach. [Computer methods in applied mechanics and engineering](#) 172, 109–143.
- Moreno-Mateos, M.A., Gonzalez-Rico, J., Nunez-Sardinha, E., Gomez-Cruz, C., Lopez-Donaire, M.L., Lucarini, S., Arias, A., Muñoz-Barrutia, A., Velasco, D., Garcia-Gonzalez, D., 2022. Magneto-mechanical system to reproduce and quantify complex strain patterns in biological materials. [Applied Materials Today](#) 27, 101437.
- Mukherjee, D., Rambašek, M., Danas, K., 2021. An explicit dissipative model for isotropic hard magnetorheological elastomers. [Journal of the Mechanics and Physics of Solids](#) 151, 104361.
- Ohno, N., Okumura, D., Noguchi, H., 2002. Microscopic symmetric bifurcation condition of cellular solids based on a homogenization theory of finite deformation. [Journal of the Mechanics and Physics of Solids](#) 50, 1125–1153.
- O’Masta, M.R., Dong, L., St-Pierre, L., Wadley, H., Deshpande, V.S., 2017. The fracture toughness of octet-truss lattices. [Journal of the Mechanics and Physics of Solids](#) 98, 271–289.
- Onck, P., Andrews, E., Gibson, L., 2001. Size effects in ductile cellular solids. part i: modeling. [International Journal of Mechanical Sciences](#) 43, 681–699.
- Panetta, J., Isvoranu, F., Chen, T., Siéfert, E., Roman, B., Pauly, M., 2021. Computational inverse design of surface-based inflatables. [ACM Transactions on Graphics \(TOG\)](#) 40, 1–14.
- Papka, S., Kyriakides, S., 1994. In-plane compressive response and crushing of honeycomb. [Journal of the Mechanics and Physics of Solids](#) 42, 1499–1532.
- Papka, S., Kyriakides, S., 1998. Experiments and full-scale numerical simulations of in-plane crushing of a honeycomb. [Acta Materialia](#) 46, 2765–2776.
- Perales-Martínez, I.A., Palacios-Pineda, L.M., Lozano-Sánchez, L.M., Martínez-Romero, O., Puente-Cordova, J.G., Elías-Zúñiga, A., 2017. Enhancement of a magnetorheological pdms elastomer with carbonyl iron particles. [Polymer Testing](#) 57, 78–86.

-
- Pierard, O., Gonzalez, C., Segurado, J., Llorca, J., Doghri, I., 2007. Micromechanics of elasto-plastic materials reinforced with ellipsoidal inclusions. [International Journal of Solids and Structures](#) 44, 6945–6962.
- Portela, C.M., Vidyasagar, A., Krödel, S., Weissenbach, T., Yee, D.W., Greer, J.R., Kochmann, D.M., 2020. Extreme mechanical resilience of self-assembled nanolabyrinthine materials. [Proceedings of the National Academy of Sciences](#) 117, 5686–5693.
- Prusty, R., Narayan, R., Scherer, M., Steiner, U., Deshpande, V., Fleck, N., Ramamurty, U., 2020. Spherical indentation response of a ni double gyroid nanolattice. [Scripta Materialia](#) 188, 64–68.
- Rintoul, M.D., Torquato, S., 1997. Reconstruction of the structure of dispersions. [Journal of colloid and interface science](#) 186, 467–476.
- Roberts, A., Garboczi, E., 2001. Elastic moduli of model random three-dimensional closed-cell cellular solids. [Acta Materialia](#) 49, 189 – 197.
- Roberts, A.P., Teubner, M., 1995. Transport properties of heterogeneous materials derived from gaussian random fields: Bounds and simulation. [Physical Review E](#) 51, 4141–4154.
- Ronan, W., Deshpande, V.S., Fleck, N.A., 2016. The tensile ductility of cellular solids: the role of imperfections. [International Journal of Solids and Structures](#) 102, 200–213.
- Roudavski, S., 2009. Towards morphogenesis in architecture. [International journal of architectural computing](#) 7, 345–374.
- San Marchi, C., Mortensen, A., 2001. Deformation of open-cell aluminum foam. [Acta materialia](#) 49, 3959–3969.
- Schaedler, T.A., Carter, W.B., 2016. Architected cellular materials. [Annual Review of Materials Research](#) 46, 187–210.
- Schaedler, T.A., Jacobsen, A.J., Torrents, A., Sorensen, A.E., Lian, J., Greer, J.R., Valdevit, L., Carter, W.B., 2011. Ultralight metallic microlattices. [Science](#) 334, 962–965.
- Schoen, A.H., 1970. Infinite periodic minimal surfaces without self-intersections. [NASA Technical Reports](#) .
- Schröder-Turk, G.E., Wickham, S., Averdunk, H., Brink, F., Gerald, J.F., Poladian, L., Large, M., Hyde, S., 2011. The chiral structure of porous chitin within the wing-scales of callophrys rubi. [Journal of structural biology](#) 174, 290–295.
- Schwarz, H.A., 1972. Gesammelte mathematische abhandlungen. volume 260. [American Mathematical Soc.](#)

- Segurado, J., Llorca, J., 2002. A numerical approximation to the elastic properties of sphere-reinforced composites. [Journal of the Mechanics and Physics of Solids](#) 50.
- Simone, A., Gibson, L., 1998. Effects of solid distribution on the stiffness and strength of metallic foams. [Acta Materialia](#) 46, 2139–2150.
- Singamaneni, S., Tsukruk, V.V., 2010. Buckling instabilities in periodic composite polymeric materials. [Soft Matter](#) 6, 5681–5692.
- Smith, M., 2009. ABAQUS/Standard User’s Manual, Version 6.9. [Dassault Systèmes Simulia Corp](#), United States.
- Smith, M., Guan, Z., Cantwell, W., 2013. Finite element modelling of the compressive response of lattice structures manufactured using the selective laser melting technique. [International Journal of Mechanical Sciences](#) 67, 28–41.
- Smith, T.L., 1963. Ultimate tensile properties of elastomers. i. characterization by a time and temperature independent failure envelope. [Journal of Polymer Science Part A: General Papers](#) 1, 3597–3615.
- Soyarslan, C., Blümer, V., Bargmann, S., 2019. Tunable auxeticity and elastomechanical symmetry in a class of very low density core-shell cubic crystals. [Acta Materialia](#) 177, 280–292.
- Spyrou, L., Brisard, S., Danas, K., 2019. Multiscale modeling of skeletal muscle tissues based on analytical and numerical homogenization. [Journal of the Mechanical Behavior of Biomedical Materials](#) 92, 97 – 117.
- Symons, D.D., Fleck, N.A., 2008. The imperfection sensitivity of isotropic two-dimensional elastic lattices. [Journal of Applied Mechanics](#) 75.
- Tancogne-Dejean, T., Diamantopoulou, M., Gorji, M.B., Bonatti, C., Mohr, D., 2018. 3d plate-lattices: An emerging class of low-density metamaterial exhibiting optimal isotropic stiffness. [Advanced Materials](#) 30, 1803334.
- Tankasala, H., Deshpande, V., Fleck, N., 2017. Tensile response of elastoplastic lattices at finite strain. [Journal of the Mechanics and Physics of Solids](#) 109, 307–330.
- Tarantino, M., Mortensen, A., 2022. On the bulk compressibility of close-packed particles and their composites. [Composites Part A: Applied Science and Manufacturing](#) 161, 107106.
- Tarantino, M., Zerhouni, O., Danas, K., 2019. Random 3d-printed isotropic composites with high volume fraction of pore-like polydisperse inclusions and near-optimal elastic stiffness. [Acta Materialia](#) 175, 331 – 340.

-
- Tarantino, M.G., Danas, K., 2019. Programmable higher-order euler buckling modes in hierarchical beams. [International Journal of Solids and Structures](#) 167, 170–183.
- Tekoglu, C., Gibson, L., Pardoan, T., Onck, P., et al., 2011. Size effects in foams: Experiments and modeling. [Progress in Materials Science](#) 56, 109–138.
- Teubner, M., 1991. Level surfaces of gaussian random fields and microemulsions. [Europhysics Letters \(EPL\)](#) 14, 403–408.
- Thornton, P., Magee, C., 1975. Deformation characteristics of zinc foam. [Metallurgical Transactions A](#) 6, 1801–1807.
- Tidball, J.G., Wehling-Henricks, M., 2004. Evolving therapeutic strategies for duchenne muscular dystrophy: targeting downstream events. [Pediatric Research](#) 56, 831–841.
- Torquato, S., 1997. Effective stiffness tensor of composite media—i. exact series expansions. [Journal of the Mechanics and Physics of Solids](#) 45, 1421 – 1448.
- Torquato, S., 2002. Random Heterogeneous Materials: Microstructure and Macroscopic Properties. [Springer, New York](#).
- Triantafyllou, T., Gibson, L., 1990. Multiaxial failure criteria for brittle foams. [International journal of mechanical sciences](#) 32, 479–496.
- Triantafyllidis, N., Schraad, M., 1998. Onset of failure in aluminum honeycombs under general in-plane loading. [Journal of the Mechanics and Physics of Solids](#) 46, 1089–1124.
- van Nuland, T., van Dommelen, J., Geers, M., 2021. An anisotropic voronoi algorithm for generating polycrystalline microstructures with preferred growth directions. [Computational Materials Science](#) 186, 109947.
- Wang, F., Sigmund, O., 2021. 3d architected isotropic materials with tunable stiffness and buckling strength. [Journal of the Mechanics and Physics of Solids](#) 152, 104415.
- Wang, L., Limodin, N., El Bartali, A., Charkaluk, E., 2021. Coupling of x-ray computed tomography and surface in situ analysis combined with digital image correlation method to study low cycle fatigue damage micromechanisms in lost foam casting a319 alloy. [Fatigue & Fracture of Engineering Materials & Structures](#) 44, 916–932.
- Warren, W.E., Kraynik, A.M., 1997. Linear Elastic Behavior of a Low-Density Kelvin Foam With Open Cells. [Journal of Applied Mechanics](#) 64, 787–794.
- Widom, B., 1966. Random sequential addition of hard spheres to a volume. [The Journal of Chemical Physics](#) 44, 3888–3894.
- Wu, J., Aage, N., Westermann, R., Sigmund, O., 2017. Infill optimization for additive manufacturing—approaching bone-like porous structures. [IEEE transactions on visualization and computer graphics](#) 24, 1127–1140.

- Zerhouni, O., 2019. A study on the effective elastic properties of random porous materials: 3D Printing, Experiments and Numerics. Ph.D. thesis. [Institut Polytechnique de Paris](#).
- Zerhouni, O., Brisard, S., Danas, K., 2021. Quantifying the effect of two-point correlations on the effective elasticity of specific classes of random porous materials with and without connectivity. [International Journal of Engineering Science](#) 166, 103520.
- Zerhouni, O., Tarantino, M., Danas, K., 2019. Numerically-aided 3d printed random isotropic porous materials approaching the hashin-shtrikman bounds. [Composites Part B: Engineering](#) 156, 344 – 354.
- Zerhouni, O., Tarantino, M.G., Danas, K., Hong, F., 2018. Influence of the internal geometry on the elastic properties of materials using 3d printing of computer-generated random microstructures, in: [2018 SEG International Exposition and Annual Meeting](#), OnePetro.
- Zhao, Z.L., Zhou, S., Feng, X.Q., Xie, Y.M., 2018. On the internal architecture of emergent plants. [Journal of the Mechanics and Physics of Solids](#) 119, 224–239.

Titre : Génération assistée par ordinateur, impression 3D et étude expérimentale de matériaux poreux et composites

Mots clés : Matériaux architecturés, Matériaux poreux, Croissance de cavités, Fabrication additive, Expériences de déformation finie, Homogénéisation

Résumé : Cette étude porte sur la conception assistée par ordinateur, l'impression 3D, la simulation numérique à grandes transformations et la caractérisation expérimentale de géométries aléatoires, en mettant l'accent sur les matériaux poreux. En particulier, nous cherchons à quantifier l'effet des architectures aléatoires sur la réponse mécanique en grandes transformations de géométries poreuses aléatoires et périodiques bien choisies. Nous proposons une nouvelle famille de matériaux poreux de type Voronoï appelés M-Voronoï contenant de pores de taille hétérogène et de ligaments d'épaisseur variable. Ces matériaux peuvent atteindre des densités relatives très faibles, et sont obtenus à l'aide de simulations numériques par un processus de croissance de pores dans une matrice élastique non linéaire et à grandes transformations. La méthode M-Voronoï proposée est versatile et peut être appliquée pour créer des géométries aléatoires bidimensionnelles et tridimensionnelles avec (an-)isotropie contrôlée. Dans la suite de l'étude, nous nous sommes intéressés à la caractérisation expérimentale des matériaux poreux ainsi obtenus. Ceux-ci ont été fabriqués par impression 3D polymère via la technologie PolyJet en utilisant une résine, appelée TangoBlack, polymère hautement visqueuse, dont la loi de comportement a été quantifiée à l'aide des essais mécaniques et caractérisé par un modèle viscoélastique

non linéaire formulé pour les élastomères isotropes incompressibles. Par la suite, des essais de compression uniaxiales ont été menés pour étudier la réponse mécanique de structures poreuses 3D-imprimées en TangoBlack. Ceux-ci ont montrés que, dans le régime de grandes transformations les géométries M-Voronoï ont des propriétés mécaniques améliorées du fait de leur architecture poreuse. Notamment, leur réponse sous compression durcie bien avant la densification et devient similaire à celle de géométries Voronoï aléatoires érodées à de faibles densités. Dans la dernière partie de cette étude, nous avons étudié à l'aide de simulations numériques les propriétés mécaniques des géométries poreuses aléatoires tridimensionnelles constituées de M-Voronoï, de matériaux poreux polydispersés avec des vides sphériques, et des géométries classiques de type TPMS. Les simulations ont été menées à grandes transformations sous une charge de compression tout en considérant la matrice comme un matériau élastique-parfaitement plastique sans durcissement. Ces résultats ont montré que l'écoulement plastique accrue dans les géométries à topologies aléatoires par rapport aux structures périodiques TPMS. Ce comportement est expliqué en observant que la déformation se localise dans les géométries avec motif périodique, contrairement aux géométries aléatoires qui présentent une localisation plutôt diffusée.

Title : Computer-aided generation, 3D-printing and experimental study of porous and composite materials

Keywords : Architected materials, Porous materials, Void growth, Additive manufacturing, Finite strain experiments, Homogenization

Abstract : The present study deals with computer-aided design, 3D-printing, large strain numerical simulation, and experimental testing of random geometries with focus on porous materials. In particular, we attempt to assess the effect of random porous features on the mechanical response at large strain by comparing the response of well-chosen random and periodic porous geometries. We propose a novel computer-aided design strategy to obtain a new type of random Voronoi-type porous materials called M-Voronoi with smooth void shapes and variable intervoid ligament sizes that can reach very low relative densities. This is achieved via a numerical, large strain, nonlinear elastic, void growth mechanical process. The proposed M-Voronoi method is general and can be applied to create both two and three-dimensional random geometries and allows the formation of isotropic or anisotropic materials. In the next part of the study, we fabricate the designed porous materials with a polymer 3D-printer via PolyJet technology and a UV-curable resin called TangoBlack which is a highly viscous soft polymer with brittle fracture. Meanwhile, the viscous behavior of TangoBlack is studied under uniaxial tensile, loading-unloading, and relaxation tests on a new proposed specimen geometry and is subsequently characterized by a nonlinear rubber viscoelastic model for incompressible isotropic elastomers. We then use this

material to 3D-print the designed two-dimensional porous materials with square representative geometries and isotropic/anisotropic features in terms of void size and realization. The mechanical response of the fabricated porous materials is experimentally investigated by testing them under uniaxial large strain compression and low strain rates. We show that the randomness of the proposed M-Voronoi geometries and their non-uniform intervoid ligament size leads to enhanced mechanical properties at large compressive strains with no apparent peak-stress and strong hardening well before densification, while they become very close to random eroded Voronoi geometries at low densities. In the last part of this study, we investigate numerically the mechanical properties of the three-dimensional random porous geometries consisting of M-Voronoi, polydisperse porous materials with spherical voids, and classical TPMS-like geometries. The simulations are performed at large strains under compression loading while considering the matrix an elastic-perfectly plastic material without hardening. We observe enhanced plastic flow stress in the geometries with random topologies as opposed to the TPMS periodic structures. This behavior is explained by noting that deformation localizes in geometries with a periodic pattern, contrary to the random geometries which exhibit a rather diffused localization.